Nanoarchitecture of hippocampal mossy fiber-CA3 pyramidal neuron synapses

by

Olena Kim

April, 2022

A thesis submitted to the
Graduate School
of the
Institute of Science and Technology Austria
in partial fulfillment of the requirements
for the degree of
Doctor of Philosophy

Committee in charge:
Eva Benková, Chair
Peter Jonas
Ryuichi Shigemoto
Christian Rosenmund

The thesis of Olena Kim, titled “Nanoarchitecture of hippocampal mossy fiber-CA3 pyramidal neuron synapses”, is approved by:

Supervisor: Peter Jonas, ISTA, Klosterneuburg, Austria

Signature: _____

Committee Member: Ryuichi Shigemoto, ISTA, Klosterneuburg, Austria

Signature: _____

Committee Member: Christian Rosenmund, Charité - Universitätsmedizin Berlin, Berlin, Germany

Signature: _____

Defense Chair: Eva Benková, ISTA, Klosterneuburg, Austria

Signature: _____

Signed page is on file

ISTA Thesis, ISSN: 2663-337X

I hereby declare that this thesis is my own work and that it does not contain other people's work without this being so stated; this thesis does not contain my previous work without this being stated, and the bibliography contains all the literature that I used in writing the dissertation.

I declare that this is a true copy of my thesis, including any final revisions, as approved by my thesis committee, and that this thesis has not been submitted for a higher degree to any other university or institution.

I certify that any republication of materials presented in this thesis has been approved by the relevant publishers and co-authors.

Signature: _____

Olena Kim

April, 2022

Signed page is on file

Abstract

One of the fundamental questions in Neuroscience is how the structure of synapses and their physiological properties are related. While synaptic transmission remains a dynamic process, electron microscopy provides images with comparably low temporal resolution (Studer et al., 2014). The current work overcomes this challenge and describes an improved “Flash and Freeze” technique (Watanabe et al., 2013a; Watanabe et al., 2013b) to study synaptic transmission at the hippocampal mossy fiber-CA3 pyramidal neuron synapses, using mouse acute brain slices and organotypic slices culture. The improved method allowed for selective stimulation of presynaptic mossy fiber boutons and the observation of synaptic vesicle pool dynamics at the active zones. Our results uncovered several intriguing morphological features of mossy fiber boutons. First, the docked vesicle pool was largely depleted (more than 70%) after stimulation, implying that the docked synaptic vesicles pool and readily releasable pool are vastly overlapping in mossy fiber boutons. Second, the synaptic vesicles are skewed towards larger diameters, displaying a wide range of sizes. An increase in the mean diameter of synaptic vesicles, after single and repetitive stimulation, suggests that smaller vesicles have a higher release probability. Third, we observed putative endocytotic structures after moderate light stimulation, matching the timing of previously described ultrafast endocytosis (Watanabe et al., 2013a; Delvendahl et al., 2016).

In addition, synaptic transmission depends on a sophisticated system of protein machinery and calcium channels (Südhof, 2013b), which amplifies the challenge in studying synaptic communication as these interactions can be potentially modified during synaptic plasticity. And although recent study elucidated the potential correlation between physiological and morphological properties of synapses during synaptic plasticity (Vandael et al., 2020), the molecular underpinning of it remains unknown. Thus, the presented work tries to overcome this challenge and aims to pinpoint changes in the molecular architecture at hippocampal mossy fiber bouton synapses during short- and long-term potentiation (STP and LTP), we combined chemical potentiation, with the application of a cyclic adenosine monophosphate agonist (i.e. forskolin) and freeze-fracture replica immunolabelling. This method allowed the localization of membrane-bound proteins with nanometer precision within the active zone, in particular, P/Q-type calcium channels and synaptic vesicle priming proteins Munc13-1/2. First, we found that the number of clusters of Munc13-1 in the mossy fiber bouton active zone increased significantly during STP, but decreased to lower than the control value during LTP. Secondly, although the distance between the calcium channels and Munc13-1s did not change after induction of STP, it shortened during the LTP phase. Additionally, forskolin did not affect Munc13-2 distribution during STP and LTP. These results indicate the existence of two distinct mechanisms that govern STP and LTP at mossy fiber bouton synapses: an increase in the readily realizable pool in the case of STP and a potential increase in release probability during LTP. “Flash and freeze” and functional electron microscopy, are versatile methods that can be successfully applied to intact brain circuits to study synaptic transmission even at the molecular level.

Acknowledgments

First of all, I would like to thank my supervisor Prof. Peter Jonas for giving me the opportunity to work on my doctoral project in his laboratory, for the support and guidance during my studies. Moreover, Prof. Jonas taught me to be confident and passionate about the things that interest me and to defend my professional opinion. Furthermore, I would like to say thank you to Prof. Ryuichi Shigemoto for providing scientific advice and carefully reading my doctoral thesis. To Prof. Christian Rosenmund for critically reading the dissertation.

Furthermore, I would also like to acknowledge Dr. Carolina Borges-Merjane, a colleague and a friend. Throughout the whole project, she taught me to find unconventional solutions to problems, determination, and patience to repeat necessary experiments and to recognize repetition-worthy ones. Additionally, I thank Dr. Benjamin Sutter for fruitful discussions and excellent pieces of advice. Furthermore, I thank the entire Peter Jonas laboratory, all members contributed to the success of the project and made the time in the lab very rewarding.

In addition, I would like to thank Electron Microscopy Facility at ISTA, in particular Dr. Vanessa Zheden, Dr. Walter Kaufman, and Daniel Gütl, for their outstanding scientific support and patience with teaching newcomers electron microscopy techniques. Moreover, I would like to acknowledge Pre-clinical facility at ISTA, Michael Schunn, and Victoria Wimmer for taking care of the animal colony.

Finally, I am grateful to the whole cohort of 2015 students. In particular, I want to thank Feyza Nur Arslan and Marijo Jevtic for their friendship and support in an academic and non-academic manner.

The project has received funding from the European Research Council and European Union's Horizon 2020 research and innovation programme (ERC 692692 and Marie Sklodowska-Curie 708497) and from Fond zur Förderung der Wissenschaftlichen Forschung (Z 312-B27 Wittgenstein award; W1205-B09).

I dedicate this doctoral dissertation to my family and friends in Ukraine, who supported me and believed in me throughout my doctoral training.

About the Author

Olena Kim was born in the beautiful and courageous city of Kyiv, the capital of Ukraine. There she obtained Bachelor's and Master's degrees with honors in Biology and Biophysics respectfully. In 2015, she moved to Austria to start her doctoral studies at the Institute of Science and Technology Austria (ISTA). Here she joined the lab of Professor Peter Jonas, which is focused on the investigation of synaptic communication in hippocampal microcircuits. Her PhD project is about understanding the relation between function and structure during neuronal activity.

During her training, Olena presented parts of her work at several conferences and meetings, such as Gordon Research Conference on Synaptic Transmission (2018) and Society for Neuroscience Annual Meeting (2018). In addition, she in collaboration with Leica Microsystems gave a webinar about the new method of cryo-fixation that she developed in the scope of her PhD project. Moreover, in 2021 Olena together with her colleague Dr. Carolina Borges-Merjane received the Fritz-Grasenick-Award 2019 from the Austrian Society for Electron Microscopy for the best published work in the field of electron microscopy.

List of Collaborators, Publications, and Presentations

Borges-Merjane C*, **Kim O***, and Jonas P. “Functional electron microscopy (“flash and freeze”) of identified cortical synapses in acute brain slices” Neuron, 2020; 105(6):992-1006, DOI: https://doi.org/10.1016/j.neuron.2019.12.022 [Cover Article]

**co-authors with equal contributions. Kim O. (organotypic slice culture) performed all experiments and data analysis.*

Kim O, Borges-Merjane C, and Jonas P. “Functional analysis of the docked vesicle pool in hippocampal mossy fiber terminals by electron microscopy.” Intrinsic Activity, 2019; 7 (Suppl. 1): A3.27, DOI: doi:10.25006/IA.7.S1-A3.27 *(Conference Abstract)*

Kim O, Borges-Merjane C, Jonas P. “Structural Correlates of Transmitter Release and Readily Releasable Vesicle Pool at Hippocampal Mossy Fiber Synapses.” Gordon Research Conference on Synaptic Transmission 2018, Waterville Valley, NH, U.S.A. *(Poster)*

Borges-Merjane C, **Kim O**, and Jonas P. “Structural Correlates of Transmitter Release and Readily Releasable Vesicle Pool at Hippocampal Mossy Fiber Synapses.” Program No. 559.11, Society for Neuroscience Annual Meeting 2018, San Diego, CA, U.S.A. *(Poster)*

Leroux F, **Kim O**, and Borges-Merjane C. “High-pressure freezing: Revealing functional mechanisms of synaptic transmission.” Leica Microsystems Webinar 2020, https://www.leica-microsystems.com/high-pressure-freezing-revealing-functional-mechanisms-of-synaptic-transmission/

Table of Contents

List of Figures

List of Tables

List of Abbreviations

AC – adenylyl cyclase

ACSF – artificial cerebrospinal fluid

AMPA – α-amino-3-hydroxy-5-methyl-4-isoxazolepropionic acid

AP – action potential

AZ – active zone

CA – cornu ammonis

cAMP – cycle adenosine monophosphate

CAST – CAZ-associated structural protein

DAG – diacylglycerol

DBSCAN – density-based spatial clustering of applications with noise

DIV – days *in vitro*

DMSO – dimethyl sulfoxide

ELKS – protein rich in the amino acids E, L, K, and S

EM – electron microscopy

EPSC – excitatory post-synaptic currents

FRIL – freeze-fracture immunolabeling

FS – freeze substitution

FSK – forskolin

GC – granule cell

HFS – high-frequency stimulation

HPF – high-pressure freezing

IN – interneuron

LTP – long-term potentiation

MEC – medial entorhinal cortex

MF – mossy fiber

MFB – mossy fiber bouton

Munc – mammalian uncoordinated homology

NGS – normal goat serum

NMDA – N-methyl-D-aspartate

NND – nearest neighbor distance

PA – puncta adherentia

PB – phosphate buffer

PFA – paraformaldehyde

PIP_2 – phosphatidylinositol 4,5-bisphosphate

PN – pyramidal neuron

PPF – paired-pulse facilitation

Prox1 – Prospero homeobox 1

PTP – post-tetanic potentiation

RIM – Rab3-interacting molecule

RIM-BP – Rab3-interacting molecule-binding protein

RRP – readily releasable pool

SNAP-25 – synaptosomal associated protein of 25 kilodaltons

SNARE – soluble N-ethylmaleimide-sensitive factor attachment protein receptor

STP – short-term potentiation

SV – synaptic vesicle

TBS – Tris-buffered saline

TEM – transmission electron microscopy

TTX – tetrodotoxin

VAMP – vesicular associated membrane protein

VGCC – voltage-gated calcium channels

HBSS – Hanks' Balanced Salt Solution

CHAPTER 1. INTRODUCTION

1.1 Hippocampus as a key element in memory formation

The human brain is an extraordinarily complex organ consisting of almost 90 billion cells, called neurons (Azevedo et al., 2009), which can control basic physiological functions, such as respiration, as well as higher cognitive functions, such as analysis of a novel environment and problem-solving (Diamond, 1990). The hippocampus (from greek ἱππόκαμπος, “seahorse”) is located in the medial temporal lobe and is one of the most studied regions in the brain (Bird and Burgess, 2008). It is involved in the Papez’s circuit, which also consists of anterior thalamus nuclei, mammillary bodies of the hypothalamus, and cingulate cortex (Fig. 1-1; Bird and Burgess, 2008). The hippocampus, not only in humans but also in rodents, is highly connected to other brain regions: the amygdala, temporal lobe, and parietal lobes through the entorhinal cortex (Fig. 1-1). It is an important part of the limbic system in the mammalian brain and plays an essential role in learning and memory formation, especially during spatial exploration and establishment of cognitive maps (O’Keefe, 1978; Milner et al., 1998). The involvement of the hippocampus in memory formation was first hypothesized in the work with the famous H.M. patient (Scoville and Milner, 1957). That report described a case of a patient that was surgically treated to relieve epileptic seizures; in the process, the hippocampus and surrounding temporal lobe structures were removed. As a result of this procedure, H.M. could not form new declarative memories, which are memories that can be consciously accessible. However, semantic memory and short-term memory stayed intact (Scoville and Milner, 1957).

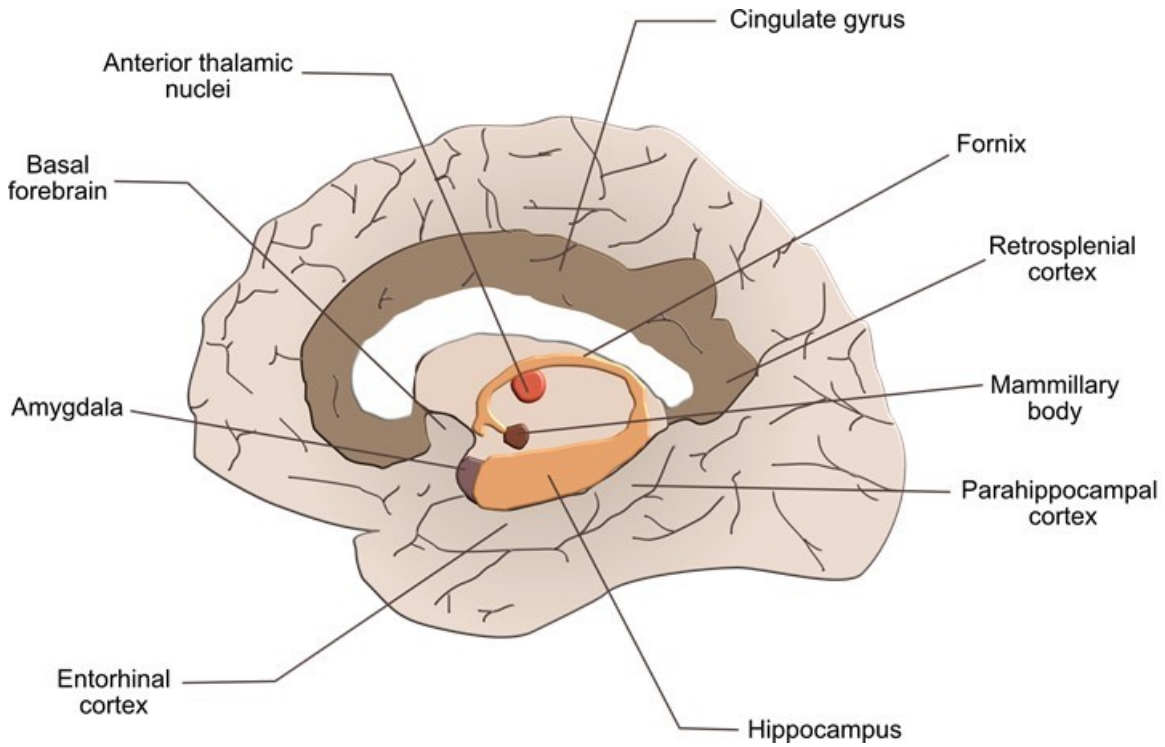

Figure 1-1. The human hippocampus and surrounding structures. The hippocampus is located in the medial temporal lobe is connected to the amygdala, other parts of the temporal lobe, and the entorhinal cortex (based on Bird and Burgess, 2008).

This discovery opened up an avenue to a new field of research - the neurobiology and computational basis of memory formation in humans and animal models (Bird and Burgess, 2008). Now it is well established that there are two distinct coding processes taking place in the hippocampus: pattern separation and pattern completion (Leutgeb and Leutgeb, 2007). The former leads to a multiplication of differences in an input signal. In contrast, pattern completion reactivates neural representation from only a subset of that representation. Both are linked to particular microcircuits and cell types in the hippocampal formation (Guzman et al., 2016; Espinoza et al., 2018).

1.2 Microcircuits in the hippocampus

The hippocampus is a layered structure consisting of the dentate gyrus (DG; molecular layer with dendrites from cell bodies of granule cells (GCs)), hilus, and hippocampus proper (cornu ammonis regions - CA1, CA2, CA3; Fig. 1-2). The main input to the hippocampus comes from the medial entorhinal cortex (MEC), which projects to the dendrites of GCs and pyramidal cells in the CA1 region (Fig.1-2). This is the beginning of the well-known trisynaptic pathway, the canonical hippocampal circuit. Next GCs of DG project mossy fiber (MF) axons to CA3 pyramidal neurons (PN), which in turn send Schaffer collaterals, axons of CA3 neurons, to the CA1 area (Fig. 1-2; Witter and Amaral, 2004). According to several recent reports, DG and CA3 regions play important roles in pattern separation and pattern completion, respectively (Guzman et al., 2016; Espinoza et al., 2018; Guzman et al., 2021). MF axons and terminals ensure a smooth transition between these processes. Moreover, they are very unique structures, that do not have any analogs in the ortex (see Section 1.4. Hippocampal mossy fiber bouton microcircuits).

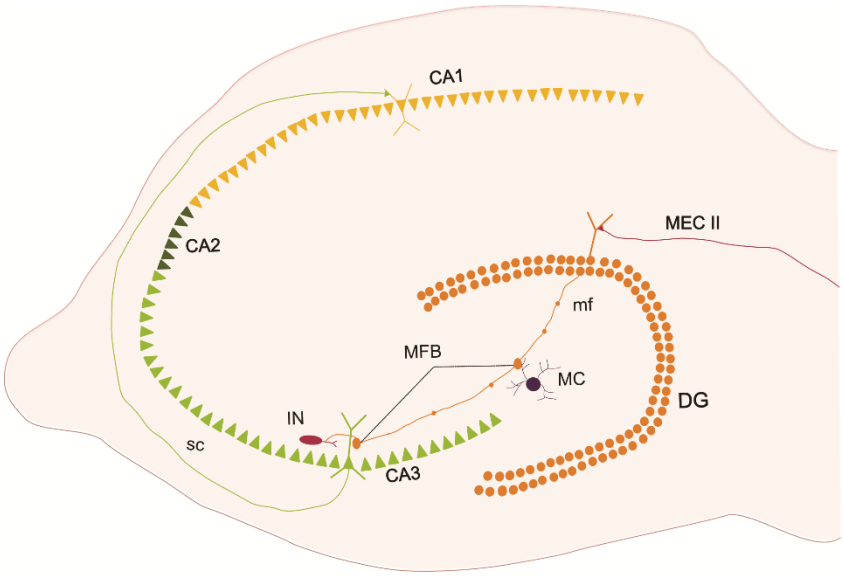

Figure 1-2. The structure of hippocampal formation. The dentate gyrus (DG) receives input from medial entorhinal cortex layer 2 (MEC II, rose line). In turn, GCs (orange circles) of DG send mossy fiber (mf, orange line) axons, through hilus with mossy cells (MC, purple circle), to CA3 PN (green triangles). CA3 PNs connect to CA1 PNs (yellow triangles) with Schaffer collaterals (sc; green line), bypassing CA2 PNs (dark green triangles). Mf forms two types of terminals mossy fiber boutons (MFB) on MCs and CA3 PNs, and small terminals on interneurons (IN).

Mossy fibers were first discovered by the Spanish histologist and neuroscientist Santiago Ramón y Cajal at the end of the 19th century (Ramón y Cajal, 1894; Ramón y Cajal, 1911). He documented the existence of hippocampal connections with rather

distinct morphology and called them “fibre moussues” or mossy fibers (MF), the unmyelinated axons of GCs. Subsequent anatomical studies reported the presence of three types of MF terminals (Fig. 1-2; Amaral, 1979; Claiborne et al., 1986; Frotscher et al., 1991; Acsády et al., 1998):

- large mossy fiber boutons (MFB) that project onto CA3 PN and mossy cells in the hilus (diameter 2–8 µm);
- small filopodial extensions (diameter 0.5–2.0 µm) that are connected to inhibitory interneurons in the hilus and stratum lucidum;
- small *en passant* varicosities (diameter 0.5–2.0 µm) terminate on GABAergic interneurons (IN).

It is unmistakable that the morphological and physiological properties of synapses determine the circuity dynamics and coding capabilities of a neural network (Rebola et al., 2019). And this is also true for the aforementioned MF terminals and their synapses (Vyleta et al., 2016; Vandael et al., 2020). Regulation of neuronal output is strongly dependent on temporal and spatial summation, that act like integrators of synaptic events of different magnitudes, locations, and durations (Magee and Johnston, 2005; Spruston, 2008). For example, coincident pre- and postsynaptic firing or repetitive presynaptic activity can lead to a strengthening of synapses between two or more neurons with variable duration (Bliss and Gardner-Medwin, 1973; Abraham et al., 2002; Vyleta et al., 2016). Other ways to express synaptic plasticity, the ability of a synapse to change its strength and activity, are increased presynaptic potency in activating the postsynaptic site or recruitment of postsynaptic receptor complexes. Notably, these changes contribute to the cellular basis of learning and memory in the hippocampus (Nicoll and Malenka, 1995; Nicoll and Schmitz, 2005; Lüscher et al., 2012).

1.3 Synaptic transmission

The information flow in the hippocampus, as in the whole brain in general, relies on the accurately functioning synapses, where the release of neurotransmitters from the presynaptic side into the synaptic cleft activates receptors on the postsynaptic side. Ion-flux through receptors leads to membrane potential change in the postsynaptic dendrite (Fig. 1-3A; del Castillo and Katz, 1954; Heuser and Reese, 1981; Sheng and Kim, 2011; Wang and Dudko, 2021). Further, this change in postsynaptic membrane potential will travel to the neuronal soma, and upon the spatial or temporal summation of signals from multiple synapses, will evoke an action potential (AP) that can subsequently travel down the axon to activate the next postsynaptic neuron. This intricate procedure relies on a specific sequence of events that occur at the presynaptic terminal in less than a millisecond (Fig. 1-3A):

1. AP arrives at the presynaptic terminal, depolarizing the membrane.
2. Voltage-gated calcium channels (VGCC) open, increasing local intracellular Ca^{2+} ions concentration.
3. Ca^{2+} ions activate calcium sensors of transmitter release.
4. Synaptic vesicles (SV) are exocytosed: the fusion protein machinery is activated and SV fuses with the plasma membrane, releasing neurotransmitters and activating postsynaptic receptors.

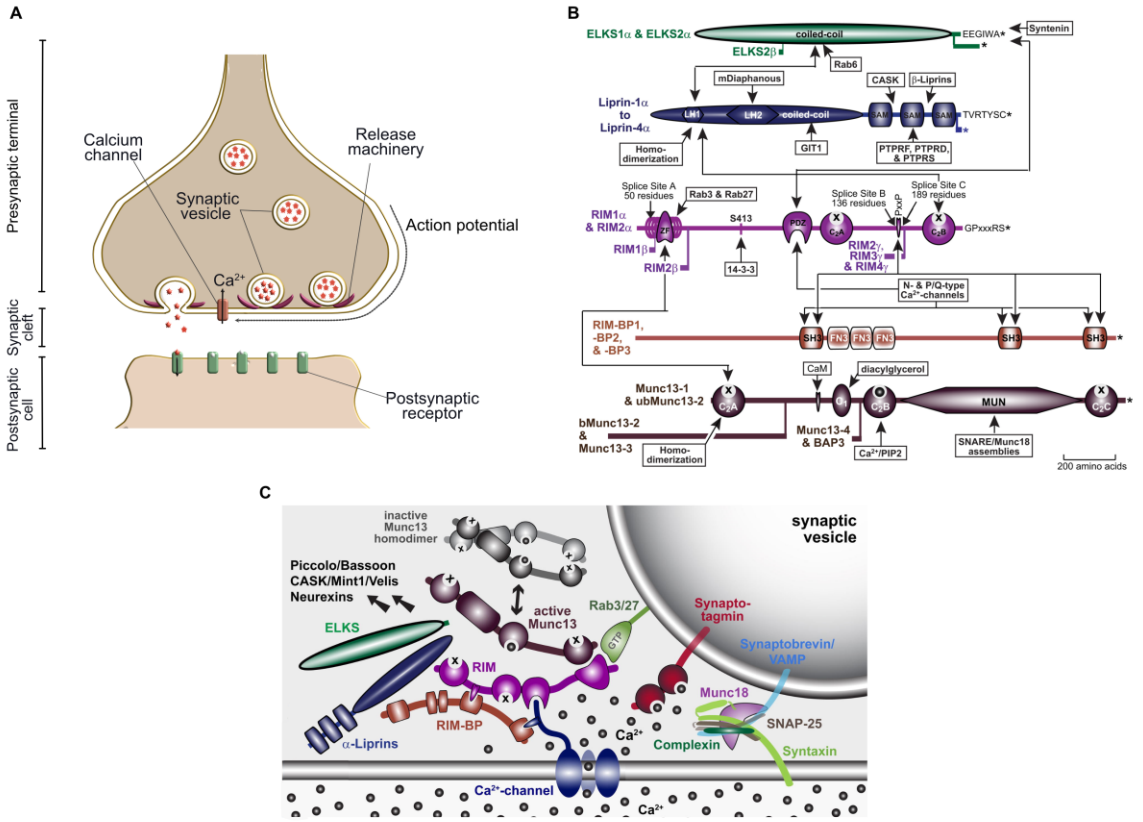

Figure 1-3. Synapses are key elements of neural communication. **(A),** Scheme of synaptic connections consisting of presynaptic terminal, with calcium channels, synaptic vesicles, and release machinery, synaptic cleft, and postsynaptic cell with neurotransmitter receptors. **(B),** Schematic depiction of five core AZ proteins and their domains. **(C),** Active zone proteins and their interactions with each other. (B, C) modified from Südhof, 2012.

Therefore, synaptic transmission is a process that transforms electrical signals (changes in membrane potential, AP generation) to chemical signals (Ca^{2+} ions inflow and neurotransmitter release), that in turn are converted again into the electrical response at the postsynaptic side (Borst and Sakmann, 1996; Sabatini and Regehr, 1996; Eggermann et al., 2012). This milliseconds long process takes place in a specific part of the presynaptic plasma membrane, called the active zone (AZ; Couteaux and Pécot-Dechavassine, 1970; Dreyer et al., 1973) and depends on precise mechanisms controlled by the sophisticated protein release machinery (Fig. 1-3B–C; Südhof, 2012; Südhof, 2013a; Südhof, 2013b).

1.3.1 Active zone architecture

The AZ protein machinery is composed of detergent insoluble proteins that are heterogeneous in their composition, function, and size. In the results of extensive biochemical, immunohistochemical, and genetic studies, we can identify the key elements of the SV release machinery: Rab3-interacting molecule (RIM), mammalian uncoordinated homology 13 (Munc13) protein, Rab3-interacting molecule-binding protein (RIM-BP), α-liprin, and the protein rich in the amino acids E, L, K, and S (ELKS) or CAZ-associated structural protein (CAST) (Fig1-3B; Südhof, 2012; Südhof, 2013b). The first three are multidomain proteins composed of a string of identifiable modules and often have several isoforms in the mammalian brain (Fig. 1-3B; Augustin et al., 1999a; Mittelstaedt and Schoch, 2007; Kaeser et al., 2008), whereas α-liprin and

ELKS exhibit a simpler structure (Fig. 1-3B). The primary function of these five core proteins is precise docking and priming of SVs and anchoring VGCCs in the AZ. In addition, they can position (tether) undocked SV near the AZ (Han et al., 2011; Kaeser et al., 2011; Kaeser et al., 2012; Imig et al., 2014).

Another important element of the AZ proteome is the SNARE (soluble N-ethylmaleimide-sensitive factor attachment protein receptor) complex (Südhof, 2012; Südhof, 2013a; Südhof, 2013b). Specifically, the SNARE complex brings the SV and plasma membrane together, thus enabling fusion and overcoming the repulsion of electrostatic forces (Weber et al., 1998; Tucker et al., 2004). It consists of v-SNARE synaptobrevin-2 (Syb2, also known as vesicular associated membrane protein (VAMP)), t-SNARE syntaxin-1 (Syx1), and synaptosomal associated protein of 25 kilodaltons (SNAP-25) (Söllner et al., 1993). In addition, Munc18 (mammalian uncoordinated 18) protein also interacts with the SNARE complex, with a role in promoting or inhibiting its' assembly (see section 1.3.2. Munc13s mediate vesicle priming and release; Ma et al., 2015; Shu et al., 2020).

1.3.2 Munc13s mediate vesicle priming and release

An invertebrate homolog of Munc13 – unc-13 was first identified in *C. elegans* as a gene encoding a diacylglycerol (DAG)-binding protein whose mutation caused diverse defects in the nervous system (Maruyama and Brenner, 1991). Several years later, Brose and colleagues characterized the mammalian homologs of UNC-13 and found that Munc13 proteins are essential for SV priming and release (Brose et al., 1995; Augustin et al., 1999a; Augustin et al., 1999b).

The mammalian brain contains several isoforms of the Munc13 protein – Munc13-1, -2, and -3, with molecular mass 200 kDa, 220 kDa, and 240 kDa, respectively (Fig. 1-4A–Aii; Brose et al., 1995; Augustin et al., 1999a). Except for a ubiquitously expressed Munc13-2 splice variant (ubMunc13-2), Munc13 proteins are specifically expressed in the brain. In addition to ubMunc13-2, a brain-specific less abundant isoform (called bMunc13-2) could be identified in the brain (Breustedt et al., 2010). Both ubMunc13-2 and bMunc13-2, as well as Munc13-1, are expressed in the hippocampus (Fig. 1-4A, B–Bi; Augustin et al., 1999a; Breustedt et al., 2010). All three isoforms contain the C_1 domain, C_2B domain, a large MUN domain, and a C-terminal Ca^{2+}-independent C_2C domain. However, the N-terminal regions of only Munc13-1 and ubMunc13-2 contain an independent C_2A domain and a central calmodulin-binding site (Fig. 1-4C). In contrast, bMunc13-2 has a different, even longer N-terminal region upstream of the C_1 domain and double calmodulin-binding sequence (Fig. 1-4C; Koch et al., 2000). Munc13-1 C_1 and C_2B regions flank expanded MUN domain, with their binding sites open in the same direction (Fig. 1-4C; Xu et al., 2017). On the other hand, the Ca^{2+}-independent C_2C domain is opposing the MUN domain at the other end. Thus, Munc13-1 has the ability to potentially bridge two membranes: the C_2C domain binds to the vesicle membrane and the C_1 and C_2B region binds to the plasma membrane (Liu et al., 2016; Xu et al., 2017; Quade et al., 2019; Padmanarayana et al., 2021). Each of the domains has distinct binding functions (Fig. 1-4C):

- C_1 region binds DAG and controls phorbol ester-dependent facilitation (Rhee et al., 2002; Basu et al., 2007);
- The C_2A domain binds to RIM zinc fingers (Tan et al., 2022)

- the C_2B domain is a Ca^{2+} ions and PIP_2-(phosphatidylinositol 4,5-bisphosphate) binding site and was reported to mediate short-term plasticity (Shin et al., 2010);
- the important MUN domain, “opens” syntaxin-1, triggers SNARE complex assembly (Ma et al., 2011; Magdziarek et al., 2020);
- C_2C domain can bind to membranes, although weakly, in a Ca^{2+}-independent manner (Quade et al., 2019; Padmanarayana et al., 2021).

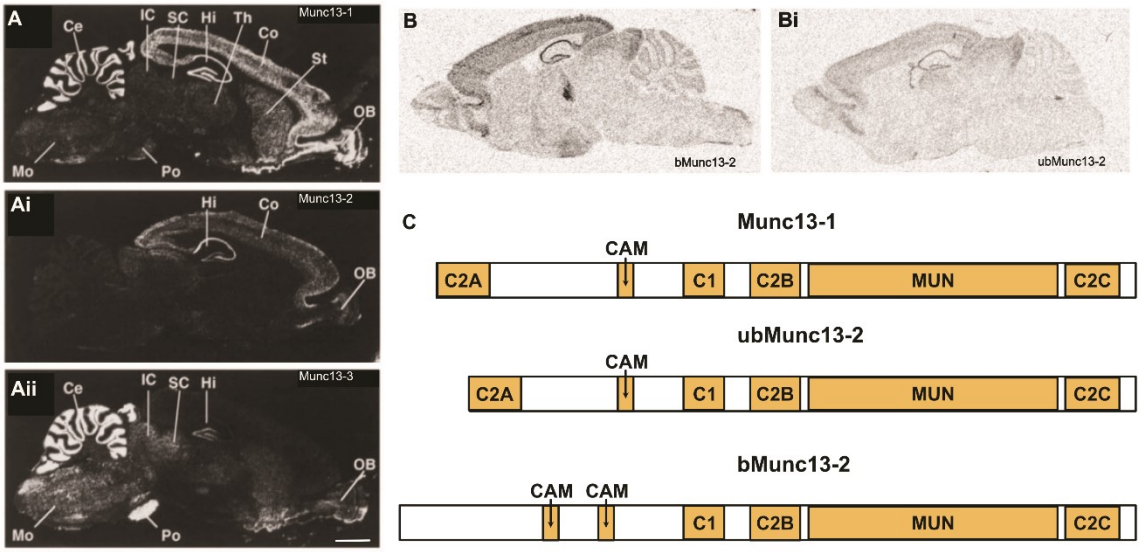

Figure 1-4. Distribution and structure of Munc13 proteins. **(A-Aii),** Expression levels of Munc13-1, Munc13-2, and Munc13-3 isoforms in the murine brain: Ce, cerebellum; Co, cerebral cortex; Hi, hippocampus; IC, inferior colliculus; Mo, medulla oblongata; OB, olfactory bulb; Po, pons; SC, superior colliculus; St, striatum; Th, thalamus. Scale bar 3.5 mm. (modified from Augustin et al., 1999). **(B-Bi),** mRNA levels of two splice variants of Munc13-2 (bMunc13-2 and ubMunc13-2) in the mouse hippocampus (modified from Breustedt et al., 2010). **(C),** The structure of the major hippocampal Munc13 proteins. Notably, bMUnc13-2 lacks C_2A domains but contains two calmodulin-binding domains (CAM).

As was mentioned in the previous section (1.3.1), Munc13 plays an important role in neurotransmitter exocytosis and synaptic transmission. The essential function of Munc13 is to make SVs fusion-competent, by priming the SNARE complex and adjacent SV. Remarkably, loss of function of Munc13 mutations leads to complete impairment of SV exocytosis in dissociated neuronal cultures and partial arrest of synaptic transmission in neuromuscular junction and autaptic hippocampal synapses (Varoqueaux et al., 2002; Varoqueaux et al., 2005).

Priming and SNARE complex assembly is a multistep process, which starts with the binding of monomeric Munc13 to the RIM protein in the AZ (Fig. 1-5). Although bMunc13-2 does not bind to RIM, ELKS1 can localize bMunc13-2 to the AZ (Kawabe et al., 2017). Next, “inactive” syntaxin-1, bound to Munc18, is activated by Munc13 MUN domain and Munc18 – together they “open” syntaxin-1 and expose its’ SNARE motif (Fig. 1-5). At the same time, C_1, C_2B, and C_2C domains of Munc13-1 bind the AZ membrane with the SV membrane. Meanwhile, Munc18 is bound to synaptobrevin, providing a template for SNARE complex formation. This leads to the assembly of t-SNAREs syntaxin-1, SNAP-25, the v-SNARE synaptobrevin-2/VAMP-2 into a joined structure (Söllner et al., 1993; Hanson et al., 1997; Poirier et al., 1998; Sutton et al., 1998). Upon Ca^{2+} ions entry via VGCCs, the calcium sensor synaptotagmin is activated (Südhof, 2013b), and subsequently SNAREs form four trans- alpha-helical

bundles and trigger membrane fusion (Südhof and Rothman, 2009; Ma et al., 2013). In addition, a recent report showed that there are two spherical orientations of the Munc13-1 C_1-C_2B region that can lead to SV priming and make it more plastic during repeated activity (Camacho et al., 2021).

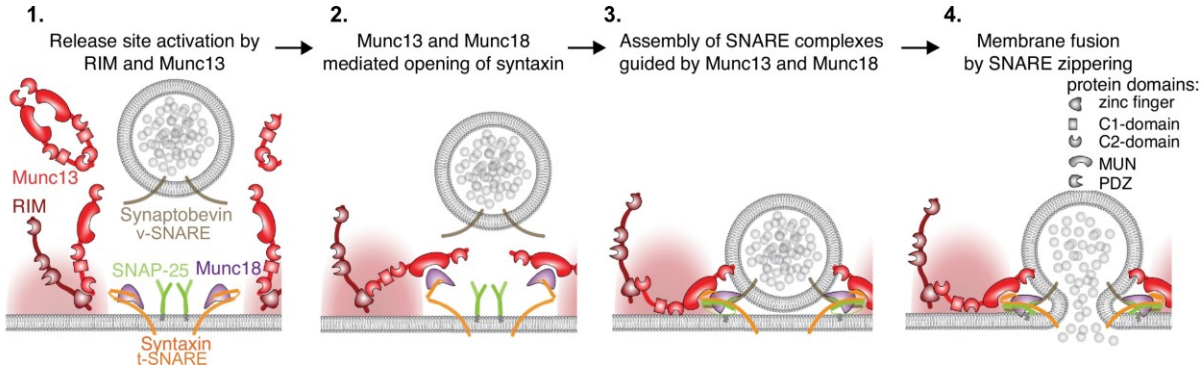

Figure 1-5. Munc13-driven exocytosis of synaptic vesicles. 1. Monomers of Munc13 are recruited by RIM to activate a release site. **2.** Munc13 and Munc18 activate syntaxin-1 to allow for the assembly of the SNARE complex. **3.** In addition to Munc13 and Munc18, complexin, synaptotagmin, or other SNARE-binding proteins may regulate SNARE complex formation. **4.** In the last step, SNARE complex forms a four-alpha-helical bundle that forces the vesicular and target membranes to fuse (modified from Kaeser and Regehr, 2017).

Remarkably, this priming step could be considered a limiting factor of the readily releasable pool (RRP) of SVs, which consist of SVs that are ready for immediate release and have high release probability (Kaeser and Regehr, 2017). First of all, only primed SV can be released; an initial amount of primed SV can define synaptic strength and amplitude of the release. Second, the priming speed affects the replenishment rate and subsequently the size of RRP (Neher and Brose, 2018).

Notably, the Munc13 protein has multilevel regulation mechanisms. First, the large MUN domain is controlled by the C_1 and C_2B domains and the calmodulin-binding region, promoting augmentation of the SV exocytosis in a DAG and PIP_2 dependent manner (Rhee et al., 2002; Junge et al., 2004; Shin et al., 2010). Second, most of the Munc13 molecules in the terminal form dimers with their N-terminal C_2A domains, which renders the MUN domain inactive (Dulubova et al., 2005; Deng et al., 2011). When the zinc-finger of RIM protein binds to the Munc13 C_2A domain, it activates Munc13, through disruption of the homodimers. Therefore, the role of the RIM protein in priming consists of activating Munc13. Deng et al. (2011) showed that synapses lacking RIM proteins had lower levels of vesicle priming, which was rescued with the expression of mutant Munc13 that is constitutively monomeric, and therefore active. Altogether, Munc13 is a crucial protein for priming, bringing the SV and SNARE complex together.

1.4 Hippocampal MFB microcircuits

Remarkably, the morphology of MFs supports the idea that they can generate a robust but sparse synaptic connection. MFBs connect GCs of the DG to thorny excrescences of CA3 PN in stratum lucidum and mossy cells in the hilus (Fig. 1-2, 1-6A; Amaral et al., 1990; Frotscher et al., 1994; Frotscher et al., 2006; Rollenhagen et al., 2007; Wilke et al., 2013). This hypothesis is supported by work by Amaral et al. (1990), which estimated that one MF axon diverges and forms ~15 large MFBs, and one CA3 PN receives converging input from ~50 MFBs. Furthermore, large MFB connect the same or distinct CA3 PN (Fig. 1-6B; Chicurel and Harris, 1992; Galimberti et al., 2006; Rollenhagen et al., 2007).

1.4.1 Unique morphology of MFB

MFBs are unusually large in size, up to 5 µm in transverse diameter, 110 µm^2 in surface area, and 13 µm^3 in volume (Rollenhagen et al. 2007; Rollenhagen and Lübke, 2010). In comparison, other cortical terminals are almost 6 times smaller than MFBs (Rollenhagen and Lübke, 2006). Interestingly, despite a small initial release probability, MFBs are filled with SVs of various sizes (Henze et al., 2002; Borges-Merjane et al., 2020). In addition, almost 12% of the total volume of large MF terminals is filled with mitochondria that can potentially regulate intraterminal calcium concentration and affect neurotransmitter release (Rizzuto et al., 2000; Verstreken et al., 2005).

Two types of membrane specializations were found between MFBs and CA3 thorny excrescences: AZs, mainly on spiny excrescences, and puncta adherentia (PA), which are adhesion complexes on dendritic shafts (Fig. 1-6A, 1-7). First, the majority AZs in MFBs appear to be perforated rather than continuous (80%; Fig. 1-7B; Rollenhagen et al., 2007). Individual AZs, both perforated and continuous, in MFBs were equivalent in size to those in the calyx of Held in young rats (Fig. 1-7B–C; 0.11 and 0.10 µm^2 respectively; Sätzler et al., 2002) and to those in climbing fiber synapses and parallel fiber synapses in the cerebellum (0.14 and 0.13 µm^2 respectively; Xu-Friedman et al., 2001), but significantly larger than Schaffer collateral synapses on CA1 PN (0.06 µm^2; Harris and Stevens, 1989). Interestingly, the number of AZs per single bouton decreased during development from ~30 (P28) to ~18 (adult rat, Rollenhagen et al., 2007). However, other studies with young adult rats estimated that there are up to 37 release sites on MFBs (Chicurel and Harris, 1992). In addition, the distance between neighboring AZs varied greatly (0.32–0.60 µm). Thus, the crosstalk between release sites may occur presynaptically via Ca^{2+} ions diffusion and postsynaptically via glutamate spillover in the synaptic cleft, similarly to cerebellar MF synapses (DiGregorio et al., 2002).

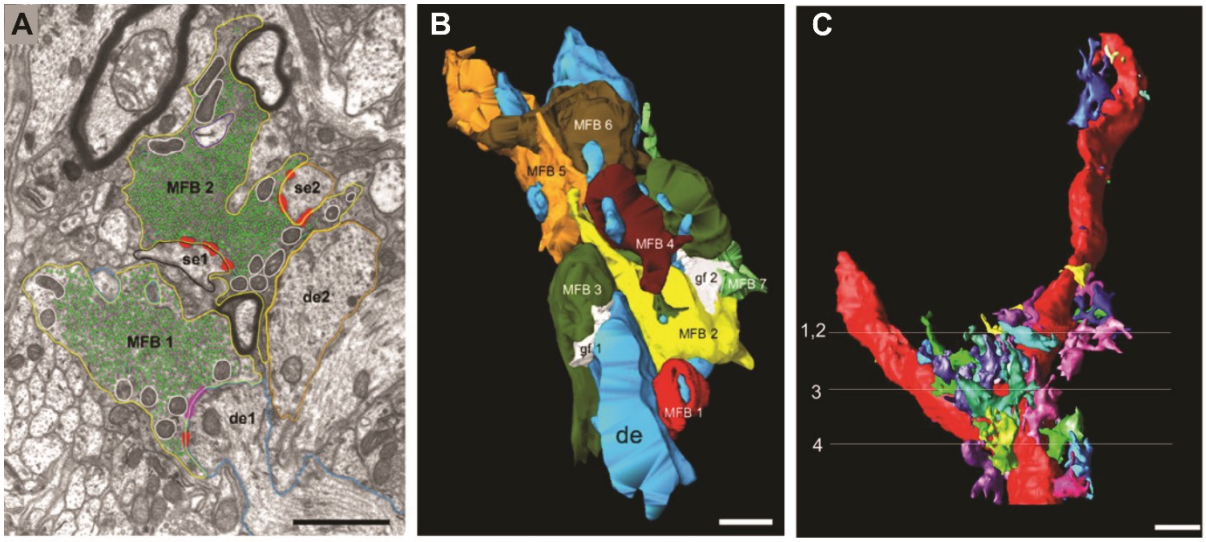

Figure 1-6. Unique morphology of MFB synapses. (A), Electron micrograph depicting two mossy fiber boutons (MFB1 and MFB2, yellow outline) with their postsynaptic targets: dendrites (de1 and de2, blue and orange outlines) and thorny excrescences (se1 and se2, black and orange outlines). AZs are marked in red. PA are in magenta. Green dots represent synaptic vesicles. **(B),** Separate individual mossy fiber boutons (MFB, various colors) innervated single postsynaptic dendrite (de, blue). **(A, B),** Scale bar 1 µm (modified from Rollenhagen et. al., 2007). **(C),** 3D reconstruction of CA3 apical dendrite from serial block-face electron micrographs. Note high complexity of postsynaptic thorny excrescences. Numbers indicate different imaging views. Scale bar 2 µm (modified from Wilke et al., 2013).

Second, PAs can be identified in electron micrographs by two electron-dense parallel bands at the pre- and postsynaptic membranes, without synaptic vesicles and the characteristic broadening of the synaptic cleft (Rollenhagen and Lübke, 2010). Additionally, unlike calyx of Held synapses, where PAs are located between AZs, PAs at individual MFBs locate selectively on the dendritic shaft, spatially segregated from AZs on spines. This arrangement prevents PA involvement in the prevention of AZ crosstalk and neurotransmitter spillover, as they are unable to separate physically numerous adjacent AZ like in calyx of Held.

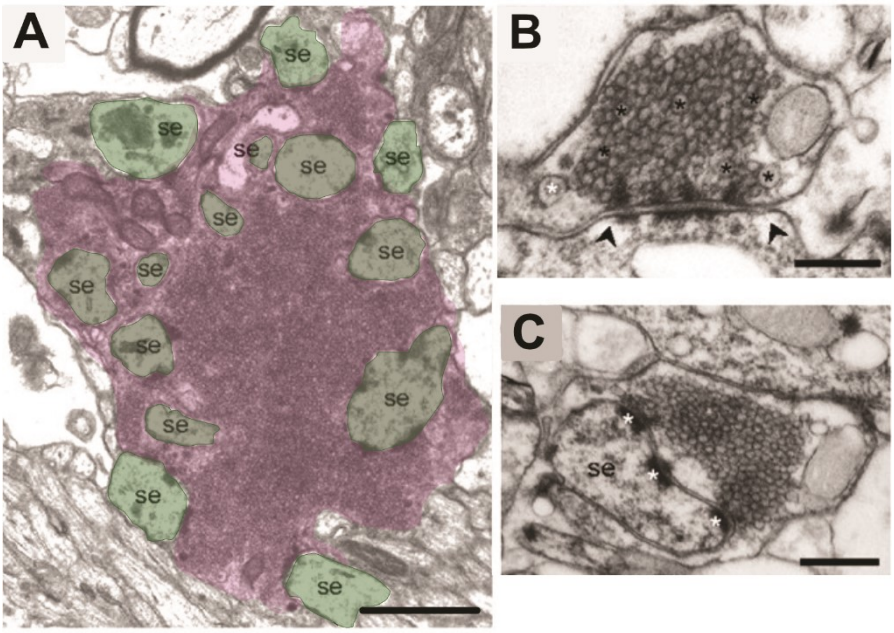

Figure 1-7. Ultrastructure of vesicle pool and active zones at MFB. (A), Electron micrograph of MFB (in magenta) and multiple thorny excrescences (se) from young adult rats. Whole terminal is homogenously filled with synaptic vesicles. Scale bar 500 nm. **(B),** Representative image of perforated active zone (black arrowheads). Dense core (white asterisks) and large clear synaptic vesicles (black asterisks) are visible inside the terminal. **(C),** Representative image of three separate active zones (white asterisks) without synaptic cleft widening between them. (B, C) Scale bar 250 nm. (A-C) modified from Rollenhagen et. al., 2007.

The organization of the pool of SVs, in particular RRP, recycling and reserve pools, as measured by imaging, capacitance measurements, and quantal analysis studies, is another crucial intrinsic component for synaptic efficacy and plasticity (Rosenmund and Stevens, 1996; Schneggenburger et al., 1999; Hallermann et al., 2003; Neher and Brose, 2018). Recycling and reserve pool consist of SVs that can be released during moderate and intense stimulation respectively (Rizzoli and Betz, 2005). In addition, majority SVs inside the terminal correspond to the reserve pool and are scarcely released, unlike RRP and recycling pool that usually maintain synaptic transmission. Individual MFBs are filled with SVs throughout the entire terminal (Fig. 1-7A; Rollenhagen et al., 2007; Borges-Merjane et al., 2020) encompassing 4.2–6.4 % of the total volume of the MFB. Three different types of vesicles are found in MFBs:

- small clear vesicles, with a mean diameter of ~31 nm for adult rats, (Rollenhagen et al., 2007);
- large clear vesicles (~70 nm) that made up 1% of the total pool (Henze et al., 2002);
- dense-core vesicles, which are a rare occurrence in central synapses (Rollenhagen et al., 2007).

The total pool of SV in MFB decreases with age and consists of ~25,000 SVs at P28 and ~16,000 in adult rats (Rollenhagen and Lübke, 2010). The number of SVs in small filopodia, on the other hand, was found to be 200–700, which was two orders of magnitude less than in large boutons. To correlate SV numbers and location to functionally defined RRP, recycling, and the reserve pools, Rollenhagen et al. (2007) used distance from vesicle to AZ as criteria: RRP was defined as SVs within 60 nm (~2 vesicle diameters), recycling pool within 200 nm (~5 vesicle diameters), and reserve pool within 500 nm (~15 vesicle diameters). It was estimated that the total RRP per single MFB in P28 rats was 1200 vesicles, and in adult rats 600 vesicles – equivalent to 4% of the entire pool of SVs and consistent with the decrease in the total amount of SVs per bouton seen during development. On the other hand, measurements of capacitance change at hippocampus MFBs indicated the presence of a huge releasable pool ('maxipool'), with approximately 1400 vesicles (Hallermann et al., 2003). However, despite its large size, the structural correlate of the releasable pool only accounts for a small portion (~850) of the entire pool. Intriguingly, according to the same criteria, the RRP was significantly larger in calyx of Held synapses. Nevertheless, the recycling pool was four times higher in MFBs than in the calyx synapses, and the reserve pool, when calculated for individual AZs, was 10-fold higher at MFBs (Rollenhagen and Lübke, 2010). Yet all these parameters can only partially explain synaptic transmission properties at individual MFB synapses, and a need for a reliable method to correlate the structure and function of a synapse is apparent.

1.4.2 Biophysical and coding properties of MFB

Signaling in the hippocampal MFBs appears to be exceedingly complex (Debanne, 2004; Bischofberger et al., 2006a). First, the duration of the presynaptic AP does not remain constant over time but rather broadens with repeated activation, similarly to neocortical axons (Geiger and Jonas, 2000; Shu et al., 2007). Second, subthreshold synaptic events passively propagate from the cell body to MF terminals of GCs (Alle and Geiger, 2006). Thus, both AP ("digital") and subthreshold ("analog") signals can code information in the MF circuit (Alle and Geiger, 2006; Bischofberger et al., 2006a).

Moreover, MFBs rely on three major types of VGCCs in determining computation capacities and governing synaptic transmission: P/Q- ($Ca_V2.1$), N-type ($Ca_V2.2$), R-type ($Ca_V2.3$) calcium channels (Li et al., 2007), each with different gating properties. Direct measurements from the MFB terminal identified $Ca_V2.1$ as a predominant type, mediating 61% of calcium currents, followed by $Ca_V2.2$ and $Ca_V2.3$ with 24 and 15% respectively, which corroborated previous studies (Castillo et al., 1994; Pelkey et al., 2006). These ratios correspond to an estimated ~1300 $Ca_V2.1$, ~500 $Ca_V2.2$, and ~160 $Ca_V2.3$ channels on average in the whole MFB terminal (Li et al., 2007).

Remarkably, $Ca_V2.3$ channels have quite different biophysical properties and vary largely from $Ca_V2.1$s and $Ca_V2.2$s, which behave quite similarly. Activation and deactivation time constants are comparable between $Ca_V2.1$ and $Ca_V2.2$. However, the $Ca_V2.3$ activation curve was shifted toward more positive values (Wheeler et al., 1996; Colecraft et al., 2000). Furthermore, MFB $Ca_V2.1$ and $Ca_V2.2$ exhibited fast gating and a large activation threshold. On the other hand, and unlike at Calyx of Held synapse, at MFB synapses $Ca_V2.3$s show lower activation threshold, with slower activation and deactivation kinetics (Bourinet et al., 1996; Wu et al., 1999; Li et al., 2007).

The present difference in gating properties is more advantageous during complex signaling at MFBs and AP broadening. First, short APs have a larger efficacy in activating $Ca_V2.1$ channels, whereas broader APs have similar efficacy in activating all three channel types. As a result, AP broadening will cause selective recruitment of $Ca_V2.2$ and $Ca_V2.3$ channels. In addition, subthreshold voltage signals will also activate $Ca_V2.3$ channels selectively. Thus, they can affect synaptic strength and be involved in different types of plasticity at this synapse (Breustedt et al., 2003; Dietrich et al., 2003).

Basal synaptic strength is largely determined by the coupling distance: the distance between calcium channels (source of Ca^{2+} ions) and calcium sensor (synaptotagmin-1 protein on SV). The diffusion time of Ca^{2+} ions depends on the distance and, as a result, synaptic transmission demands a tight packing of the necessary molecules involved in SV release (Eggermann et al., 2012). The stronger synapses with high initial release probability (Pr) show shorter distances between VGCC and fusion sights. For example, it was estimated that the coupling distance in parvalbumin-positive basket cells in the hippocampus is in the range of 10-20 nm (Bucurenciu et al., 2008). In addition, calyx of Held also exhibit relatively short distances, that vary between 5 to 30 nm (Chen et al., 2015; Nakamura et al., 2015; Keller et al., 2015). Therefore, both these synapses are considered to be tightly coupled. On the other hand, Vyleta and Jonas (2014) demonstrated that the coupling distance between calcium sensor and release machinery at the MFBs is ~75 nm, which is several times larger than in the calyx of Held. This loose-coupling explains the low initial Pr (Vandael et al., 2020). Moreover, it is possible that in plastic states of MFBs, the coupling distance can change and subsequently affect the Pr (Midorikawa and Sakaba, 2017). All together, the current functional evidence indicates that MFB synapses are “weak” synapses, that rely on various VGCCs during repetitive stimulation. But the precise interactions between calcium channels and release machinery remain unknown.

1.4.3 Diverse types of plasticity at MFB synapse

MFB synapses not only present unique morphology but also display uncommon forms of plasticity. Unlike at other hippocampal synapses, for example at Schaffer collaterals-CA1 PN synapses, plasticity at MFB-CA3 PN is expressed and induced presynaptically, and is N-methyl-D-aspartate (NMDA) receptor-independent (Nicoll and Schmitz, 2005). Paired-pulse facilitation (PPF), as a form of presynaptic short-term plasticity (STP) at this synapse, is notably high – with the observed paired-pulse ratio that can reach more than three (Salin et al., 1996). Moreover, this uncommonly high PPF can only be observed at MFB-CA3 PN synapses, as other MF terminals, such as filopodial extensions, show little facilitation due to the variation in initial (basal) probability of vesicle release (Jonas et al., 1993; Toth et al., 2000). In addition to PPF, MFB-CA3 PN synapses present pronounced frequency facilitation, post-tetanic potentiation, and long-term potentiation (Fig. 1-8; Salin et al., 1996).

Post-tetanic potentiation or PTP is a type of STP in which synaptic strength increases in response to high-frequency stimulation (HFS) (Fig. 1-8A; Langdon et al., 1995). HFS can lead to diverse responses in synaptic plasticity. In some cases, but not always, augmentation after HFS can be distinguished from PTP, which lasts from 30 seconds to several minutes and decays with a time constant of 5–10 seconds (Zucker and Regehr, 2002). PTP, as a form of STP, is generally thought to be of presynaptic nature. PTP at MFB-CA3 PN synapse increases the conductance level of the postsynaptic cell but does not affect the decay time constant of excitatory

postsynaptic currents and input resistance (Griffith, 1990). In addition, NMDA-receptor antagonists had no effect on PTP, hinting at its presynaptic nature. This hypothesis was recently corroborated by paired electrophysiological recordings and functional electron microscopy (EM), in a study that showed that the RRP and the docked vesicle pool in the presynaptic terminal increase after induction of PTP (Fig. 1-8D–H; Vandael et al., 2020). Moreover, the amplitude of PTP depends on the number and frequency of the stimulus but can be induced even by a short train of 18 pulses (Griffith, 1990; Habets and Borst, 2005; Vandael et al., 2020). Moreover, MFBs are referred to as "conditional detonator", that is, they can reliably discharge its postsynaptic target after a burst of stimuli, due to a combination of facilitation with temporal summation. And PTP at MFB-CA3 PN synapses leads to a switch from conditional detonation to full detonation (Henze et al., 2002; Vyleta et al., 2016). Therefore, after PTP, a single presynaptic AP at a MFB, can lead to a direct postsynaptic AP at the CA3 PN, without summation, which is a very rare occurrence in the brain. Furthermore, PTP at MFBs has anti-associative properties and depends on the absence of postsynaptic calcium signaling (Vandael et al., 2021).

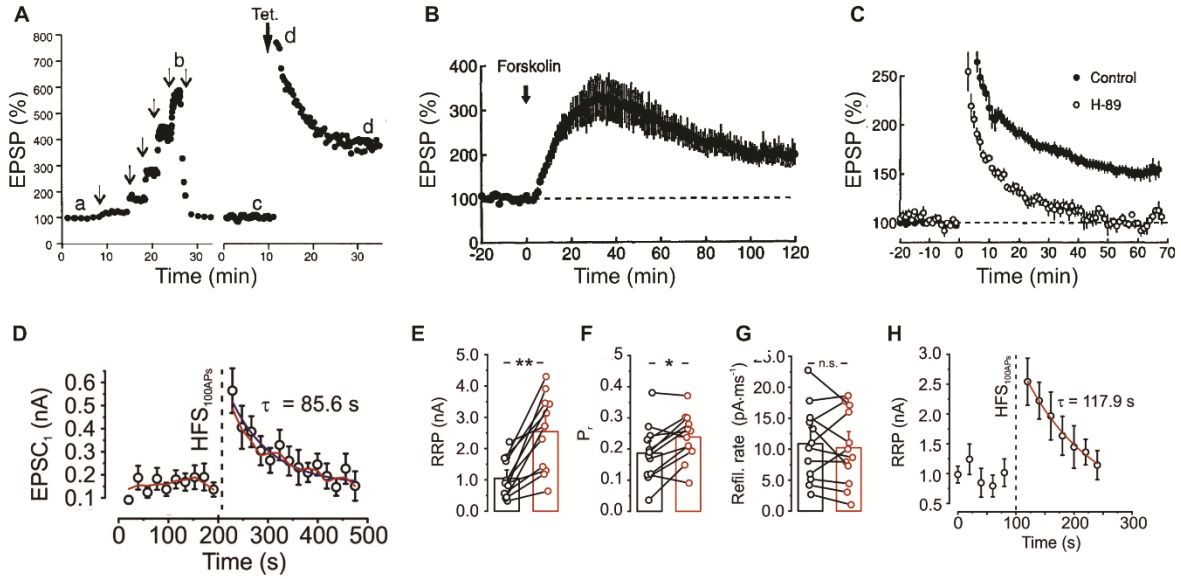

Figure 1-8. Different types of plasticity could be induced at MFB synapses. **(A),** Both STP and LTP can be induced at MFBs. a-b: frequency facilitation, arrows indicate stimulation frequency 0.0125, 0.025, 0.05, 0.1, 0.2, 0.33 Hz. c: baseline before HFS stimulation: 100 Hz for 1 s repeated 4 times (Tet.). d: PTP followed by early LTP after HFS (modified from Salin et al., 1996). **(B),** Persistent chemical LTP induced by application of 50 µM forskolin at MFBs. **(C),** Antagonist of PKA, H-89, abolishes chemical LTP at MFB synapses. (B, C) modified from Weisskopf et al., 1994. **(D),** Average $EPSC_1$ amplitude before and after PTP induction during the MFB-CA3 PN recording. **(E-G),** Summary bar graphs of RRP (E), Pr (F), refilling rate (G) before (black) and after (red) PTP induction. Height of the bar represents mean value. (H) Change of RRP size with time. (D-H) modified from Vandael et al., 2020.

Apart from short-term plasticity, MFB synapses undergo long-term potentiation (LTP) (Fig. 1-8A; Langdon et al., 1995; Nicoll and Schmitz, 2005). LTP, as a form of long-term plasticity, is present at several synapses and is related to learning and memory formation. LTP in MFBs can be induced *in vitro* with the application of several (2–4) long HFS trains (Langdon et al., 1995; Salin et al., 1996). Interestingly, similarly to PTP, LTP at MFB-CA3 PN synapse has a presynaptic origin and is believed to be NMDAR-independent. The works in which NMDAR activity was blocked did not affect the induction of hippocampal MFB LTP (Harris and Cotman, 1986; Zalutsky and Nicoll, 1990). Furthermore, postsynaptic calcium plays an insignificant role in MF LTP, similar to short-term plasticity at this synapse. Furthermore, despite some reports

(Yeckel et al., 1999) experiments with calcium uncaging in CA3 PNs (Wang et al., 2004), which increased intracellular Ca^{2+} ions concentration by applying depolarizing pulses (Lei et al., 2003), and loaded postsynaptic cells with calcium chelator, did not affect MF LTP or even depressed presynaptic vesicle release.

Additionally, it is hypothesized that MFB LTP is induced by an increase in neurotransmitter release. The quantal study, which included coefficient of variation, failure analysis, and capacitance measurements in the presence of calcium chelator, revealed that MF LTP is linked to a higher likelihood of neurotransmitter release (Tong et al., 1996; Xiang et al., 1994; Midorikawa and Sakaba, 2017). LTP in GC autapses could be linked to the activation of “quiet” synapses or release sites, in addition to an increase in release probability (Tong et al., 1996). Optical imaging of postsynaptic calcium transients in slice culture reached a similar conclusion (Reid et al., 2004).

Both PTP and LTP depend on a surge in presynaptic cycle adenosine monophosphate (cAMP), a signaling molecule that plays a significant role in mediating both types of potentiation (Huang et al., 1994; Weisskopf et al. 1994; Lopez-Garcia et al., 1996; Vandael et al., 2020). The chemical compound forskolin activates adenylyl cyclases (AC; i.e. AC1 and AC8) and can mimic the effects of HFS (Fig. 1-8B; Huang et al., 1994; Weisskopf et al., 1994; Tong et al., 1996; Lopez-Garcia et al., 1996) and induce chemical STP and LTP (cSTP; cLTP). In addition, cAMP-dependent protein kinase A (PKA) blockers, such as H-89, inhibit MF PTP and LTP (Fig. 1-8C; Weisskopf et al., 1994; Vandael et al., 2020). Although the activation of the AC1 signaling pathway is well established, the final substrates of PKA remain unresolved. It was proposed that RIM1α, as well as Rab3, can undergo phosphorylation during STP or LTP (Castillo et al., 1997; Castillo et al., 2002). Both RIM and Rab3 are important for anchoring SVs to Munc13 and the SNARE complex, however, they might not be directly affected by PKA activation.

Despite all that is known regarding PTP and LTP at this synapse and its importance in the hippocampal circuit, there is a gap in the knowledge in what the mechanisms underlying presynaptic LTP and PTP are. And new methods should aim to elucidate structural and biophysical changes at the hippocampal MFB-CA3 PN synapses during plasticity induction.

1.5 Relation between structure and function of synapses

One of the fundamental questions in neuroscience is how the structure and function of synapses are connected. Even though a lot of progress has been made to elucidate this issue, several fundamental aspects of synaptic transmission remain unresolved. For instance, endocytosis at central synapses remains to be the topic of debate. Although classical works indicated the presence of clathrin-dependent endocytosis, recently a clathrin-independent mode of endocytosis was described (Watanabe et al., 2013b; Delvendahl et al., 2016; Chanaday and Kavalali, 2018). Moreover, despite extensive works on the determination of the overlap between the functionally defined RRP and the morphological docked vesicle pool (Schikorski and Stevens, 2001; Imig et al., 2014; Wang et al., 2016), many aspects of their relation remain unclear. For example, there are reports that the RRP and docked vesicle pool are indentical (Schikorski and Stevens, 2001; Imig et al., 2014). Others suggested that the RRP and the docked pool are only partially overlapping and a non-docked pool can also contribute to the RRP (Wang et al., 2016). Finally, controversial aspects of mechanisms of exocytosis remains unresolved; for instance, whether transmitter is released by transient fusion pores ("kiss-and-run”) or by full collapse of synaptic vesicles (Aravanis et al., 2003; Lisman et al., 2007; Chanaday et al., 2019). Addressing

these and many other questions requires structural and functional analysis of rigorously identified synapses.

EM is the classical method for studying the morphological properties of neurons. Although EM enables researchers to determine the structure of the synapse with nanometer precision, it can only capture static images, which typically represent the time point of fixation of the biological preparation. Additionally, chemical fixation with formaldehyde might compromise the native structure of the synapse, for example by inducing tissue shrinkage or vesicle fusion (Korogod et al., 2015). Other methods of visualization, such as two-photon and optical superresolution imaging, allow examination of synaptic transmission in fresh living specimens in real-time. For instance, FM dyes, transmitter ligand ("sniffer") proteins, quantum dots, and synapto-pHluorins, are used in the exocytosis and transmitter release studies (Ariel and Ryan, 2010). Nevertheless, the optical resolution of these sophisticated techniques is still incomparable to EM, thus, insufficient to identify individual AZs or single SVs. Therefore, the need for new techniques with adequate nanometer spatial and millisecond temporal resolutions is evident.

Heuser et al. (1979) successfully combined electrical stimulation with rapid tissue freezing of frog muscle and performed concurrent structural and functional analysis of synapses. This approach revealed structural confirmation of the quantal hypothesis and the first descriptions of SV exocytosis and endocytosis. Due to the fragile nature of central synapses, which are highly susceptible to hypoxia, this method cannot be applied to fresh mammalian brain tissue. However, some of these limitations have been overcome by combining rapid optogenetic stimulation of identified presynaptic neurons with high-pressure freezing (HPF), a technique called "flash and freeze" (Watanabe et al., 2013a). Although "flash and freeze" has been successfully applied in the *C. elegans* nervous system (Watanabe et al., 2013a) and dissociated cultured neurons (Watanabe et al., 2013b), freezing of intact brain tissue – such as acute slices – remained a challenge. In particular, it has been widely presumed that it would be impossible to apply HPF techniques to standard acute slice preparations since the thickness and density of the tissue will result in prolonged water vitrification and ice crystal damage, despite earlier efforts (Studer et al., 2014). Because our understanding of synaptic function is based largely on electrophysiological analysis of acute slice preparations (Edwards et al., 1989; Bischofberger et al., 2006b), the available techniques leave a huge gap between structural and functional data, making a unified understanding of synaptic transmission impossible.

Furthermore, the precise molecular composition of live synapses as well as dynamics of AZ proteins are still unknown. Even though, recent work from Rebola et al. (2019) correlated the freeze-fracture replica immunolabeling data of calcium channels and Munc13-1 protein with calcium imaging measurements under basal conditions, the behavior of priming molecules during STP and LTP remains unresolved.

1.6 Aims of the study

The main goal of this study is to elucidate morphological, physiological, and molecular correlates of synaptic transmission in a specific cortical synapse, the MFB-CA3 PN synapse in hippocampus. Precisely this study aims to overcome evident methodological difficulties and determine structural and molecular changes at MFB synapses that govern their basal activity, STP, and LTP. In order to achieve this goal, a reliable method was established that enables scientists to directly correlate functional and structural properties of cortical synapses in an intact circuit.

First, chapter 3 of the current study presents an enhanced "Flash and Freeze" technique for probing structural changes during synaptic transmission at identifiable cortical synapses at precisely defined time points. The improved “Flash and Freeze” procedure can be used on both acute slices and organotypic slice cultures, unlike previously published techniques. The utilization of thin acute slices, enhanced carrier shape, improved recovery techniques, and optimized cryoprotection made this achievable. With this improved method, it was possible to optically stimulate GCs with high-frequency stimulation, which depleted the docked vesicle pool at the hippocampal MFB synapses, implying that the functionally defined RRP and the structurally defined docked vesicle pool are overlapping. Furthermore, the presence of endocytic pits after moderate stimulation provided structural evidence for ultrafast clathrin-independent endocytosis at this synapse. Altogether, for the first time these findings elucidate the link between the stimulus strength and corresponding presynaptic ultrastructural changes at the MFBs, and open a new avenue of research in the field of synaptic transmission, called functional EM.

Second, chapter 4 describes how the newly developed HPF technique is widely applicable and can be slightly modified for gold freeze-fracture replica immunolabeling of MFBs to investigate the nanoscale arrangements of MFB AZs and distribution of calcium channels and Munc13 proteins at the nanometer level. As a result, the presence of three types of VGCCs ($Ca_v2.1$, $Ca_v2.2$, and $Ca_v2.3$) and two isoforms of Munc13 protein (Munc13-1 and Munc13-2) was confirmed at the MFB synapses. In addition, for the first time, it was shown that MFB AZs underwent dynamic molecular rearrangement after induction of cSTP and cLTP. First, the number of clusters of Munc13-1 protein in the MFB AZs increased significantly during cSTP but decreased to lower than the control value during cLTP. Secondly, the distance between the calcium channels and Munc13-1s changed after induction of cSTP, and it remained shortened during the LTP phase. In short, these results indicate the increase in the RRP can only occur during cSTP, and cLTP relies on the distinct mechanism of potentiation. Furthermore, this is the first direct and successful comparison of the molecular composition and ultrastructure at the MFB synapses during cSTP and cLTP. Finally, future investigations can employ the same functional EM approaches to examine whether aforementioned processes are common phenomena in other cortical synapses.

CHAPTER 2. MATERIALS AND METHODS

2.1 Experimental animal procedures

2.1.1 Animals

Animals were bred in a colony maintained in the preclinical animal facility at ISTA. All procedures strictly complied with ISTA, Austrian, and European ethical regulations for animal experiments, and were approved by the Bundesministerium für Wissenschaft, Forschung und Wirtschaft of Austria (BMWFW-66.018/010-WF/V/36/2015, BMWFW-66.018/0008-V/3b/2018 and 2020-0.648.587).

To achieve labeling, as well as expression of a light-activated channelrhodopsin specifically in hippocampal GCs, Cre-dependent Prox1-CreER^{T2} line (Bazigou et al., 2011) and a Tg(Prox1-Cre)SJ32Gsat/Mmucd line (Mutant Mouse Resource & Research Centers) were used. Reporter lines were a B6;129S6-Gt(ROSA)26Sor$^{tm9(CAG-tdTomato)Hze}$/J reporter line (The Jackson Laboratory; line #007905), a B6;129S-Gt(ROSA)26Sor$^{tm32(CAG-COPA*H124R/EYFP)Hze}$/J reporter line (The Jackson Laboratory; line #012569) and C57BL6/J wild-type animals. Experiments were performed in acute slices and organotypic slice cultures from male and female mice. Genotype of transgenic animals was confirmed by PCR, with DNA extracted from toe or ear clippings. For acute slice experiments in Prox1-CreER^{T2}, tamoxifen (Sigma-Aldrich) injections were made from a stock solution of 20 or 30 mg ml^{-1} in corn oil (Sigma-Aldrich). For maximum expression of channelrhodopsin in GCs, each mouse received two intraperitoneal (IP) injections of tamoxifen at 100 mg kg^{-1} of mouse body weight, given 2–3 days apart or one IP injection, in case of higher concentration of stock solution. Mice were used for experiments after a minimum of 10 days after injections. For organotypic slice culture experiments, 5 µM of 4-hydroxytamoxifen in ethanol (Sigma-Aldrich) was added to culture medium for 24 hours on the 7th day *in vitro* (DIV). Cultures were then used for experiments 2–3 weeks (21–28 DIV) after tamoxifen application.

To determine antibody specificity against $Ca_V2.1$ (P/Q-), $Ca_V2.2$ (N-) and $Ca_V2.3$ (R-) types of calcium channels following conditional and full knock-out transgenic mouse lines were used respectively: *Cacna1a$^{Citrine(+/+)}$* (Stefan Herlitze, Mark et al., 2011*)* crossed with Tg(Prox1-Cre)SJ32Gsat/Mmucd, Cacna1$^{btm1a(KOMP)Wtsi}$/HMmucd (Mutant Mouse Resource & Research Centers) and Cacna1e^{tm1Ttan} (Tsutomu Tanabe, Saeguse et al., 2000). Similar to previous lines, mice were genotyped, DNA extracted from toe or ear clippings, to insure homozygosity of progenies.

2.1.2 Tissue preparation

Acute slices were prepared as previously described for optimal preservation of the hippocampal MF tract (Bischofberger et al., 2006b) from 21–40-day-old mice (P25–40). Mice were lightly anesthetized with isoflurane and rapidly decapitated. The brain was dissected from the skull and blocking “magic-cut” was performed under ice-cold high-sucrose solution containing: 87 mM NaCl, 75 mM sucrose, 25 mM $NaHCO_3$, 10 mM D-glucose, 2.5 mM KCl, 1.25 mM NaH_2PO_4, 0.5 mM $CaCl_2$, and 7 mM $MgCl_2$, equilibrated with 5% CO_2/95% O_2. Transverse hippocampal slices were sectioned at 200–300 µm thickness for electrophysiology experiments and at 150–200 µm for high-pressure freezing (HPF), using a vibratome (VT1200S, Leica Microsystems) in ice-cold high-sucrose solution. Slices were transferred to a maintenance chamber, and recovered at 35°C for 30–45 min. For HPF, slices from left and right hemisphere were stored in different chambers (see section 2.4.2 High-pressure freezing with light-stimulation). After recovery, slices were kept at room temperature (~23°C) until

recording, for up to 4–5 hours. For HPF, after recovery and until freezing, slices were transferred to a second set of maintenance chambers filled with artificial cerebrospinal fluid (ACSF) solution, identical to solution used for electrophysiology recordings, containing: 125 mM NaCl, 25 mM D-glucose, 25 mM $NaHCO_3$, 2.5 mM KCl, 1.25 mM NaH_2PO_4, 2 mM $CaCl_2$, and 1 mM $MgCl_2$, equilibrated with 5% CO_2/95% O_2. Finally, 5–10 min prior to freezing, slices were transferred into a chamber filled ACSF at 37°C, as all freezing experiments were performed from physiological temperature (37°C).

For organotypic slice culture experiments, tissue was extracted from 5–8-day-old animals (P5–8). Hippocampal organotypic slice cultures were prepared from both hemispheres using the Stoppini-type method (Stoppini et al., 1991; Kerr et al., 2008). The entire hippocampus with entorhinal cortex was dissected and cut perpendicularly to the longitudinal axes into 300 µm slices, using a McIllwain tissue chopper. Hippocampus extraction and cutting were performed in a medium containing Hanks' Balanced Salt Solution (HBSS, Gibco) and 20% D-glucose (Braun). Slices were placed on microporous membrane inserts (0.4 µm, 30 mm) floating on culture media containing 50% minimum essential medium, 25% basal medium Eagle, 25% heat inactivated horse serum, 2 mM glutamax (all from Gibco), and 0.62% D-glucose (Braun), pH 7.2. Slice cultures were kept at 37°C and 5% CO_2, until used for HPF or electrophysiology experiments.

2.2 Immunofluorescence for confocal microscopy

For immunohistochemistry, mice were anesthetized with isoflurane and transcardially perfused with warm (~37°C) 0.1 M phosphate buffer (PB) solution, pH 7.35, followed by ice-cold 4% paraformaldehyde (PFA) in 0.1 M PB. Brains were dissected, incubated overnight in 4% PFA and rinsed with 0.1 M PB prior to sectioning. Hippocampal horizontal sections (50 µm thickness) were cut in 0.1 M PB using a vibratome (Leica VT1200S). After 14 DIV organotypic slice cultures were fixed using 4% PFA in 0.1 M PB at 4°C for 30 min. After sectioning or, for cultures, directly after fixing, the tissue was washed in 0.1 M PB and subsequently incubated for 1 hour in blocking solution (10% normal goat serum (NGS) in PB). Next, tissue was incubated for 72 hours with primary antibody (0.1 M PB with 0.4% Triton, 5% NGS and 1:500 rabbit anti-NeuN; Invitrogen) at 4°C, followed by washes with 0.1 M PB. Subsequently, tissue was incubated for 24 hours with secondary antibody (0.1 M PB with 0.3% Triton, 5% NGS and 1:1000 goat anti rabbit Alexa 647; Invitrogen). Samples were then washed and incubated in DAPI (0.00003 mg ml^{-1}) for 10 min and subsequently mounted with Prolong Gold antifade embedding medium (Invitrogen). Immunofluorescence images were taken with a confocal microscope (Leica SP5 upright) with sequential scanning of fluorescent signals using an air-objective (10x/numerical aperture 0.3 or 20x/numerical aperture 0.5). Confocal images were analyzed with Fiji open source software. Cell-counting for the tamoxifen dose-response curve was done in Imaris (Oxford Instruments).

2.3 Electrophysiology and pharmacology of MFBs

2.3.1 Electrophysiological recordings and light stimulation

After tissue preparation, slices and cultures were transferred to a recording chamber and superfused with ACSF at physiological temperature (~37°C). For acute slice recordings, slices a Zeiss Axioskop 2 FS Plus microscope, equipped with DIC optics and a 60x water immersion Olympus objective was used. For slice culture experiments, organotypic slice cultures were visualized with a Zeiss Axio Examiner D1 microscope and a 63x water immersion Zeiss Plan-Apochromat objective.

tdTomato and channelrhodopsin were observed and stimulated with a high-power LED head (LED4D212; Thorlabs) and 4-channel LED driver (DC4104; Thorlabs) in combination with Semrock BrightLine single-band bandpass filters: 536/40 nm and 607/70 nm with a 562 nm dichroic mirror for tdTomato excitation, and 458/64 nm and 531/40 nm with a 506 nm dichroic mirror for channelrhodopsin stimulation with 470 nm wavelength were used. To mimic light stimulation characteristics of the Leica EM ICE high-pressure freezing machine LED range (intensity at specimen 5.5–8.0 mW mm^{-2}) at the tissue surface, the microscope light path was optimized with a cage system, consisting of two cage plates and four assembly rods (all Thorlabs), and with a 10x objective for wide-field stimulation. Timing and intensity of light pulses were repeatedly checked by photodiode PDA10A - Si Fixed Gain Detector (Thorlabs).

Patch electrodes were pulled from borosilicate glass capillaries (2 mm outer diameter, 0.5 mm wall thickness; Hilgenberg) with a horizontal puller (P-1000, Sutter Instrument). For whole-cell recordings in acute slices and cultures, pipettes were filled with intracellular solution containing: 135 mM K-gluconate, 20 mM KCl, 2 mM $MgCl_2$, 2 mM Na_2ATP, 0.1 mM EGTA, and 10 mM HEPES (297–300 mOsm, pH 7.28). Signals were recorded with a Multiclamp 700A (acute slices) or an Axopatch 200A amplifier (Axon Instruments; slice cultures) and digitized with a CED 1401 plus interface (Cambridge Electronic Design). Pulse generation and data acquisition were performed using FPulse version 3.3.3 (U. Fröbe, Freiburg, Germany) and Igor Pro (WaveMetrics). Data were analyzed with Stimfit version 0.14.13 (Guzman et al., 2014) or Axograph Software version 1.7.2.

2.3.2 Pharmacological experiments

During electrophysiology recordings, tetrodotoxin (TTX) (voltage-gated Na^+ channels blocker, BioTrend or Alomone Labs) and polyvinylpyrrolidone (PVP) were delivered by bath application at concentrations specified in the results section. For HPF control experiments, samples were incubated with TTX-containing ACSF for ~10 min prior to freezing (see section 2.4.2. High-pressure freezing with light stimulation).

To induce chemical potentiation in MFB synapses, 50 µM forskolin (FSK; Cat. No. 1099, Tocris Bioscience) in dimethyl sulfoxide (DMSO; Sigma Aldrich) was applied to ACSF solution, slices were incubated for 5 min at ~37°C. Acute slices were then high-pressure frozen 5 min and 30 min after the onset of FSK application (see section 2.4.4. High-pressure freezing for freeze-fracture experiments).

2.4 Sample preparation for electron microscopy experiments

2.4.1 Pre-embedding immunolabeling for electron microscopy

Animals were perfused as described for immunohistochemistry (see section 2.2. Immunofluorescence for confocal microscopy), but with ice-cold 4% PFA and 0.05% glutaraldehyde in 0.1 M PB, pH 7.4. Brains were sectioned at 70 µm in 0.1 M PB and sections were stored in 0.025% NaN_3 in PB at 4°C. For cryo-protection, samples were transferred to sucrose solutions of increasing concentration (5%, 10%, and 20% in PB), for 1 hour each and left overnight in 20% sucrose solution at 4°C. Samples were transferred to a 12-well plate. Next, plates were placed directly onto liquid nitrogen (floating) for about 1 min. The plate was removed and samples were thawed rapidly with large volumes of 0.1 M PB. Samples were re-infiltrated with 20% sucrose and freeze-thaw was repeated 2 to 3 times. For immunolabeling, samples were first washed in 50 mM Tris-buffered saline (TBS; 0.9% NaCl, pH 7.4). Next, sections were incubated in 50 mM glycine in TBS for 1 hour, blocked in 10% normal serum and 2% BSA in TBS and incubated in rabbit polyclonal anti-GFP primary

antibody (1:5000, Abcam) for 36 hours at 4°C in TBS with 2% BSA. After wash in TBS, sections were incubated with biotinylated IgG anti-rabbit secondary antibody (1:400, Vector laboratories) in TBS with 2% BSA overnight at 4°C. Next, samples underwent reaction with streptavidin biotin complex (ABC kit, Vector laboratories). Solution A (1/100) and B (1/100) were mixed in TBS with 0.2% BSA and samples were incubated for 3 hours. Next, samples were incubated in 0.5 mg ml^{-1} DAB in TB for 5 min, with 0.003% hydrogen peroxide in TB. Subsequently, samples were washed and post-fixed in 1% glutaraldehyde in 0.1 M PB for 20 min. Samples were contrasted by incubation with 1% osmium tetroxide (Science Services) in 0.1 M PB for 45 min followed by incubation in 1% uranyl acetate and 50% ethanol for 30 min in darkness. Next they went through a series of dehydration steps in ethanol and infiltrated in propylene oxide, followed by infiltration with 1:2 and 2:1 Durcupan resin (10 g reagent A, 10 g B, 0.3 g C, and 0.3 g D) and propylene oxide mix, and embedded in pure Durcupan resin overnight.

2.4.2 High-pressure freezing with light stimulation

HPF was performed with a Leica EM ICE high-pressure freezing apparatus (Leica Microsystems) equipped with a blue LED light stimulation module 460 nm wavelength; LED intensity at specimen 5.5– 8.0 mW mm^{-2}). The Leica ICE table was kept at 40°C at all times during specimen sandwich assembly to keep all materials and samples close to physiological temperature. The freezing chamber was kept at 37°C. After slicing and recovery procedures, hippocampal acute slices were frozen in filler medium containing 15% PVP (Sigma Aldrich) as a cryoprotectant in ACSF, equilibrated with 5% CO_2/95% O_2 and kept at 37°C. The 15% PVP concentration was determined based on a concentration gradient control experiment. Lower concentrations than 15% lead to low tissue adherence to carriers and greater ice crystal formation and tissue damage, while higher concentrations lead to frequent irreversible adherence of tissue to carriers causing surface damage, as well as potentially unknown adverse biological effects. The specimen sandwich was assembled with a 6 mm diameter sapphire system, including transparent half-cylinder cartridges (Leica Microsystems) for light stimulation, a middle-plate (Leica Microsystems), two 120 µm sapphire discs, a 150 or 200-µm thick spacer ring, and a 450- or 400-µm thick top ring (Leica Microsystems or Engineering Office M. Wohlwend, Sennwald, Switzerland). The outer diameter of sapphire disks and rings was 6 mm. The inner diameter of the rings was 5 mm for larger slices and 4 mm for smaller slices. The 4 mm inner diameter rings were more stable and were less likely to break, however, they required longer infiltration during freeze-substitution. The order of assembly was as follows: the bottom sapphire disk was placed on the middle plate, followed by the spacer ring with a drop of filler medium over the ring to adhere it to the sapphire disk, the sample, and the top sapphire disk. Slices were transferred carefully but quickly to the sapphire disk, using a paintbrush number 4 or curved spatula, always covered with solution, keeping the slice as flat as possible. The optical fiber for light stimulation was located on the top of the freezing chamber. Left and right brain hemispheres were frozen separately, for indisputable tracking of the light-stimulated side based on hippocampal morphology, until embedding with the light-stimulated side facing down. Organotypic slice cultures were frozen in filler medium containing 15% BSA (Sigma Aldrich) in ACSF at 37°C (Studer et al., 2014). The optimum concentration of BSA, was also determined based on a concentration gradient control, as for PVP. Cultures were taken out of the incubator and the tissue attached to membrane was cut out with a 4 mm biopsy punch (Ted Pella). The time

from taking the slice cultures out of incubator until freezing was less than 10 min. For freezing cultures, “hybrid” sandwiches were used. They consisted of a 6 mm metal carrier (5 mm inner diameter, type A, Leica) at the bottom, and a 6 mm 120-µm thick sapphire disk with a 200-µm thick 6 mm top ring (Engineering Office M. Wohlwend) on the top. Each culture, with the membrane facing down, was placed in the metal carrier well covered with filler solution and closed with the sapphire disk for subsequent light stimulation. This configuration increased the stability of the sandwich and the control of light-stimulated side orientation, as it was always facing the sapphire disk.

2.4.3 Freeze-substitution and ultramicrotomy

For the first day of freeze-substitution, the HPF samples were transferred from liquid nitrogen to vials with 0.1% tannic acid (Sigma Aldrich) in acetone, frozen in liquid nitrogen. Vials were then transferred to either a Leica EM AFS1 or AFS2 kept at −90°C, and shaken for 22–24 hours (samples with 5 mm inner diameter sapphire rings) and at least 26 hours (4 mm) to ensure that the sandwich opens for proper infiltration. On the second day, samples were washed 3–4 times, while kept inside the FS machines, with acetone chilled to −90°C for 10 min each. Next, the contrasting cocktail with 2% osmium (Science services (EMS)) and 0.2% uranyl acetate (Serva) in acetone, also first chilled to −90°C, was added to each vial and shaken overnight. For organotypic slice cultures, samples were kept at −90°C for 6 hours. For acute slices, samples were kept at −90°C for 7–10 hours. Next, the temperature was raised to −60°C within 2 hours (15°C/hour) and kept at −60°C for 3 hours (3.5 hours for 4 mm diameter spacers); then raised to −30°C in 4 hours (7.5°C/hour), and kept at −30°C for 3 hours (3.5 hours for 4 mm inner diameter spacers); then raised to 0°C in 3 hours (10°C/hour). Samples were kept at 0°C only for ~10 min. Once the substitution protocol was concluded, the vials were transferred to ice for washes with ice-cold acetone, 3 times for 10 min each. They were then transferred to room-temperature glass dishes, always submerged in acetone, to visually check that the slices and cultures were intact, all sandwiches properly opened, and the tissue adequately infiltrated. They were then washed twice with propylene oxide for 10 min each, and infiltrated with hard Durcupan resin (11.4 g reagent A, 10 g B, 0.3 g C, and 0.1 g D; all Sigma-Aldrich) at 2:1, 1:1, and 1:2 propylene oxide/Durcupan resin mix for 1 hour each, shaking. They were then left in pure resin overnight, and embedded in BEEM capsules. Capsules were polymerized overnight at 100°C. Acute slices were embedded with care to ensure that the light-stimulated side of the slice was facing down. Each slice culture was separated from the carrier and embedded with stimulated tissue (not membrane side) facing down for ultramicrotomy. Cured resin blocks were trimmed with glass knives and 70 nm ultrathin sections were cut with a Leica EM UC7 ultramicrotome with Diatome Histo diamond knives. Sections were picked up on Formvar-coated copper slot grids for transmission electron microscopy (TEM) imaging. Post-staining was done in 2 or 4% uranyl acetate for 10 minutes followed by lead citrate for 2–3 minutes.

2.4.4 High-pressure freezing for freeze-fracture experiments

For freeze-fracture experiments with chemically fixed samples, animals were anesthetized with 6% ketamine (MSD Animal Health) and 3% xylazine (Livisto) mixture in saline and transcardially perfused, similarly to immunohistochemistry (see section 2.2. Immunofluorescence for confocal microscopy), with ice-cold 2% PFA in 0.1 PB solution. Brains were extracted and washed once in fresh 0.1 M PB. Then they were sectioned transversally into 150 µm slices in ice-cold 0.1 M PB. Afterwards, sections

were kept until freezing in 30% glycerol in 0.1 M PB solution, at least overnight. DG and CA3 regions of hippocampus were dissected using 1.5 mm biopsy puncher (Science services (EMS)). Sections were cryo-fixed with an HPM10F high-pressure freezing apparatus (BAL-TEC), using 4.6 mm gold plated carries for freeze-fracture (Leica Microsystems) with 150 µm thick double-sided tape.

Freeze fracture replicas were produced using three freeze fracture machines interchangeably: JFD V (Jeol), BAF060 and ACE 900 (Leica Microsystems). Using the tensile fracture approach in all three cases, samples were fractured at -120°C under high vacuum and followed with evaporation of layered carbon (C) and platinum (Pt) on the surfaces of the slices: the first C layer was 5 nm thick, the second Pt layer was 2 nm, and the final third C layer was 20 nm. Afterwards, replicas were brought to room temperature and transferred to glass tubes containing 2.5% SDS solution in TBS. The replicas were digested in SDS solution for 18 hours, shaking at 80°C. Afterwards, prepared replicas were kept in the same SDS solution until immunolabeling experiments.

For examination of replicas from acute hippocampal slices, the tissue was prepared as in the sections 2.1.2. Tissue preparation and 2.4.2 High-pressure freezing with light stimulation. However, the 4.6 mm gold plated carriers with 150 µm double sided tape were used and no light stimulation was applied.

2.4.5 Freeze-fracture replica immunolabeling (FRIL)

All replicas were handled with utmost care during all steps to insure they stayed intact. Washes were done in porcelain 12-well plates and replicas were transferred with a glass rod. First, replicas were washed with fresh 2.5% SDS in TBS solution for 10 min shaking at room temperature. Then they were transferred to 0.1% Tween in 0.05% BSA in TBS buffer solution and washed for 10 min. Afterwards, sections are washed three times for 15 min in 0.05% BSA in TBS, before blocking for 90 min in 5% BSA. Then, replicas were incubated in primary antibody with varying concentrations in 2% BSA in TBS (Table 1) overnight, shaking at 15°C. Afterwards, replicas were washed three times in 0.05% BSA in TBS 15 min each and again blocked with 5% BSA in TBS for 90 min. In case of double labelling experiments, replicas were incubated in second primary antibodies (Table 1) overnight, shaking at 15°C. Next, the same washing and blocking steps were repeated and secondary antibodies (Table 1) at concentration 1:40 in 2 % BSA in TBS were applied overnight at 15°C, once or twice, depending on the number of primary antibodies applied. Sections were picked up on Formvar-coated copper mesh grids for TEM imaging. Notably, the Munc13-1 antibodies were chosen based on the extensive use in fluorescent microscopy and EM (Rebola et al., 2019; Karlocai et al., 2021; Hilton et al., 2022).

For unequivocal distinction of secondary antibodies in case of double labelling, two sizes of gold conjugated particles were used – 5 and 10 nm. Batches of antibodies were tested and a distribution of the particle sizes showed clear separation between two populations.

Table 1. Antibodies used for freeze-fracture replica immunolabeling.

ANTIBODY	CONCENTRATION (µg/µl)	SOURCE (IDENTIFIER)
anti-Cav2.1 (P/Q-type) rabbit	2.5	Synaptic systems (Cat:152 203)
anti-Cav2.1 (P/Q-type) Guinea pig	1.66	Synaptic systems (Cat:152 205)
anti-Ca2.2 (N-type) rabbit	2.5	Synaptic systems (Cat:152 305)
anti-Ca2.2 (N-type) Guinea pig	2.5	Synaptic systems (Cat:152 303)
anti-Cav2.3 (R-type) Guinea pig	2.5	Genovac
anti-Munc13-1 rabbit	2.5	Synaptic systems (Cat:126 103)
anti-Munc13-2 rabbit	2.5	Synaptic systems (Cat:126 203)
anti-RIM 1/2 rabbit	1.6	Synaptic systems (Cat:140 203)
anti-Neurexin 1/2/3 rabbit	1.6	Synaptic systems (Cat:175 003)
anti-ELKS rabbit	1.6	Donation from Prof. Toshihisa Ohtsuka (Yamanashi University Medical School)
Goat anti-rabbit 5 nm gold conjugated	3.3	BBI Solutions OEM Ltd (Cat: EM.GAR5)
Goat anti-Guinea pig 10 nm gold conjugated	3.3	BBI Solutions OEM Ltd (Cat: EM.GAG10)

2.5 TEM imaging, active zone profile and FRIL analyses

All EM micrographs were analyzed blindly towards the condition of stimulation. Parameters used to recognize well-preserved frozen samples and identified synapses were overall appearance with minimal evidence of extracellular space, smooth and continuous membrane surfaces, double membranes regularly spaced, easily recognizable compact mitochondria with regular and visible cristae, cell bodies and dendrites with abundant microtubules, and nuclei with uniform chromatin (Studer et al., 2014). Hippocampal MFBs were identified in the hippocampal CA3b and CA3c subregions. They were found in high density along the MF tract in *stratum lucidum*, adjacent to *stratum pyramidale*. They were recognized based on previously well-characterized morphological features: large size, high density of clear SVs, presence of large dense-core vesicles, high-density of mitochondria, multiple synaptic contacts with large spines, and nonsynaptic *puncta adhaerentia* contacts with dendritic shafts. AZs were defined as the presynaptic membrane regions directly opposed to the postsynaptic density (asymmetric contacts), with accumulation of clear and round vesicles in close proximity to the membrane and characteristic widening of the synaptic cleft (Chicurel and Harris, 1992; Rollenhagen et al., 2007; Zhao et al., 2012a; Zhao et al., 2012b). Ultrastructure analysis focused on identifying the number of vesicles docked at identified AZ areas and their measured diameters. Additionally, structures identified in the peri-active zone area within 150 nm of the edge of AZ, presumably represent endocytotic structures. The analysis focused on a region 20–50 µm below the surface of the slice. This range corresponds also to the acute slice depth used for electrophysiology recordings.

Images of micrographs of ultrathin sections were taken with a transmission electron microscope (Thermo Fisher/FEI Tecnai 10, 80 kV acceleration voltage) with an OSIS Megaview III G3 camera and Radius acquisition software. All EM images were analyzed with Fiji open source software. Brightness and contrast were adjusted in Fiji, according to inherent contrast of the image, to optimize double membrane visualizations and accurate measurements. Several AZ profiles were distinctly analyzed per mouse sample and each group that underwent light-stimulation, also including non-light-stimulated transgenic animals controls (non-LS), had an N of 3 mice. Vesicles that were in direct contact with the active zone membrane were considered “docked”. Numbers of docked vesicles per profile were specified per 100 nm of AZ length for reliable comparison. For direct comparison of diameter measurements across groups, raw histogram counts were divided by the total length of AZ analyzed for each corresponding experimental condition. The resulting histograms display vesicle density (per 100 nm of active zone) as a function of vesicle diameter. All vesicle counting and imaging analyses were done with the experimenter blind to the condition tested on the sample.

Replicas were imaged with the same transmission electron microscope (Thermo Fisher/FEI Tecnai 10, 80 kV acceleration voltage) with an OSIS Megaview III G3 camera and Radius acquisition software. Similarly to the ultrathin sections, MFBs were observed in *stratum lucidum* of the CA3b/c regions, along the MF tract. MFBs were identified based on their location, size of the terminals, availability of attached cross fracture with numerous SVs and several putative AZs on the P-face of plasma membrane (Hagiwara et al., 2005). ImageJ Fiji open source software was used for the analysis of all replica micrographs. AZs were recognized based on the P-face location, distribution of intermembrane particles (IMPs) and labelling of AZ proteins. Gold particles, as well as AZ area, were manually segmented and their corresponding coordinates used for the point-pattern analysis. Number of gold particles per AZ was specified per 0.1 μm^2 of AZ area and used as a labeling density criteria for direct comparison across groups. Pairwise distances between two types of particles(point patterns) were calculated as Euclidian distance from each point of point pattern A to each point from point pattern B, which resulted in the distance matrix for each AZ. Next, the mean of the distance matrix was calculated and reported. Nearest neighbor distance (NND), for singe point pattern and between two points patterns, was calculated as an Euclidian distance from each point to its nearest neighbor. NNDs for random point patterns were calculated from randomly distributed Poisson point patterns with equal to experimental intensity. Mean NNDs were calculated as mean value of obtained matrixes of distances within or between point patterns.

Density-based spatial clustering of applications with noise (DBSCAN; Ester et al., 1996) was performed to determine the number of clusters of different types of calcium channels and Munc13s. The minimum number of point per cluster was set to 2. In addition, the size of neighbourhood ε, the distance between two points that can be part of same cluster, was determined from “knee” value of K-Nearest Neighbor (KNN) plot for each analysed AZ. NND and clustering analysis was done in R (RStudio) using spatstat (2.0-1) and dbscan (1.1-8) CRAN packages.

2.6 Statistical analysis

Statistical analyses were performed with Prism 8 (GraphPad Software), Origin 2019 (Origin Lab) and RStudio. All data groups were tested for normality with D’Agostino-Pearson test, followed by Kruskal-Wallis non-parametric one-way ANOVA.

Data groups were then compared using unpaired or paired t-test (specified as appropriate) or two-tailed non-parametric Mann-Whitney U test. Cumulative frequencies between the replica groups were compared with Kolmogorov-Smirnov test. For graphical representation of statistics, * indicates $p < 0.05$, ** $p < 0.01$, *** $p < 0.001$, and **** $p < 0.0001$. In figures and text, error bars report standard deviation and, as specifically stated, mean or median.

To determine whether distributions of vesicle diameter were comprised of one or two components, unbinned vesicle diameter data were analyzed by maximum likelihood fitting. Data were fit with a single normal distribution, a sum of two normal distributions, a skewed normal distribution, and a function with a sigmoidal rise, exponential decline, and shift. The model with two normal distributions was compared against all other models, using the log-likelihood ratio. Statistical significance values were obtained by bootstrap analysis (Efron and Tibshirani, 1998). Original data were duplicated 1000 times, shuffled by random permutation, and re-segmented into blocks of original length, resulting in 1000 resampled data sets. These data sets were analyzed by maximum-likelihood fitting, similar to the original data. Finally, the distribution of the log–likelihood ratios was compared against the Akaike information criterion. To provide a rigorous testing of the two-component model, the log likelihood for the best one-component model was used for comparison.

CHAPTER 3. FUNCTIONAL ELECTRON MICROSCOPY ("FLASH AND FREEZE") OF HIPPOCAMPAL MOSSY FIBER SYNAPSES

A fundamental question in Neuroscience is how synaptic structure and physiological properties are related. Electrophysiology has elucidated mechanisms of synaptic transmission, while EM has provided insight into morphological properties of synapses. While attempts to perform concurrent structural and functional analysis combined electrical stimulation or optogenetic stimulation with rapid tissue freezing have elucidaded important aspects of exocytosis and endocytosis (Heuser et al., 1979; Watanabe et al., 2013a; Watanabe et al., 2013b), these methods cannot be readily applied to mammalian brain tissue, as used for electrophysiology. In order to overcome this challenge, an improved functional EM technique was developed, which enabled the investigation of synaptic transmission at the hippocampal MFB-CA3 PN synapse, using mouse acute brain slices and organotypic slices culture. Moreover, it allowed us to selectively stimulate the presynaptic MFBs and examine SV dynamics at AZs with millisecond precision and nanometer resolution. The following chapter describes the methodology and unexpected results of optogenetic MFB stimulation.

3.1 Genetic targeting and optogenetic activation of hippocampal GCs

One of the most critical aspects of the current study was to perform functional EM experiments on a specific cortical synapse – the hippocampal MFB-CA3 PN synapse. Therefore, numerous control experiments were performed to overcome several difficulties and to ensure the work with the identified synapse of interest.

First, a method to selectively activate the presynaptic neurons, in this case, GCs giving rise to the hippocampal MF axonal tract and MFBs, was developed. Prospero homeobox 1 (Prox1) is a transcription factor found to selectively express in adult GCs and dictate hippocampal GC identity (Lavado et al., 2010; Ming and Song, 2011) (Fig. 3-1, 3-2). Therefore, two Cre-dependent transgenic mouse lines were used:

- Prox1-Cre, a mouse line with constitutive Cre expression
- Prox1-CreER^{T2}, a line with inducible Cre (Bazigou et al., 2011).

Both lines were crossed with a reporter line expressing tdTomato, a red fluorescent protein. This enabled a quantitative analysis of the proportion of Cre-positive GCs at the single-cell level, in double immunofluorescent labeling experiments with NeuN, a pan-neuronal protein (Fig. 3-1). Based on the colocalization quantification, in the Prox1-Cre line, 88.3% of GCs expressed tdTomato. In the Prox1-CreER^{T2} line, the expression of tdTomato was tamoxifen dose-dependent, approaching the expression in Prox1-Cre mice at high doses (200 mg kg^{-1}; 83.2% in acute slices; 89.3% in slice cultures).

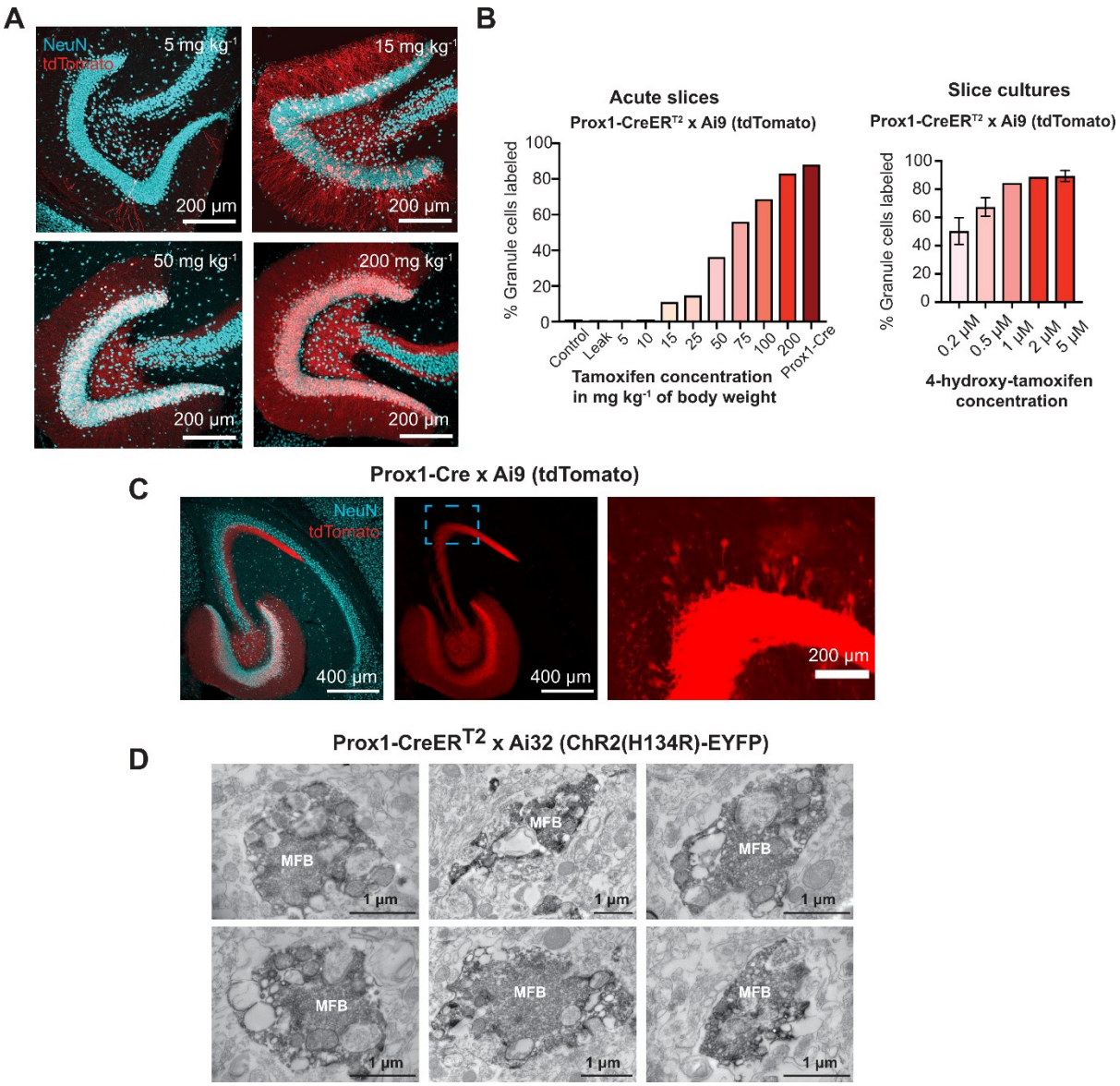

Figure 3-1. Specific labeling and channelrhodopsin expression in hippocampal GCs. (A–B), Dose response curve of tamoxifen in Prox1-CreERT2 x Ai9 mice. Neurons were labelled based on NeuN immunoreactivity (cyan) and GCs with Cre activated by tamoxifen were identified based on tdTomato fluorescence (red). **(C),** Similar labeling as done for cell counting in (A) and (B), showing labeling of unidentified interneurons in the CA3 region of Prox1-Cre mice, in the right panel (inset from the blue region in the middle panel. **(D),** Pre-embedding immunolabeling of mice from the Prox1-CreERT2 x Ai32 mice, in which channelrhodopsin is fused to EYFP. Primary anti-GFP antibody and DAB/hydrogen peroxidase reaction was used to localize channelrhodopsin in mossy fiber boutons (MFB) at the EM level. Scale bar sizes are indicated on the figure (Borges-Merjane et al., 2020).

In Prox1-Cre mice, since Cre is functional from birth, we observed developmentally dependent tdTomato labeling of unidentified interneurons and glia cells (Fig. 3-1C). Therefore, for the rest of the experiments described in this chapter, Prox1-CreER^{T2} with timed tamoxifen injections to juvenile mice was used, because the labeling in this line was exclusively restricted to GCs (Fig. 3-1). Prox1-CreER^{T2} line was crossed with an Ai32 (ChR2(H134R)-EYFP) line, followed by injecting high doses of tamoxifen *in vivo* for acute brain slice experiments, or by application of high concentrations of 4-OH-tamoxifen *in vitro* to organotypic slice cultures (Fig. 3–2B). This led to strong channelrhodopsin expression in a large number of GCs.

Next, control electrophysiological recordings determined the optimal settings for optogenetic stimulation in both acute slices and organotypic slice culture (Fig. 3-2C–O). The intensity of light pulses was matched to the intensity reached in the HPF apparatus (5.5–8.0 mW mm^{-2}; see Chapter 2. Materials and Methods; Fig. 3-2A; see Chapter 2. Materials and Methods). Neurons in acute slices and organotypic slice culture demonstrated diverse responses to light stimulations. In acute slices, single 1-ms pulse reliably evoked APs in GCs with minimum latency, while in slice cultures 5-ms pulses were required (Fig. 3-2C–D; in acute slices 1-ms pulses 0.68 ± 0.13 ms (mean ± SD) and 5-ms pulses 0.76 ± 0.18 ms, n = 8 GCs; in slice cultures 5-ms pulses 0.82 ± 0.16 ms, n = 15 GCs). In addition, it was found that trains of 10 pulses reliably evoked APs in GCs for stimulation frequencies of up to 20 Hz (Fig. 3-2E). Hence, the maximum stimulation frequency was limited to 20 Hz.

Prolonged trains of 1-ms pulses evoked APs with reduced reliability in acute slices. This is noticeable, in particular, at the last 2 seconds of a 5-s stimulation protocol, with 100 light-pulses at 20 Hz repetition rate, whereas trains of 5-ms pulses reliably evoked APs throughout the stimulus train (Fig. 3-2F–G; AP success rate for full 100-pulse train, 1-ms pulses 0.50 ± 0.32 (mean ± SD), 5-ms pulses 0.96 ± 0.10, p = 0.0034; for last 2 s of train, 1-ms pulses 0.30 ± 0.27, 5-ms pulses 0.86 ± 0.22, p = 0.0014; n = 7 GCs). For organotypic slice culture, 1-ms light pulses were not sufficient to elicit APs in GCs, while 5-ms pulses evoked APs reliably. Interestingly, more failures were observed in slice culture than in acute slices, possibly because of the increased intrinsic activity of cultured cells. However, 5-ms pulses evoked occasionally more than 1 AP in slice culture (Fig. 3-2C,H). Altogether, reliable single and repetitive light stimulation of GCs was achieved with Prox1-CreER^{T2} driven expression of channelrhodopsin.

To test whether stable synaptic transmission can be elicited after optogenetic stimulation of GCs, recordings from CA3 PNs were performed. Both single light pulses as well as 20-Hz trains of 5-ms pulse stimuli led to reliable induction of excitatory post-synaptic currents (EPSCs) (Fig. 3-2I–N). Consistent with previous observations in GCs, frequencies above 20-Hz showed impaired temporal resolution and fidelity of transmission. From a 5-pulse train, at higher frequencies, peak amplitudes of EPSCs started to overlap, and PPR became variable (Fig. 3-2M–N). Again, acute slices and slice culture unveiled several dissimilarities in CA3 PN responses. Slice cultures had a longer and more variable latency, and slower and more variable rise times (Fig. 3-2J; latency acute slice 4.54 ± 0.62 ms (mean ± SD), n = 10 CA3 PNs; slice culture 6.70 ± 2.02 ms, n = 14 CA3 PNs; P = 0.0036; 20-80% rise time acute slices 1.72 ± 0.62 ms, n = 9 CA3 PNs; slice cultures 3.42 ± 2.14 ms, n = 14 CA3 PNs; p = 0.019). This can be attributed due to network rearrangement during the culture growth process *in vitro*. Moreover, occasionally, inhibitory post-synaptic currents (IPSCs) were present in organotypic slice culture. However, very little recruitment of inhibition with 20-Hz trains of 5-ms pulses and no IPSCs were observed in acute slices, only evoked EPSCs were present.

Additionally, to confirm that EPSCs were evoked by APs generated in GCs, as a result of optical stimulation, we bath-applied the sodium channel blocker tetrodotoxin (TTX; 1 µM) to block AP generation. TTX blocked both APs in GCs and EPSCs in CA3 pyramidal cells (Fig. 3-2K; % change in EPSC amplitude 93.2 ± 3.9 %; p = 0.0005; n = 3 CA3 PNs). Thus, based on the electrophysiology experiments, single 5-ms pulses and trains of 5-ms light pulses at 20-Hz were used in subsequent HPF experiments (Fig. 3-2O). Notably, stimulus paradigms such as the long train, with 50 or 100 stimuli at 20 Hz, were previously used to deplete the RRP (Rosenmund and Stevens, 1996;

Murthy and Stevens, 1999), and may also be strong enough to induce short-term plasticity.

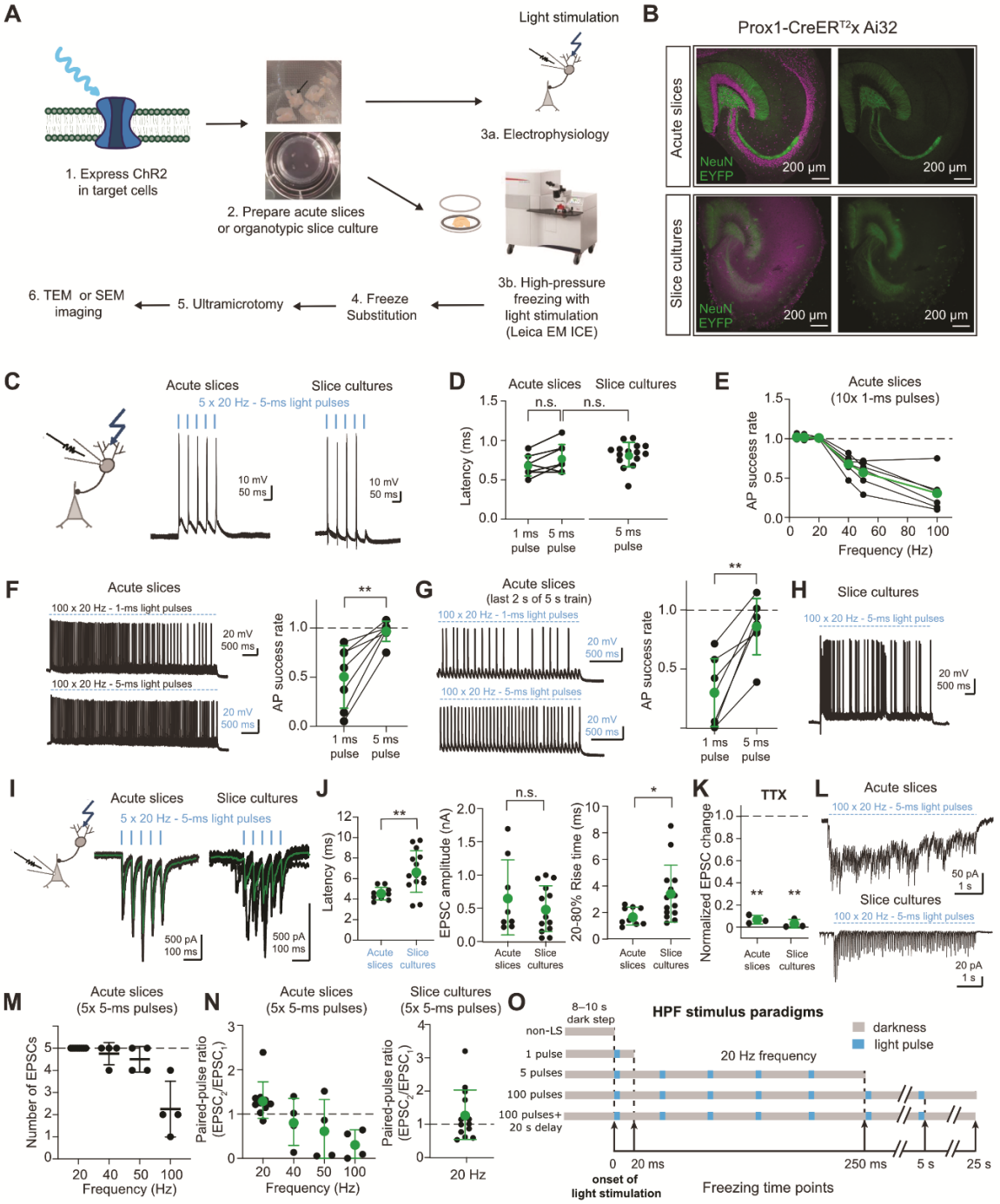

Figure 3-2. Selective optogenetic stimulation of hippocampal GCs. (A), Diagram of "flash and freeze" experimental workflow. **(B),** Confocal images of hippocampal acute slices (top) and slice cultures (bottom) of a mouse expressing ChR2-YFP under control of the Prox1 promoter (green), targeting specifically GCs in the DG, superimposed with NeuN labeling (magenta). **(C-H),** Electrophysiology recordings from GCs in acute slices and slice cultures with APs evoked by direct ChR2 activation. **(I-N),** Electrophysiology recordings from CA3 PN with EPSCs evoked by synaptic transmission. **(O),** Graphic representation of optogenetic stimulus paradigms for HPF experiments, based on the assessment of stimulus efficacy by electrophysiology (Borges-Merjane et al., 2020).

3.2 Optimization HPF of acute slices and organotypic slice cultures

A final challenge to overcome, was the evident need to develop a reliable technique for HPF of acute slices, to examine central synapses in their natural network environment and correlate structural and functional changes during synaptic transmission. Previously, a few studies successfully performed HPF in live organotypic slice cultures (Studer et al., 2014; Imig et al., 2014). Thus, cryo-fixation experiments in organotypic slice cultures were used as a reference point for the technical optimization, and were done in parallel with development of HPF procedure of acute slices (Fig. 3-3, 3-4, 3-5).

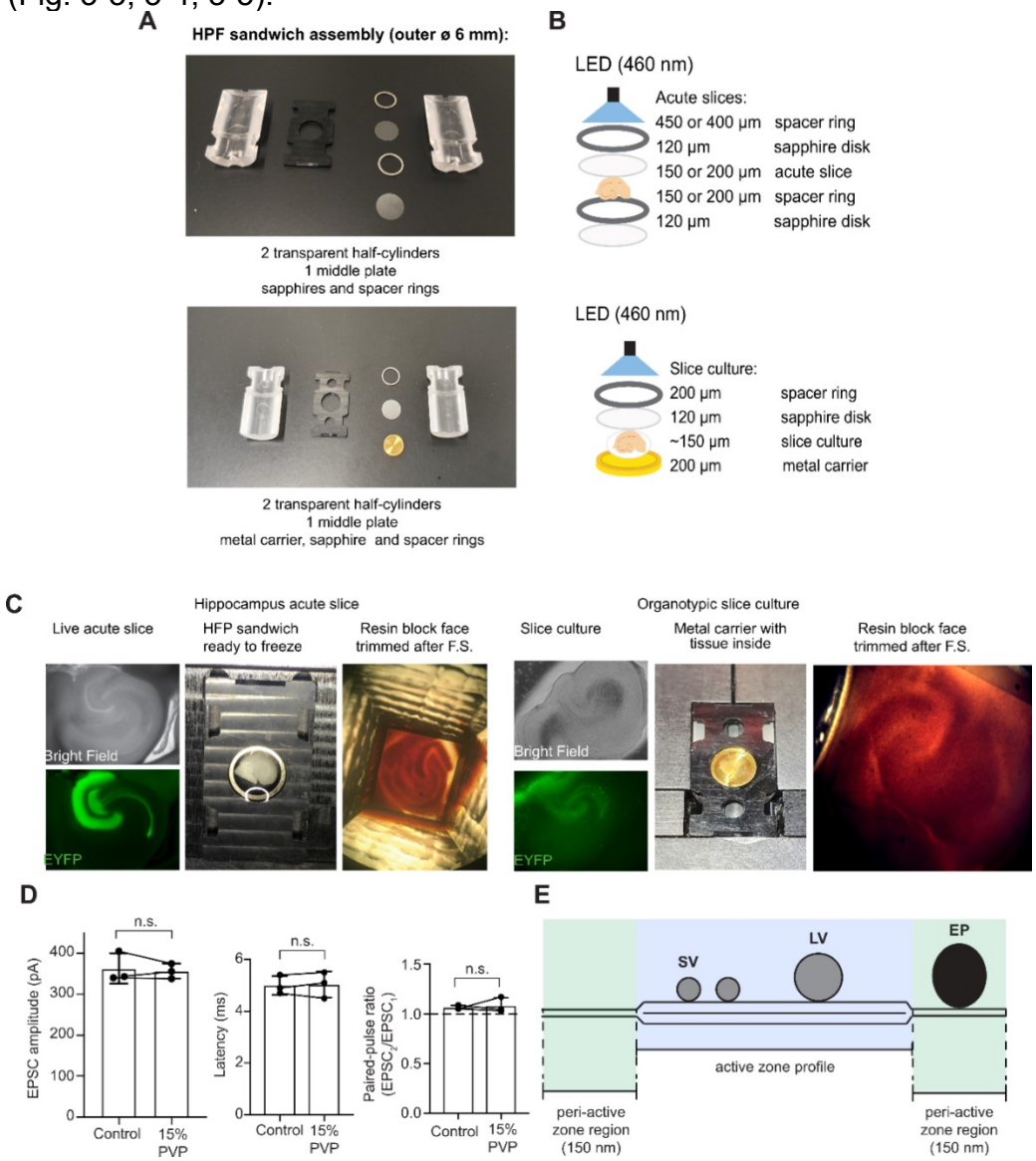

Figure 3-3. High-pressure freezing of acute slices and slice culture. (A), Materials used for HPF with light-stimulation of acute slices (top panel) and slice culture (bottom panel). **(B),** Graphic representation of HPF sandwich assembly for acute slices and slice cultures. **(C),** Example of a live acute slice (left panel) and slice culture (right panel) used for either electrophysiology experiments or HPF, expressing ChR2 in GCs; assembled sandwiches and metal carrier with hippocampus just prior to HPF and example resin block face after trimming, showing the intact target brain areas. **(D),** Light-evoked EPSC recordings from CA3 pyramidal neurons after bath application of 15% PVP showed no significant difference to control in amplitude, latency, or paired-pulse ratio. Bars and whiskers show mean ± SD. **(E),** Cartoon illustrating parameters measured for each experiment. These are length of active zone (AZ) profile; number of docked vesicles in AZ; diameter of docked vesicles within the AZ (small (SV) and large (LV) vesicles); number of structures in the peri-AZ region (putative endocytic pits (EP)), with peri-AZ defined as the region from the edge of the AZ up to 150 nm; diameter of the EPs in the peri-active zone. (modified from Borges-Merjane et al., 2020).

Several methodological improvements were made for successful freezing of acute slices (Fig. 3-3A–C, 3-4A–M). First, 150- and 200-µm thick slices were used for freezing, to promote rapid freezing and water vitrification (Fig. 3-3B–C, 3-4A–M). Although 150-µm ones contained less deterioration in the core of the tissues, caused by ice crystals, 200-µm thick slices were more resistant to mechanical damage. In addition, the 200 µm thickness is in good accordance with the calculated thickness of slice culture after 14-21 DIV (Guy et al., 2011). Thus, this thickness range was selected in acute slices and slice culture experiments. Second, with the goal to employ a slice recovery procedure to retain neural activity from live neurons for stimulation prior to HPF, the same recovery protocols as those used for electrophysiological experiments were applied (Bischofberger et al., 2006b): slices were incubated for 30–45 min at ~35°C after slicing in sucrose solution and transferred to recording ACSF solution. Third, carrier size for HPF was found to be critical for the maintenance of healthy tissue. Carriers with 6 mm outer diameter accommodate acute slice and slice culture preparations containing the whole hippocampal network, including part of the surrounding tissue, keeping the neural circuit intact (see Chapter 2. Materials and Methods; Fig. 3-3).

Furthermore, carrier assembly and careful tissue transfer were optimized to avoid additional mechanical stress to thin acute slice and slice culture. Briefly, carrier sandwich for acute slices consisted of two transparent sapphire discs with a metal O-ring spacer in the middle (Fig. 3-3B). For HPF of slice culture, a metal carrier with sapphire disk on top was used (Fig. 3-3B). This hybrid system resulted in a more stable sandwich configuration for slice cultures, as metal carriers provided a tight fit to hold the membrane of each culture in place. Transfer of acute slices was done using a large brush to keep the slice flat and avoid drying without ACSF solution. Slices were precisely centered to maintain tissue integrity intact, as well as to avoid sapphire breakage and/or poor freezing quality. In acute slices, 15% polyvinylpyrrolidone (PVP) in ACSF was used as cryopotectant filler medium and resulted in the most well-preserved ultrastructure. The tissue was exposed to PVP only during sandwich assembly, with a drop of filler medium before sandwich closure. To ensure that the addition of PVP was not affecting responses to the light stimulus, the effects of 15% PVP on GC APs and light-evoked EPSCs in CA3 pyramidal cells were tested. Latency, EPSC peak amplitude, and PPR did not change significantly (Fig. 3-3; latency 5.03 ± 0.50 ms (mean ± SD), $p = 0.930$; % change in EPSC amplitude 1.7 ± 29.1 %; $p = 0.7644$; PPR 1.07 ± 0.09; $p = 0.3345$; n = 3 CA3 neurons).

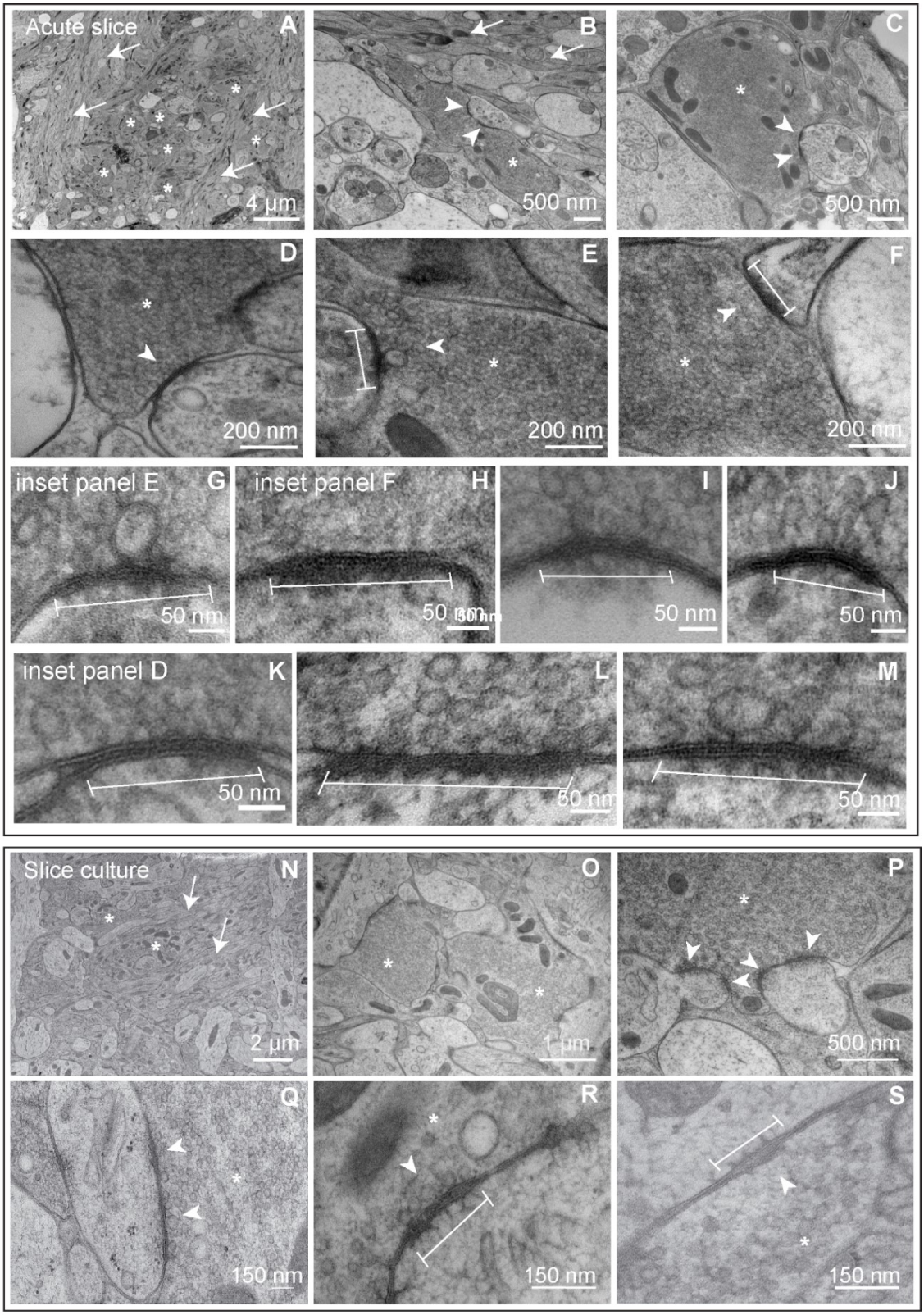

Figure 3-4. Ultrastructure of high-pressure frozen acute slices and organotypic slice cultures. Example TEM micrographs, showing quality of ultrastructure in acute slices (frozen in 15% PVP) in **(A–M**) and slice cultures (frozen in 15% BSA) in **(N–S)**, from lower to higher magnification. Images were taken from the mossy fiber tract in stratum lucidum of the CA3 region, primarily CA3b and CA3c, and show mossy fiber axons (arrows), putative MFBs (asterisks), AZs (arrowheads), and postsynaptic densities (bars). Displayed micrographs in this figure are representative of all samples, from different mice, used for analysis of controls and light-stimulated tissue. Scale bar sizes are indicated on the figure (Borges-Merjane et al., 2020)

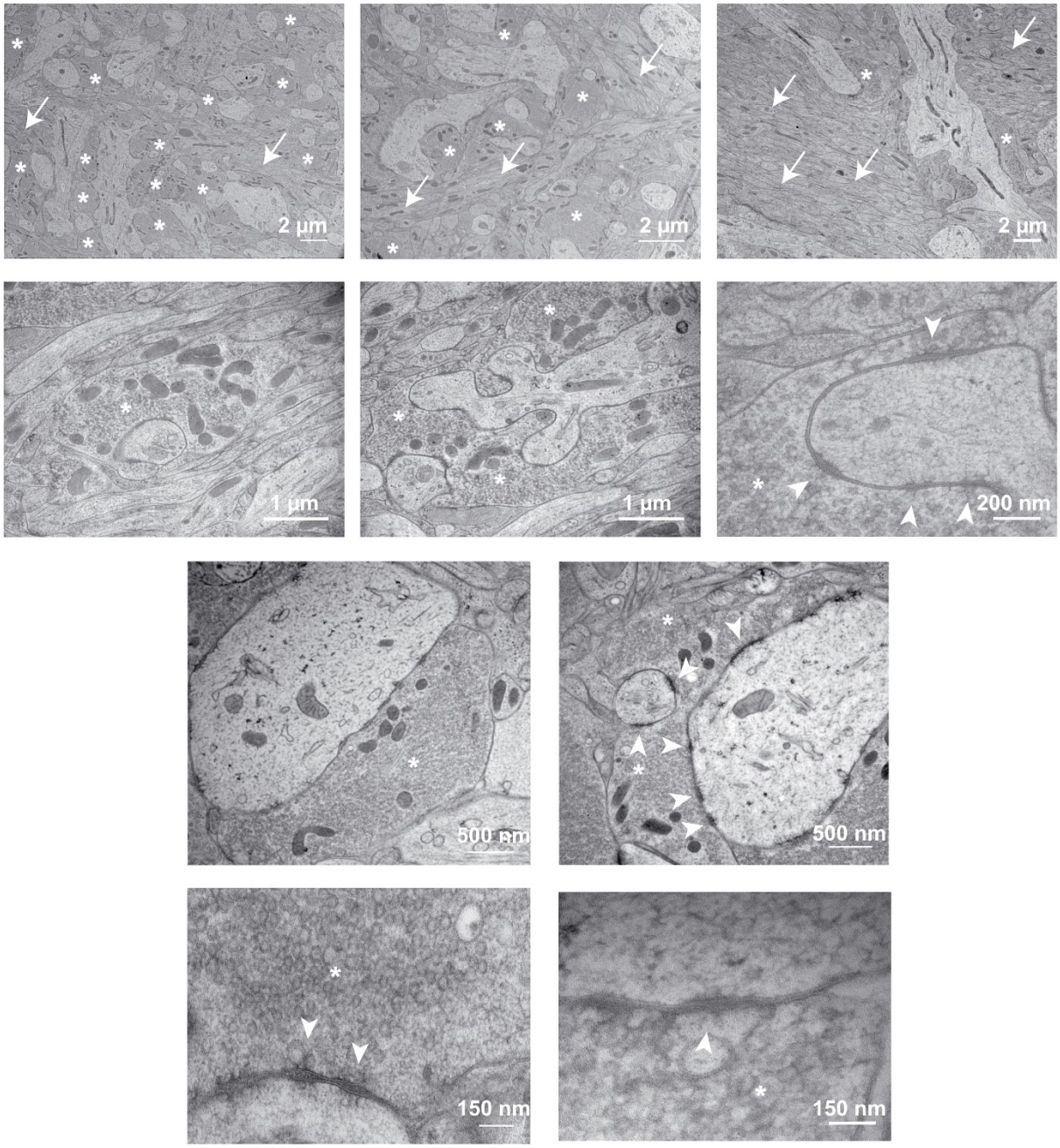

Figure 3-5. Additional images of organotypic hippocampal slice culture. Organotypic slice cultures of mouse hippocampus, frozen in 15% BSA, with a hybrid sapphire and metal carrier system, show well-preserved ultrastructure after high-pressure freezing. TEM images of high-pressure frozen samples sectioned at 70 nm, at different magnifications. Images were taken from the mossy fiber tract region corresponding to stratum lucidum in the CA3 region, primarily CA3b and CA3c; mossy fiber axons (arrows), putative MFBs (asterisks), and AZs (arrowheads) are indicated. Scale bar sizes are indicated on the figure (Borges-Merjane et al., 2020).

The next step in the EM sample preparation workflow is freeze-substitution (FS) (Fig. 3-2A). To find optimal parameters, different FS protocols were tested. Based on other studies that applied HPF in fresh (non-chemically fixed) organotypic slice cultures and acute slices (Studer et al., 2014; Imig et al., 2014), the following parameters were changed: presence of tannic acid treatment, osmium tetroxide concentration, duration of FS steps (in presence or absence of shaking), different temperature steps and various post-staining parameters. The implementation of a constant shaking device that fits on top of the automated freeze substitution system (Goldammer et al., 2016) led to several improvements. Firstly, by gently shaking

throughout the FS, unopened sapphire sandwiches opened gently during FS without damaging the slices, enabling thorough infiltration. Secondly, it notably shortened duration of FS to 2 days (see Chapter 2. Materials and Methods). After the resulting accelerated FS procedure, samples underwent room-temperature Durcupan resin embedding, ultrathin-sectioning and imaging (Fig. 3-2A).

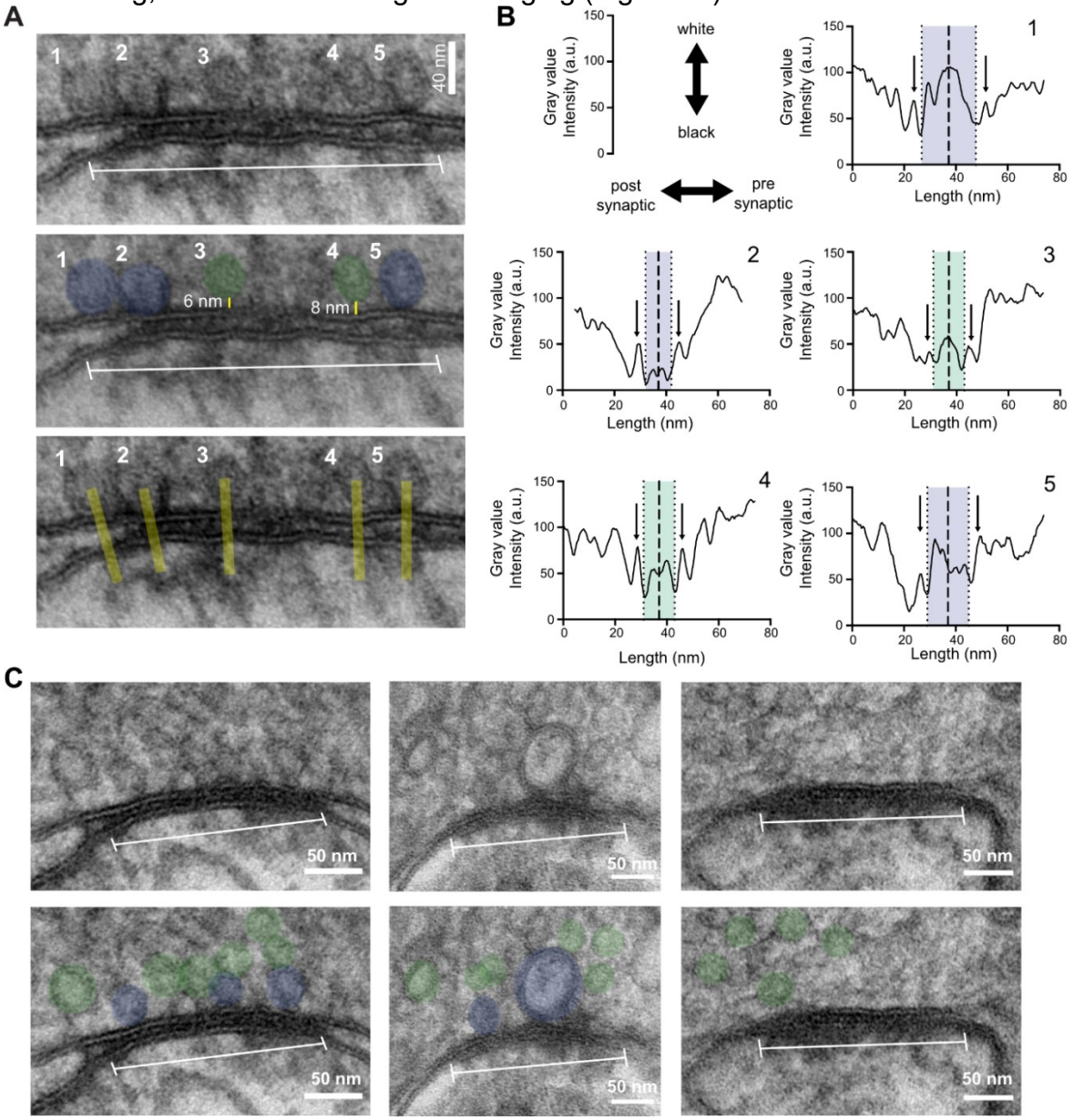

Figure 3-6. Criteria for docked synaptic vesicles. Vesicles were considered docked when less than 5 nm away from the active zone membrane. **(A),** Left panel: example AZ from control samples; middle panel: 3 clearly identified docked (blue) and 2 undocked vesicles (green; at 6 nm and 8 nm away from the membrane); right panel: lines (yellow) used for the intensity profile plots in B. **(B),** Gray value intensity plots for each vesicle shown at the example active zone in A. We can identify the synaptic cleft (shaded area) and the adjacent membranes, including dark bilayer leaflets and bright center (black arrows). **(C),** Examples of other AZs denoting smaller and larger docked, and a few identified undocked vesicles marked. The right panel shows an active zone profile without docked vesicles. Scale bar sizes are indicated on the figure (Borges-Merjane et al., 2020).

Following this procedure, adequate preservation of the ultrastructure in acute slices, and organotypic slice cultures was accomplished, which was comparable to frozen slice cultures with more conventional procedures (15% bovine serum albumin (BSA); Studer et al., 2014; Fig. 3-4, 3-5). Thus, the optimized method is applicable to both acute slices and organotypic slice cultures.

3.3 Analysis of synaptic ultrastructure under basal conditions

In the scope of this study, great attention was given to the ultrastructural analysis of the AZ area in MFBs, in particular the number of docked SVs and their sizes (Fig. 3-6, 3-7, 3-8). Moreover, general inspection of the ultrastructure of MFBs unraveled several morphological features, including large size, high density of clear SVs, presence of large dense-core vesicles, high-density of mitochondria, multiple synaptic contacts with large spines, and nonsynaptic PA contacts with dendritic shafts. All above mention characteristics are in good accordance with previous studies (Chicurel and Harris, 1992; Henze et al., 2002; Rollenhagen et al., 2007). Before focusing on light stimulated samples, number and diameter of docked vesicles were compared between wild-type (WT) and transgenic non-stimulated (non-LS) control groups with or without TTX and the two types of preparations (acute slices versus organotypic slice cultures; Fig. 3-7, 3-8).

The TTX control enabled assessment of the contribution of basal AP activity to changes in the size of the docked pool. The number of docked vesicles was normalized per 100 nm of AZ profile. Both number and diameter of docked vesicles were not significantly different among the three control conditions in acute slices (Fig. 3-7, Table 2; in WT: number of docked vesicles 1.25 ± 0.46 (mean ± SD), median 1.23; docked vesicle diameter 38.9 ± 13.4 nm, median 35.1 nm; n = 123 AZ profiles, n = 366 vesicles, N = 2 mice; in non-LS: number of docked vesicles 1.16 ± 0.49, median 1.14; docked vesicle diameter 37.7 ± 13.4 nm; median 33.8 nm; n = 116 AZ profiles, n = 280 vesicles, N = 3 mice; in non-LS+TTX: number of docked vesicles 1.15 ± 0.57; median 1.07 ; docked vesicle diameter 39.7 ± 15.1 nm; median 34.4 nm; n = 102 AZ profiles, n = 252 vesicles, N = 2 mice; significance for number of docked vesicles: WT vs non-LS $p = 0.5428$; WT vs non-LS+TTX $p = 0.6465$; non-LS vs non-LS+TTX $p > 0.9999$; significance for vesicle diameter: WT vs non-LS $p = 0.1962$; WT vs non-LS+TTX $p = 0.8194$; non-LS vs non-LS+TTX $p > 0.9999$).

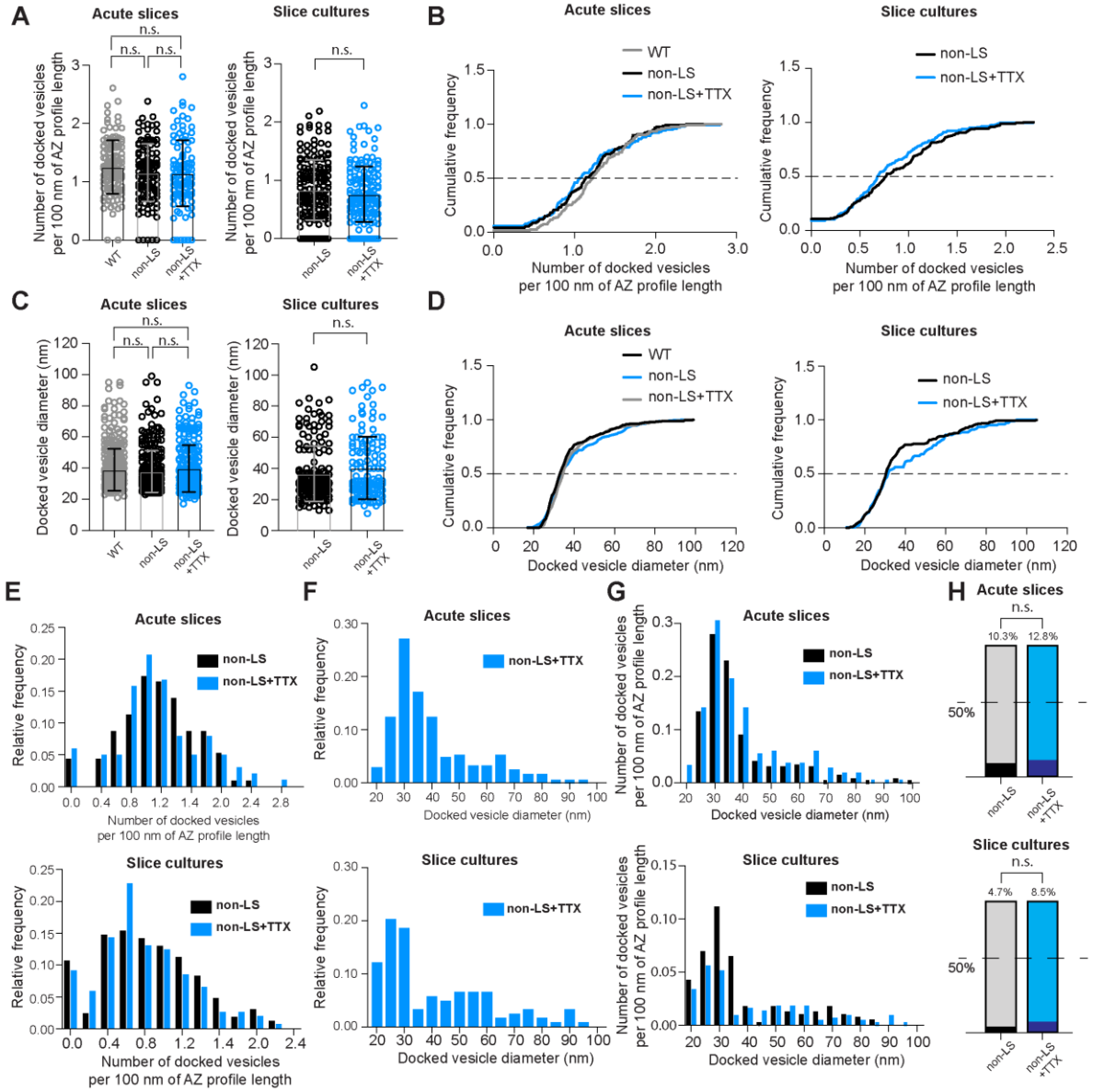

Figure 3-7. Unstimulated samples show no significant difference from TTX control group. (A), Number of docked vesicles remained unchanged in the presence of TTX in both acute slices and slice cultures. **(B),** Cumulative frequency of data shown in (A) for all groups. **(C),** Diameter of docked vesicles also remained unchanged in the presence of TTX. **(D),** Cumulative frequency of the data shown in (C) for all groups. **(E),** Relative frequency distribution histograms for the number of docked vesicles in controls and in the presence of TTX for acute slices (top) and slice cultures (bottom). **(F),** Relative frequency distribution for the diameter of docked vesicles in the presence of TTX for acute slices (top) and slice cultures (bottom). **(G),** Comparison of the distribution of the docked vesicle diameter between control and in the presence of TTX, for acute slices (top) and slice cultures (bottom). **(H),** Stacked bars displaying the percentage of active zones with pits in peri-active zone regions, per group, in both acute slices Bars and whiskers denote mean ± SD (Borges-Merjane et al., 2020).

Interestingly, slice cultures exhibited significantly smaller number of docked vesicles with smaller diameter compared to acute slice preparation (Fig. 3-8, Table 2; in culture non-LS: number of docked vesicles (mean ± SD) 0.84 ± 0.52; median 0.77; docked vesicle diameter 36.7 nm ± 17.8 nm; median 31.5 nm; n = 170 AZ profiles, n = 171 vesicles, N = 3 mice; non-LS acute slices vs non-LS slice cultures: number of docked vesicles $p < 0.0001$ and diameter $p < 0.05$; Fig. 3-7A). In slice cultures, measurement from TTX-treated samples were also not significantly different than those taken from the control non-LS group (Fig. 3-7; in non-LS+TTX: number of docked vesicles 0.77 ± 0.48; median 0.69; docked vesicle diameter 40.3 ± 20.1 nm;

median 32.8 nm; n = 154 AZ profiles, n = 124 vesicles, N = 2 mice; non-LS *vs* non-LS+TTX: number of docked vesicles p > 0.9999 and vesicle diameter p > 0.9999).

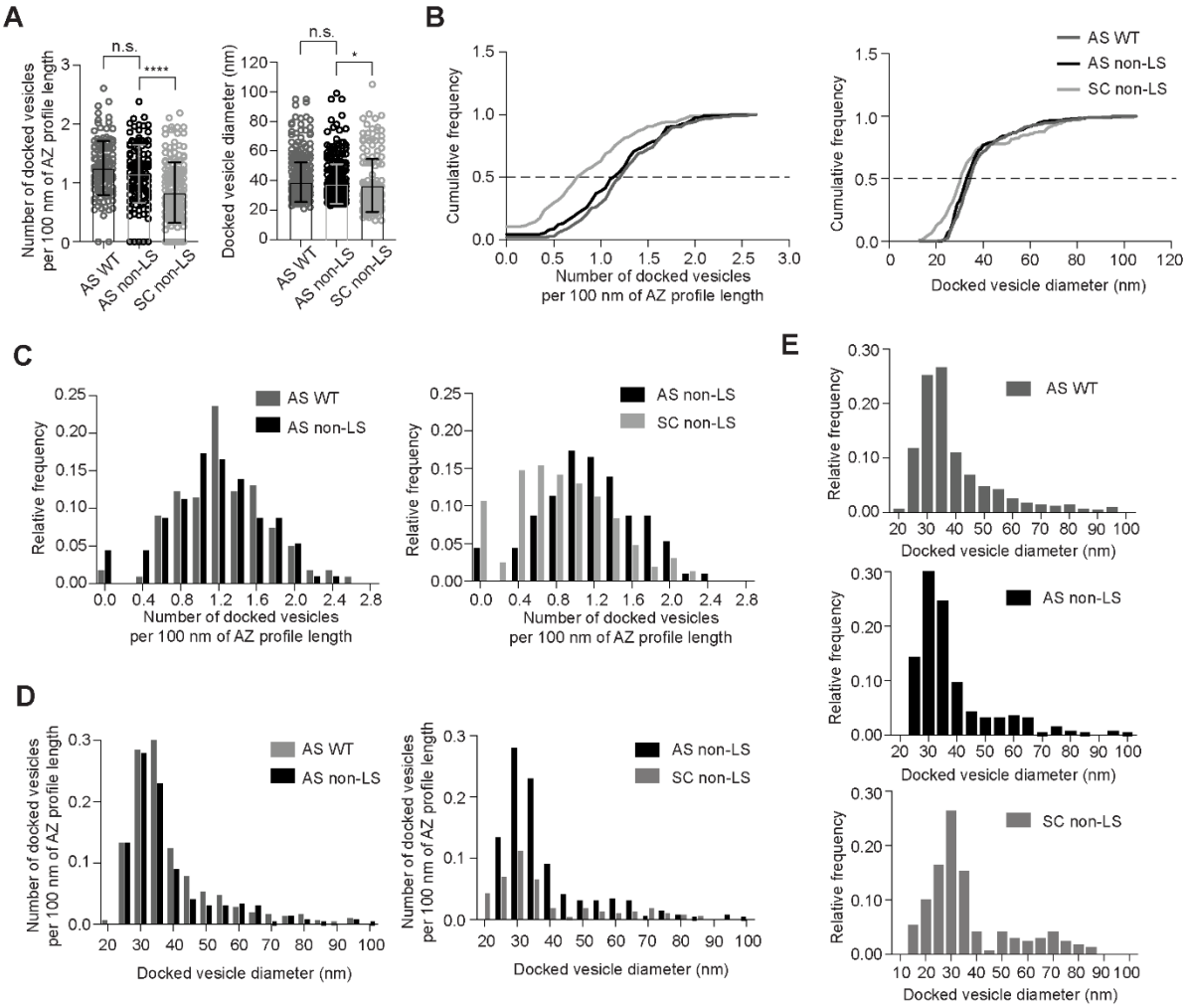

Figure 3-8. MFBs in acute slices have more docked vesicles and larger diameter vesicles than in slice cultures. **(A),** Left panel, scatter plot of the number of docked vesicles per 100 nm of active zone length, in acute slices (AS) from wild-type (WT) animals and from non light-stimulated transgenic animals (non-LS), and slice cultures (SC) from non light-stimulated transgenic animals (non-LS). Right panel, scatter plot of the diameter of docked vesicles in each group. Bars and whiskers show mean ± SD. **(B),** Cumulative plots of the data displayed in A for the number of docked vesicles (left) and docked vesicle diameter (right). **(C),** Histograms with the relative frequency distribution of number of docked vesicles per 100 nm of active zone length compared between acute slices controls (WT vs non-LS) and between acute slices and slice cultures (AS non-LS vs SC non-LS). **(D),** Histograms of docked vesicle diameter compared between acute slices controls (WT vs non-LS) and between acute slices and slice cultures (AS non-LS vs SC non-LS). **(E),** Histograms showing the individual relative frequency distribution of docked vesicle diameter for acute slices and slice cultures (Borges-Merjane et al., 2020).

Furthermore, the distribution of docked vesicles diameter also differed between acute slices and slice culture. Analysis of docked vesicles in organotypic slice culture revealed a bimodal distribution of sizes, but in acute slices it was continuous and right-skewed (Fig. 3-8D,E). Maximum-likelihood analysis revealed no significant improvement of the fit with two components in acute slices (p = 0.59), but a significant improvement in organotypic slice cultures (p < 0.001; Methods). All things considered, these results indicate that both the number and diameter of docked vesicles are similar across different control conditions in acute slices, whereas number and diameter are slightly, but significantly higher in acute slices than in organotypic slice cultures, which could be a result of increased intrinsic activity of organotypic slice culture.

Table 2. Number and diameter of docked synaptic vesicles before and after light stimulation in acute slices and organotypic slice culture.

Sample	Acute slices	Slice culture
	Mean number of SVs per 100 nm AZ profile length ± SD (median)	
WT	1.25 ± 0.46 (1.23)	-
Non-LS	1.16 ± 0.49 (1.14)	0.84 ± 0.52 (0.77)
1 pulse	1.03 ± 0.44 (0.99)	0.54 ± 0.42 (0.51)
5 pulses at 20 Hz	0.83 ± 0.54 (0.86)	0.35 ± 0.34 (0.35)
100 pulses at 20 Hz	0.33 ± 0.39 (0.25)	0.11 ± 0.24 (0.00)
100 pulses at 20 Hz + 20 s delay	1.45 ± 0.61 (1.39)	0.94 ± 0.52 (0.89)
	Mean docked vesicle diameter ± SD (median)	
WT	38.9 ± 13.4 (35.1)	-
Non-LS	37.7 ± 13.4 (33.8)	36.7 ± 17.8 (31.5)
1 pulse	44.0 ± 15.0 (38.2)	52.5 ± 16.2 (50.1)
5 pulses at 20 Hz	40.8 ± 14.8 (35.2)	46.9 ± 22.5 (45.3)
100 pulses at 20 Hz	38.9 ± 12.1 (35.4)	44.1 ± 15.7 (45.1)
100 pulses at 20 Hz + 20 s delay	43.8 ± 18.9 (37.0)	38.3 ± 15.1 (34.0)

3.4 Stimulus-dependent depletion of the docked vesicle pool

Next, optically stimulated acute slices and slice culture were cryo-fixed (Fig. 3-9, 3-10). After application of mild and strong stimulation, the number and diameter of docked vesicles in AZ profiles of MFBs were quantified (Fig. 3-9, 3-10). The following electrophysiologically tested light stimulation paradigms were applied, with 5-ms light pulses (Fig. 3-2O):

- 1 pulse of light (evoked 1 AP in acute slices, or 1–2 in the case of slice cultures);
- short train of 5 pulses at 20 Hz;
- long train of 100 pulses at 20 Hz, a stimulation protocol commonly used to deplete the RRP (Rosenmund and Stevens, 1996; Murthy and Stevens, 1999), and also strong enough to induce short-term plasticity;
- long train of 100 pulses at 20 Hz with 20 s freezing delay, a stimulation protocol that may reveal refilling after depletion, as well as potential structural plasticity.

According to earlier studies with the “flash and freeze” method (Watanabe et al., 2013a; Watanabe et al., 2013b), putative SV fusion pits (Ω-shapes) could be observed after a single light pulse. Thus, we applied one 5-ms pulse to capture possible Ω-shapes in the MFB AZs. For the brief and long trains, at 20 Hz stimulating rate, samples were frozen 50 ms after the last pulse onset (Fig. 3-2O), which corresponded respectively to 250 ms and 5 s after the onset of the first light stimulus. Finally, to investigate replenishment of the docked vesicle pool in MFB AZs, a delay was added between the end of stimulation and freezing onset. In this case, samples were stimulated with a long 100-pulse train lasting 5 seconds, and frozen 20 s after the last pulse in the train (Fig. 3-2O). Again, the number of docked vesicles was normalized per 100 nm of AZ profile length. Additionally, structural correlates of both exocytosis and endocytosis were examined across all groups.

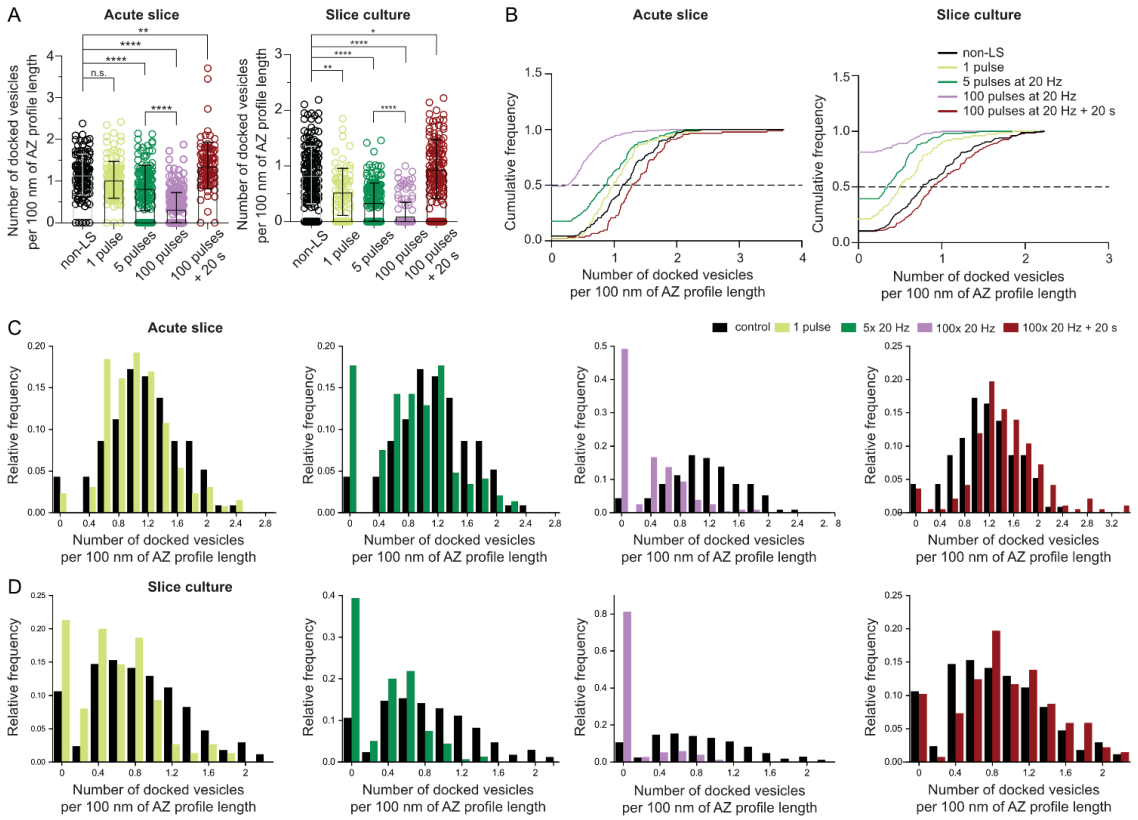

Figure 3-9. The number of docked vesicles decreases in an activity-dependent manner in both acute slices and slice cultures. (A), Scatter plot of the number of docked vesicles per 100 nm of active zone length, in acute slices (left) and slice cultures (right), for each stimulation paradigm. Bars and whiskers show mean ± SD. Dotted line indicates mean of non-LS control. **(B),** Cumulative plots of the data displayed in A. **(C–D),** Histograms showing the comparison of relative frequency distribution of docked vesicle numbers for acute slices (C) and slice cultures (D). Histograms compare each stimulated sample to non-LS control (modified from Borges-Merjane et al., 2020).

Comparison of the non-light stimulated samples to the stimulated group revealed several interesting phenomena in both slice culture and acute slices. First, samples that underwent single pulse stimulation showed decreased number of docked vesicles at the AZs (Fig. 3-9). However, this decrease was statistically significant only in slice culture experiments and was greater in slice culture than in acute slices (acute slices: Fig. 3-9A-C; (mean ± SD) 1.03 ± 0.44; median 0.99; n = 130 active zone profiles, N = 2 mice; p = 0.7015; Fig. 3-9A left panel; slice cultures: Fig.3-9A, B, D; 0.54 ± 0.42; median 0.51; n = 75 active zone profiles, N = 3 mice; p = 0.0017; Fig. 3-9A right panel). This result from acute slices reflects the low probability of release in MFBs, while the higher release of vesicles in cultures is likely a result of the higher excitability present in slice cultures, indicated by the ability of a single light pulse to evoke two APs in GCs. Further, after a single light-pulse, the mean diameter of docked vesicles increased in acute slices and slice culture (acute slices: Fig. 3-10A–D; (mean ± SD) 44.0 ± 15.0 nm; median 38.2 nm; n = 130 AZ profiles, n = 177 vesicles, N = 2 mice; p < 0.0001; Fig. 3-10A left panel; slice cultures: Fig. 3-10A,B,E,F; (mean ± SD) 52.5 ± 16.2 nm; median 50.1 nm; n = 75 AZ profiles, n = 40 vesicles, N = 3 mice; p < 0.0001; Fig. 3-10A right panel), suggesting that the vesicles with smaller diameter are release first and have higher release probability.

Second, a short train of 5 light pulses at 20 Hz resulted in significant decrease in number of docked vesicles in acute slices and slice culture compared to the control non-LS group (Fig. 3-9A–C; (mean ± SD) 0.83 ± 0.54; median 0.86; n = 147 AZ profiles, N = 3 mice non-LS control *vs* 5 pulses p < 0.0001 and 1 pulse *vs* 5 pulses p

= 0.0169; Fig. 3-9A left panel; slice cultures: 0.35 ± 0.34; median 0.35; n = 160 AZ profiles, N = 3 mice; non-LS control *vs* 5 pulses p < 0.0001 and 1 pulse *vs* 5 pulses p = 0.0203; Fig. 3-9A right panel). Additionally, the diameter of docked vesicles was again significantly different from non-LS control for both acute slices (Fig. 3-10A-D; (mean ± SD) 40.9 ± 14.8 nm; median 35.2 nm; n = 147 AZ profiles, n = 251 vesicles, N = 3 mice; p = 0.0029; Fig. 3-10A left panel) and slice cultures (Fig. 3-10A,B, E, F; (mean ± SD) 46.9 ± 22.5 nm; median 45.3 nm; n = 160 AZ profiles, n = 60 vesicles, N = 3 mice; p = 0.0124; Fig. 3-10A right panel). Albeit being still larger than control, the magnitude of the change was smaller than after a single pulse and was significant only in acute slices (p = 0.0014), and an indication that larger diameter vesicles also got released. Furthermore, in accordance with the previous "flash and freeze" studies that uncovered ultrafast endocytosis (Watanabe et al., 2013a; Watanabe et al., 2013b), the number of putative endocytic pits in the peri-active zone area, within 150 nm from the AZ edge, was significantly increased after the short 5-pulse train, compared to all other groups (Fig. 3-11; acute slices non-LS control *vs* 1 pulse p > 0.9999; non-LS control *vs* 5 pulses p < 0.0001; non-LS control *vs* 100 pulses p > 0.9999 and slice cultures non-LS control *vs* 1 pulse p > 0.9999; non-LS control *vs* 5 pulses p < 0.0001; non-LS control *vs* 100 pulses p > 0.9999). Moreover, other studies, involving capacitance measurements from hippocampal MF terminals, show fast endocytosis with a time constant of 470 ms at near-physiological temperature (Hallermann et al., 2003; Delvendahl et al., 2016), which is consistent with the Watanabe et al., (2013b) time frame of 100–300 ms, when ultrafast endocytic pits could be observed attached to the plasma membrane. The short stimulus train of 5 pulses at 20 Hz, used in the present experiments, lasted 250 ms from the first pulse. Thus, such putative endocytic structures may have originated as a consequence of the first few ~~3–4~~ pulses on the train. In addition, the diameter of these putative endocytic structures was, on average, 63.6 ± 3.5 nm, approximately twice the size of a synaptic vesicle, and was not significantly different among groups (Fig. 3-11).

After a long train of 100 light pulses at 20 Hz, the number of docked vesicles decreased substantially from non-LS control conditions in both preparations (Fig. 3-9; acute slices (mean ± SD) 0.33 ± 0.39; median 0.25; n = 234 AZ profiles, N = 3 mice; p < 0.0001; Fig. 3-9A left panel; slice culture (mean ± SD) 0.11 ± 0.24; median 0.00; n = 155 AZ profiles, N = 3 mice; p < 0.0001; Fig. 3-9A right panel). This observation could indicate the potential overlap of the functionally defined RRP and the docked vesicle pool, previously hypothesized in Schikorski and Stevens, 2001. However, even though a large fraction of docked vesicles was absent from the AZs, 28.5 % of the control value were present. This can be explained because either not all docked vesicles are part of the RRP or the docked vesicle pool undergoes rapid refilling during the 5-s stimulus train, or due to both. In addition, unlike other light stimulated groups, the diameter of docked vesicles was not significantly different, albeit slightly larger than in control conditions (acute slices: Fig. 3-10A-D; (mean ± SD) 38.9 ± 12.1 nm; median 35.4 nm; n = 234 active zone profiles, n = 128 vesicles, N = 3 mice; p > 0.9999; Fig. 3-10A left panel; slice cultures: Fig. 3-10A, B, E,F; 44.1 ± 15.7 nm; median 45.1 nm; n = 155 active zone profiles, n = 27 vesicles, N = 3 mice; p > 0.9999; Fig. 3-10A right panel), an indication that both small and larger vesicles were released.

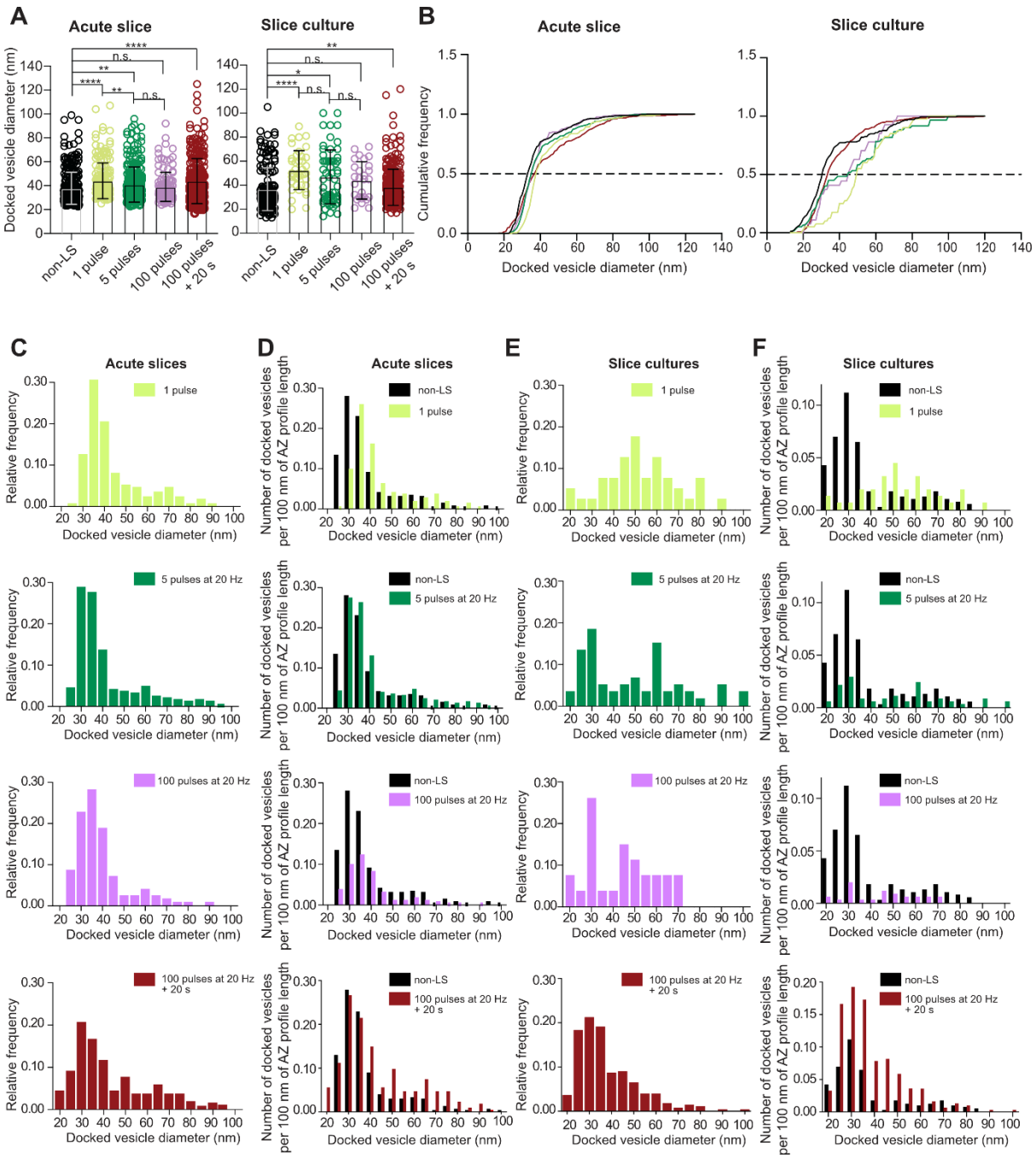

Figure 3-10. The mean diameter of docked vesicles changes in an activity-dependent manner in both acute slices and slice cultures. (A), Scatter plot of the diameter of docked vesicles measured in acute slices (left) and slice cultures (right), for each stimulation paradigm. Bars and whiskers show mean ± SD. Dotted line indicates mean of non-LS control. **(B),** Cumulative plots of the data displayed in A. **(C),** Histograms showing the relative frequency distribution of docked vesicle diameter for stimulated groups in acute slices. **(D),** Comparison of docked vesicle diameter between non-LS control and stimulated groups in acute slices. **(E),** Histograms showing the relative frequency distributions of docked vesicle diameter for stimulated groups in slice cultures. **(F),** Comparison of docked vesicle diameter between non-LS control and stimulated groups in slice cultures (modified from Borges-Merjane et al., 2020).

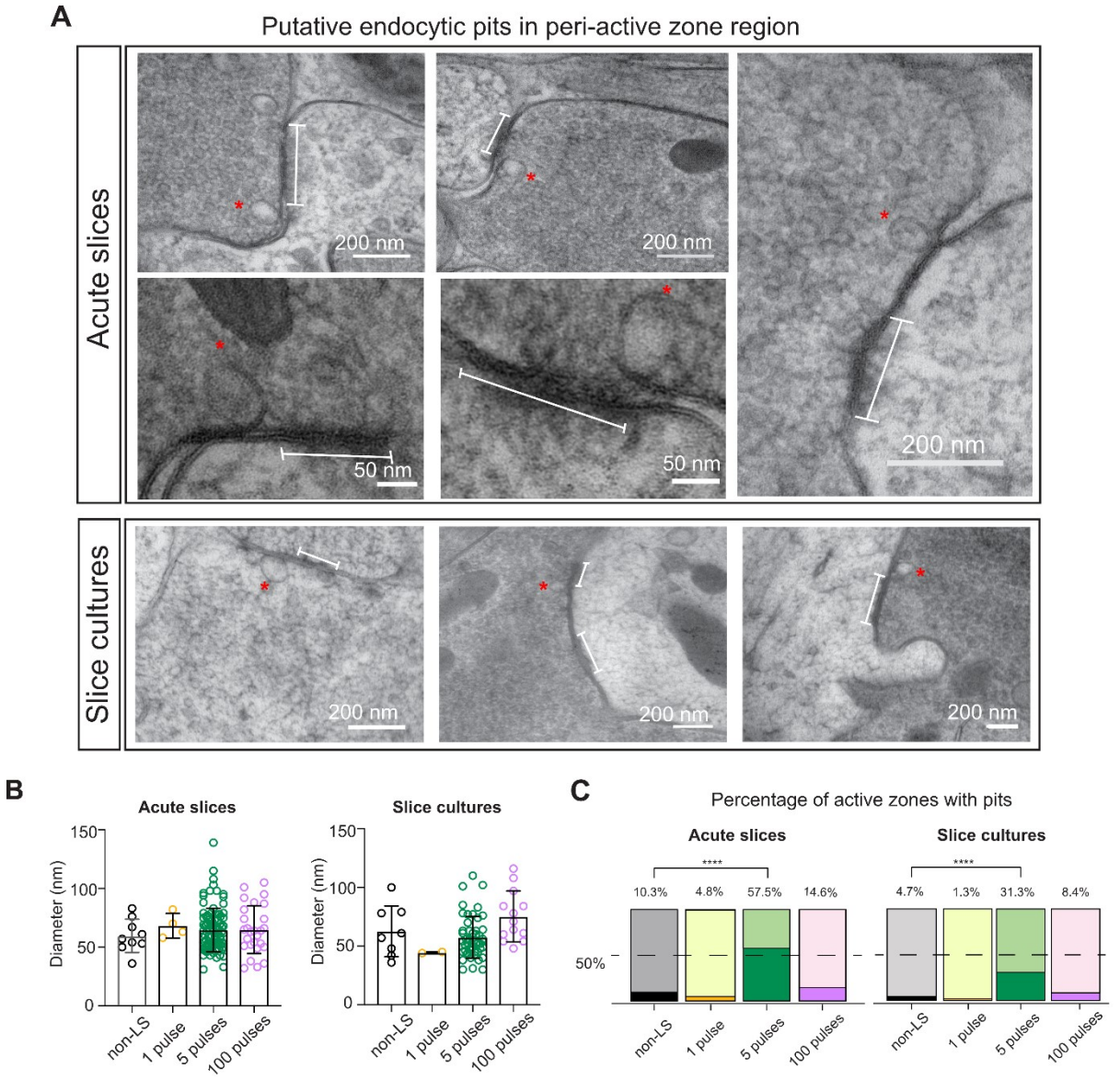

Figure 3-11. Presence of putative endocytic pits in peri-active zone regions. (A), Example EM micrographs depicting putative endocytic pits (red asterisks) in acute slices (top) and slice cultures (bottom). Scale bar sizes are indicated on the figure. **(B),** Scatter plot displaying the measured diameter of pits in each condition, in both acute slices and slice cultures. Bars show mean and standard deviation. Group statistic comparisons were not significant. **(C),** Stacked bars displaying the percentage of active zones with pits in peri-active zone regions, per group, in both acute slices (total active zones counted: non-LS n = 116 AZs, 1 pulse n = 84 AZs, 5 pulses n = 146 AZs, 100 pulses n = 219 AZs) and slice cultures (total active zones counted: non-LS n = 170 AZs, 1 pulse n = 78 AZs, 5 pulses n = 160 AZs, 100 pulses n = 155 AZs). Bars and whiskers denote mean ± SD; only significant statistic representations are shown in graphs (Borges-Merjane et al., 2020).

Finally, the samples, that underwent stimulation with the long train and were frozen after a 20 s delay, showed intriguing results. The number of docked vesicles was increased in comparison with non-LS tissue in acute slices (Fig. 3-9A-C; (mean ± SD) 1.45 ± 0.61; median 1.39; n = 193 AZ profiles, N = 3 mice; $p < 0.01$, Fig. 3-9A left panel) and slice cultures (Fig. 3-9A-C; (mean ± SD) 0.94 ± 0.52; median 0.89; n = 137 AZ profiles, N = 3 mice; $p < 0.05$, Fig. 3-9A right panel). Moreover, while the median remained unchanged, the mean diameter of docked vesicles also increased after the 20 s recovery period. This is an indication that while small vesicles still represented the largest fraction of docked vesicles, more SVs of larger diameter became docked to AZs as compared to control conditions (acute slices: Fig. 3-10A-D; (mean ± SD)

43.8 ± 18.9 nm; median 37.0 nm; n = 193 AZ profiles, n = 278 vesicles, N = 3 mice; $p < 0.0001$; Figure 3-10A left panel; slice cultures: Fig. 3-10A, B, E,F; 38.3 ± 15.1 nm; median 34.0 nm; n = 137 AZ profiles, n = 282 vesicles, N = 3 mice; $p < 0.01$; Fig. 3-10A right panel). This enlargement of the number of SVs in the docked vesicle pool and of their mean diameter agrees with electrophysiological pair recording from MFB-CA3 PN synapses, which showed not only an increase in the RRP size, but also in the mEPSC amplitude after induction of short-term potentiation (Vandael et al., 2020). Thus, this data not only suggests again a connection between the RRP and the docked vesicle pool, but also uncovers important structural changes during STP at MFBs. Altogether, this complete data set is also the first direct parallel comparison of the structure and function of MFB synapses in acute slices and slice cultures.

CHAPTER 4. NANOTOPOGRAPHY OF THE HIPPOCAMPAL MFB-CA3 PN SYNAPSES

Despite a large body of work on the morphological and physiological properties of synapses, the links between structure and function remain enigmatic. Although recent studies elucidated a potential correlation between physiological and morphological properties of synapses under basal conditions and during synaptic plasticity (see Chapter 3. Functional electron microscopy ("flash and freeze") of hippocampal mossy fiber synapses; Vandael et al., 2020), the corresponding molecular changes remain unknown. Moreover, synaptic transmission inherently relies on a sophisticated system of protein machinery and calcium channels (see section 1.3. Synaptic transmission; Südhof, 2013b) which amplifies the challenge in studying synaptic communication at the molecular level. Interactions between these molecular players can be potentially be modified during synaptic plasticity. Thus, to pinpoint changes in the molecular architecture at MFB synapses during plasticity, we combined chemical potentiation, by the AC activator forskolin, and FRIL of VGCCs and synaptic proteins in mouse hippocampus. This method allowed us to localize membrane-bound proteins with nanometer precision within the AZ, particularly $Ca_v2.1$, $Ca_v2.2$, $Ca_v2.3$ calcium channels and Munc13-1/2s, putative markers of primed vesicles. The following chapter focuses on the detailed description of VGCCs and AZ proteins distribution in chemically fixed and fresh MFBs under basal conditions and during STP and LTP.

4.1 Nanodistribution of voltage gated calcium channels and Munc13 proteins in chemically fixed AZs of MFBs

4.1.1 Three types of voltage gated calcium channels (VGCCs) in MFB AZs

Synaptic transmission is a calcium-dependent process that relies on VGCCs, as a Ca^{2+} ions source (see section 1.3. Synaptic transmission). Previous electrophysiological work elucidated the role of various types of VGCC found in hippocampal MFB (Li et al., 2007), in particular P/Q- ($Ca_v2.1$), N- ($Ca_v2.2$) and R-type ($Ca_v2.3$). However, information on the precise location with nanometer resolution of VGCCs in AZs of MFBs is still lacking. Thus, first, freeze-fracture replica immunolabelling (FRIL) was performed to investigate several aspects of these calcium channels (Figures 4-1, 4-2). Immunolabeling in FRIL uses gold-conjugated secondary antibodies to identify the location of specific proteins. In this case, not only location of each channel type at the AZ can be identified, but, in addition, analysis of the distance between particles indicates clustering patterns and the amount of labeling, that is the number of gold particles, will reflect expression level. The number of corresponding gold particles was normalized to 0.1 μm^2 of AZ area and the specificity of the antibodies was determined in conditional and full knock-out (KO) animal models (see Chapter 2. Materials and Methods; Figure 4-2).

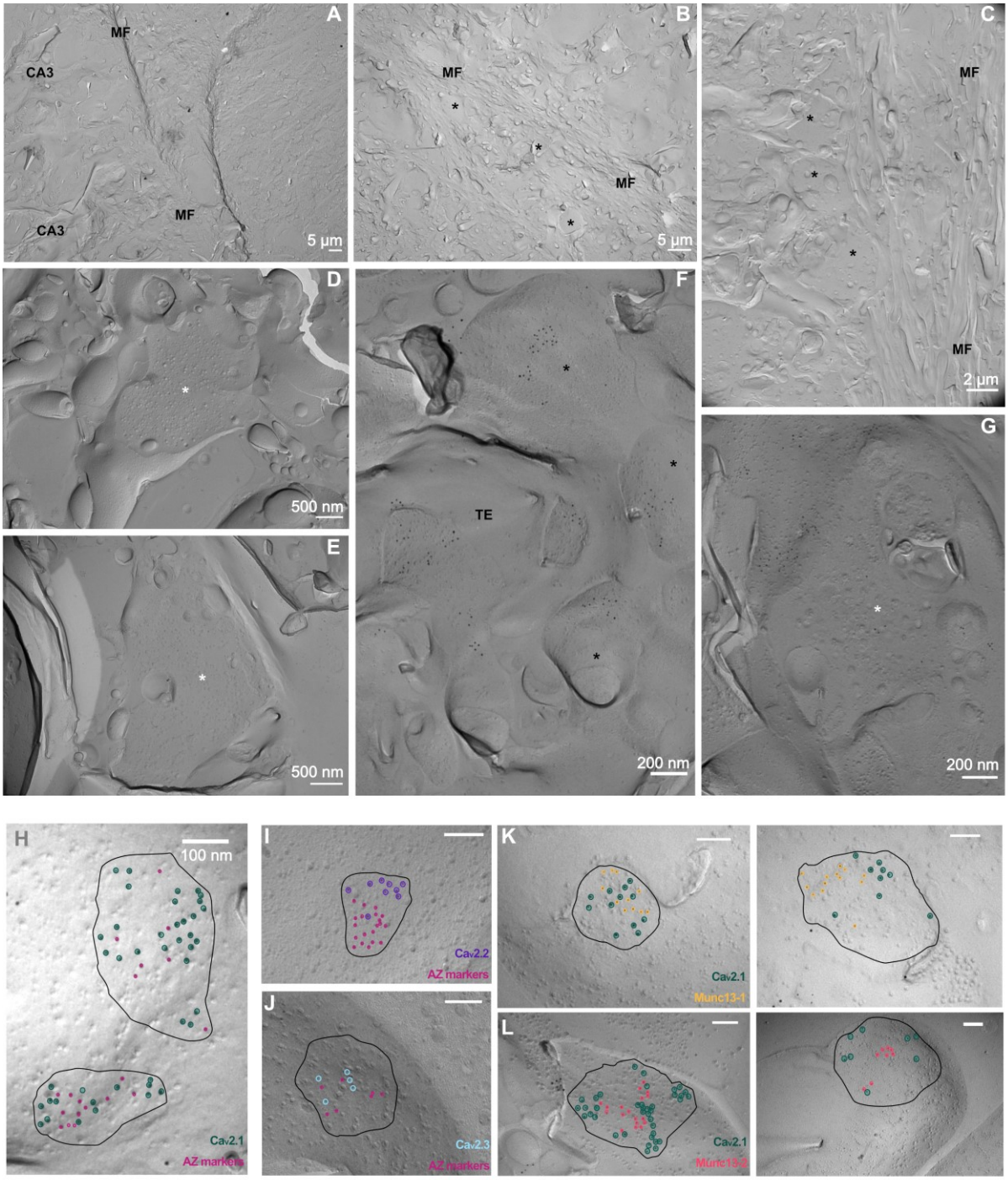

Figure 4-1. Freeze-fracture replicas of chemically fixed and HPF hippocampal slices. **(A–C),** Example TEM micrographs, showing ultrastructural quality of stratum lucidum of the CA3 region, with mossy fiber axons (MF), putative mossy fiber boutons (black asterisks). **(D–F),** Putative mossy fiber boutons in higher magnification, with cross fracture of the terminal with visible synaptic vesicles (white asterisks) and putative post-synaptic thorny excrescences (TE). **(H–J),** Mossy fiber AZ (black line) labeled against AZ markers (RIM 1/2, ELKS and neurexin) and $Ca_V2.1$ (H), $Ca_V2.2$ (I) and $Ca_V2.3$ (J). **(K–L),** Mossy fiber AZ labelled against $Ca_V2.1$ and Munc13-1 (K) and Munc13-2 (L). (A–H) scale bar sizes are indicated on the figure, (I–L) scale bar sizes are same as in (H).

The labelling was significantly decreased in KO control samples compered to WT terminals (Figures 4-2A–C; $Ca_v2.1$ WT: number of particles per 0.1 μm^2 of AZ area 27.9 ± 13.0 (mean ± SD), median 26.5, n = 35 AZ, N = 3 mice; $Ca_v2.1$ cKO: 0.8 ± 1.7, median 0, n = 74 AZ , N = 3 mice, p<0.00001; $Ca_v2.2$ WT: 8.9 ± 5.8, median 8.3, n = 43 AZ , N = 3 mice; $Ca_v2.2$ KO*:* 0.6 ± 1.3, median 0, n = 70 AZ , N = 3 mice, p<0.00001; $Ca_v2.3$ WT: 5.7 ± 5.0, median 4.3, n = 101 AZ, N = 3 mice; $Ca_v2.3$ KO: 0.6 ± 1.3, median 0, n = 60 AZ, N = 3 mice, p < 0.00001). All three types of calcium channels were found in AZs of putative MFBs (Figures 4-1I-J, 4-2A-Cii). In addition, the synaptic location was confirmed with co-labeling with a mixture of antibodies against AZ proteins: RIM 1/2, neurexin, and ELKS. Putative $Ca_v2.1$ channels had the highest labeling density, followed by $Ca_v2.2$ and $Ca_v2.3$ (Fig. 4-2). Therefore, $Ca_v2.1$ is the dominant VGCC type present in MFB terminals, as previously demonstrated with electrophysiology experiments (Li et al., 2007). Moreover, the estimated numbers of VGCCs by FRIL and functional electrophysiological measurements in a whole MFB were comparable between each other and showed a similar trend in their distribution (Table 3).

Table 3. Comparison of estimated numbers of VGCC in mossy fiber bouton synapses.

Calcium channel type	Electrophysiological estimation (Li et al., 2007)	FRIL estimation, mean per 0.1 μm^2 x 29 (mean number of AZs in MFB; Rollenhagen et al., 2007)
$Ca_v2.1$ (P/Q-type)	1300	809
$Ca_v2.2$ (N-type)	500	258
$Ca_v2.3$ (R-type)	160	165

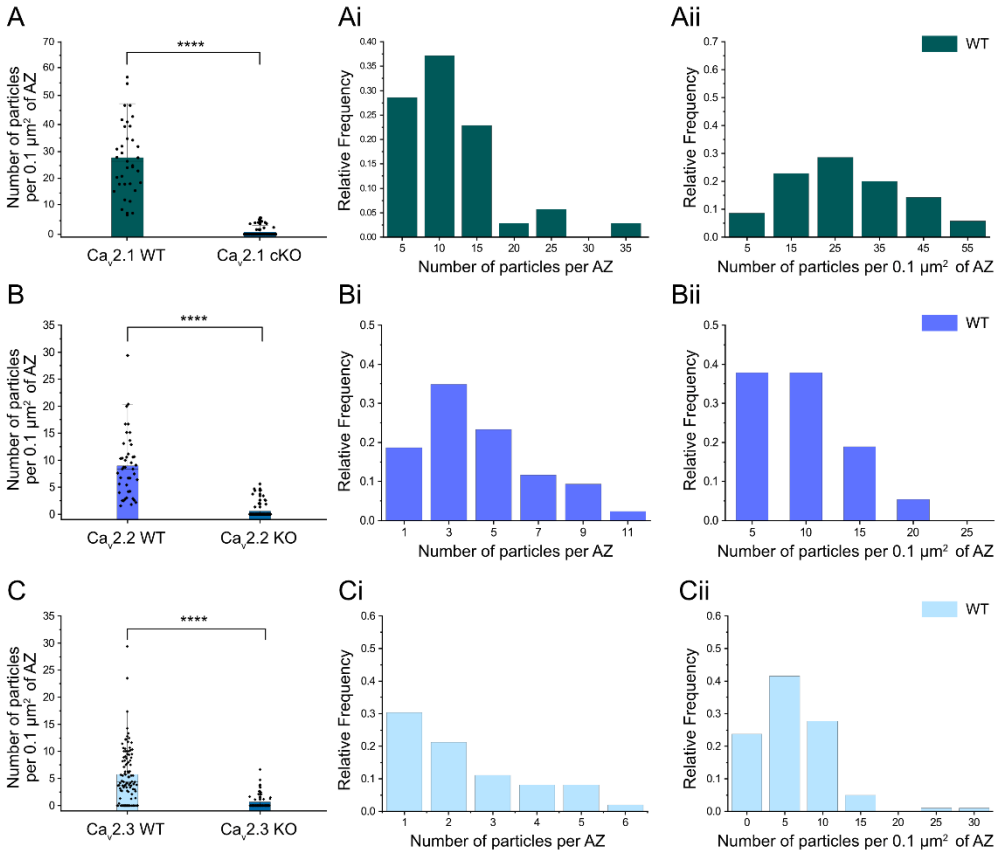

Figure 4-2. Labeling of VGCCs in wild type and transgenic MFBs. (A, B, C), Scatter plot of the number of particles per 0.1 µm^2 of AZ area, in wild type (WT) and conditional knock out (cKO) or full knock out (KO) for Ca$_V$2.1 (A), Ca$_V$2.2 (B) and Ca$_V$2.3 (C) animals. Bars and whiskers show mean + SD. Black line indicates median. **(Ai, Bi, Ci),** Histogram of relative frequency distribution of number of particles per whole AZ in wild type mice for Ca$_V$2.1 (Ai), Ca$_V$2.2 (Bi) and Ca$_V$2.3 (Ci). **(Aii, Bii, Cii),** Histograms of relative frequency distribution of wild type data shown in (A, B, C) accordingly.

Next, the spatial distribution of calcium channel particles within AZs was examined. Nearest neighbor distance (NND) analysis showed that Ca$_V$2.1, Ca$_V$2.2 and Ca$_V$2.3 channels exhibited spatial preference and are positioned closer to each other, compared with randomly simulated point patterns. Thus, they appeared to cluster at the AZ (Fig. 4-3A–B, NND-Ca$_V$2.1: mean 30.1 ± 10.4 (mean ± SD), median 27.9, n = 166 AZ, N = 6 mice; NND-Ca$_V$2.1-Null: 54.9 ± 26.6 (mean ± SD), median 49.2, n = 166 simulations, NND-Ca$_V$2.1 vs. NND-Ca$_V$2.1-Null $p < 0.0001$; Fig. 4-4A-B, NND-Ca$_V$2.2: mean 36.9 ± 22.6 (mean ± SD), median 32.9, n = 33 AZ, N = 3 mice; NND-Ca$_V$2.2-Null: 112.6 ± 67.7 (mean ± SD), median 90.4, n = 33 simulations, NND-Ca$_V$2.2 vs. NND-Ca$_V$2.2-Null $p < 0.0001$; Fig. 4-5A-B, NND-Cav2.3: mean 47.7 ± 24.4 (mean ± SD), median 42.1, n = 45 AZ, N = 3 mice; NND-Ca$_V$2.3-Null: 91.7 ± 46.8 (mean ± SD), median 86.1, n = 45 simulations, NND-Ca$_V$2.3 vs. NND-Ca$_V$2.3-Null $p < 0.0001$). Moreover, NND analysis showed that the distribution of remaining particles in the active zones of KO animals were not significantly different from randomly distributed samples (NND-Ca$_V$2.1cKO vs. NND-Ca$_V$2.1cKO-Null $p = 0.58$; NND-Ca$_V$2.2KO vs. NND-Ca$_V$2.2KO-Null $p = 0.24$; NND-Ca$_V$2.3KO vs. NND-Ca$_V$2.3KO-Null $p = 0.40$). Ca$_V$2.1 data set was pooled from several experiments and included double labeling samples with Munc13-1 (see section 4.1.3. Spatial interactions between Ca$_V$2.1 channels and Munc13s.)

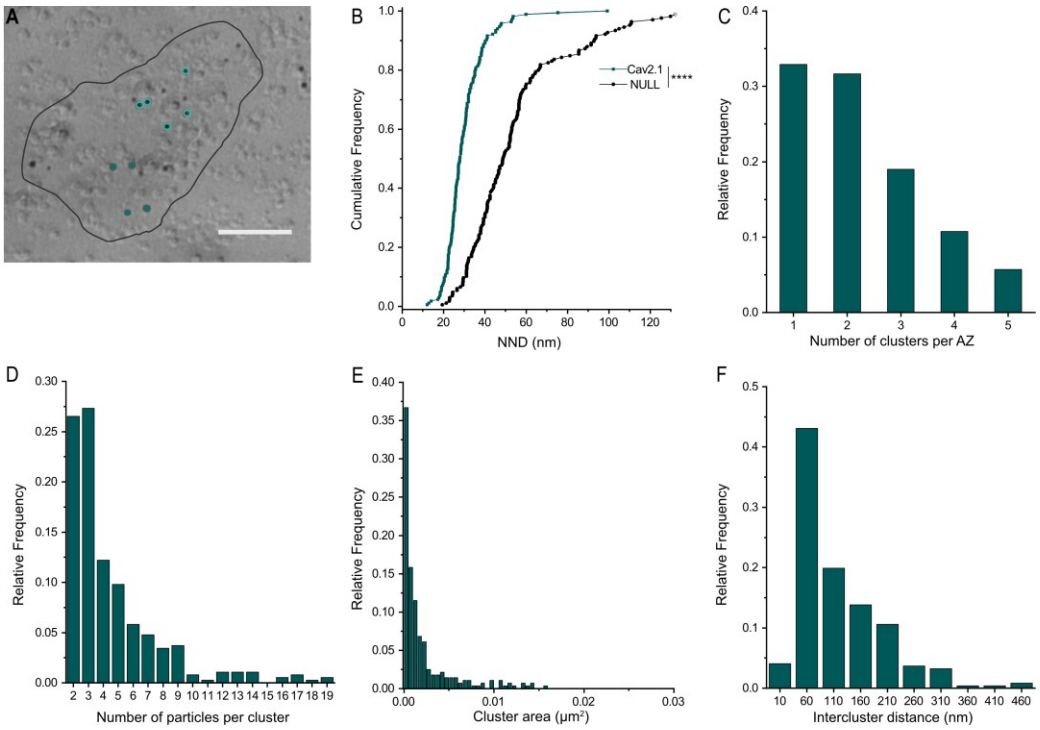

Figure 4-3. $Ca_V2.1$ channels form clusters within MFB AZs. (A), Mossy fiber AZ (black line) with two putative $Ca_V2.1$ clusters (filled and empty green circles) with Munc13-1s (smaller black dots). Scale bar size 100 nm. **(B),** Cumulative plots of mean NND between experimental $Ca_V2.1$ point patterns (green) and randomly simulated data (black). **(C),** Histogram of relative frequency distribution of number of clusters per AZ. **(D),** Histogram of relative frequency distribution of number of particles per cluster. **(E),** Histogram of relative frequency distribution of area of each cluster. **(F),** Histogram of relative frequency distribution of minimal distance between clusters.

Next, density-based spatial clustering of applications with noise (DBSCAN) analysis was performed to determined number of clusters and their characteristics (Ester et al., 1996; Rebola et al., 2019). First, $Ca_V2.1$ channels formed two clusters within AZs (Fig. 4-3C, $Ca_V2.1$ number of clusters per AZ: 2.4 ± 1.4 (mean ± SD), median 2, n = 165 AZ, N = 6 mice). Number of gold particles (as a reflection of number of channels) per cluster, cluster area and intercluster distance varied greatly across synapses (Figure 3D-F; number of particles per cluster: 4.5 ± 3.3 (mean ± SD), median 3, n = 165 AZ, n = 378 clusters, N = 6 mice; cluster area (µm^2) 0.002 ± 0.004 (mean ± SD), median 0.001, n = 165 AZ, n = 278 clusters, N = 6 mice; intercluster distance (nm) 116.7 ± 80.3 (mean ± SD), median 91.9, n = 165 AZ, n = 246 pairs of clusters, N = 6 mice).

$Ca_V2.2$ and $Ca_V2.3$ channels also formed clusters within MFB AZs, yet their number was lower than particle numbers for Cav2.1 (Fig. 4-4A, C; $Ca_V2.2$: number of clusters per AZ 1.40 ± 0.70 (mean ± SD), median 1, n = 33 AZ, N = 3 mice; Fig. 4-5A, C; $Ca_V2.3$: 1.38 ± 0.57, median 1, n = 26 AZ, N = 3 mice). Moreover, number of particles that belong to one cluster was smaller in both $Ca_V2.2$ and $Ca_V2.3$ samples, yet the distance between clusters was longer only in $Ca_V2.3$ samples (Fig 4-4D–F; $Ca_V2.2$: number of particles per cluster: 2.8 ± 0.9 (mean ± SD), median 3, n = 33 AZ, n = 37 clusters, N = 3 mice; cluster area (µm^2) 0.004 ± 0.005 (mean ± SD), median 0.002, n = 33 AZ, n = 25 clusters, N = 3 mice; intercluster distance (nm) 113.8 ± 74.5 (mean ± SD), median 83.0, n = 33 AZ, n = 37 pairs of clusters, N = 3 mice; Fig, 4-5D–F; $Ca_V2.3$: number of particles per cluster: 2.6 ± 0.6 (mean ± SD), median 3, n = 26 AZ, n = 36 clusters, N = 3 mice; cluster area (µm^2) 0.0008 ± 0.007 (mean ± SD), median 0.0005, n = 26 AZ, n = 22 clusters, N = 3 mice; intercluster distance (nm) 156.9

± 128.2 (mean ± SD), median 124.39, n = 26 AZ, n = 11 pairs of clusters, N = 3 mice). This data highlights that the most abundant type of VGCCs in MFB is $Ca_v2.1$.

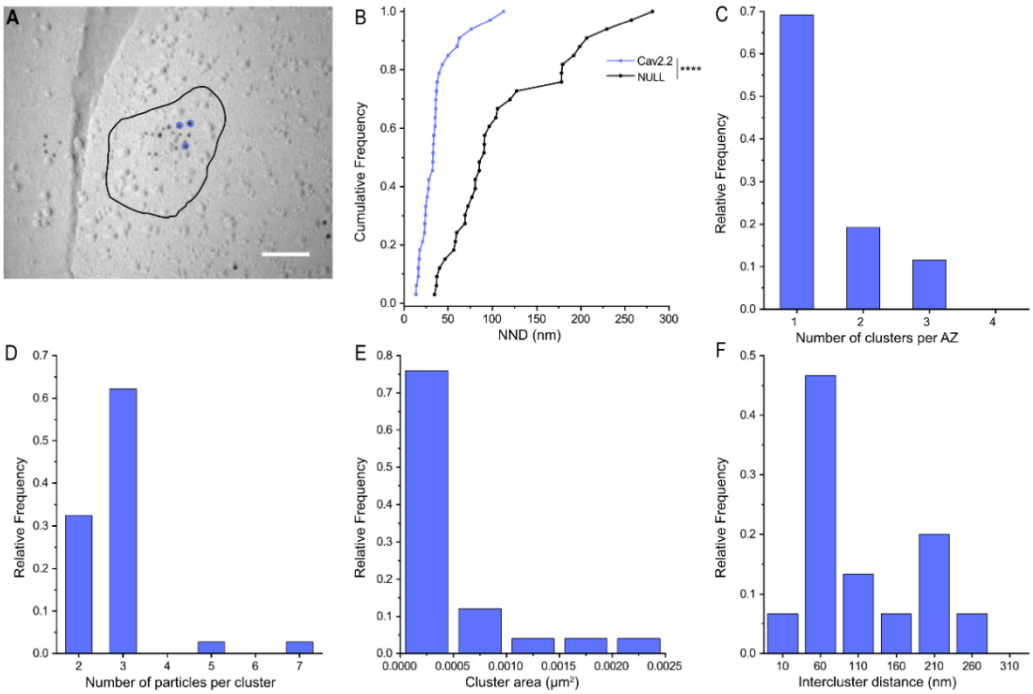

Figure 4-4. $Ca_v2.2$ channels form clusters within MFB AZs. (A), Mossy fiber AZ (black line) with one putative $Ca_v2.2$ cluster (empty blue circles) and AZ markers (smaller black dots). Scale bar size 100 nm. **(B),** Cumulative plots of mean NND between experimental $Ca_v2.2$ point patterns (blue) and randomly simulated data (black). **(C),** Histogram of relative frequency distribution of number of clusters per AZ. **(D),** Histogram of relative frequency distribution of number of particles per cluster. **(E),** Histogram of relative frequency distribution of area of each cluster. **(F),** Histogram of relative frequency distribution of minimal distance between clusters.

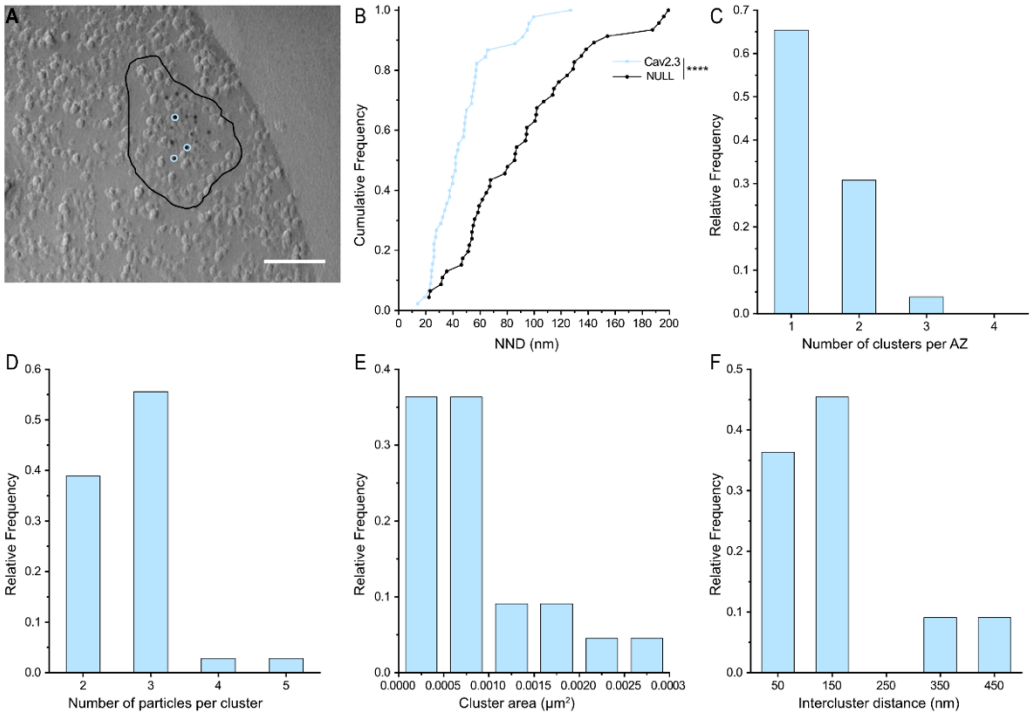

Figure 4-5. $Ca_v2.3$ channels cluster inside MFB AZs. (A), Mossy fiber AZ (black line) with one putative $Ca_v2.3$ cluster (empty light blue circles) and AZ markers (black dots). Scale bar size 100 nm. **(B),** Cumulative plots of mean

NND between experimental $Ca_V2.3$ point patterns (light blue) and randomly simulated data (black). **(C),** Histogram of relative frequency distribution of number of clusters per AZ. **(D),** Histogram of relative frequency distribution of number of particles per cluster. **(E),** Histogram of relative frequency distribution of area of each cluster. **(F),** Histogram of relative frequency distribution of minimal distance between clusters.

4.1.2 Expression of Munc13s in in MFB active zones

The Munc13 protein is a crucial part of the release machinery that regulates fusion of SVs in AZs. The two most prominent isoforms of Munc13 proteins in hippocampal MFBs are Mun13-1 and Munc13-2 (Augustin et al., 1999a). The precise location of Munc13 proteins determines the fidelity of SV release, by priming release sites within an AZ. However, their exact AZ location and level of expression remained unresolved at the most synapses, including MFBs. FRIL enabled the labeling of single Munc13s proteins and confirmed the presence of both isoforms in MFBs synapses (Fig. 4-1K–L, 4-6). Interestingly, the density of the labeling was significantly larger for Munc13-2 particles than Munc13-1 (Fig. 4-6A–Aii; Munc13-1: 13.4 ± 7.7 (mean ± SD), median 12.2, n = 146 AZ, N = 5 mice; Munc13-2: 23.3 ± 11.8 (mean ± SD), median 20.0, n = 78 AZ, N = 3 mice; Munc13-1 vs. Munc13-2: $p < 0.0001$).

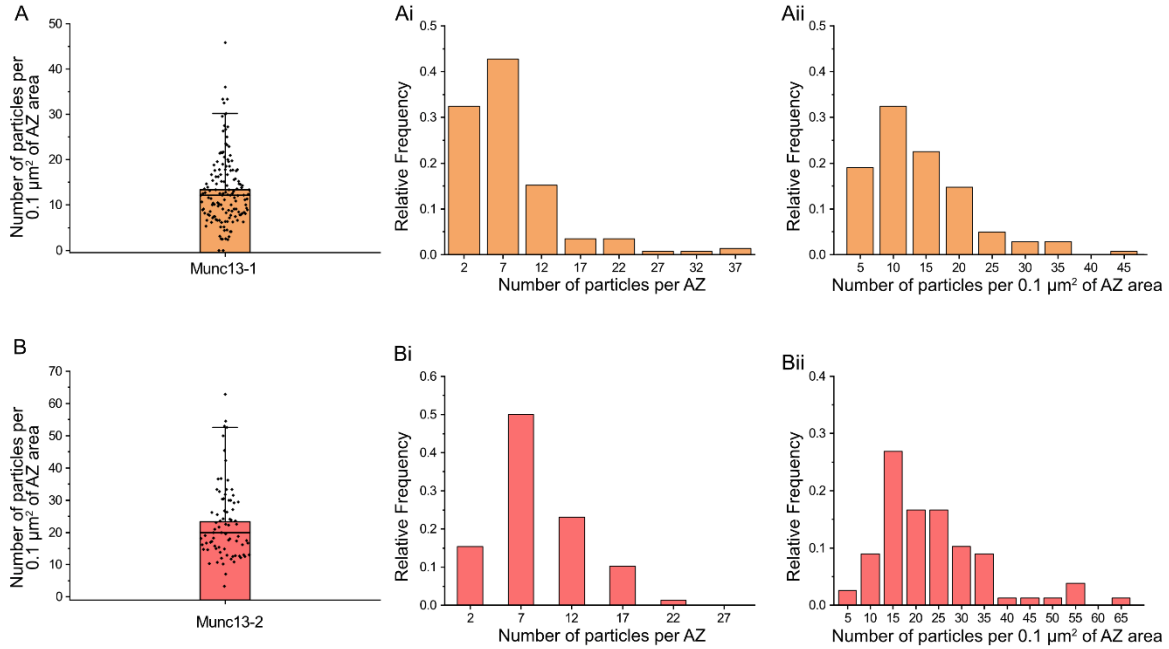

Figure 4-6. Labeling of Munc13 proteins in MFBs. **(A, B),** Scatter plot of the number of Munc13-1 (A) and Munc13-2 (B) particles per 0.1 µm² of AZ area. Bars and whiskers show mean + SD. Black line indicates median. **(Ai, Bi),** Histogram of relative frequency distribution of number of particles per whole AZ in Munc13-1 (Ai) and Munc13-2 (Bi) samples. **(Aii, Bii),** Histograms of relative frequency distribution of data shown in (A, B) accordingly.

Similarly to VGCCs, NND analysis revealed that Munc13s tended to form clusters within AZs (Fig. 4-7A–B; NND-Munc13-1: 41.2 ± 33.6 (mean ± SD), median 31.9, n = 140 AZ, N = 5 mice; NND-Munc13-1-Null: 83.2 ± 44.9 (mean ± SD), median 73.1, n = 140 simulations, NND-Munc13-1 vs. NND-Munc13-1-Null $p < 0.0001$; Fig. 4-8A–B; NND-Munc13-2: 29.5 ± 10.8 (mean ± SD), median 27.3, n = 78 AZ, N = 3 mice; NND-Munc13-2-Null: 61.5 ± 27.6 (mean ± SD), median 50.8, n = 78 simulations, NND-Munc13-2 vs. NND-Munc13-2-Null $p < 0.0001$). In addition, the number of clusters per AZ was comparable between the two protein isoforms with a median of 2 clusters per AZ (Fig. 4-7C; Munc13-1: number of clusters per AZ: 1.8 ± 1.2 (mean ± SD), median

2, n = 108 AZ, N = 5 mice; Fig. 4-8C; Munc13-2: 2.3 ± 1.3 (mean ± SD), median 2, n = 76 AZ, N = 3 mice). Other characteristics of the Munc13 clusters varied greatly in both groups (Fig. 4-7D–F, Munc13-1 number of particles per cluster: 3.5 ± 2.4 (mean ± SD), median 3, n = 108 AZ, n = 194 clusters, N = 3 mice; cluster area (μm^2): 0.001 ± 0.003 (mean ± SD), median 0.0004, n = 108 AZ, n = 128 clusters, N = 5 mice; intercluster distance (nm): 157.6 ± 92.0 (mean ± SD), median 150.2, n = 108 AZ, n = 142 pairs of clusters, N = 5 mice; Fig. 4-8D–F, Munc13-2 number of particles per cluster: 2.6 ± 0.6 (mean ± SD), median 3, n = 76 AZ, n = 151 clusters, N = 3 mice; cluster area (μm^2): 0.001 ± 0.001 (mean ± SD), median 0.0005, n = 76 AZ, n = 96 clusters, N = 3 mice; intercluster distance (nm): 146.0 ± 81.1 (mean ± SD), median 132.2, n = 76 AZ, n = 138 pairs of clusters, N = 3 mice; Table 4).

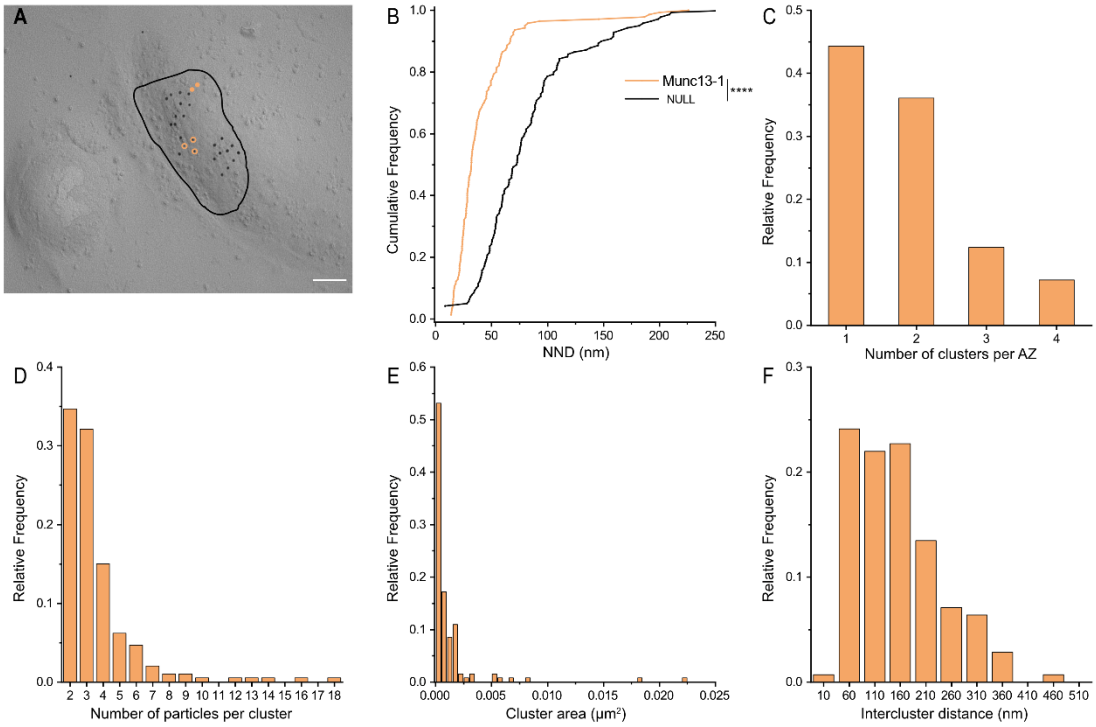

Figure 4-7. Munc13-1s cluster inside MFB AZs. (A), Mossy fiber AZ (black line) with two putative Munc13-1 clusters (filled and empty orange circles) and $Ca_V2.1$ particles (black dots). Scale bar size 100 nm. **(B),** Cumulative plots of mean NND between experimental Mun13-1 point patterns (orange) and randomly simulated data (black). **(C),** Histogram of relative frequency distribution of number of clusters per AZ. (D), Histogram of relative frequency distribution of number of particles per cluster. **(E),** Histogram of relative frequency distribution of area of each cluster. **(F),** Histogram of relative frequency distribution of minimal distance between clusters.

The number of Munc13 clusters can be indicative of the number of docked SVs (Rebola et al., 2019) or the size of the primed vesicle pool (Wang et al., 2016; Tan et al., 2022). The predicted number of docked SVs in MFB synapses is ~ 20 vesicles per AZ (Borges-Merjane at al. 2020). This number is significantly larger than the combined number of Munc13-1 and Munc13-2 clusters per AZ, ~ 4 clusters in total. On the other hand, the direct paired recordings from MFB-CA3 PN synapses estimated the RRP to be ~20 vesicles per a whole bouton (Vandael et al., 2020). However, although this number is significantly smaller than docked vesicles estimates, it correlates with the Munc13 clustering results. Therefore, Munc13 clusters probably indicate the amount of SVs in AZ that are primed for release.

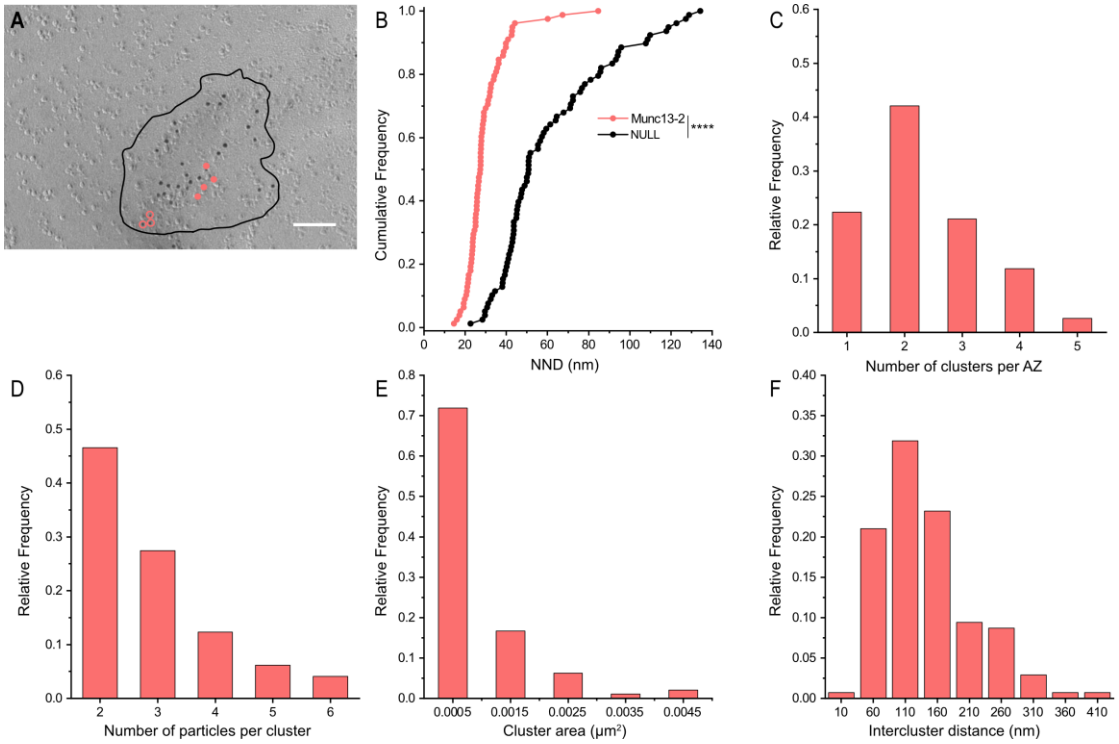

Figure 4-8. Munc13-2 proteins form clusters within MFB AZs. **(A),** Mossy fiber AZ (black line) with two putative Munc13-2 clusters (filled and empty pink circles) and $Ca_V2.1$ particles (black dots). Scale bar size 100 nm. **(B),** Cumulative plots of mean NND between experimental Mun13-1 point patterns (pink) and randomly simulated data (black). **(C),** Histogram of relative frequency distribution of number of clusters per AZ. **(D),** Histogram of relative frequency distribution of number of particles per cluster. **(E),** Histogram of relative frequency distribution of area of each cluster. **(F),** Histogram of relative frequency distribution of minimal distance between clusters.

4.1.3 Spatial relation between $Ca_V2.1$ channels and Munc13s

The hippocampal MF synapses are referred to as “weak” synapses, due to their low initial release probability (Lawrence et al., 2004; Vyleta and Jonas, 2014; Vyleta et al., 2016). This could be partially explained by loose coupling between calcium source (VGCCs) and calcium sensor (synaptotagmin) in MFBs (Vyleta and Jonas, 2014). To investigate structural correlates of this phenomenon, FRIL experiments with co-labeling of Cav2.1 and Munc13-1 or Munc13-2 were performed (Fig. 4-1K, L; 4-9). The calculated mean pairwise distances from both experimental groups were significantly shorter than the distances between randomly simulated patterns (Fig. 4-9A-Aii; Cav2.1/Munc13-1: mean distance: 117.7 ± 41.9 (mean ± SD), median 108.5, n = 84 AZ, N = 3 mice; Cav2.1/Munc13-1-Null: 150.6 ± 54.0 (mean ± SD), median 139.2, n = 84 simulations, $p < 0.0001$; Fig. 4-9B-Bii; Cav2.1/Munc13-2: mean NND: 102.2 ± 32.1 (mean ± SD), median 106.0, n = 55 AZ, N = 3 mice; Cav2.1/Munc13-2-Null: 139.8 ± 32.9 (mean ± SD), median 136.4, n = 55 simulations, $p < 0.0001$). In addition, mean pairwise distance was slightly longer in Munc13-1 in comparison to Munc13-2 samples, yet not statistically significant ($p = 0.1$).

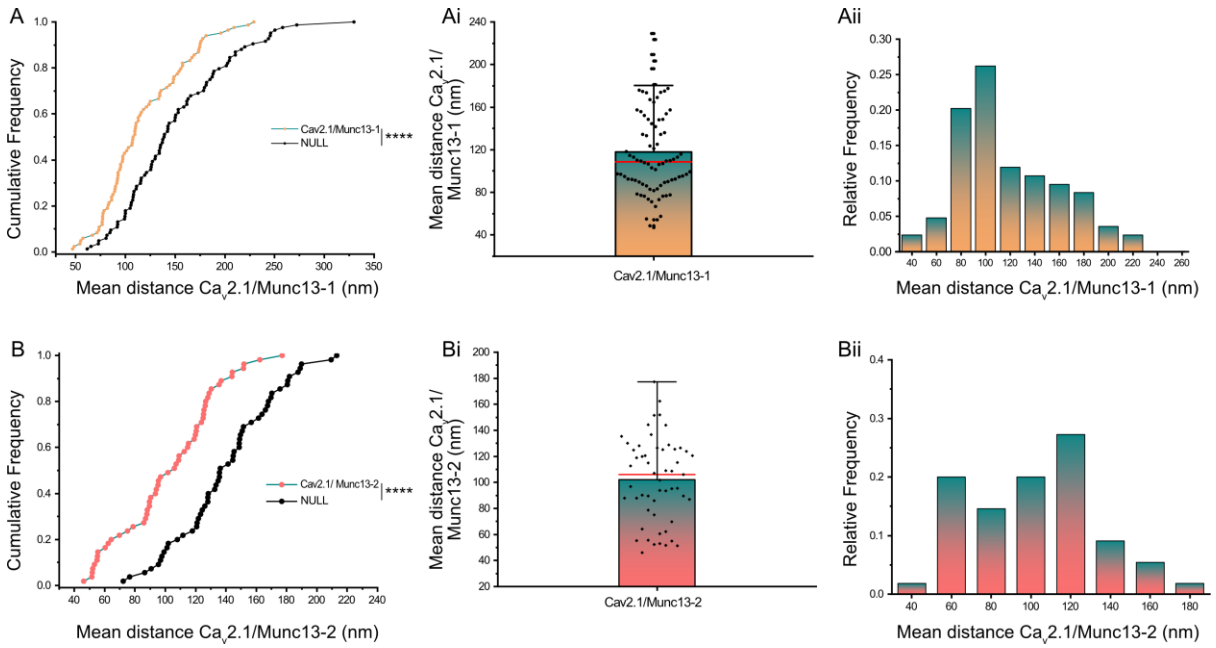

Figure 4-9. Structural coupling distance between Cav2.1 and Munc13-1/2. (A, B), Cumulative plots of mean pairwise distance between experimental Cav2.1/Mun13-1 point patterns (A) and Cav2.1/Mun13-2 (B). Experimental data (colored line), randomly simulated data (black). **(Ai, Bi),** Scatter plot of the mean distance between Cav2.1 and Munc13-1 (Ai) or Munc13-2 (Bi). Bars and whiskers show mean + SD. Red line indicates median. **(Aii, Bii),** Histograms of relative frequency distribution of data shown in (Ai, Bi) accordingly.

However, the measured mean pairwise distance between $Ca_V2.1$ and Munc13-1/2 was larger than the functional estimates of 73-88 nm, distance between VGCCs and calcium sensor (synaptotagmin; Vyleta and Jonas, 2014). The discrepancy between previous functional and current structural measurements can be attributed to the difference in location of synaptotagmins, that are bound to SV membrane, and Munc13s, that are attached to plasma membrane (Südhof, 2012; Südhof, 2013a). Additionally, the length of primary and secondary ABs could contribute to the prolongation of the measured distances.

4.2 Freeze fracture of frozen acute hippocampal slices

4.2.1 FRIL of VGCCs and Munc13s in acute slices

In the previous section, FRIL experiments with chemically fixed brain slices were described. Although, while it remains to be the gold standard in electron microscopy, recent studies showed that chemical paraformaldehyde and glutaraldehyde fixation can alter ultrastructure of brain tissue (Korogod at al., 2015, Maus et al., 2020). Thus, the pioneering method combination of FRIL with high-pressure freezing of fresh brain tissue (Borges-Merjane et al., 2020) was implemented; specifically, freeze-fractured replicas were prepared from acute hippocampal slices (Fig. 4-10; see Chapters 2. Materials and Methods; 3. Functional electron microscopy ("flash and freeze") of hippocampal mossy fiber synapses).

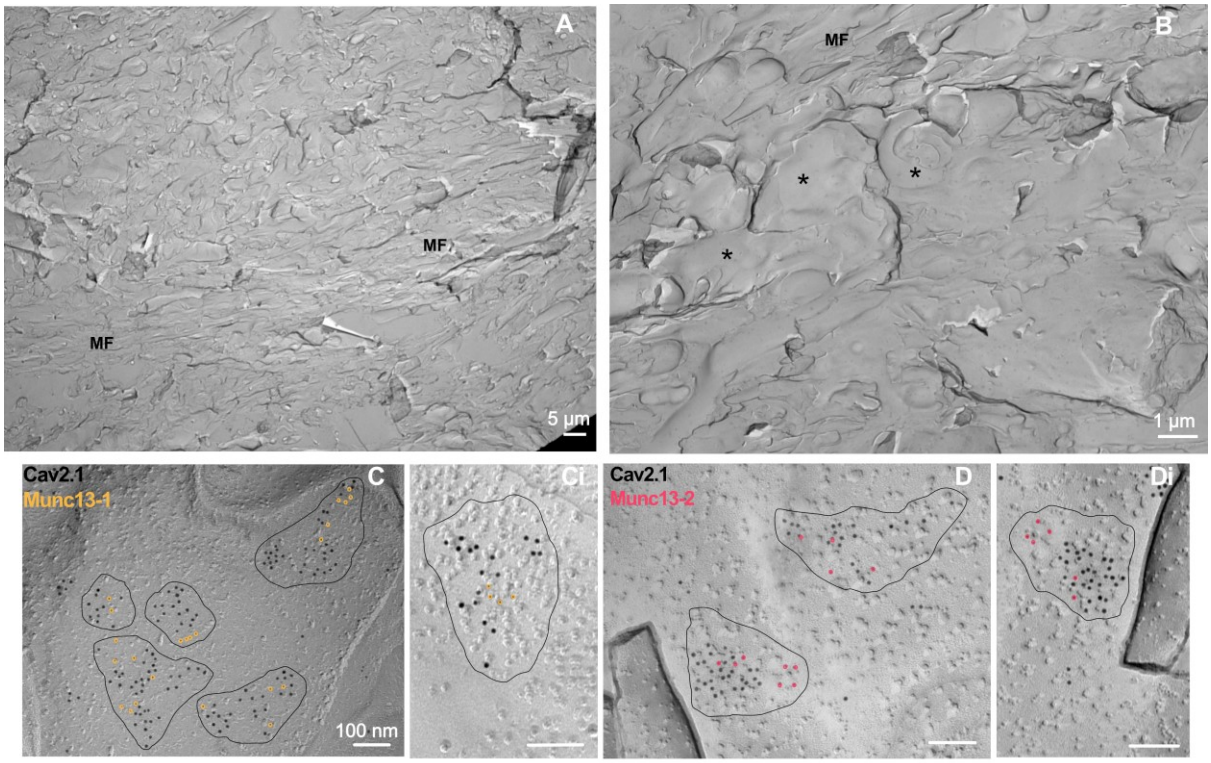

Figure 4-10. Freeze-fracture replicas of fresh acute and HPF hippocampal slices. (A–B), Example TEM micrographs, showing ultrastructural quality of stratum lucidum of the CA3 region, with mossy fiber axons (MF), putative MFBs (black asterisks). **(C–Di),** Mossy fiber AZ (black line) labeled against $Ca_V2.1$ and Munc13-1 (C-Ci) and Munc13-2 (D-Di). (A–Di) scale bar sizes are indicated on the figure (C-Di) scale bar sizes are same as in (C).

Using this approach, to preserve a near-native state, immunolabelling experiments described in the last two sections to determined VGCCs and Munc13 proteins distribution were repeated (Fig. 4-10, 4-11). Main focus was given to the $Ca_V2.1$ channels, as this was found to be the most abundant type in MFBs. Remarkably, the density of the $Ca_V2.1$ labeling was significantly increased from chemically fixed samples (Fig 4-11A-Aii; 35.0 ± 15.6 (mean ± SD), median 34.2, n = 91 AZ, N = 2 mice; fixed vs. acute $p < 0.001$). In addition, Munc13-1 labeling density was also increased in fresh acute slices (Fig. 4-11B-Bii; number of particles per 0.1 μm^2 of AZ area 18.9 ± 9.4 (mean ± SD), median 17.5, n = 40 AZ, N = 2 mice; fixed vs. acute: $p < 0.001$). However, Munc13-2 particles showed decreased labeling density with AZs (Fig. 4-11C-Cii; 15.2 ± 9.3 (mean ± SD), median 13.6, n = 40 AZ, N = 2 mice; fixed vs. acute: $p < 0.0001$). These results clearly indicate that chemical fixation can affect the labeling efficacy of mentioned antibodies.

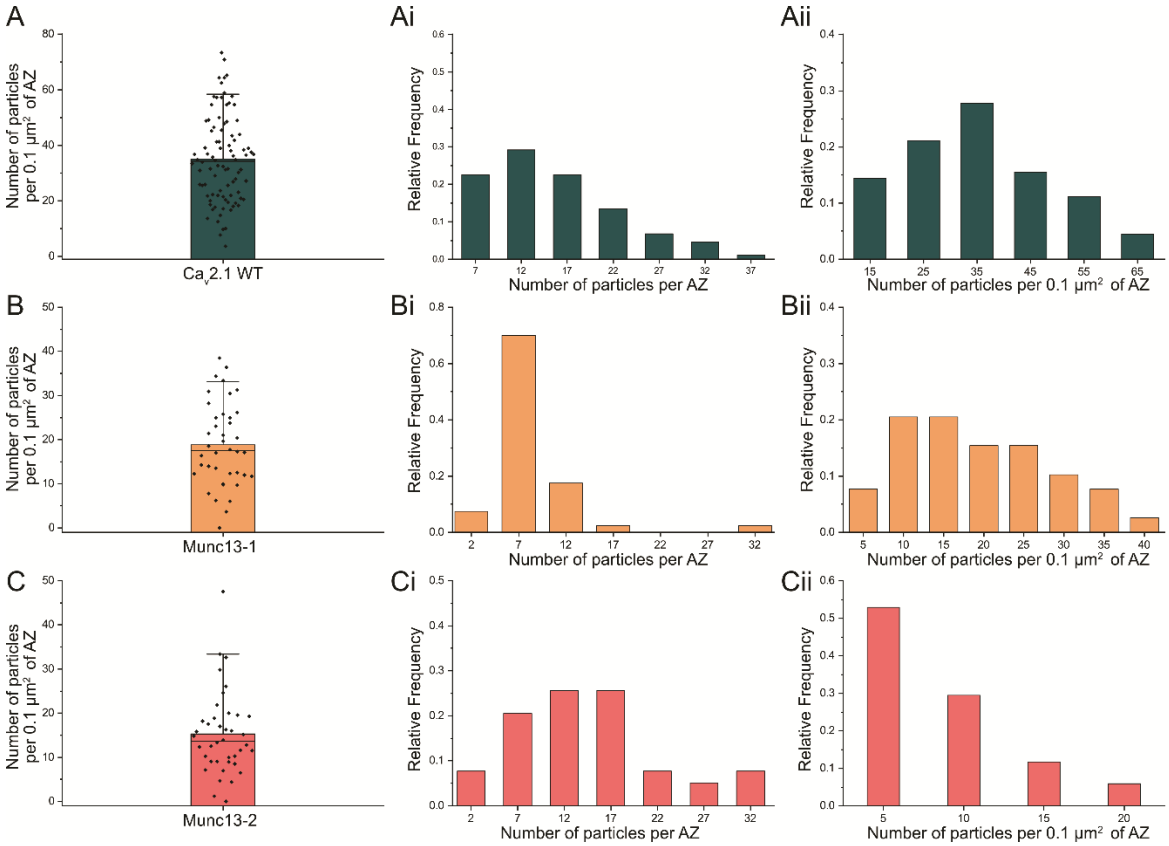

Figure 4-11. Labeling of $Ca_V2.1$ channels. and Munc13 proteins in fresh acute MFBs. (A, B, C), Scatter plot of the number of $Ca_V2.1$ (A), Munc13-1 (B) and Munc13-2 (C) particles per 0.1 µm^2 of AZ area. Bars and whiskers show mean + SD. Black line indicates median. **(Ai, Bi, Ci),** Histogram of the relative frequency distribution of the number of particles per whole AZ in $Ca_V2.1$ (Ai), Munc13-1 (Bi), and Munc13-2 (Ci) samples. **(Aii, Bii, Cii),** Histograms of relative frequency distribution of data shown in (A, B, C) accordingly.

Next, NND analysis again indicated a tendency of $Ca_V2.1$ and Munc13s particles to cluster within AZs, as the cumulative frequency curves of experimental data were significantly different from randomly distributed samples: (Fig. 4-12A,13A, 14A; NND-$Ca_V2.1$: mean 25.7 ± 7.7 (mean ± SD), median 23.3, n = 91 AZ, N = 2 mice; NND-$Ca_V2.1$-Null: 49.3 ± 26.6 (mean ± SD), median 42.9, n = 91 simulations, NND-$Ca_V2.1$ vs. NND-$Ca_V2.1$-Null: $p < 0.0001$; NND-Munc13-1: 28.5 ± 9.0 (mean ± SD), median 26.3, n = 40 AZ, N = 2 mice; NND-Munc13-1-Null: 68.3 ± 32.5 (mean ± SD), median 68.3, n = 40 simulations, NND-Munc13-1 vs. NND-Munc13-1-Null: $p < 0.0001$; NND-Munc13-2: 38.5 ± 17.2 (mean ± SD), median 30.3, n = 40 AZ, N = 2 mice; NND-Munc13-2-Null: 80.25 ± 34.6 (mean ± SD), median 69.2, n = 40 simulations, NND-Munc13-2 vs. NND-Munc13-2-Null: $p < 0.0001$).

Interestingly, the mean number of $Ca_V2.1$ and Munc13-1 clusters in fresh acute slices was higher in comparison to fixed samples (Fig. 4-12B, 13B; Cav2.1: 3.0 ± 1.2 (mean ± SD), median 3, n = 91 AZ, N = 2 mice, fixed vs. acute $p < 0.05$; Munc13-1: 2.3 ± 0.9 (mean ± SD), median 2, n = 39 AZ, N = 2 mice, fixed vs. acute $p < 0.01$). Moreover, although Munc13-2 particles density was decreased in the fresh acute MFBs, the number of Munc13-2 clusters was not significantly changed, albeit slightly lower (Fig, 4-14B; number of clusters per AZ 2.1 ± 1.1 (mean ± SD), median 2, n = 35 AZ, N = 2 mice, fixed vs. acute $p = 0.2182$).

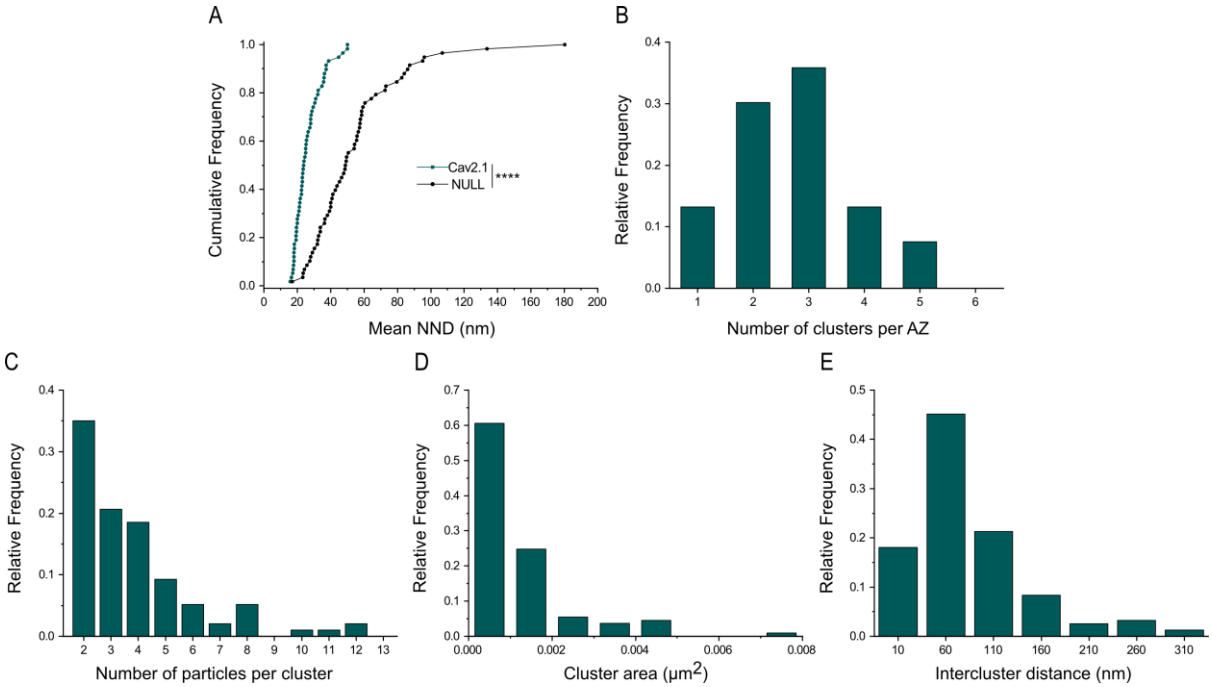

Figure 4-12. Cav2.1 channels form more clusters within fresh acute MFB AZs. (A), Cumulative plots of mean NND between experimental $Ca_V2.1$ point patterns (green) and randomly simulated data (black). **(B),** Histogram of relative frequency distribution of number of clusters per AZ. **(C),** Histogram of relative frequency distribution of number of particles per cluster. **(D),** Histogram of relative frequency distribution of area of each cluster. **(E),** Histogram of relative frequency distribution of minimal distance between clusters

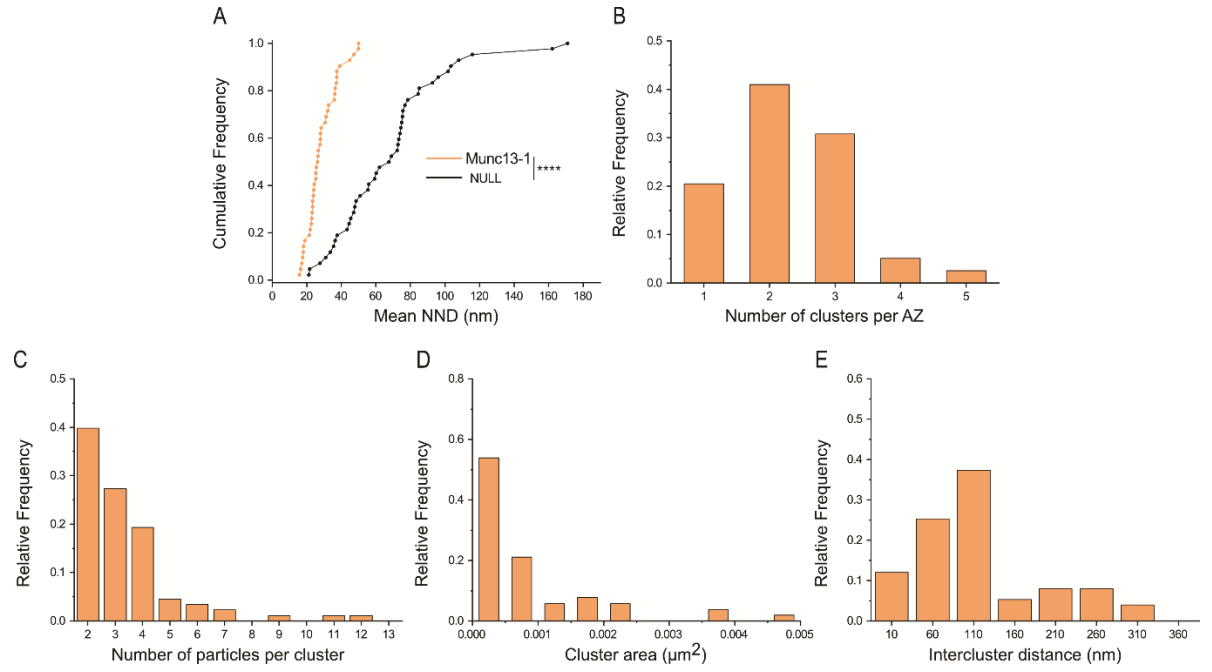

Figure 4-13. Munc13-1 proteins form more clusters within fresh acute MFB AZs. **(A),** Cumulative plots of mean NND between experimental Munc13-1 point patterns (orange) and randomly simulated data (black). **(B),** Histogram of relative frequency distribution of number of clusters per AZ. **(C),** Histogram of relative frequency distribution of number of particles per cluster. **(D),** Histogram of relative frequency distribution of area of each cluster. **(E),** Histogram of relative frequency distribution of minimal distance between clusters.

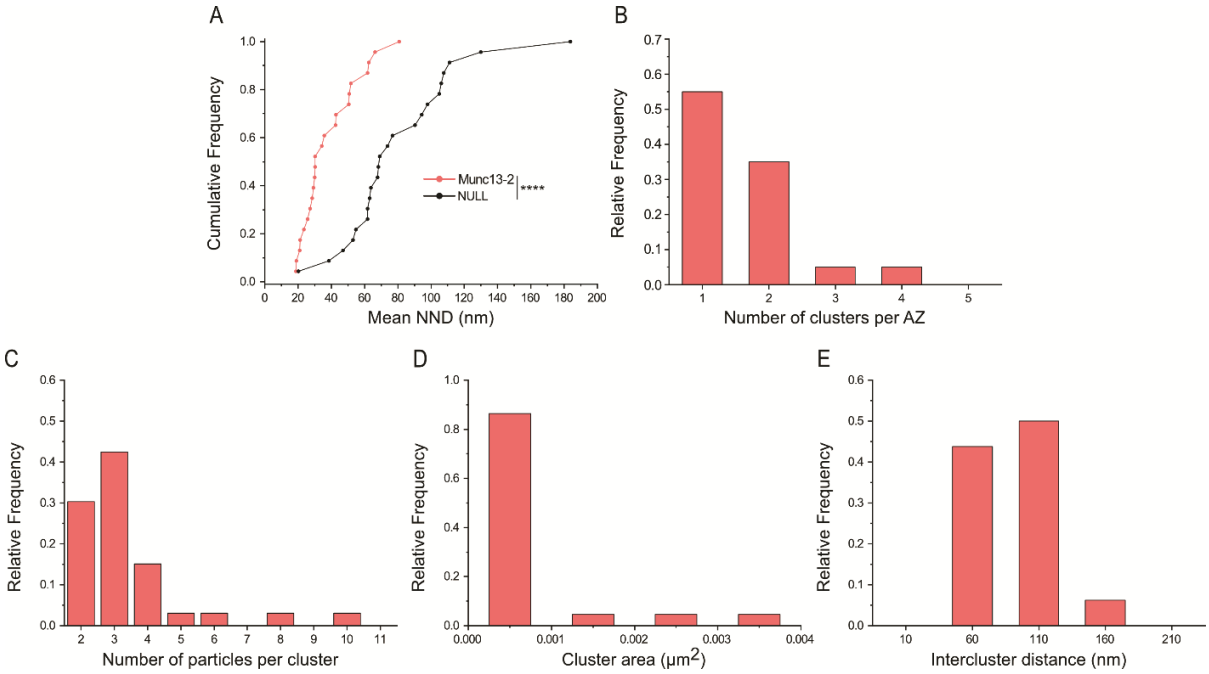

Figure 4-14. The number of Munc13-2 clusters remains the same within fresh acute MFB AZs. (A), Cumulative plots of mean NND between experimental Munc13-2 point patterns (pink) and randomly simulated data (black). **(B),** Histogram of relative frequency distribution of number of clusters per AZ. **(C),** Histogram of relative frequency distribution of number of particles per cluster. **(D),** Histogram of relative frequency distribution of area of each cluster. **(E),** Histogram of relative frequency distribution of minimal distance between clusters.

Other parameters also differed considerably between two chemically fixed and fresh acute sample groups (Fig. 12C–E, 13C–E, 14C–E; Table 4; $Ca_V2.1$: cluster area fixed vs. acute: $p < 0.05$, intercluster distance fixed vs. acute: $p < 0.001$; Munc13-2: intercluster distance fixed vs. acute: $p < 0.05$). All mentioned results indicate that chemical fixation or acute slicing can lead to AZ reorganization and ultrastructural differences between chemically fixed and fresh cryo-fixed samples.

4.2.2 VGCCs and Munc13s interactions in fresh mossy fiber active zones

Single particle analysis for $Ca_V2.1$ channels, Munc13-1, Munc13-2 proteins reveal large discrepancy in replicas from fixed or fresh brain tissue. Thus, it is possible that the interactions between two types of particles, or two types of point patterns, are altered during paraformaldehyde perfusion. Therefore, analysis of NND between $Ca_V2.1$ and Munc13-1 or 2 particles was done (Fig. 4-15). Measured mean pairwise distance for both groups was significantly shorter, compared to random data sets (Fig. 4-15A-Aii; $Ca_V2.1$/Munc13-1: mean distance: 114.5 ± 33.7 (mean ± SD), median 113.8, n = 40 AZ, N = 2 mice; $Ca_V2.1$/Munc13-1-Null: 141.2 ± 36.3 (mean ± SD), median 137.3, n = 40 simulations, $p < 0.01$; Fig. 4-15B-Bii; $Ca_V2.1$/Munc13-2: mean distance: 104.4 ± 41.2 (mean ± SD), median 99.2, n = 40 AZ, N = 2 mice; $Ca_V2.1$/Munc13-2-Null: 142.8 ± 39.9 (mean ± SD), median 135.9, n = 40 simulations, $p < 0.0001$), hence confirming measurements from fixed samples. In addition, the values of mean distances were comparable to those from the fixative treated group, although they were slightly shorter ($Ca_V2.1$/Munc13-1: fixed vs. acute: $p = 0.9273$; $Ca_V2.1$/Munc13-2: fixed vs. acute: $p = 0.8417$).

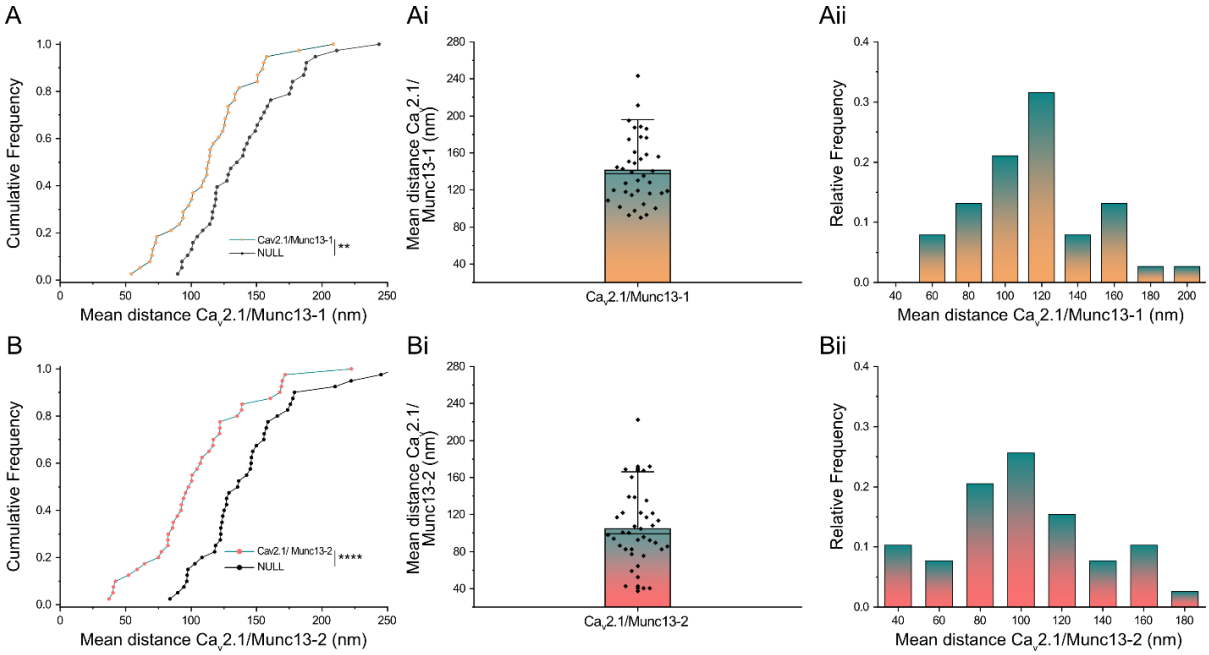

Figure 4-15. Structural coupling distance between $Ca_V2.1$ and Munc13-1/2 in fresh acute MFBs. (A, B), Cumulative plots of mean pairwise distance between experimental $Ca_V2.1$/Mun13-1 point patterns (A) and $Ca_V2.1$/Mun13-2 (B). Experimental data (colored line), randomly simulated data (black). **(Ai, Bi),** Scatter plot of the mean distance between $Ca_V2.1$ and Munc13-1 (Ai) or Munc13-2 (Bi). Bars and whiskers show mean + SD. Black line indicates median. **(Aii, Bii),** Histograms of relative frequency distribution of data shown in (Ai, Bi) accordingly.

In light of these results, either freshly frozen tissue, as well as chemically fixed samples, can be used for FRIL experiments with preserved ultrastructure, despite affected antigenicity as long as the proper controls are performed. Moreover, the labeling specificity of used Munc13-1 antibodies needs to estimated, using KO controls.

Table 3. Properties of Cav2.1, Munc13-1 and Munc13-2 clusters in chemically fixed and fresh acute MFBs.

		Fixed				Fresh				
		N	Mean	SD	Median	N	Mean	SD	Median	**p-value**
$Ca_V2.1$	# clusters per AZ	165	2.4	1.4	2	74	3.0	1.2	3	< 0.05
	# particles per cluster	378	4.5	3.3	3	189	5.2	7.9	4	0.1042
	Cluster area (μm^2)	278	0.002	0.004	0.001	109	0.001	0.001	0.001	< 0.05
	Intercluster distance (nm)	246	116.7	80.3	91.9	279	93.7	64.0	75.1	< 0.001
Munc13-1	# clusters per AZ	108	1.8	1.2	2	39	2.3	0.9	2	< 0.01
	# particles per cluster	194	3.5	2.3	3	88	3.3	1.9	3	0.5329
	Cluster area (μm^2)	128	0.001	0.002	0.0004	52	0.001	0.001	0.0005	0.5329
	Intercluster distance (nm)	142	157.6	92.0	150.2	75	116.5	76.3	95.3	0.9592
Munc13-2	# clusters per AZ	76	2.3	1.3	2	35	2.1	1.1	2	0.2182
	# particles per cluster	151	2.6	0.6	3	74	3.4	1.9	3	0.4005
	Cluster area (μm^2)	96	0.001	0.001	0.0005	44	0.001	0.001	0.001	0.4088
	Intercluster distance (nm)	138	146.0	81.1	132.2	60	101.3	62.6	92.6	< 0.05

4.3 Nanotopographical alterations in mossy fiber bouton synapses after plasticity induction

4.3.1 VGCC and Munc13s distribution in mossy fiber boutons after forskolin application

MFB-CA3 PN synapses exhibit wide range of short- and long-term plasticity (STP, LTP), in particular potentiation (Salin et al., 1996; Nicoll and Schmitz, 2005; see section 1.4.3. Diverse types of plasticity at MFB synapse). However, unlike other hippocampal synapses, plasticity is induced and expressed presynaptically in MFBs (Nicoll and Schmitz, 2005). Two different mechanisms may be involved: an increase in the probability of vesicle release (Pr) or an expansion of the RRP. Forskolin (FSK) is a powerful activator of the cAMP signaling pathway and is routinely used to induce chemical potentiation in hippocampal GCs (Weisskopf et al., 1994; Lopez-Garcia et al., 1996; Alle et al., 2001). Considering these effects, FSK can potentially alter the AZ molecular nanoarchitecture and distribution of VGCCs or other AZ proteins in MFB terminals. Therefore, to check this hypothesis, acute hippocampal slices were treated with 50 µM FSK and frozen at two specific time points (Fig. 4-16L). First, samples were cryo-fixed immediately after a 5-min FSK incubation period (FSK no delay), as this time point corresponds to the peak of STP, in our case chemical STP (cSTP; Fig. 4-16L; Alle et al., 2001). Next, the second group of samples was frozen 25 min after the 5-min FSK application (FSK + 25 min), to capture early chemical LTP (cLTP) in hippocampal MFBs (Fig. 4-16L; Lopez-Garcia et al., 1996). After HPF, samples were fractured under standard conditions (see Chapter 2. Materials and Methods) and replicas were labeled with anti-$Ca_V2.1$, -Munc13-1, and -Munc13-2 antibodies (Fig. 4-16A–K). First, $Ca_V2.1$ labeling density did not change after FSK application compared to DMSO control samples (Fig. 4-17A-Ai; DMSO: number of particles per 0.1 µm^2 of AZ area 36.6 ± 12.3 (mean ± SD), median 35, n = 130 AZ, N = 5 mice; FSK no delay: 38.8 ± 15.3 (mean ± SD), median 23.8, n = 52 AZ, N = 3 mice; FSK + 25 min: 38.1 ± 13.5 (mean ± SD), median 36.9, n = 96 AZ, N = 2 mice; DMSO vs. FSK no delay: p = 0.3598; DMSO vs. FSK + 25 min: p = 0.3597; FSK no delay vs. FSK + 25 min: p = 0.7586).

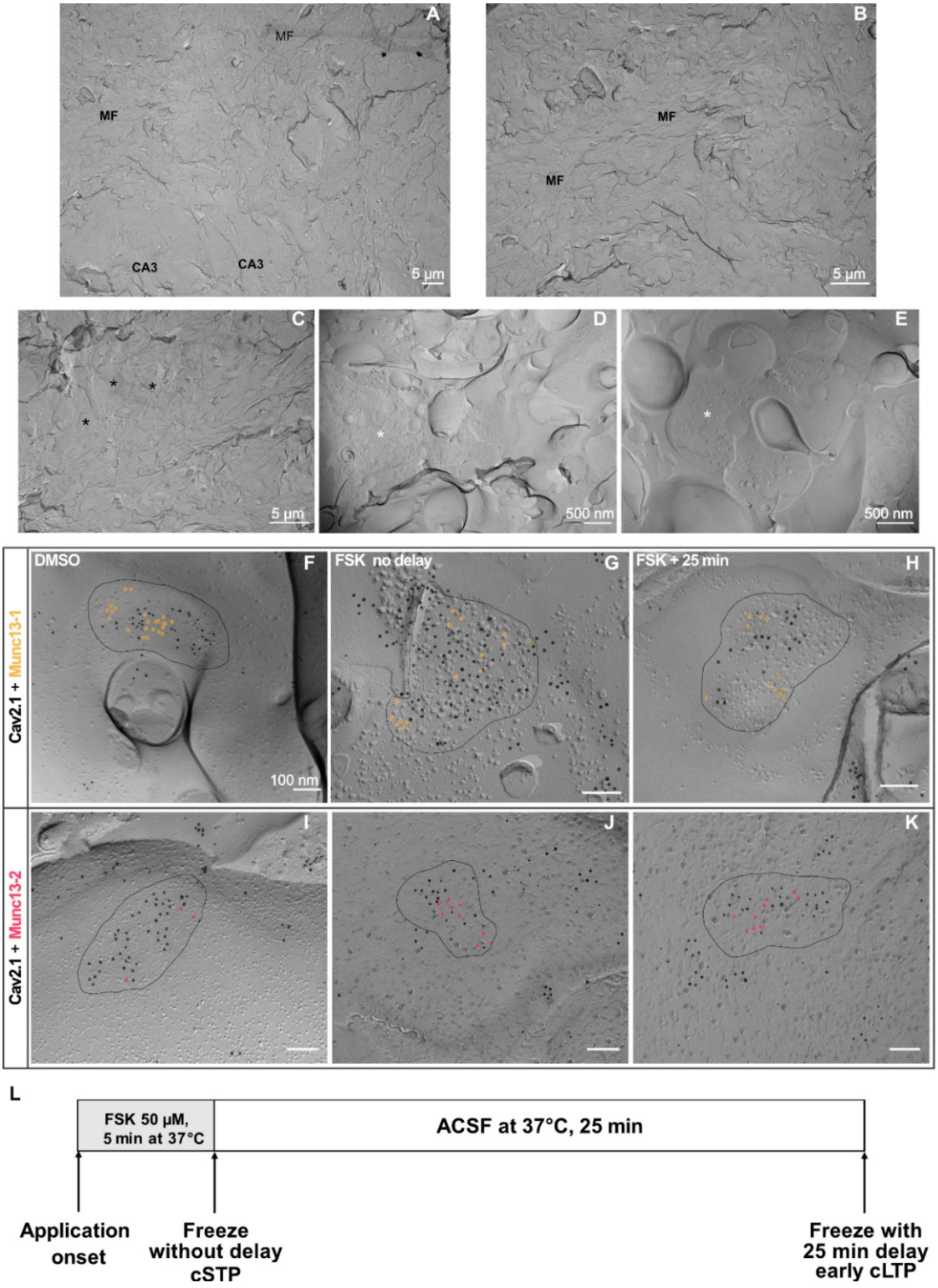

Figure 4-16. Freeze-fracture replicas of acute hippocampal slices after FSK application. (A–C), Example TEM micrographs, showing ultrastructural quality of stratum lucidum of the CA3 region, with mossy fiber axons (MF), putative mossy fiber boutons (black asterisks). **(D–E),** Putative MFBs in higher magnification, with cross fracture of the terminal with visible synaptic vesicles (white asterisks). **(F–H),** Mossy fiber AZs (black line) co-labelled against $Ca_V2.1$ (black) and Munc13-1 (orange circles) in DMSO control (F), FSK no (G) and with 25 min delay (H) freezing. **(I–K),** Mossy fiber AZs (black line) co-labelled against $Ca_V2.1$ (black) and Munc13-2 (pink circles) in DMSO control (I), no (J) and with 25 min delay (K) freezing. **(L),** Schematic representation of the time course of the experiment, with a 5 min FSK treatment, and freezing time points for cSTP immediately after FSK incubation and for cLTP 25 min after FSK incubation. STP: short-term plasticity; LTP: long-term plasticity. (A–F) scale bar sizes are indicated on the figure, (G–K) scale bar sizes are same as in (F).

In addition, neither Munc13-1 nor Mun13-2 particle density was altered in the presence of FSK (Fig. 4-17B-Bi; Munc13-1: DMSO: number of particles per 0.1 µm^2 of AZ area 26.0 ± 12.5 (mean ± SD), median 23.4, n = 66 AZ, N = 5 mice; FSK no delay: 30.1 ± 13.3 (mean ± SD), median 28.0, n = 51 AZ, N = 3 mice; FSK + 25 min: 28.4 ± 11.7 (mean ± SD), median 27.0, n = 46 AZ, N = 2 mice; DMSO vs. FSK no delay: p = 0.06895; DMSO vs. FSK + 25 min: p = 0.1709; FSK 5 min vs. FSK + 25 min: p = 0.5427; Fig. 4-17C-Ci; Munc13-2: DMSO: 22.9 ± 11.2 (mean ± SD), median 21.2, n = 65 AZ, N = 5 mice; FSK no delay: 22.6 ± 11.6 (mean ± SD), median 21.4, n = 49 AZ, N = 3 mice; FSK + 25 min: 20.2 ± 10.2 (mean ± SD), median 18.5, n = 69 AZ, N = 2 mice; DMSO vs. FSK no delay: p = 0.9543; DMSO vs. FSK + 25 min: p = 0.1165; FSK no delay vs. FSK + 25 min: p = 0.1395).

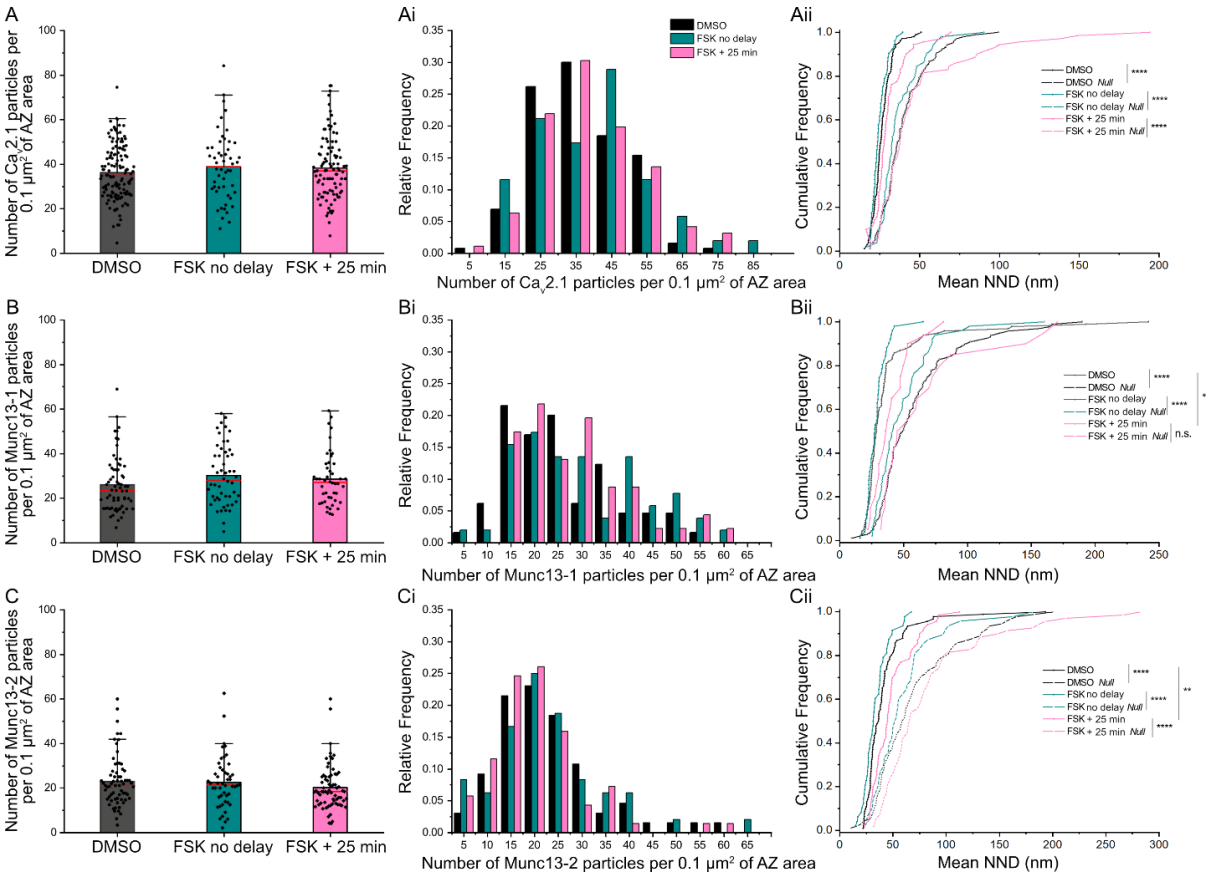

Figure 4-17. Labeling of $Ca_V2.1$ and Munc13 proteins in MFBs of acute hippocampal slices after FSK treatment. (A, B), Scatter plot of the number of $Ca_V2.1$ (A), Munc13-1 (B) and Munc13-2 (C) particles per 0.1 µm^2 of AZ area in DMSO control (grey), no delay (green) and 25 min (pink) after FSK treatment. Bars and whiskers show mean + SD. Red line indicates median value. **(Ai, Bi, Ci)**, Histograms of relative frequency distribution of data shown in (A, B, C) accordingly. **(Aii, Bii,Cii),** Cumulative plots of mean NND between experimental $Ca_V2.1$ (Aii), Mun13-1 (Bii) and Munc13-2 (Cii) point patterns and randomly simulated data in treated groups; the color scheme is identical to A,B. Experimental data (line with filled circles), randomly simulated data (line with empty circles).

Next, NND analysis was done to investigate whether the topography of VGCCs and Munc13s proteins at the AZ was affected by FSK. First of all, Cav2.1 channels and Munc13s retained their propensity to form clusters in all conditions, as cumulative frequency curves of experimental data were significantly different from the ones of randomly distributed particles (Fig. 4-17Aii, Bii, Cii). Mean NNDs between $Ca_V2.1$ particles were significantly shorter than random distributions in all 3 groups (Fig. 4-17Aii; DMSO: mean NND (nm) 26.6 ± 6.2 (mean ± SD), median 25.8, n = 106 AZ, N

= 5 mice; DMSO-Null: 40.3 ± 15.0 (mean ± SD), median 36.8, n = 106 simulations; FSK no delay: 25.0 ± 4.8 (mean ± SD), median 23.9, n = 52 AZ, N = 3 mice; FSK no delay-Null: 37.2 ± 13.1 (mean ± SD), median 32.8, n = 52 simulations; FSK + 25 min: 30.7 ± 10.5 (mean ± SD), median 28.0, n = 71 AZ, N = 2 mice; FSK + 25 min-Null: 47.7 ± 31.5 (mean ± SD), median 37.8, n = 71 simulations; DMSO vs. DMSO-Null $p < 0.0001$; FSK no delay vs. FSK no delay-Null $p < 0.0001$; FSK + 25 min vs. FSK + 25 min-Null $p < 0.0001$).

Second, Munc13-2 NNDs showed similar behavior (Fig. 4-17Cii; DMSO: mean NND (nm) 41.2 ± 23.4 (mean ± SD), median 36.2, n = 92 AZ, N = 5 mice; DMSO-Null: 69.5 ± 40.0 (mean ± SD), median 58.9, n = 92 simulations; FSK no delay: 33.7 ± 12.0 (mean ± SD), median 31.3, n = 48 AZ, N = 3 mice; FSK no delay-Null: 59.2 ± 31.7 (mean ± SD), median 52.2, n = 48 simulations; FSK + 25 min: 48.4 ± 19.1 (mean ± SD), median 44.5, n = 70 AZ, N = 2 mice; FSK + 25 min-Null: 82.8 ± 52.2 (mean ± SD), median 65.2, n = 70 simulations; DMSO vs. DMSO-Null $p < 0.0001$; FSK no delay vs. FSK no delay-Null $p < 0.0001$; FSK + 25 min vs. FSK + 25 min-Null $p < 0.0001$).

However, although Munc13-1 particles were biased to cluster within AZs in control and the 5-min FSK treated samples without delay, they failed to be statistically different from random data set in the sample group frozen with a 25 min delay after FSK treatment (Fig. 4-17Bii; DMSO: mean NND (nm) 37.5 ± 32.2 (mean ± SD), median 28.7, n = 99 AZ, N = 5 mice; DMSO-Null: 59.0 ± 33.5 (mean ± SD), median 49.2, n = 99 simulations; FSK no delay: 28.9 ± 8.1 (mean ± SD), median 27.6, n = 51 AZ, N = 3 mice; FSK no delay-Null: 49.1 ± 23.9 (mean ± SD), median 41.8, n = 51 simulations; FSK + 25 min: 40.5 ± 15.4 (mean ± SD), median 36.6, n = 20 AZ, N = 2 mice; FSK + 25 min-Null: 66.9 ± 42.8 (mean ± SD), median 48.9, n = 20 simulations; DMSO vs. DMSO-Null $p < 0.0001$; FSK no delay vs. FSK no delay-Null $p < 0.0001$; FSK + 25 min vs. FSK + 25 min-Null $p = 0.1745$).

Finally, all three proteins showed an increase in NND 30 min after FSK application onset in comparison to control group ($Ca_V2.1$: DMSO vs. FSK + 25 min: $p < 0.01$; Munc13-1: $p < 0.01$; Munc13-2: $p < 0.001$, Wilcoxon rank sum test). This prolongation of distances is very evident by the shift of cumulative frequency curve towards the right (Fig. 4-17Aii, Bii, Cii; $Ca_V2.1$: DMSO vs. FSK + 25 min: $p = 0.06791$, Munc13-1: $p < 0.05$; Munc13-2: $p < 0.001$, Kolmogorov-Smirnov test). Considering these observations, chemical potentiation affects the distribution of AZ proteins, in particular $Ca_V2.1$ and Munc13-1/2.

Table 4. Properties of Cav2.1, Munc13-1 and Munc13-2 clusters after 5-min FSK treatment.

		$Ca_V2.1$				Munc13-1				Munc13-2			
		N	Mean	SD	Median	N	Mean	SD	Median	N	Mean	SD	Median
DMSO	# clusters per AZ	139	2.7	1.1	3	90	2.4	1.1	2	60	1.8	0.7	2
	# particles per cluster	325	4.5	3.6	3	79	3.2	1.4	3	108	3.38	1.6	3
	Cluster area (μm^2)	261	0.002	0.003	0.0001	112	0.002	0.005	0.0001	73	0.001	0.001	0.0001
	Intercluster distance (nm)	403	94.0	61.5	79.3	203	91.8	57.6	76.1	61	97.0	53.5	94.2
FSK no delay	# clusters per AZ	51	3.1	1.5	3	51	3.3	1.5	3	42	1.8	0.9	2
	# particles per cluster	162	5.1	4.2	4	171	4.3	3.8	3	72	3.2	1.3	3
	Cluster area (μm^2)	119	0.003	0.005	0.0001	112	0.003	0.006	0.001	54	0.001	0.002	0.00004
	Intercluster distance (nm)	222	115.3	81.7	95.5	244	116.9	76.6	94.2	49	122.9	126.3	98.7
FSK + 25 min	# clusters per AZ	87	2.4	1.1	2	44	1.9	1.0	2	68	1.6	0.6	2
	# particles per cluster	104	3.2	1.4	3	83	3.2	1.3	3	39	2.8	1.0	3
	Cluster area (μm^2)	128	0.001	0.001	0.0001	53	0.0001	0.0001	0.00001	49	0.0001	0.0001	0.00004
	Intercluster distance (nm)	175	80.5	64.0	57.6	50	73.6	36.2	74.1	42	63.0	36.1	47.1

4.3.2 Number of clusters changes after forskolin application

Next, DBSCAN analysis was used to examine the spatial behavior of $Ca_V2.1$ Munc13-1 and Munc13-2 clusters (Fig. 4-18; Table 5). First, the mean number of $Ca_V2.1$ clusters cryo-fixed without delay after the 5-min FSK treatment did not change, yet with the 25-min delay the number of clusters decreased (Fig. 4-18A; DMSO: number of clusters per AZ: 2.7 ± 1.1 (mean ± SD), median 3, n = 139 AZ, N = 5 mice; FSK no delay: 3.1 ± 1.5 (mean ± SD), median 3, n = 51 AZ, N = 3 mice; FSK + 25 min: 2.4 ± 1.1 (mean ± SD), median 2, n = 87 AZ, N = 2 mice; DMSO vs. FSK no delay: $p = 0.1167$; DMSO vs. FSK + 25 min: $p < 0.05$).

Second, Munc13-1 particles behaved in a slightly different way. Numbers of Munc13-1 clusters increased significantly in samples cryo-fixed without delay FSK application, but, in contrast, the number of clusters decreased in samples cryo-fixed with the added 25 min delay after treatment (Fig. 4-18Ai; DMSO: number of clusters per AZ: 2.4 ± 1.1 (mean ± SD), median 2, n = 90 AZ, N = 5 mice; FSK no delay: 3.3 ± 1.5 (mean ± SD), median 3, n = 51 AZ, N = 3 mice; FSK + 25 min: 1.9 ± 1.0 (mean ± SD), median 2, n = 44 AZ, N = 2 mice; DMSO vs. FSK no delay: $p < 0.0001$; DMSO vs. FSK + 25 min: $p < 0.01$). The decrease in the number of clusters can be attributed to the increased randomness of Munc13-1 particles 30 min after FSK treatment onset. Moreover, both Munc13-1 cluster area and intercluster distance exhibited time dependence: intercluster distance only transiently increased immediately after FSK treatment, and cluster area decreased only at later cryo-fixation time point (Fig. 4-18 Ci, Di; Table 5; intercluster distance: DMSO vs. FSK no delay: $p < 0.001$; DMSO vs. FSK + 25 min: $p = 0.118$; cluster; cluster area: DMSO vs. FSK no delay: $p = 0.3939$; DMSO vs. FSK + 25 min: $p < 0.01$).

Finally, unlike $Ca_V2.1$ and Munc13-1, Munc13-2 did not show any alterations in their cluster number, but did show change in intercluster distances and cluster area in samples cryo-fixed with a delay after FSK treatment (Fig. 4Aii, Cii, Dii; Table 5; number of clusters per AZ: DMSO vs. FSK no delay: $p = 0.8124$; DMSO vs. FSK + 25 min: $p = 0.186$; intercluster distance: DMSO vs. FSK no delay: $p = 0.3767$; DMSO vs. FSK + 25 min: $p < 0.001$; cluster area: DMSO vs. FSK no delay: $p = 0.09485$; DMSO vs. FSK + 25 min: $p < 0.01$). This finding is unexpected, as previous reports showed altered synaptic transmission and STP in Munc13-2 KO neuronal cultures (Rosenmund et al., 2002). Despite the absence of changes in the number of Munc13-2 clusters, the increase in Munc13-1 clusters agrees with previously published work, where an expansion of the RRP is described during STP (Vandael et al., 2020; Kobbersmed et al., 2020).

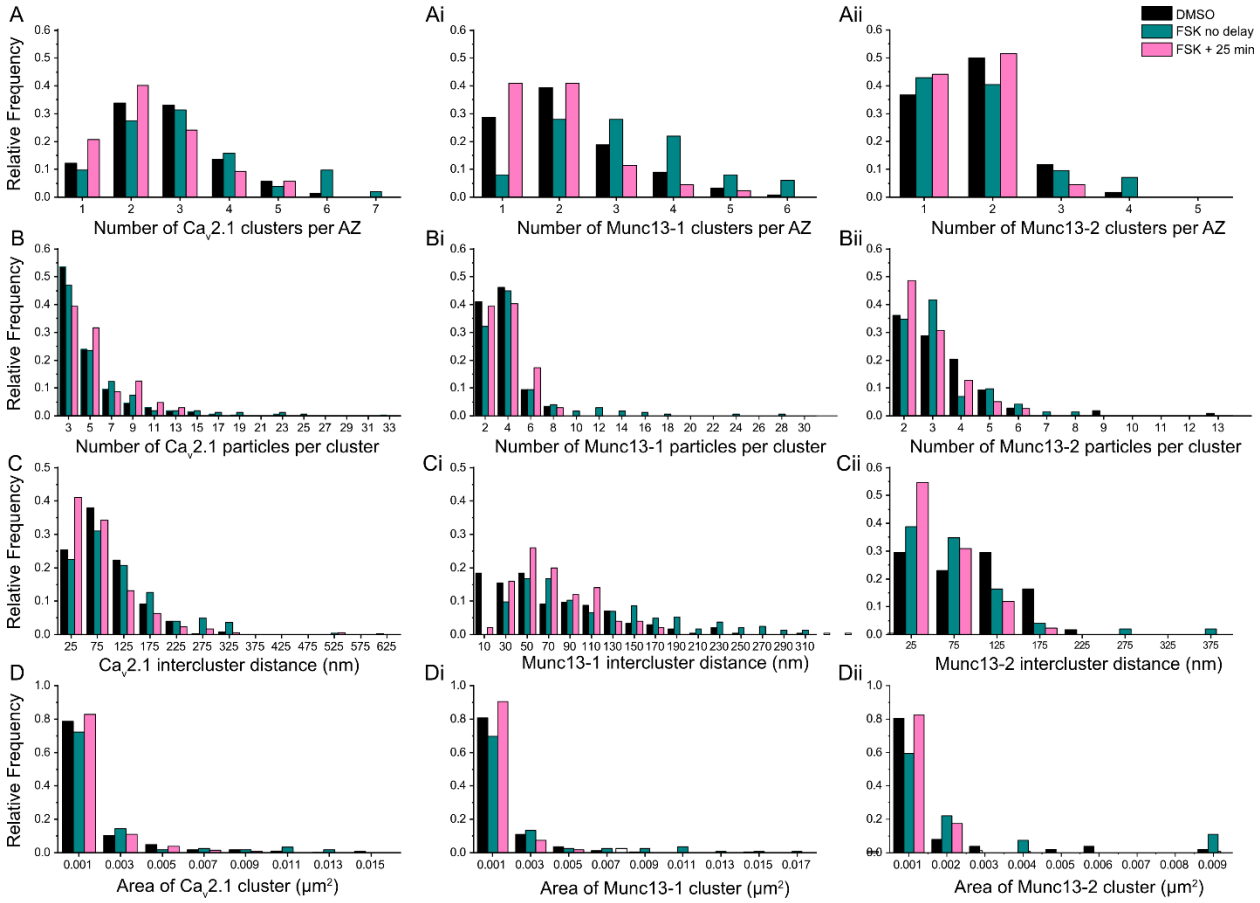

Figure 4-18. $Ca_V2.1$ and Munc13s clusters exhibit temporal changes after FSK application. (A–Aii), Histogram of relative frequency distribution of number of clusters per active zone of $Ca_V2.1$ (A), Munc13-1 (Ai), and Munc13-2 (Aii) particles in DMSO control (grey), no delay (green) and 25 min (pink) after FSK treatment. **(B–Bii),** Histogram of relative frequency distribution of number of particles per cluster of $Ca_V2.1$ (B), Munc13-1 (Bi), and Munc13-2 (Bii); the color scheme is identical to A–Aii. **(C–Cii),** Histogram of the relative frequency distribution of the minimal distance between $Ca_V2.1$ (C), Munc13-1 (Ci) and Munc13-2 (Cii); clusters color scheme is identical to A–Aii. **(D–Dii),** Histogram of relative frequency distribution of area of each cluster of $Ca_V2.1$ (D), Munc13-1 (Di) and Munc13-2 (Dii) particles; color scheme is identical to A–Aii.

4.3.3 Interactions between $Ca_V2.1$ and Munc13-1 alter after chemical potentiation

To determine whether coupling distance changes after plasticity induction, NND analysis between $Ca_V2.1$ and Munc13-1/2 point patterns was performed. The mean pairwise distance between particles was calculated from all three conditions (DMSO control, no delay, and 25-min delay after a 5-min FSK treatment) in two sample groups co-labeled for $Ca_V2.1$ and Munc13-1 or Munc13-2 (Fig. 4-19). First, the change in $Ca_V2.1$/Munc13-1 cumulative frequency curve is immediately noticed, as it is significantly shifted to smaller values along the abscissa in samples with the 25-min delay after FSK application (Fig. 4-19A; DMSO vs. FSK + 25 min: $p < 0.0001$, Kolmogorov-Smirnov test). However, the change is absent in samples cryo-fixed with no delay after plasticity induction (DMSO vs. FSK no delay: $p = 0.155$, Kolmogorov-Smirnov test). Moreover, the mean pairwise distance in samples cryo-fixed with no delay was not significantly different from the control group, albeit being slightly bigger (Fig. 4-19Ai, Aii; DMSO: distance (nm): 105.8 ± 27.8 (mean ± SD), median 101.4, n = 93 AZ, N = 5 mice; FSK no delay: 113.5 ± 33.2 (mean ± SD), median 108.6, n = 51 AZ, N = 3 mice; DMSO vs. FSK no delay: $p = 0.137$).

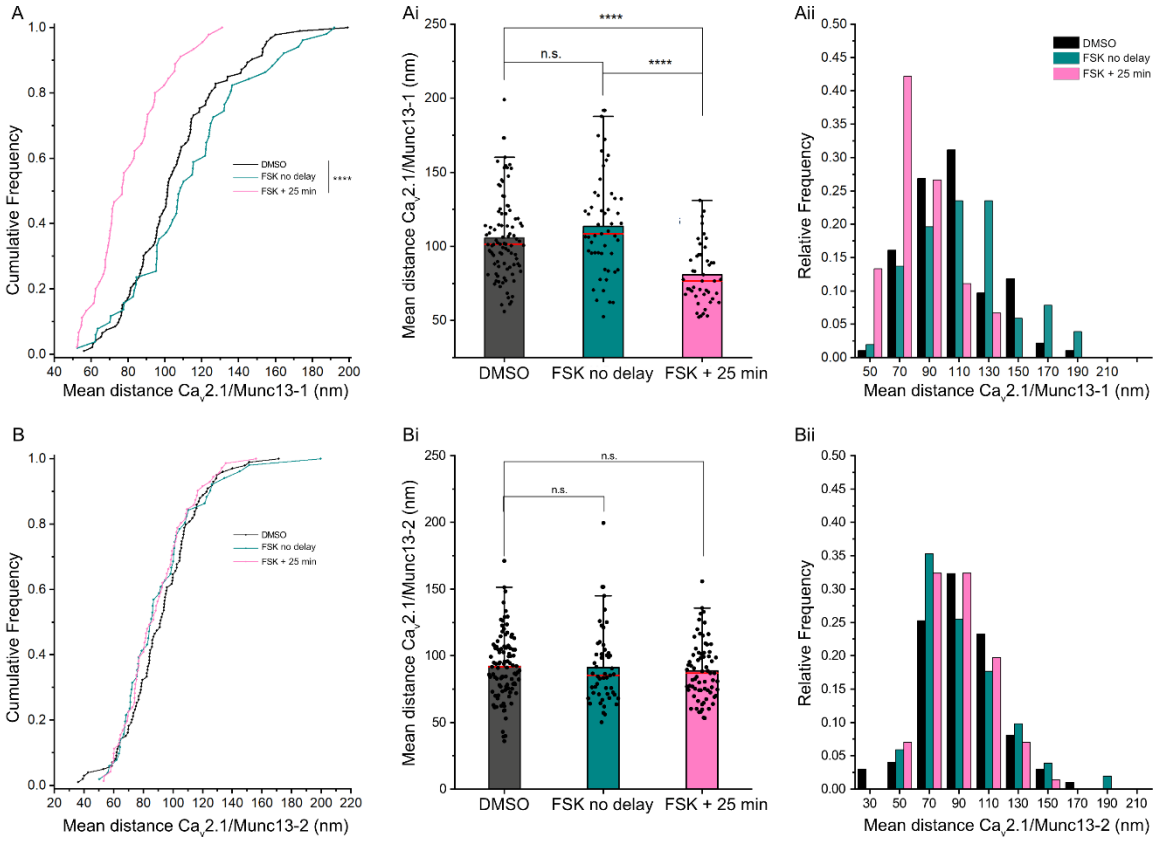

Figure 4-19. Structural coupling distance between Cav2.1 and Munc13-1/2 in FSK treated samples. (A, B), Cumulative plots of mean pairwise distances between experimental Cav2.1/Mun13-1 point patterns (A) and Cav2.1/Mun13-2 (B) in DMSO control (grey), no delay (green) and 25 min (pink) after FSK treatment. **(Ai, Bi),** Scatter plot of the mean pairwise distances between Cav2.1 and Munc13-1 (Ai) or Munc13-2 (Bi); color scheme is identical to (A, B). Bars and whiskers show mean + SD. Red line indicates median value. **(Aii, Bii),** Histograms of relative frequency distribution of data shown in (Ai, Bi) accordingly.

Yet the mean distances between $Ca_V2.1$ and Munc13-1 became notably shorter 25 min after FSK application (Fig. 4-19Ai, Aii; FSK + 25 min: 80.8 ± 20.2 (mean ± SD), median 97.2, n = 45 AZ, N = 2 mice; DMSO vs. FSK + 25 min: $p < 0.0001$, FSK no delay vs. FSK + 25 min: $p < 0.0001$). The lack of change in the distance between calcium channels and docked-and-primed vesicles in samples cryo-fixed with no delay after FSK treatment corroborates electrophysiology measurements, which showed that Pr does not change during STP (Vandael et al., 2020).

On the other hand, the analysis of mean NND between $Ca_V2.1$ and Munc13-1 particles revealed that the distances decreased in both samples groups, no delay and 25-min delay after a 5-min FSK treatment (Fig. 4-20A–Aii). First, the cumulative frequency curves of FSK treated samples were shifted towards the left and were significantly different in comparison to DMSO control (Fig. 4-20A; DMSO vs. FSK no delay: $p < 0.05$; DMSO vs. FSK + 25 min: $p < 0.05$, Kolmogorov-Smirnov test).

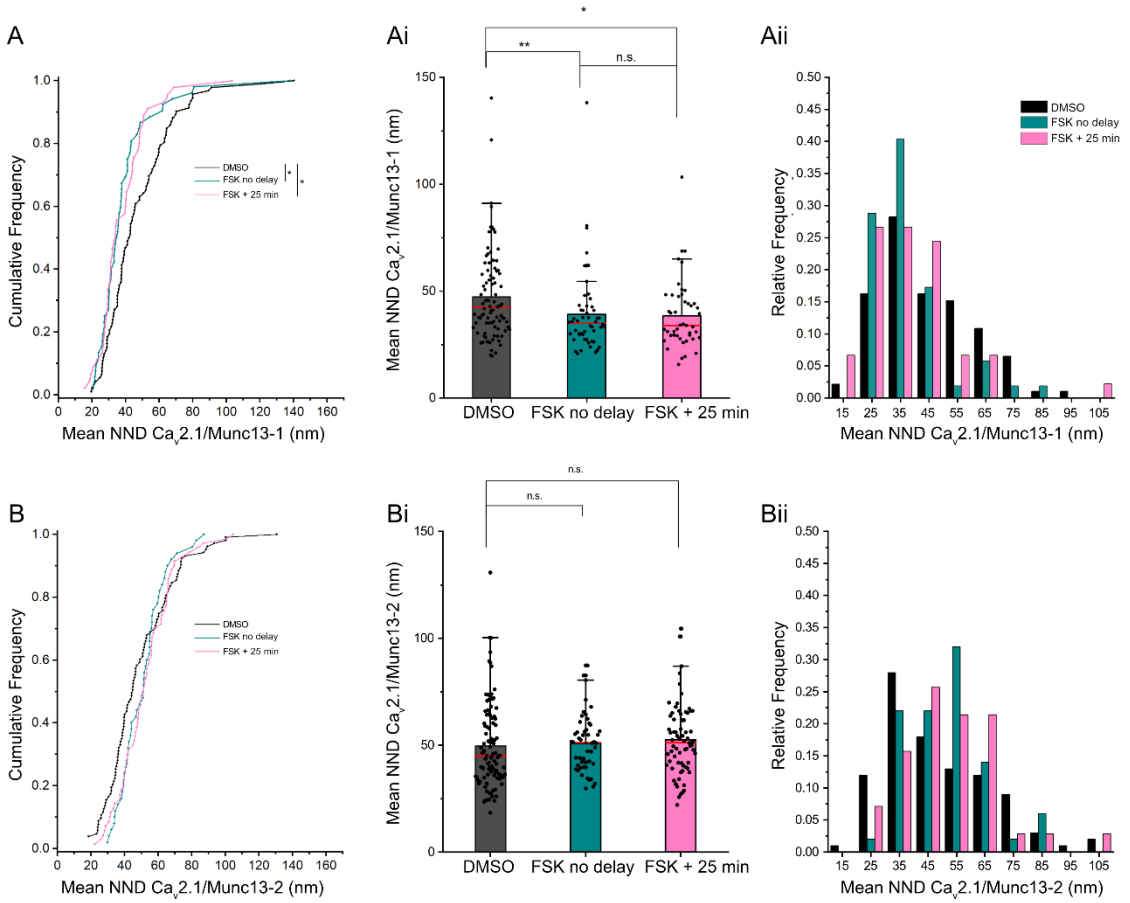

Figure 4-20. Mean NND between $Ca_V2.1$ and Munc13-1/2 in FSK treated samples. (A, B), Cumulative plots of mean NND between experimental $Ca_V2.1$/Mun13-1 point patterns (A) and $Ca_V2.1$/Mun13-2 (B) in DMSO control (grey), no delay (green) and 25 min (pink) after FSK treatment. **(Ai, Bi),** Scatter plot of the mean NND between $Ca_V2.1$ and Munc13-1 (Ai) or Munc13-2 (Bi); color scheme is identical to (A, B). Bars and whiskers show mean + SD. Red line indicates median value. **(Aii, Bii),** Histograms of relative frequency distribution of data shown in (Ai, Bi) accordingly.

Second, the mean NND values decreased immediately and 25 min after FSK application (Fig. 4-20Ai–Aii; DMSO: NND (nm): 47.4 ± 20.9 (mean ± sd), median 42.3, n = 93 AZ , N = 5 mice; FSK no delay: 39.2 ± 19.5, median 34.9, n = 51 AZ, N = 3 mice; FSK + 25 min: 38.4 ± 15.7, median 34.0, n = 45 AZ, N = 2 mice; DMSO vs. FSK + 25 min: $p < 0.01$, DMSO vs. FSK +25 min: $p < 0.05$, FSK no delay vs. FSK + 25 min: $p = 0.9612$).

Munc13-2 can also prime SVs in AZs and possibly contribute to changes in Pr (Varoqueaux et al., 2002). Thus, next samples co-labelled with Cav2.1 and Munc13-2 were examined (Fig. 4-19B–Bii). Mean pairwise distance did not change across groups and cumulative distribution was not statistically different, contrary to $Ca_V2.1$/Munc13-1 samples (Fig. 4-19B; DMSO vs. FSK no delay: $p = 0.5278$, DMSO vs. FSK + 25 min: $p = 0.155$, Kolmogorov-Smirnov test; Fig. Bi–Bii; DMSO: mean distance (nm): 92.1 ± 24.6 (mean ± sd), median 91.6, n = 99 AZ , N = 5 mice; FSK no delay: 91.1 ± 27.9, median 85.3, n = 51 AZ, N = 3 mice; FSK + 25 min: 88.6 ± 22.1, median 86.9, n = 71 AZ, N = 2 mice; DMSO vs. FSK no delay: $p = 0.3785$, DMSO vs. FSK + 25 min: $p = 0.2398$). In addition, no change in the mean NNDs was observed (Fig. 4-20; DMSO vs. FSK no delay: $p = 0.2194$, DMSO vs. FSK + 25 min: $p = 0.1603$, Kolmogorov-Smirnov test; Fig. Bi–Bii; DMSO: NND (nm): 49.7 ± 19.9 (mean ± SD), median 45.0, n = 99 AZ , N = 5 mice; FSK no delay: 50.9 ± 13.3, median 51.2, n = 51 AZ, N = 3 mice; FSK + 25 min: 52.5 ± 16.5, median 51.2, n = 71 AZ, N = 2 mice; DMSO

vs. FSK no delay: p = 0.3894, DMSO vs. FSK + 25 min: p = 0.2246). This indicates that the Munc13-1 protein isoform is the major priming factor in hippocampal MFBs, involved in expression of cSTP and cLTP.

4.3.4. Number of docked synaptic vesicles increased after forskolin application

Next to determine the effect of chemical potentiation on the docking of SVs, acute slices after DMSO or FSK treatment underwent HPF and FS (Fig. 4-21,4-22; see Chapter 2. Materials and Methods; Borges-Merjane et al., 2020). Again, the number and diameter of docked vesicles was normalized per 100 nm of AZ profile length. Intriguingly, the number of docked vesicles increased after FSK application and cryo-fixed with no delay, while in samples cryo-fixed 25 min after FSK treatment, the number of docked vesicles was not different from DMSO control (Fig. 4-21A, Aii; DMSO: number of docked vesicles per 100 nm AZ profile length: 0.79 ± 0.50 (mean ± SD), median 0.82, n = 42 AZ, N= 2 mice; FSK no delay: 1.09 ± 0.60, median 1.16, n = 56 AZ, N= 3 mice; FSK + 25 min: 0.68 ± 0.70, median 0.70, n = 32 AZ, N= 2 mice; DMSO vs. FSK no delay: p < 0.01, DMSO vs. FSK + 25 min: p = 0.3464). This change could also be observed in cumulative plots, where the curve for the sample group fixed with no delay was shifted towards the right (Fig. 4-21Ai; DMSO vs. FSK no delay: p < 0.001). Although there was an increase in the number of empty AZs in samples frozen with the 25-min delay, it was not statistically significant (Fig. 4-21Ai; DMSO vs. FSK + 25 min: p = 0.358, Kolmogorov-Smirnov test).

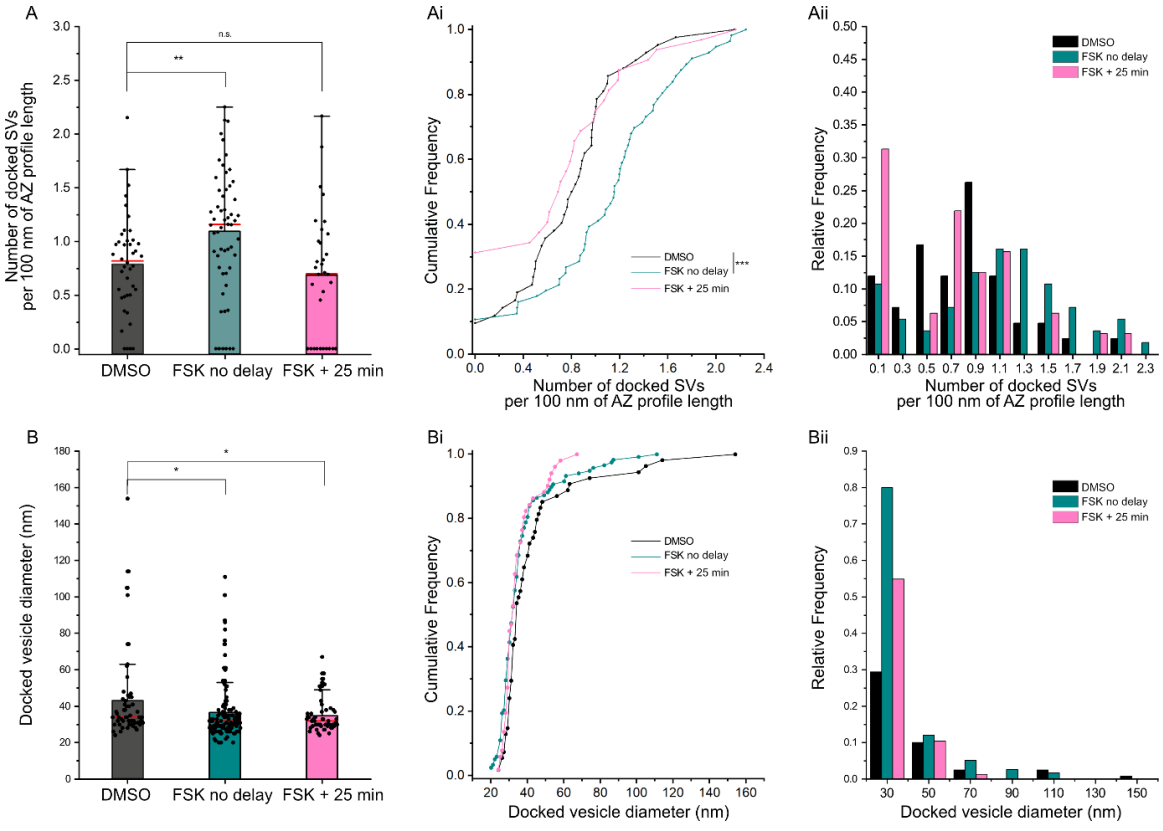

Figure 4-21. The number and diameter of docked vesicles changes after FSK application. (A), Scatter plot of the number of docked vesicles per 100 nm of AZ length in DMSO control (grey), no delay (green) and 25 min (pink) after FSK treatment. Bars and whiskers show mean + SD. Red line indicates median value. **(Ai),** Cumulative plots of the data displayed in A. **(Aii),** Histograms showing the comparison of relative frequency distribution of docked vesicle numbers in treatment groups; color scheme is identical to A. **(B),** Scatter plot of the diameter of docked vesicles measured in DMSO control (grey), no delay (green) and 25 min (pink) after FSK treatment. Bars and whiskers show mean + SD. Red line indicates median value. **(Bi),** Cumulative plots of the data displayed in B.

(Bii), Histograms showing the relative frequency distributions of docked vesicle diameter for treated groups; color scheme is identical to B.

In addition, also the diameter of docked vesicles changed upon application of FSK (Fig. 4-21B–Bii). Both groups, cryo-fixed with and without delay after treatment, showed decreased vesicle diameter compared to control, probably indicating addition of smaller SVs to AZ (Fig. 4-21B–Bii; DMSO: docked vesicle diameter (nm): 42.9 ± 24.4 (mean ± SD), median 34, n = 42 AZ, n = 54 vesicles, N= 2 mice; FSK no delay: 36.5 ± 15.9, median 32, n = 56 AZ, n = 118 vesicles, N= 3 mice; FSK + 25 min: 34.8 ± 9.3, median 32, n = 32 AZ, n = 51 vesicles, N= 2 mice; DMSO vs. FSK no delay: $p < 0.05$, DMSO vs. FSK + 25 min: $p < 0.05$). All things considered, these results indicate that transient increase in Munc13-1 clusters is correlated with enlargement of the docked vesicle pool.

CHAPTER 5. CONCLUSIONS AND DISCUSSION

To date, modern cellular neuroscience exhibits a significant gap between structural data obtained with EM and functional data, obtained with electrophysiology or optical imaging. EM provides static images while having exceptional spatial resolution (Palay, 1956; Schikorski and Stevens, 1997; Rollengahen et al., 2007; Harris and Weinberg, 2012; Meier and Beckmann, 2017). Electrophysiology, on the other hand, has millisecond temporal resolution but limited spatial information. Furthermore, a variety of distinct preparations have been used during morphological and functional investigations. Electrophysiology is primarily performed in acute slices, but with EM perfusion fixed brains are used, as it provides optimal tissue preservation (Blanton et al., 1989; Edwards et al., 1989; Bischofberger et al., 2006b; Shigemoto and Joesch, 2017; Kubota et al., 2018). Correlating structural and functional data is thus a significant challenge. The current research provides the first functional EM measurements at an identified mammalian synapse in an intact cortical network, bridging the gap between structural and functional analyses, to the best of current state of the art.

5.1 Comparison with previous techniques

Functional EM ("Flash and Freeze") has been effectively applied to the nervous system of *C. elegans* as well as mouse neuronal dissociated cell culture (Watanabe et al., 2013a; Watanabe et al., 2013b). Despite the method's strength, the approach is difficult to apply to intact mammalian preparations like organotypic slice cultures or acute brain slices. However, such progress is crucial, if the technique is to be applied to precisely defined mammalian central synapses with correlated structural and functional studies of synaptic transmission (Blanton et al., 1989; Edwards et al., 1989; Bischofberger et al., 2006b; Neher, 2017). A number of technological advancements have allowed us to overcome the constraints of conventional procedures. First, reducing the acute slices' thickness rendered an optimal ultrastructural preservation. Second, following the conventional cutting procedure, a recovery period at near-physiological temperature, which has been shown to improve slice quality in electrophysiological experiments (Bischofberger et al., 2006b), has been included. Third, to perfectly match the thickness and lateral dimensions of the slice, the specimen sandwich was redesigned, thus, preserving the whole network. Fourth, we optimized cryoprotectant concentration and timing by applying PVP or BSA right before stimulation and freezing. The slices and cultures were stimulated at physiological temperature; therefore, both were kept at around 37°C for at least 10 minutes before freezing. Finally, an expedited freeze-substitution protocol was introduced. These enhancements resulted in improved ultrastructure of acute slices, comparable to that of high-pressure frozen organotypic slice culture, which had previously been employed for HPF investigations without optogenetic stimulation (Studer et al., 2014; Imig et al., 2014; Zhao et al., 2012a; Zhao et al., 2012b).

5.2 Insights into mechanisms of mossy fiber synaptic transmission

The hippocampal MFB-CA3 PN synapse, a crucial synapse in the hippocampus's trisynaptic circuit (Andersen et al., 1971; Rolls and Treves, 1994; Bischofberger et al., 2006a), reveals numerous unexpected elements of its structure and function (Fig. 5-1). The docked vesicle pool in the AZs at hippocampus MF synapses is significantly decreased by 71.5 and 87 % in acute slices and slice culture, respectively, after persistent presynaptic activation (i.e. 20 Hz stimulation for 1 s). Therefore, suggesting that, at MFB synapses, the RRP and docked vesicle pool

strongly overlap (Schikorski and Stevens, 2001; Imig et al., 2014; Wang et al., 2016). In addition, after PTP induction and a 20 s recovery period, the docked vesicle pool not only returned to basal level but increased in both acute slices and organotypic slice culture (Fig. 5-1). Thus, corroborating electrophysiological findings, that it is primarily an increase in the RRP that influences potentiation during PTP (Vandael et al., 2020).

Second, our findings show that the diameter of vesicles at MFB-CA3 PN synapses varied and skewed toward bigger dimensions (Henze et al., 2002). Since the stimulation decreased the mean diameter of docked vesicles, the most logical explanation is that the smaller vesicles have a higher release probability and are released first with recurrent stimulation. Indeed, the fusion rate of vesicles rises with membrane curvature (Martens et al., 2007; Lin et al., 2012), possibly because the stress of the vesicular membrane curvature offers additional energy for bilayer fusion.

Finally, our findings show that mild repeated stimulation (i.e. 5 stimuli at 20 Hz) causes formation of endocytic pits, possibly via a clathrin-independent mechanism. As a result, our findings provide the first direct ultrastructural evidence for clathrin-independent endocytosis at the hippocampal MFB-CA3 PN synapse, as was previously suggested by capacitance measurements (Hallermann et al., 2003; Delvendahl et al., 2016). However, unlike other functional EM study of cultured MFB synapses (Imig et al., 2020), this endocytic structures were observed only after mind stimulation. This discrepancy in the results can be explained by different types of culturing methods (interface vs. roller tube), application of cryo-protectant (15 % BSA vs. no cryo-protectant), and transgenic mouse line used (Prox1CreER^{T2} vs. Dock10-Cre). Nevertheless, our findings provide persuasive proof of the power of the method, which can abet in the generation of novel insights into the fundamental operations of synaptic transmission at identified mammalian cortical synapses.

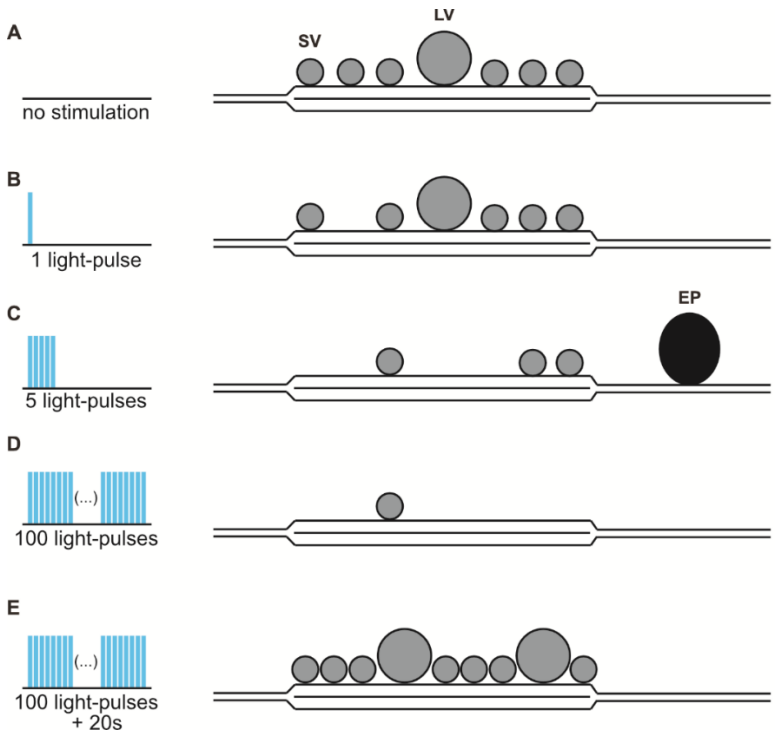

Figure 5-1. Schematic representation of stimulus-dependent depletion and recovery of docked vesicles. **(A),** AZ under basal condition containing small and large vesicles (SV and LV). **(B),** One pulse results in the fusion of SVs. **(C),** Stronger stimulation leads to the higher fusion rate of both SVs and LVs, and the formation of endocytic pits (EP). **(D),** Train of stimuli results in almost complete depletion of docked vesicles. **(E),** Overfilling of docked vesicles pool after train stimulation and recovery period.

5.3 Molecular composition of MFB during cSTP and cLTP

FRIL experiments allowed us the investigation of the molecular composition of MFB AZs under basal and plastic states (Fig 5.2). First, we confirmed that MFB synapses express three types of calcium channels: $Ca_V2.1$ (P/Q-type), $Ca_V2.2$ (N-type), and $Ca_V2.3$ (R-type), with the majority of the calcium channels being $Ca_V2.1$ as shown previously in MFB synapses (Li et al., 2007). In addition, the morphological coupling distance between calcium channels and priming proteins Munc13-1/2 in MFB in fixed samples is comparable to the functionally computed distance between calcium source and calcium sensor (Vyleta and Jonas, 2014). These results are the first known comparison between structurally and functionally defined coupling distance at MFB-CA3 PN synapses.

Second, to investigate the molecular changes in the MFB synapses after induction of chemical potentiation in acute slices, it was possible to adapt the aforementioned new method of HPF of acute slices, to perform freeze-fracture of fresh samples only with small alterations (Fig. 5-2). In our freezing assay, we wanted to capture two types of plasticity – cSTP and cLTP. Accordingly, samples were cryo-fixed either without delay (cSTP) or 25 min after FSK treatment (cLTP). Remarkably, chemical potentiation did not affect Munc13-2 protein distribution, despite previous evidence of augmentation of SV release after plasticity induction in Munc13-2-dependent hippocampal synapses in dissociated cultures (Rosenmund et al., 2002). However, our results are corroborated by previous studies in acute slices, where cLTP was not abolished in Munc13-2 KO (Breustedt et al., 2010). This discrepancy between current and previous study with dissociated neuronal cultures may be explained with synapse-specific nature of FSK effects and the difference in stimulation (chemical vs. electrical).

On the other hand, the number of Munc13-1 clusters increased during cSTP. However, this increase was transient, as the number of clusters decreased below control levels in cLTP. Moreover, we found that the number of docked SVs notably increased to a similar degree as the number of clusters in cSTP. Thus, this effect matched the effect of optogenetic stimulation, which induced PTP and led to the expansion of the RRP (Fig. 5-1; Vandael et al., 2020). The results of the FRIL experiments lead to an interesting assumption: although the RRP with Munc13-1 clusters and docked vesicle pool strongly correlate (Imig et al., 2014; Rebola et al. 2019), they describe different functional and structural states of SVs and cannot be directly compared (Wang et al., 2016; Kaeser and Regehr, 2017; Tan et al. 2022). It is possible that in the current immunolabeling assay, only tightly docked vesicles are identified (Miki et al., 2018; Neher and Brose 2018), which might explain the discrepancy in the numbers of Munc13 clusters and docked vesicles. Future work should be aimed to elucidate the differences between these criteria of synaptic release.

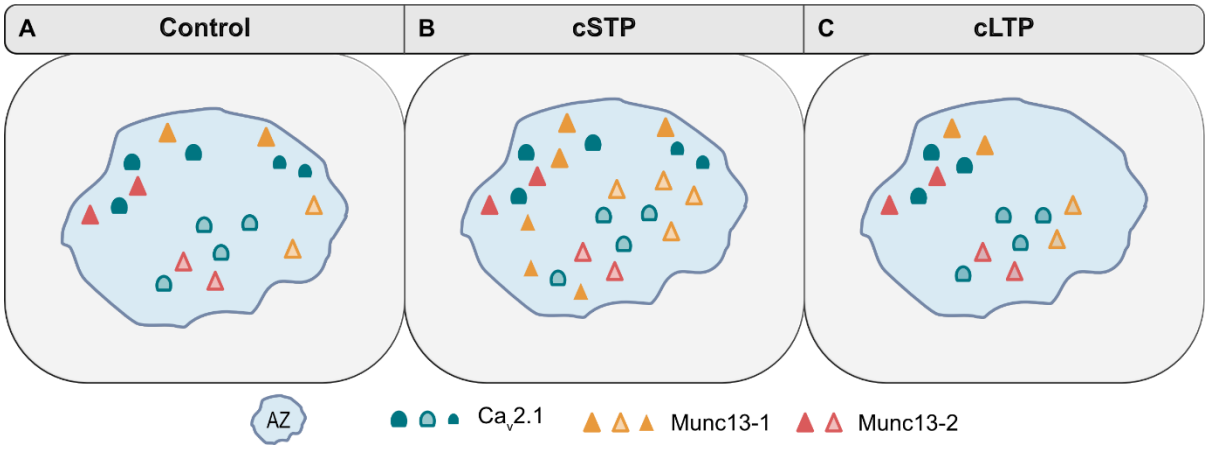

Figure 5-2. Scheme of forskolin-induced remodeling of mossy fiber active zones during cSTP and cLTP. (A), AZ under basal control conditions with clusters of $Ca_V2.1$ channels, Munc13-1, and Munc13-2 proteins. **(B),** During cSTP the number of Munc13-1 clusters increases, AZs becomes denser. **(C),** During cLTP, the number of Cav2.1s and Munc13-1s decreases and the distance between particles shortens. AZ becomes more compact.

Thirdly, the morphologically defined coupling distance changed in a time-dependent manner, remaining the same during cSTP and shortening during the cLTP phase (Fig. 5-2). However, the NND between calcium channels and Munc13-1 proteins decreased immediately after FSK application. Still the magnitude of change was smaller than the increase in the number of Munc13-1 clusters during cSTP, similarly to the effects of HFS (Vandael et al., 2020).

These results suggest the existence of two distinct mechanisms that govern cSTP and cLTP at MFB synapses: an increase in the RRP in the case of cSTP and a potential increase in Pr during cLTP. On one hand, AC1 and subsequent PKA activity may directly affect Munc13s or other vesicle-associated proteins, such as synaptobrevin of SNARE complex or synapsin (Seino and Shibasaki, 2005; Gitler et al., 2008; Patzke et al., 2019), resulting in enhanced docking and priming of SVs over a short period of time during cSTP. Contrarily, at the later time point of chemically induced plasticity, high levels of cAMP and CCAAT-enhancer-binding proteins (c/EBP) can act as transcription factors and regulate cLTP expression, and act as molecular substrates of learning and long-term memory formation (Davis and Squire, 1984; Castellucci et al., 1989; Crow and Forrester, 1990; Alberini et al., 1994; Tully et al., 1994). Furthermore, although calcium channels were also reported to be important for the induction and possibly expression of different types of plasticity, (Breustedt et al., 2003; Fukaya et al., 2021), our results show that the number of $Ca_V2.1$ clusters is downregulated during cLTP. Hence, it is possible that at the later time point, a parallel signaling pathway is activated, which affects different types of calcium channels and possibly other components of the AZ proteome in a contrasting manner. In this case, it is likely that RIM protein would be involved, as it acts upstream of Munc13 during priming. RIM stabilizes calcium channel clusters and the location of SVs in a PIP_2-dependent manner (Zarebidaki et al., 2020), thus avoiding the cAMP signaling pathway and relying on PLC activity (Lipstein et al., 2021).

En mass it is evident that synapses are adaptable structures that can become plastic to comply with ever-changing input, or maintain homeostatic activity (Davis, 2013). Previously, it was established that classical Hebbian LTP at CA3-CA1 PN synapses is expressed postsynaptically and relies on the dynamic increase in AMPA (α-amino-3-hydroxy-5-methyl-4-isoxazolepropionic acid) receptor density of in the postsynaptic density (PSD) (Nicoll and Malenka, 1999). However, this molecular plasticity is not limited to the PSD. The current study shows that these dynamic

changes occur also at the presynaptic terminal in the AZ during both cSTP and cLTP, which expression depends on two distinct mechanisms. Moreover, it is possible that the same mechanisms govern STP and LTP after HFS.

5.4 Implications of mossy fiber terminal structure for circuit activity

The expansion of the vesicle pool during STP could be advantageous for short-term memory processing in the hippocampus (Squire and Zola-Morgan, 1991). The time course of MFB STP, and in particular PTP, is highly correlated with the time course of short-time memory (Squire and Zola-Morgan, 1991; Deadwyler et al., 1996). Moreover, STP has a long decay time course that could be extended even more in the absence of activity or the presence of neuromodulators such as noradrenalin or serotonin (Huang and Kandel, 1996; Patzke et al., 2019). Furthermore, SV pool upregulation may be especially well-suited for information storage in the sparsely active dentate gyrus-CA3 circuit (Perna-Andrade and Jonas, 2014; Zhang et al., 2020), for instance in delayed nonmatch-to-sample tasks or during spatial navigation (Deadwyler et al., 1996; Wiebe and Stäubli, 1999; Zhang et al., 2020).

On the other hand, the increase in Pr, through the shortening of coupling distance in a cAMP-dependent manner, could be advantageous during long-term memory (Huang and Kandel, 1994; Midorikawa and Sakaba 2017). Although the PTP pool mechanism is highly energy-efficient, persistent SV recycling requires continuous input of energy and could be draining during long periods (Attwell and Laughlin, 2001; Li and Sheng, 2022). Thus, precise positioning of release sites closer to calcium source ensures reliable transmission with possible minimum energy costs. However, only early-stage cLTP is described here, and different energy demands could become apparent at a later stage.

Lastly, the employment of distinct plasticity mechanisms underlies the role of MFB synapse as a “smart teacher” that triggers maintenance of short- and long-term memory with maximum storage capacity in an energy-efficient way (Bischofberger et al. 2006a; Vandael et al., 2021). However, more work is needed to confirm this hypothesis. In addition, the other MF synapses (from filopodia extensions and en passant boutons) can affect the circuitry in a completely different way. Since, unlike MFB-CA3 PN synapses, MF-interneuron synapses exhibit much lower levels of facilitation and even short-term depression (Toth et al., 2000). Future work combining electrophysiological analysis and functional EM is needed to further investigate the morphological correlates of synaptic plasticity at this synapse and its involvement in memory processing.

5.5 Future perspectives of new high-pressure freezing method

The improved functional EM method described here is versatile and has a lot of room for further development. For instance, the technique could potentially be used with FRIL or post-embedding immunogold analysis. This work demonstrated that the HPF method can be adapted for this purpose, and further development to allow for light-stimulation would be advantageous. This combination is powerful to disclose not only the static molecular arrangement of presynaptic proteins like calcium channels but also dynamic alterations in the topography of AZs during synaptic plasticity. Moreover, functional EM can also be combined with chemogenetics in a variety of ways. For example, persistent chemogenetic manipulation of activity *in vivo* followed by acute optogenetic activation of synapses *in vitro* may allow dissection of the processes underlying presynaptic homeostatic plasticity (Davis, 2013; Davis and Müller, 2015). Finally, pharmacological interventions, as shown with FSK, can be

readily implemented into the method. As a result, structural characterization of pharmacogenetically and pharmacologically altered synapses is possible using functional EM.

The technique is applicable to many brain areas and different sample preparations, and hence to a wide range of synapses in intact networks. Thus, allowing in-depth investigation of similarities and differences in activity-dependent changes across central synapses by genetically targeting specific cell types across distinct brain areas and synapses. This, in turn, may lead to answers to some fundamental questions. For example, whether SVs undergo full fusion or if neurotransmitter is released via temporary fusion pores (Aravanis et al., 2003; Lisman et al., 2007), as described for dense-core vesicles (Chiang et al., 2014). The proposed technique could also help in the investigation of depletion and refilling properties of the RRP and recycling pool behavior at MFBs and other central synapses. Finally, the novel method shines the light on the mechanics of STP and LTP, where the same phenomena of synaptic strengthening can have distinct underlying mechanisms depending on the synapse; for example, hippocampus MFBs and calyx of Held (Langdon et al., 1995; Alle et al., 2001; Habets and Borst, 2007; Vandael et al., 2020).

Because the new method can be used on both acute slices and organotypic slice cultures, it will be valuable in determining the synaptic phenotypes of mouse mutants with lethal phenotypes, which can only be examined in slice culture and not acute slices (Kerr et al., 2008). The significant parallels and fine dissimilarities between acute slices and organotypic slice culture, quantified in this research, will serve as a reference framework for interpreting these findings. In addition, the novel technique may be valuable for studying structural alterations generated by disease states like epilepsy, Alzheimer diseases, and depression (Small et al., 2011), which can only be investigated in cultures or cerebral organoids, but not in acute slices (Accardi et al., 2018; Wickham et al., 2018; Chiaradia and Lancaster, 2020). Thus, structural and functional mechanisms of transmission in intact, genetically perturbed, and disease-affected synapses may be revealed by functional EM techniques.

REFERENCES

Abraham, W.C., Logan, B., Greenwood, J.M., and Dragunow, M. (2002). Induction and experience-dependent consolidation of stable long-term potentiation lasting months in the hippocampus. J Neurosci 22, 9626–9634.

Accardi, M.V., Huang, H., and Authier, S. (2018). Seizure liability assessments using the hippocampal tissue slice: Comparison of non-clinical species. Journal of Pharmacological and Toxicological Methods 93, 59–68.

Acsády, L., Kamondi, A., Sík, A., Freund, T., and Buzsáki, G. (1998). GABAergic cells are the major postsynaptic targets of mossy fibers in the rat hippocampus. J Neurosci 18, 3386–3403.

Alberini, C.M., Ghirardi, M., Metz, R., and Kandel, E.R. (1994). C/EBP is an immediate-early gene required for the consolidation of long-term facilitation in Aplysia. Cell 76, 1099–1114.

Alle, H., and Geiger, J.R.P. (2006). Combined analog and action potential coding in hippocampal mossy fibers. Science 311, 1290–1293.

Alle, H., Jonas, P., and Geiger, J.R. (2001). PTP and LTP at a hippocampal mossy fiber-interneuron synapse. Proc Natl Acad Sci USA 98, 14708–14713.

Amaral, D.G. (1979). Synaptic extensions from the mossy fibers of the fascia dentata. Anat Embryol (Berl) 155, 241–251.

Amaral, D.G., Ishizuka, N., and Claiborne, B. (1990). Neurons, numbers and the hippocampal network. Prog Brain Res 83, 1–11.

Andersen, P., Bliss, T.V.P., and Skrede, K.K. (1971). Lamellar organization of hippocampal excitatory pathways. Exp Brain Res 13, 222–238.

Aravanis, A.M., Pyle, J.L., Harata, N.C., and Tsien, R.W. (2003). Imaging single synaptic vesicles undergoing repeated fusion events: kissing, running, and kissing again. Neuropharmacology 45, 797–813.

Ariel, P., and Ryan, T.A. (2010). Optical mapping of release properties in synapses. Front Neural Circuits 4, 18.

Attwell, D., and Laughlin, S.B. (2001). An energy budget for signaling in the grey matter of the brain. J Cereb Blood Flow Metab 21, 1133–1145.

Augustin, I., Betz, A., Herrmann, C., Jo, T., and Brose, N. (1999a). Differential expression of two novel Munc13 proteins in rat brain. Biochem J 337 (Pt 3), 363–371.

Augustin, I., Rosenmund, C., Südhof, T.C., and Brose, N. (1999b). Munc13-1 is essential for fusion competence of glutamatergic synaptic vesicles. Nature 400, 457–461.

Azevedo, F.A.C., Carvalho, L.R.B., Grinberg, L.T., Farfel, J.M., Ferretti, R.E.L., Leite, R.E.P., Jacob Filho, W., Lent, R., and Herculano-Houzel, S. (2009). Equal numbers of neuronal and nonneuronal cells make the human brain an isometrically scaled-up primate brain. J Comp Neurol 513, 532–541.

Basu, J., Betz, A., Brose, N., and Rosenmund, C. (2007). Munc13-1 C1 domain activation lowers the energy barrier for synaptic vesicle fusion. J Neurosci 27, 1200–1210.

Bazigou, E., Lyons, O.T.A., Smith, A., Venn, G.E., Cope, C., Brown, N.A., and Makinen, T. (2011). Genes regulating lymphangiogenesis control venous valve formation and maintenance in mice. J Clin Invest 121, 2984–2992.

Bird, C.M., and Burgess, N. (2008). The hippocampus and memory: insights from spatial processing. Nat Rev Neurosci 9, 182–194.

Bischofberger, J., Engel, D., Frotscher, M., and Jonas, P. (2006a). Timing and efficacy of transmitter release at mossy fiber synapses in the hippocampal network. Pflugers Arch 453, 361–372.

Bischofberger, J., Engel, D., Li, L., Geiger, J.R.P., and Jonas, P. (2006b). Patch-clamp recording from mossy fiber terminals in hippocampal slices. Nat Protoc 1, 2075–2081.

Blanton, M.G., Lo Turco, J.J., and Kriegstein, A.R. (1989). Whole cell recording from neurons in slices of reptilian and mammalian cerebral cortex. J Neurosci Methods 30, 203–210.

Bliss, T.V., and Gardner-Medwin, A.R. (1973). Long-lasting potentiation of synaptic transmission in the dentate area of the unanaestetized rabbit following stimulation of the perforant path. J Physiol 232, 357–374.

Borges-Merjane, C., Kim, O., and Jonas, P. (2020). Functional Electron Microscopy, “Flash and Freeze,” of Identified Cortical Synapses in Acute Brain Slices. Neuron 105, 992-1006.e6.

Borst, J.G., and Sakmann, B. (1996). Calcium influx and transmitter release in a fast CNS synapse. Nature 383, 431–434.

Bourinet, E., Zamponi, G.W., Stea, A., Soong, T.W., Lewis, B.A., Jones, L.P., Yue, D.T., and Snutch, T.P. (1996). The alpha 1E calcium channel exhibits permeation properties similar to low-voltage-activated calcium channels. J Neurosci 16, 4983–4993.

Breustedt, J., Vogt, K.E., Miller, R.J., Nicoll, R.A., and Schmitz, D. (2003). Alpha1E-containing Ca2+ channels are involved in synaptic plasticity. Proc Natl Acad Sci U S A 100, 12450–12455.

Breustedt, J., Gundlfinger, A., Varoqueaux, F., Reim, K., Brose, N., and Schmitz, D. (2010). Munc13-2 differentially affects hippocampal synaptic transmission and plasticity. Cereb Cortex 20, 1109–1120.

Brose, N., Hofmann, K., Hata, Y., and Südhof, T.C. (1995). Mammalian Homologues of Caenorhabditis elegans unc-13 Gene Define Novel Family of C2-domain Proteins (∗). Journal of Biological Chemistry 270, 25273–25280.

Bucurenciu, I., Kulik, A., Schwaller, B., Frotscher, M., and Jonas, P. (2008). Nanodomain coupling between Ca2+ channels and Ca2+ sensors promotes fast and efficient transmitter release at a cortical GABAergic synapse. Neuron 57, 536–545.

Camacho, M., Quade, B., Trimbuch, T., Xu, J., Sari, L., Rizo, J., and Rosenmund, C. (2021). Control of neurotransmitter release by two distinct membrane-binding faces of the Munc13-1 C1C2B region. ELife 10, e72030.

Castellucci, V.F., Blumenfeld, H., Goelet, P., and Kandel, E.R. (1989). Inhibitor of protein synthesis blocks long-term behavioral sensitization in the isolated gill-withdrawal reflex of Aplysia. J Neurobiol 20, 1–9.

Castillo, P.E., Weisskopf, M.G., and Nicoll, R.A. (1994). The role of Ca2+ channels in hippocampal mossy fiber synaptic transmission and long-term potentiation. Neuron 12, 261–269.

Castillo, P.E., Janz, R., Südhof, T.C., Tzounopoulos, T., Malenka, R.C., and Nicoll, R.A. (1997). Rab3A is essential for mossy fibre long-term potentiation in the hippocampus. Nature 388, 590–593.

Castillo, P.E., Schoch, S., Schmitz, F., Südhof, T.C., and Malenka, R.C. (2002). RIM1alpha is required for presynaptic long-term potentiation. Nature 415, 327–330.

Chanaday, N.L., and Kavalali, E.T. (2018). Optical detection of three modes of endocytosis at hippocampal synapses. Elife 7, e36097.

Chanaday, N.L., Cousin, M.A., Milosevic, I., Watanabe, S., and Morgan, J.R. (2019). The Synaptic Vesicle Cycle Revisited: New Insights into the Modes and Mechanisms. J Neurosci 39, 8209–8216.

Chen, Z., Das, B., Nakamura, Y., DiGregorio, D.A., and Young, S.M. (2015). Ca2+ channel to synaptic vesicle distance accounts for the readily releasable pool kinetics at a functionally mature auditory synapse. J Neurosci 35, 2083–2100.

Chiang, H.-C., Shin, W., Zhao, W.-D., Hamid, E., Sheng, J., Baydyuk, M., Wen, P.J., Jin, A., Momboisse, F., and Wu, L.-G. (2014). Post-fusion structural changes and their roles in exocytosis and endocytosis of dense-core vesicles. Nat Commun 5, 3356.

Chiaradia, I., and Lancaster, M.A. (2020). Brain organoids for the study of human neurobiology at the interface of in vitro and in vivo. Nat Neurosci 23, 1496–1508.

Chicurel, M.E., and Harris, K.M. (1992). Three-dimensional analysis of the structure and composition of CA3 branched dendritic spines and their synaptic relationships with mossy fiber boutons in the rat hippocampus. J Comp Neurol 325, 169–182.

Claiborne, B.J., Amaral, D.G., and Cowan, W.M. (1986). A light and electron microscopic analysis of the mossy fibers of the rat dentate gyrus. J Comp Neurol 246, 435–458.

Colecraft, H.M., Patil, P.G., and Yue, D.T. (2000). Differential occurrence of reluctant openings in G-protein-inhibited N- and P/Q-type calcium channels. J Gen Physiol 115, 175–192.

Couteaux, R., and Pécot-Dechavassine, M. (1970). [Synaptic vesicles and pouches at the level of “active zones” of the neuromuscular junction]. C R Acad Hebd Seances Acad Sci D 271, 2346–2349.

Crow, T., and Forrester, J. (1990). Inhibition of protein synthesis blocks long-term enhancement of generator potentials produced by one-trial in vivo conditioning in Hermissenda. Proc Natl Acad Sci U S A 87, 4490–4494.

Davis, G.W. (2013). Homeostatic Signaling and the Stabilization of Neural Function. Neuron 80, 718–728.

Davis, G.W., and Müller, M. (2015). Homeostatic control of presynaptic neurotransmitter release. Annu Rev Physiol 77, 251–270.

Davis, H.P., and Squire, L.R. (1984). Protein synthesis and memory: a review. Psychol Bull 96, 518–559.

Deadwyler, S.A., Bunn, T., and Hampson, R.E. (1996). Hippocampal ensemble activity during spatial delayed-nonmatch-to-sample performance in rats. J Neurosci 16, 354–372.

Debanne, D. (2004). Information processing in the axon. Nat Rev Neurosci 5, 304–316.

Del Castillo, J., and Katz, B. (1954). The membrane change produced by the neuromuscular transmitter. J Physiol 125, 546–565.

Delvendahl, I., Vyleta, N.P., von Gersdorff, H., and Hallermann, S. (2016). Fast, Temperature-Sensitive and Clathrin-Independent Endocytosis at Central Synapses. Neuron 90, 492–498.

Deng, L., Kaeser, P.S., Xu, W., and Südhof, T.C. (2011). RIM Proteins Activate Vesicle Priming by Reversing Autoinhibitory Homodimerization of Munc13. Neuron 69, 317–331.

Diamond, A. (1990). The development and neural bases of higher cognitive functions. Introduction. Ann N Y Acad Sci 608, xiii–lvi.

Dietrich, D., Kirschstein, T., Kukley, M., Pereverzev, A., von der Brelie, C., Schneider, T., and Beck, H. (2003). Functional specialization of presynaptic Cav2.3 Ca2+ channels. Neuron 39, 483–496.

DiGregorio, D.A., Nusser, Z., and Silver, R.A. (2002). Spillover of glutamate onto synaptic AMPA receptors enhances fast transmission at a cerebellar synapse. Neuron 35, 521–533.

Dreyer, F., Peper, K., Akert, K., Sandri, C., and Moor, H. (1973). Ultrastructure of the “active zone” in the frog neuromuscular junction. Brain Res 62, 373–380.

Dulubova, I., Lou, X., Lu, J., Huryeva, I., Alam, A., Schneggenburger, R., Südhof, T.C., and Rizo, J. (2005). A Munc13/RIM/Rab3 tripartite complex: from priming to plasticity? EMBO J 24, 2839–2850.

Edwards, F.A., Konnerth, A., Sakmann, B., and Takahashi, T. (1989). A thin slice preparation for patch clamp recordings from neurones of the mammalian central nervous system. Pflugers Arch 414, 600–612.

Efron, B., and Tibshirani, R.J. (1994). An Introduction to the Bootstrap (CRC Press).

Eggermann, E., Bucurenciu, I., Goswami, S.P., and Jonas, P. (2011). Nanodomain coupling between Ca^{2+} channels and sensors of exocytosis at fast mammalian synapses. Nat Rev Neurosci 13, 7–21.

Espinoza, C., Guzman, S.J., Zhang, X., and Jonas, P. (2018). Parvalbumin+ interneurons obey unique connectivity rules and establish a powerful lateral-inhibition microcircuit in dentate gyrus. Nat Commun 9, 4605.

Ester, M., Kriegel, H.-P., Sander, J., and Xu, X. (1996). A density-based algorithm for discovering clusters in large spatial databases with noise. In Proceedings of the Second International Conference on Knowledge Discovery and Data Mining, (Portland, Oregon: AAAI Press), pp. 226–231.

Frotscher, M., Seress, L., Schwerdtfeger, W.K., and Buhl, E. (1991). The mossy cells of the fascia dentata: a comparative study of their fine structure and synaptic connections in rodents and primates. J Comp Neurol 312, 145–163.

Frotscher, M., Soriano, E., and Misgeld, U. (1994). Divergence of hippocampal mossy fibers. Synapse 16, 148–160.

Frotscher, M., Jonas, P., and Sloviter, R.S. (2006). Synapses formed by normal and abnormal hippocampal mossy fibers. Cell Tissue Res 326, 361–367.

Fukaya, R., Maglione, M., Sigrist, S.J., and Sakaba, T. (2021). Rapid Ca^{2+} channel accumulation contributes to cAMP-mediated increase in transmission at hippocampal mossy fiber synapses. Proc Natl Acad Sci U S A 118, e2016754118.

Galimberti, I., Gogolla, N., Alberi, S., Santos, A.F., Muller, D., and Caroni, P. (2006). Long-term rearrangements of hippocampal mossy fiber terminal connectivity in the adult regulated by experience. Neuron 50, 749–763.

Geiger, J.R., and Jonas, P. (2000). Dynamic control of presynaptic $Ca^{(2+)}$ inflow by fast-inactivating $K^{(+)}$ channels in hippocampal mossy fiber boutons. Neuron 28, 927–939.

Gitler, D., Cheng, Q., Greengard, P., and Augustine, G.J. (2008). Synapsin IIa controls the reserve pool of glutamatergic synaptic vesicles. J Neurosci 28, 10835–10843.

Goldammer, H., Hollergschwandtner, E., Elisabeth, N.H., Frade, P.R., and Reipert, S. (2016). Automatized Freeze Substitution of Algae Accelerated by a Novel Agitation Module. Protist 167, 369–376.

Griffith, W.H. (1990). Voltage-clamp analysis of posttetanic potentiation of the mossy fiber to CA3 synapse in hippocampus. J Neurophysiol 63, 491–501.

Guy, Y., Rupert, A.E., Sandberg, M., and Weber, S.G. (2011). A simple method for measuring organotypic tissue slice culture thickness. J Neurosci Methods 199, 78–81.

Guzman, S.J., Schlögl, A., Frotscher, M., and Jonas, P. (2016). Synaptic mechanisms of pattern completion in the hippocampal CA3 network. Science 353, 1117–1123.

Guzman, S.J., Schlögl, A., Espinoza, C., Zhang, X., Suter, B.A., and Jonas, P. (2021). How connectivity rules and synaptic properties shape the efficacy of pattern separation in the entorhinal cortex–dentate gyrus–CA3 network. Nat Comput Sci 1, 830–842.

Habets, R.L.P., and Borst, J.G.G. (2005). Post-tetanic potentiation in the rat calyx of Held synapse. J Physiol 564, 173–187.

Hagiwara, A., Fukazawa, Y., Deguchi-Tawarada, M., Ohtsuka, T., and Shigemoto, R. (2005). Differential distribution of release-related proteins in the hippocampal CA3 area as revealed by freeze-fracture replica labeling. J Comp Neurol 489, 195–216.

Hallermann, S., Pawlu, C., Jonas, P., and Heckmann, M. (2003). A large pool of releasable vesicles in a cortical glutamatergic synapse. Proc Natl Acad Sci U S A 100, 8975–8980.

Han, Y., Kaeser, P.S., Südhof, T.C., and Schneggenburger, R. (2011). RIM Determines Ca2+ Channel Density and Vesicle Docking at the Presynaptic Active Zone. Neuron 69, 304–316.

Hanson, P.I., Roth, R., Morisaki, H., Jahn, R., and Heuser, J.E. (1997). Structure and conformational changes in NSF and its membrane receptor complexes visualized by quick-freeze/deep-etch electron microscopy. Cell 90, 523–535.

Harris, E.W., and Cotman, C.W. (1986). Long-term potentiation of guinea pig mossy fiber responses is not blocked by N-methyl D-aspartate antagonists. Neurosci Lett 70, 132–137.

Harris, K.M., and Stevens, J.K. (1989). Dendritic spines of CA 1 pyramidal cells in the rat hippocampus: serial electron microscopy with reference to their biophysical characteristics. J Neurosci 9, 2982–2997.

Harris, K.M., and Weinberg, R.J. (2012). Ultrastructure of Synapses in the Mammalian Brain. Cold Spring Harb Perspect Biol 4, a005587.

Henze, D.A., Wittner, L., and Buzsáki, G. (2002). Single granule cells reliably discharge targets in the hippocampal CA3 network in vivo. Nat Neurosci 5, 790–795.

Heuser, J.E., and Reese, T.S. (1981). Structural changes after transmitter release at the frog neuromuscular junction. J Cell Biol 88, 564–580.

Heuser, J.E., Reese, T.S., Dennis, M.J., Jan, Y., Jan, L., and Evans, L. (1979). Synaptic vesicle exocytosis captured by quick freezing and correlated with quantal transmitter release. J Cell Biol 81, 275–300.

Hilton, B.J., Husch, A., Schaffran, B., Lin, T.-C., Burnside, E.R., Dupraz, S., Schelski, M., Kim, J., Müller, J.A., Schoch, S., et al. (2022). An active vesicle priming machinery suppresses axon regeneration upon adult CNS injury. Neuron 110, 51-69.e7.

Huang, Y.Y., and Kandel, E.R. (1996). Modulation of both the early and the late phase of mossy fiber LTP by the activation of beta-adrenergic receptors. Neuron 16, 611–617.

Huang, Y.Y., Li, X.C., and Kandel, E.R. (1994). cAMP contributes to mossy fiber LTP by initiating both a covalently mediated early phase and macromolecular synthesis-dependent late phase. Cell 79, 69–79.

Imig, C., Min, S.-W., Krinner, S., Arancillo, M., Rosenmund, C., Südhof, T.C., Rhee, J., Brose, N., and Cooper, B.H. (2014). The morphological and molecular nature of synaptic vesicle priming at presynaptic active zones. Neuron 84, 416–431.

Imig, C., López-Murcia, F.J., Maus, L., García-Plaza, I.H., Mortensen, L.S., Schwark, M., Schwarze, V., Angibaud, J., Nägerl, U.V., Taschenberger, H., et al. (2020).

Ultrastructural Imaging of Activity-Dependent Synaptic Membrane-Trafficking Events in Cultured Brain Slices. Neuron 108, 843-860.e8.

Jonas, P., Major, G., and Sakmann, B. (1993). Quantal components of unitary EPSCs at the mossy fibre synapse on CA3 pyramidal cells of rat hippocampus. J Physiol 472, 615–663.

Junge, H.J., Rhee, J.-S., Jahn, O., Varoqueaux, F., Spiess, J., Waxham, M.N., Rosenmund, C., and Brose, N. (2004). Calmodulin and Munc13 form a Ca2+ sensor/effector complex that controls short-term synaptic plasticity. Cell 118, 389–401.

Kaeser, P.S., and Regehr, W.G. (2017). The readily releasable pool of synaptic vesicles. Curr Opin Neurobiol 43, 63–70.

Kaeser, P.S., Kwon, H.-B., Chiu, C.Q., Deng, L., Castillo, P.E., and Südhof, T.C. (2008). RIM1alpha and RIM1beta are synthesized from distinct promoters of the RIM1 gene to mediate differential but overlapping synaptic functions. J Neurosci 28, 13435–13447.

Kaeser, P.S., Deng, L., Wang, Y., Dulubova, I., Liu, X., Rizo, J., and Südhof, T.C. (2011). RIM proteins tether Ca2+ channels to presynaptic active zones via a direct PDZ-domain interaction. Cell 144, 282–295.

Kaeser, P.S., Deng, L., Fan, M., and Südhof, T.C. (2012). RIM genes differentially contribute to organizing presynaptic release sites. Proc Natl Acad Sci U S A 109, 11830–11835.

Karlocai, M.R., Heredi, J., Benedek, T., Holderith, N., Lorincz, A., and Nusser, Z. (2021). Variability in the Munc13-1 content of excitatory release sites. Elife 10, e67468.

Kawabe, H., Mitkovski, M., Kaeser, P.S., Hirrlinger, J., Opazo, F., Nestvogel, D., Kalla, S., Fejtova, A., Verrier, S.E., Bungers, S.R., et al. (2017). ELKS1 localizes the synaptic vesicle priming protein bMunc13-2 to a specific subset of active zones. J Cell Biol 216, 1143–1161.

Keller, D., Babai, N., Kochubey, O., Han, Y., Markram, H., Schürmann, F., and Schneggenburger, R. (2015). An Exclusion Zone for Ca2+ Channels around Docked Vesicles Explains Release Control by Multiple Channels at a CNS Synapse. PLoS Comput Biol 11, e1004253.

Kerr, A.M., Reisinger, E., and Jonas, P. (2008). Differential dependence of phasic transmitter release on synaptotagmin 1 at GABAergic and glutamatergic hippocampal synapses. Proc Natl Acad Sci U S A 105, 15581–15586.

Kobbersmed, J.R., Grasskamp, A.T., Jusyte, M., Böhme, M.A., Ditlevsen, S., Sørensen, J.B., and Walter, A.M. (2020). Rapid regulation of vesicle priming explains synaptic facilitation despite heterogeneous vesicle:Ca2+ channel distances. Elife 9, e51032.

Koch, H., Hofmann, K., and Brose, N. (2000). Definition of Munc13-homology-domains and characterization of a novel ubiquitously expressed Munc13 isoform. Biochem J 349, 247–253.

Korogod, N., Petersen, C.C.H., and Knott, G.W. (2015). Ultrastructural analysis of adult mouse neocortex comparing aldehyde perfusion with cryo fixation. Elife 4.

Kubota, Y., Sohn, J., and Kawaguchi, Y. (2018). Large Volume Electron Microscopy and Neural Microcircuit Analysis. Frontiers in Neural Circuits 12.

Langdon, R.B., Johnson, J.W., and Barrionuevo, G. (1995). Posttetanic potentiation and presynaptically induced long-term potentiation at the mossy fiber synapse in rat hippocampus. J Neurobiol 26, 370–385.

Lavado, A., Lagutin, O.V., Chow, L.M.L., Baker, S.J., and Oliver, G. (2010). Prox1 Is Required for Granule Cell Maturation and Intermediate Progenitor Maintenance During Brain Neurogenesis. PLOS Biology 8, e1000460.

Lawrence, J.J., Grinspan, Z.M., and McBain, C.J. (2004). Quantal transmission at mossy fibre targets in the CA3 region of the rat hippocampus. The Journal of Physiology 554, 175–193.

Lei, S., Pelkey, K.A., Topolnik, L., Congar, P., Lacaille, J.-C., and McBain, C.J. (2003). Depolarization-induced long-term depression at hippocampal mossy fiber-CA3 pyramidal neuron synapses. J Neurosci 23, 9786–9795.

Leutgeb, S., and Leutgeb, J.K. (2007). Pattern separation, pattern completion, and new neuronal codes within a continuous CA3 map. Learn Mem 14, 745–757.

Li, S., and Sheng, Z.-H. (2022). Energy matters: presynaptic metabolism and the maintenance of synaptic transmission. Nat Rev Neurosci 23, 4–22.

Li, L., Bischofberger, J., and Jonas, P. (2007). Differential gating and recruitment of P/Q-, N-, and R-type Ca2+ channels in hippocampal mossy fiber boutons. J Neurosci 27, 13420–13429.

Lin, C.-M., Li, C.-S., Sheng, Y.-J., Wu, D.T., and Tsao, H.-K. (2012). Size-dependent properties of small unilamellar vesicles formed by model lipids. Langmuir 28, 689–700.

Lipstein, N., Chang, S., Lin, K.-H., López-Murcia, F.J., Neher, E., Taschenberger, H., and Brose, N. (2021). Munc13-1 is a Ca2+-phospholipid-dependent vesicle priming hub that shapes synaptic short-term plasticity and enables sustained neurotransmission. Neuron 109, 3980-4000.e7.

Lisman, J.E., Raghavachari, S., and Tsien, R.W. (2007). The sequence of events that underlie quantal transmission at central glutamatergic synapses. Nat Rev Neurosci 8, 597–609.

Liu, X., Seven, A.B., Camacho, M., Esser, V., Xu, J., Trimbuch, T., Quade, B., Su, L., Ma, C., Rosenmund, C., et al. (2016). Functional synergy between the Munc13 C-terminal C1 and C2 domains. Elife 5, e13696.

López-García, J.C., Arancio, O., Kandel, E.R., and Baranes, D. (1996). A presynaptic locus for long-term potentiation of elementary synaptic transmission at mossy fiber synapses in culture. PNAS 93, 4712–4717.

Lüscher, C., and Malenka, R.C. (2012). NMDA receptor-dependent long-term potentiation and long-term depression (LTP/LTD). Cold Spring Harb Perspect Biol 4, a005710.

Ma, C., Li, W., Xu, Y., and Rizo, J. (2011). Munc13 mediates the transition from the closed syntaxin-Munc18 complex to the SNARE complex. Nat Struct Mol Biol 18, 542–549.

Ma, C., Su, L., Seven, A.B., Xu, Y., and Rizo, J. (2013). Reconstitution of the vital functions of Munc18 and Munc13 in neurotransmitter release. Science 339, 421–425.

Ma, L., Rebane, A.A., Yang, G., Xi, Z., Kang, Y., Gao, Y., and Zhang, Y. (2015). Munc18-1-regulated stage-wise SNARE assembly underlying synaptic exocytosis. Elife 4, e09580.

Magdziarek, M., Bolembach, A.A., Stepien, K.P., Quade, B., Liu, X., and Rizo, J. (2020). Re-examining how Munc13-1 facilitates opening of syntaxin-1. Protein Science 29, 1440–1458.

Magee, J.C., and Johnston, D. (2005). Plasticity of dendritic function. Curr Opin Neurobiol 15, 334–342.

Mark, M.D., Maejima, T., Kuckelsberg, D., Yoo, J.W., Hyde, R.A., Shah, V., Gutierrez, D., Moreno, R.L., Kruse, W., Noebels, J.L., et al. (2011). Delayed Postnatal Loss of P/Q-Type Calcium Channels Recapitulates the Absence Epilepsy, Dyskinesia, and Ataxia Phenotypes of Genomic Cacna1A Mutations. J Neurosci 31, 4311–4326.

Martens, S., Kozlov, M.M., and McMahon, H.T. (2007). How Synaptotagmin Promotes Membrane Fusion. Science 316, 1205–1208.

Maruyama, I.N., and Brenner, S. (1991). A phorbol ester/diacylglycerol-binding protein encoded by the unc-13 gene of Caenorhabditis elegans. Proc Natl Acad Sci U S A 88, 5729–5733.

Maus, L., Lee, C., Altas, B., Sertel, S.M., Weyand, K., Rizzoli, S.O., Rhee, J., Brose, N., Imig, C., and Cooper, B.H. (2020). Ultrastructural Correlates of Presynaptic Functional Heterogeneity in Hippocampal Synapses. Cell Rep 30, 3632-3643.e8.

Meier, C., and Beckmann, A. (2018). Freeze fracture: new avenues for the ultrastructural analysis of cells in vitro. Histochem Cell Biol 149, 3–13.

Midorikawa, M., and Sakaba, T. (2017). Kinetics of Releasable Synaptic Vesicles and Their Plastic Changes at Hippocampal Mossy Fiber Synapses. Neuron 96, 1033-1040.e3.

Miki, T., Nakamura, Y., Malagon, G., Neher, E., and Marty, A. (2018). Two-component latency distributions indicate two-step vesicular release at simple glutamatergic synapses. Nat Commun 9, 3943.

Milner, B., Squire, L.R., and Kandel, E.R. (1998). Cognitive neuroscience and the study of memory. Neuron 20, 445–468.

Ming, G., and Song, H. (2011). Adult Neurogenesis in the Mammalian Brain: Significant Answers and Significant Questions. Neuron 70, 687–702.

Mittelstaedt, T., and Schoch, S. (2007). Structure and evolution of RIM-BP genes: identification of a novel family member. Gene 403, 70–79.

Murthy, V.N., and Stevens, C.F. (1999). Reversal of synaptic vesicle docking at central synapses. Nat Neurosci 2, 503–507.

Nakamura, Y., Harada, H., Kamasawa, N., Matsui, K., Rothman, J.S., Shigemoto, R., Silver, R.A., DiGregorio, D.A., and Takahashi, T. (2015). Nanoscale distribution of

presynaptic Ca(2+) channels and its impact on vesicular release during development. Neuron 85, 145–158.

Neher, E. (2017). Some Subtle Lessons from the Calyx of Held Synapse. Biophysical Journal 112, 215–223.

Neher, E., and Brose, N. (2018). Dynamically Primed Synaptic Vesicle States: Key to Understand Synaptic Short-Term Plasticity. Neuron 100, 1283–1291.

Nicoll, R.A., and Malenka, R.C. (1995). Contrasting properties of two forms of long-term potentiation in the hippocampus. Nature 377, 115–118.

Nicoll, R.A., and Malenka, R.C. (1999). Expression mechanisms underlying NMDA receptor-dependent long-term potentiation. Ann N Y Acad Sci 868, 515–525.

Nicoll, R.A., and Schmitz, D. (2005). Synaptic plasticity at hippocampal mossy fibre synapses. Nat Rev Neurosci 6, 863–876.

O'Keefe, J. (1990). A computational theory of the hippocampal cognitive map. Prog Brain Res 83, 301–312.

Padmanarayana, M., Liu, H., Michelassi, F., Li, L., Betensky, D., Dominguez, M.J., Sutton, R.B., Hu, Z., and Dittman, J.S. (2021). A unique C2 domain at the C terminus of Munc13 promotes synaptic vesicle priming. Proc Natl Acad Sci U S A 118, e2016276118.

Palay, S.L. (1956). SYNAPSES IN THE CENTRAL NERVOUS SYSTEM. J Biophys Biochem Cytol 2, 193–202.

Patzke, C., Brockmann, M.M., Dai, J., Gan, K.J., Grauel, M.K., Fenske, P., Liu, Y., Acuna, C., Rosenmund, C., and Südhof, T.C. (2019). Neuromodulator Signaling Bidirectionally Controls Vesicle Numbers in Human Synapses. Cell 179, 498-513.e22.

Pelkey, K.A., Topolnik, L., Lacaille, J.-C., and McBain, C.J. (2006). Compartmentalized Ca(2+) channel regulation at divergent mossy-fiber release sites underlies target cell-dependent plasticity. Neuron 52, 497–510.

Pernía-Andrade, A.J., and Jonas, P. (2014). Theta-gamma-modulated synaptic currents in hippocampal granule cells in vivo define a mechanism for network oscillations. Neuron 81, 140–152.

Poirier, M.A., Xiao, W., Macosko, J.C., Chan, C., Shin, Y.K., and Bennett, M.K. (1998). The synaptic SNARE complex is a parallel four-stranded helical bundle. Nat Struct Biol 5, 765–769.

Quade, B., Camacho, M., Zhao, X., Orlando, M., Trimbuch, T., Xu, J., Li, W., Nicastro, D., Rosenmund, C., and Rizo, J. (2019). Membrane bridging by Munc13-1 is crucial for neurotransmitter release. Elife 8, e42806.

Ramon y Cajal, S. (1894). The Croonian lecture.—La fine structure des centres nerveux. Proceedings of the Royal Society of London 55, 444–468.

Ramon y Cajal, S., and Azoulay, L. (1955). Histologie du systeme nerveux de l'homme et des vertebres. Histologie du systeme nerveux de l'homme et des vertebres 2v–2v.

Rebola, N., Reva, M., Kirizs, T., Szoboszlay, M., Lőrincz, A., Moneron, G., Nusser, Z., and DiGregorio, D.A. (2019). Distinct Nanoscale Calcium Channel and Synaptic

Vesicle Topographies Contribute to the Diversity of Synaptic Function. Neuron 104, 693-710.e9.

Reid, C.A., Dixon, D.B., Takahashi, M., Bliss, T.V.P., and Fine, A. (2004). Optical Quantal Analysis Indicates That Long-Term Potentiation at Single Hippocampal Mossy Fiber Synapses Is Expressed through Increased Release Probability, Recruitment of New Release Sites, and Activation of Silent Synapses. J. Neurosci. 24, 3618–3626.

Rhee, J.S., Betz, A., Pyott, S., Reim, K., Varoqueaux, F., Augustin, I., Hesse, D., Südhof, T.C., Takahashi, M., Rosenmund, C., et al. (2002). Beta phorbol ester- and diacylglycerol-induced augmentation of transmitter release is mediated by Munc13s and not by PKCs. Cell 108, 121–133.

Rizzoli, S.O., and Betz, W.J. (2005). Synaptic vesicle pools. Nat Rev Neurosci 6, 57–69.

Rizzuto, R., Bernardi, P., and Pozzan, T. (2000). Mitochondria as all-round players of the calcium game. J Physiol 529 Pt 1, 37–47.

Rollenhagen, A., and Lübke, J.H.R. (2006). The morphology of excitatory central synapses: from structure to function. Cell Tissue Res 326, 221–237.

Rollenhagen, A., and Lübke, J.H.R. (2010). The mossy fiber bouton: the “common” or the “unique” synapse? Front Synaptic Neurosci 2, 2.

Rollenhagen, A., Sätzler, K., Rodríguez, E.P., Jonas, P., Frotscher, M., and Lübke, J.H.R. (2007). Structural determinants of transmission at large hippocampal mossy fiber synapses. J Neurosci 27, 10434–10444.

Rolls, E.T., and Treves, A. (1994). Neural networks in the brain involved in memory and recall. Prog Brain Res 102, 335–341.

Rosenmund, C., and Stevens, C.F. (1996). Definition of the readily releasable pool of vesicles at hippocampal synapses. Neuron 16, 1197–1207.

Rosenmund, C., Sigler, A., Augustin, I., Reim, K., Brose, N., and Rhee, J.S. (2002). Differential control of vesicle priming and short-term plasticity by Munc13 isoforms. Neuron 33, 411–424.

Sabatini, B.L., and Regehr, W.G. (1996). Timing of neurotransmission at fast synapses in the mammalian brain. Nature 384, 170–172.

Saegusa, H., Kurihara, T., Zong, S., Minowa, O., Kazuno, A., Han, W., Matsuda, Y., Yamanaka, H., Osanai, M., Noda, T., et al. (2000). Altered pain responses in mice lacking alpha 1E subunit of the voltage-dependent Ca2+ channel. Proc Natl Acad Sci U S A 97, 6132–6137.

Salin, P.A., Scanziani, M., Malenka, R.C., and Nicoll, R.A. (1996). Distinct short-term plasticity at two excitatory synapses in the hippocampus. Proc Natl Acad Sci U S A 93, 13304–13309.

Sätzler, K., Söhl, L.F., Bollmann, J.H., Borst, J.G.G., Frotscher, M., Sakmann, B., and Lübke, J.H.R. (2002). Three-dimensional reconstruction of a calyx of Held and its postsynaptic principal neuron in the medial nucleus of the trapezoid body. J Neurosci 22, 10567–10579.

Schikorski, T., and Stevens, C.F. (1997). Quantitative Ultrastructural Analysis of Hippocampal Excitatory Synapses. J. Neurosci. 17, 5858–5867.

Schikorski, T., and Stevens, C.F. (2001). Morphological correlates of functionally defined synaptic vesicle populations. Nat Neurosci 4, 391–395.

Schneggenburger, R., Meyer, A.C., and Neher, E. (1999). Released fraction and total size of a pool of immediately available transmitter quanta at a calyx synapse. Neuron 23, 399–409.

Scoville, W.B., and Milner, B. (1957). Loss of recent memory after bilateral hippocampal lesions. J Neurol Neurosurg Psychiatry 20, 11–21.

Seino, S., and Shibasaki, T. (2005). PKA-dependent and PKA-independent pathways for cAMP-regulated exocytosis. Physiol Rev 85, 1303–1342.

Sheng, M., and Kim, E. (2011). The postsynaptic organization of synapses. Cold Spring Harb Perspect Biol 3, a005678.

Shigemoto, R., and Joesch, M. (2017). The genetic encoded toolbox for electron microscopy and connectomics. Wiley Interdiscip Rev Dev Biol 6.

Shin, O.-H., Lu, J., Rhee, J.-S., Tomchick, D.R., Pang, Z.P., Wojcik, S.M., Camacho-Perez, M., Brose, N., Machius, M., Rizo, J., et al. (2010). Munc13 C2B domain is an activity-dependent Ca2+ regulator of synaptic exocytosis. Nat Struct Mol Biol 17, 280–288.

Shu, T., Jin, H., Rothman, J.E., and Zhang, Y. (2020). Munc13-1 MUN domain and Munc18-1 cooperatively chaperone SNARE assembly through a tetrameric complex. PNAS 117, 1036–1041.

Shu, Y., Duque, A., Yu, Y., Haider, B., and McCormick, D.A. (2007). Properties of action-potential initiation in neocortical pyramidal cells: evidence from whole cell axon recordings. J Neurophysiol 97, 746–760.

Small, S.A., Schobel, S.A., Buxton, R.B., Witter, M.P., and Barnes, C.A. (2011). A pathophysiological framework of hippocampal dysfunction in ageing and disease. Nat Rev Neurosci 12, 585–601.

Söllner, T., Whiteheart, S.W., Brunner, M., Erdjument-Bromage, H., Geromanos, S., Tempst, P., and Rothman, J.E. (1993). SNAP receptors implicated in vesicle targeting and fusion. Nature 362, 318–324.

Spruston, N. (2008). Pyramidal neurons: dendritic structure and synaptic integration. Nat Rev Neurosci 9, 206–221.

Squire, L.R., and Zola-Morgan, S. (1991). The medial temporal lobe memory system. Science 253, 1380–1386.

Stoppini, L., Buchs, P.A., and Muller, D. (1991). A simple method for organotypic cultures of nervous tissue. J Neurosci Methods 37, 173–182.

Studer, D., Zhao, S., Chai, X., Jonas, P., Graber, W., Nestel, S., and Frotscher, M. (2014). Capture of activity-induced ultrastructural changes at synapses by high-pressure freezing of brain tissue. Nat Protoc 9, 1480–1495.

Südhof, T.C. (2012). The presynaptic active zone. Neuron 75, 11–25.

Südhof, T.C. (2013a). A molecular machine for neurotransmitter release: synaptotagmin and beyond. Nat Med 19, 1227–1231.

Südhof, T.C. (2013b). Neurotransmitter release: the last millisecond in the life of a synaptic vesicle. Neuron 80, 675–690.

Südhof, T.C., and Rothman, J.E. (2009). Membrane fusion: grappling with SNARE and SM proteins. Science 323, 474–477.

Sutton, R.B., Fasshauer, D., Jahn, R., and Brunger, A.T. (1998). Crystal structure of a SNARE complex involved in synaptic exocytosis at 2.4 Å resolution. Nature 395, 347–353.

Tan, C., Wang, S.S.H., de Nola, G., and Kaeser, P.S. (2022). Rebuilding essential active zone functions within a synapse. Neuron S0896-6273(22)00083-6.

Tong, G., Malenka, R.C., and Nicoll, R.A. (1996). Long-term potentiation in cultures of single hippocampal granule cells: a presynaptic form of plasticity. Neuron 16, 1147–1157.

Tóth, K., and McBain, C.J. (2000). Target-specific expression of pre- and postsynaptic mechanisms. J Physiol 525 Pt 1, 41–51.

Toth, K., Suares, G., Lawrence, J.J., Philips-Tansey, E., and McBain, C.J. (2000). Differential Mechanisms of Transmission at Three Types of Mossy Fiber Synapse. J. Neurosci. 20, 8279–8289.

Tucker, W.C., Weber, T., and Chapman, E.R. (2004). Reconstitution of Ca2+-Regulated Membrane Fusion by Synaptotagmin and SNAREs. Science 304, 435–438.

Tully, T., Preat, T., Boynton, S.C., and Del Vecchio, M. (1994). Genetic dissection of consolidated memory in Drosophila. Cell 79, 35–47.

Vandael, D., Borges-Merjane, C., Zhang, X., and Jonas, P. (2020). Short-Term Plasticity at Hippocampal Mossy Fiber Synapses Is Induced by Natural Activity Patterns and Associated with Vesicle Pool Engram Formation. Neuron 107, 509-521.e7.

Vandael, D., Okamoto, Y., and Jonas, P. (2021). Transsynaptic modulation of presynaptic short-term plasticity in hippocampal mossy fiber synapses. Nat Commun 12, 2912.

Varoqueaux, F., Sigler, A., Rhee, J.-S., Brose, N., Enk, C., Reim, K., and Rosenmund, C. (2002). Total arrest of spontaneous and evoked synaptic transmission but normal synaptogenesis in the absence of Munc13-mediated vesicle priming. Proc Natl Acad Sci U S A 99, 9037–9042.

Varoqueaux, F., Sons, M.S., Plomp, J.J., and Brose, N. (2005). Aberrant morphology and residual transmitter release at the Munc13-deficient mouse neuromuscular synapse. Mol Cell Biol 25, 5973–5984.

Verstreken, P., Ly, C.V., Venken, K.J.T., Koh, T.-W., Zhou, Y., and Bellen, H.J. (2005). Synaptic mitochondria are critical for mobilization of reserve pool vesicles at Drosophila neuromuscular junctions. Neuron 47, 365–378.

Vyleta, N.P., Borges-Merjane, C., and Jonas, P. (2016). Plasticity-dependent, full detonation at hippocampal mossy fiber-CA3 pyramidal neuron synapses. Elife 5, e17977.

Wang, B., and Dudko, O.K. (2021). A theory of synaptic transmission. Elife 10, e73585.

Wang, J., Yeckel, M.F., Johnston, D., and Zucker, R.S. (2004). Photolysis of postsynaptic caged Ca2+ can potentiate and depress mossy fiber synaptic responses in rat hippocampal CA3 pyramidal neurons. J Neurophysiol 91, 1596–1607.

Wang, S.S.H., Held, R.G., Wong, M.Y., Liu, C., Karakhanyan, A., and Kaeser, P.S. (2016). Fusion Competent Synaptic Vesicles Persist upon Active Zone Disruption and Loss of Vesicle Docking. Neuron 91, 777–791.

Watanabe, S., Rost, B.R., Camacho-Pérez, M., Davis, M.W., Söhl-Kielczynski, B., Rosenmund, C., and Jorgensen, E.M. (2013a). Ultrafast endocytosis at mouse hippocampal synapses. Nature 504, 242–247.

Watanabe, S., Liu, Q., Davis, M.W., Hollopeter, G., Thomas, N., Jorgensen, N.B., and Jorgensen, E.M. (2013b). Ultrafast endocytosis at Caenorhabditis elegans neuromuscular junctions. Elife 2, e00723.

Weber, T., Zemelman, B.V., McNew, J.A., Westermann, B., Gmachl, M., Parlati, F., Söllner, T.H., and Rothman, J.E. (1998). SNAREpins: minimal machinery for membrane fusion. Cell 92, 759–772.

Weisskopf, M.G., Castillo, P.E., Zalutsky, R.A., and Nicoll, R.A. (1994). Mediation of hippocampal mossy fiber long-term potentiation by cyclic AMP. Science 265, 1878–1882.

Wheeler, D.B., Randall, A., and Tsien, R.W. (1996). Changes in action potential duration alter reliance of excitatory synaptic transmission on multiple types of Ca2+ channels in rat hippocampus. J Neurosci 16, 2226–2237.

Wickham, J., Brödjegård, N.G., Vighagen, R., Pinborg, L.H., Bengzon, J., Woldbye, D.P.D., Kokaia, M., and Andersson, M. (2018). Prolonged life of human acute hippocampal slices from temporal lobe epilepsy surgery. Sci Rep 8, 4158.

Wiebe, S.P., and Stäubli, U.V. (1999). Dynamic filtering of recognition memory codes in the hippocampus. J Neurosci 19, 10562–10574.

Wilke, S.A., Antonios, J.K., Bushong, E.A., Badkoobehi, A., Malek, E., Hwang, M., Terada, M., Ellisman, M.H., and Ghosh, A. (2013). Deconstructing complexity: serial block-face electron microscopic analysis of the hippocampal mossy fiber synapse. J Neurosci 33, 507–522.

Witter, M.P., and Amaral, D.G. (2004). Hippocampal Formation. In The Rat Nervous System, (Elsevier Inc.), pp. 635–704.

Wu, L.G., Westenbroek, R.E., Borst, J.G., Catterall, W.A., and Sakmann, B. (1999). Calcium channel types with distinct presynaptic localization couple differentially to transmitter release in single calyx-type synapses. J Neurosci 19, 726–736.

Xiang, Z., Greenwood, A.C., Kairiss, E.W., and Brown, T.H. (1994). Quantal mechanism of long-term potentiation in hippocampal mossy-fiber synapses. J Neurophysiol 71, 2552–2556.

Xu, J., Camacho, M., Xu, Y., Esser, V., Liu, X., Trimbuch, T., Pan, Y.-Z., Ma, C., Tomchick, D.R., Rosenmund, C., et al. (2017). Mechanistic insights into neurotransmitter release and presynaptic plasticity from the crystal structure of Munc13-1 C1C2BMUN. Elife 6, e22567.

Xu-Friedman, M.A., Harris, K.M., and Regehr, W.G. (2001). Three-dimensional comparison of ultrastructural characteristics at depressing and facilitating synapses onto cerebellar Purkinje cells. J Neurosci 21, 6666–6672.

Yeckel, M.F., Kapur, A., and Johnston, D. (1999). Multiple forms of LTP in hippocampal CA3 neurons use a common postsynaptic mechanism. Nat Neurosci 2, 625–633.

Zalutsky, R.A., and Nicoll, R.A. (1990). Comparison of two forms of long-term potentiation in single hippocampal neurons. Science 248, 1619–1624.

Zarebidaki, F., Camacho, M., Brockmann, M.M., Trimbuch, T., Herman, M.A., and Rosenmund, C. (2020). Disentangling the Roles of RIM and Munc13 in Synaptic Vesicle Localization and Neurotransmission. J Neurosci 40, 9372–9385.

Zhang, X., Schlögl, A., and Jonas, P. (2020). Selective Routing of Spatial Information Flow from Input to Output in Hippocampal Granule Cells. Neuron 107, 1212-1225.e7.

Zhao, S., Studer, D., Chai, X., Graber, W., Brose, N., Nestel, S., Young, C., Rodriguez, E.P., Saetzler, K., and Frotscher, M. (2012a). Structural plasticity of spines at giant mossy fiber synapses. Front Neural Circuits 6, 103.

Zhao, S., Studer, D., Chai, X., Graber, W., Brose, N., Nestel, S., Young, C., Rodriguez, E.P., Saetzler, K., and Frotscher, M. (2012b). Structural plasticity of hippocampal mossy fiber synapses as revealed by high-pressure freezing. J Comp Neurol 520, 2340–2351.

Zucker, R.S., and Regehr, W.G. (2002). Short-term synaptic plasticity. Annu Rev Physiol 64, 355–405.

NeuroResource

Neuron

Functional Electron Microscopy, "Flash and Freeze," of Identified Cortical Synapses in Acute Brain Slices

Graphical Abstract

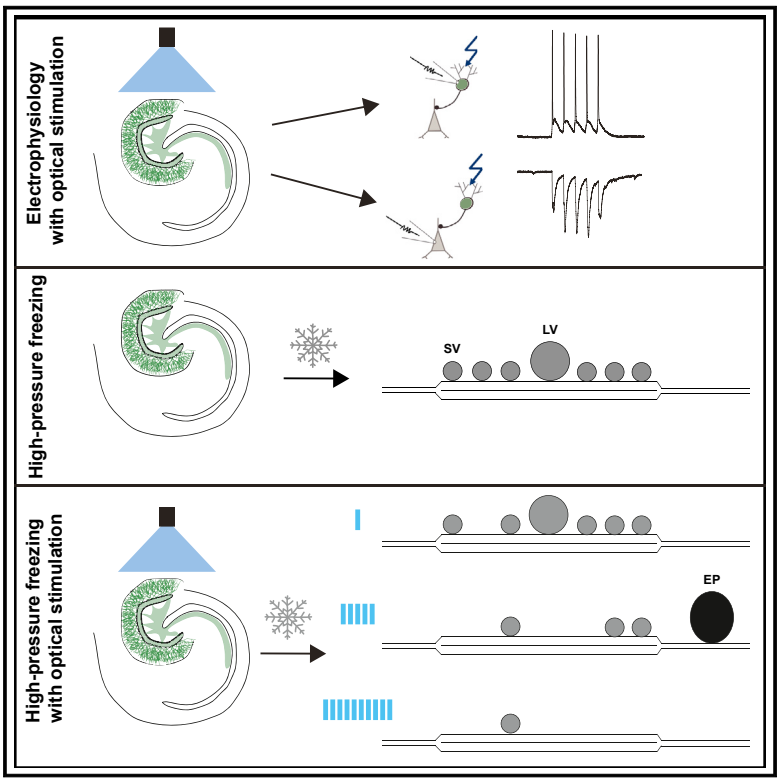

Authors

Carolina Borges-Merjane, Olena Kim, Peter Jonas

Correspondence

carolina.borges-merjane@ist.ac.at (C.B.-M.), peter.jonas@ist.ac.at (P.J.)

In Brief

Borges-Merjane et al. apply functional EM ("flash and freeze") to acute slices and organotypic slice cultures, probing vesicle pool changes at multiple time points during synaptic transmission at an identified cortical synapse, the hippocampal mossy fiber-CA3 pyramidal neuron synapse.

Highlights

- Functional EM may be applied to acute brain slices and organotypic slice cultures
- Docked vesicle pool and RRP are overlapping
- Smaller-diameter vesicles have higher release probability than larger vesicles
- Endocytic pits after moderate stimulation suggest fast endocytosis

Borges-Merjane et al., 2020, Neuron *105*, 992–1006
March 18, 2020
https://doi.org/10.1016/j.neuron.2019.12.022

CellPress

CellPress

Neuron
NeuroResource

Functional Electron Microscopy, "Flash and Freeze," of Identified Cortical Synapses in Acute Brain Slices

Carolina Borges-Merjane,[1,2,*] Olena Kim,[1,2] and Peter Jonas[1,3,*]
[1]Cellular Neuroscience, Institute of Science and Technology Austria, Am Campus 1, 3400 Klosterneuburg, Austria
[2]These authors contributed equally
[3]Lead Contact
*Correspondence: carolina.borges-merjane@ist.ac.at (C.B.-M.), peter.jonas@ist.ac.at (P.J.)
https://doi.org/10.1016/j.neuron.2019.12.022

SUMMARY

How structural and functional properties of synapses relate to each other is a fundamental question in neuroscience. Electrophysiology has elucidated mechanisms of synaptic transmission, and electron microscopy (EM) has provided insight into morphological properties of synapses. Here we describe an enhanced method for functional EM ("flash and freeze"), combining optogenetic stimulation with high-pressure freezing. We demonstrate that the improved method can be applied to intact networks in acute brain slices and organotypic slice cultures from mice. As a proof of concept, we probed vesicle pool changes during synaptic transmission at the hippocampal mossy fiber-CA3 pyramidal neuron synapse. Our findings show overlap of the docked vesicle pool and the functionally defined readily releasable pool and provide evidence of fast endocytosis at this synapse. Functional EM with acute slices and slice cultures has the potential to reveal the structural and functional mechanisms of transmission in intact, genetically perturbed, and disease-affected synapses.

INTRODUCTION

Understanding the relationship between structure and function of synapses is a key issue in neuroscience. Although synaptic structure and function have been studied for decades, several fundamental aspects of synaptic transmission remain unresolved. For example, it is controversial whether synaptic vesicles undergo exocytosis by full fusion or whether the transmitter is released by transient fusion pores (Aravanis et al., 2003; Lisman et al., 2007). Furthermore, the relationship between functionally and structurally defined synaptic vesicle pools remains unclear. Some studies have proposed that the readily releasable pool (RRP) and docked vesicle pool are identical (Schikorski and Stevens, 2001; Imig et al., 2014), whereas others have suggested that the RRP and docked vesicle pool only partially overlap and that vesicles may be released from non-docked pools (Wang et al., 2016). Finally, the mechanisms of endocytosis at central synapses remain elusive. Although it is traditionally thought that vesicles are retrieved from the plasma membrane by clathrin-dependent endocytosis, recent work implicates fast, clathrin-independent mechanisms (Watanabe et al., 2013b; Delvendahl et al., 2016; Chanaday and Kavalali, 2018). Because central synapses are highly diverse, addressing these and other questions requires structural and functional analyses of rigorously identified synapses.

Electron microscopy (EM) is the gold standard for structural analysis of synapses. Almost uniquely, EM provides spatial resolution in the nanometer range. However, a substantial disadvantage of EM is that it only captures static pictures, which typically represent the time point of fixation of the biological preparation. Furthermore, chemical fixation may change the structure of the synapse; for example, by inducing tissue shrinkage or vesicle fusion (Korogod et al., 2015). Alternatively, confocal, two-photon, and optical superresolution imaging may be used to examine synaptic transmission in not only fixed but also living specimens in real time. For example, exocytosis and transmitter release can be studied using synapto-pHluorins, styryl dyes, quantum dots, or transmitter ligand ("sniffer") proteins (Ariel and Ryan, 2010). However, these sophisticated techniques can often only be applied to dissociated cultured neurons, and it is difficult to reach sufficient resolution to identify individual active-zones or single synaptic vesicles. Thus, addressing structure-function relationships at central synapses requires techniques suitable for capturing synapses at both nanometer spatial and millisecond temporal resolutions.

Early attempts to perform concurrent structural and functional analysis of synapses combined electrical stimulation with rapid tissue freezing (Heuser et al., 1979), resulting in structural confirmation of the quantal hypothesis and characterization of synaptic vesicle cycling. Although this approach was successfully applied to the neuromuscular junction, it cannot be readily implemented at central synapses. Recently, some of these limitations were overcome by combining optogenetic stimulation of identified presynaptic neurons with high-pressure freezing (HPF), a technique called "flash and freeze" (Watanabe et al., 2013a). "Flash and freeze" has been successfully applied in the *C. elegans* nervous system (Watanabe et al., 2013a) and in dissociated cultured neurons (Watanabe et al., 2013b). However, for

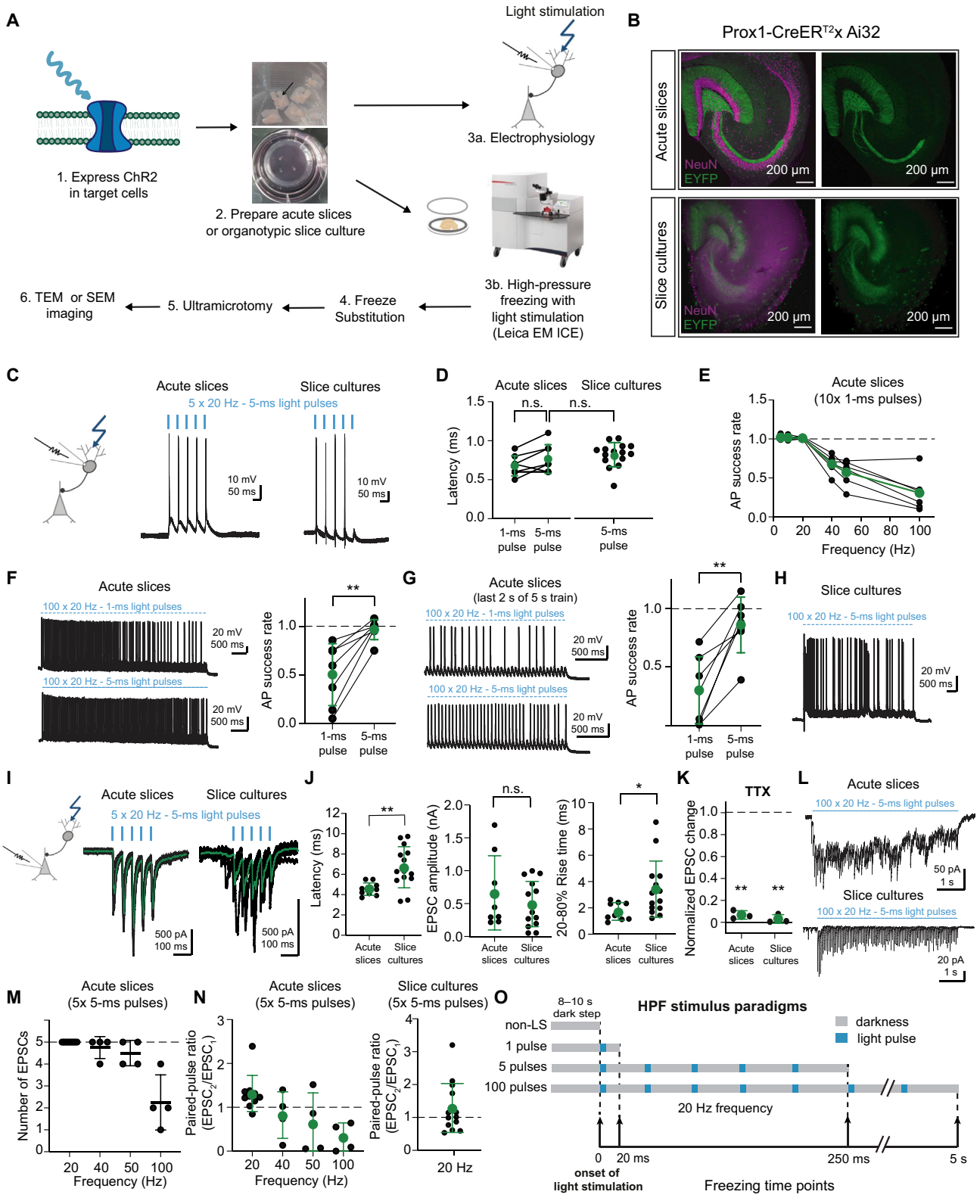

(legend on next page)

intact brain tissue, such as acute slices, selective stimulation of synapses and preservation of the ultrastructure represent severe problems. In particular, it has been widely presumed that HPF techniques cannot be routinely applied to acute slice preparations because the thickness and density of the tissue cause prolonged freezing and formation of ice crystals (Studer et al., 2014). Because our knowledge of the function of synapses is predominantly based on electrophysiological analysis of acute slice preparations (Bischofberger et al., 2006a; Blanton et al., 1989; Edwards et al., 1989; Neher, 2017), the available techniques leave a huge gap between structural and functional data, preventing a unified understanding of synaptic transmission.

Here we describe an improved "flash and freeze" technique to probe structural changes during synaptic transmission at precisely defined time points in identified cortical synapses. Unlike previously reported techniques, the method can be applied to both acute slices and organotypic slice cultures (Figure 1A). This was made possible by the use of thin acute slices, improved carrier geometry, improved recovery protocols, and optimized cryoprotection and freeze substitution. As a proof of principle, we applied the technique to the hippocampal mossy fiber synapse between dentate gyrus granule cells (GCs) and CA3 pyramidal neurons, a key synapse in the hippocampal trisynaptic circuit (Andersen et al., 1971). This synapse has several distinctive structural properties, such as a large presynaptic terminal, a huge number of synaptic vesicles, and variability in vesicle diameter (Chicurel and Harris, 1992; Acsády et al., 1998; Henze et al., 2002; Rollenhagen et al., 2007). Likewise, this synapse has several unique functional characteristics, including low initial release probability and powerful presynaptic plasticity (Salin et al., 1996; Vyleta et al., 2016). How the structural and functional properties relate to each other is unclear. With our improved method, we demonstrate that high-frequency stimulation of GCs depletes the docked vesicle pool at hippocampal mossy fiber synapses, implying that the functionally defined RRP and the structurally defined docked vesicle pool are overlapping (Rizzoli and Betz, 2005; Alabi and Tsien, 2012). Furthermore, we show the appearance of endocytic pit-like structures after moderate stimulation, providing structural evidence of a fast clathrin-independent endocytosis mechanism at this synapse (Delvendahl et al., 2016). Finally, we demonstrate that the technique is widely applicable and can be used in both acute slices and organotypic slice cultures from the mouse hippocampus as well as in acute slices from a variety of brain regions, including the cerebellum and brain stem.

RESULTS

The Prox1 Promoter Selectively Targets Hippocampal GCs

To perform functional EM experiments at identified central synapses in intact neural circuits, we faced several challenges. First, we needed to develop a method to selectively activate the presynaptic neurons; in our case, GCs giving rise to the hippocampal mossy fiber synapses. Prospero homeobox 1 (Prox1) is a transcription factor that determines hippocampal GC identity and is selectively expressed in adult GCs (Lavado et al., 2010; Ming and Song, 2011; Figure 1). To induce Cre expression specifically in GCs, we used a mouse line with constitutive Cre expression, Prox1-Cre, and a line with inducible Cre, Prox1-CreER^{T2} (Bazigou et al., 2011). To quantitatively analyze the proportion of Cre-expressing GCs at the single-cell level, we crossed these Cre lines with a tdTomato reporter line and quantified colocalization with immunoreactivity for NeuN, a pan-neuronal protein (Figures S1A and S1B). In the Prox1-Cre line, 88.3% of GCs expressed tdTomato. In the Prox1-CreER^{T2} line, expression of tdTomato was tamoxifen dose-dependent, approaching the expression in Prox1-Cre mice at high doses (200 mg kg^{-1}; 83.2% in acute slices, 89.3% in slice cultures). We opted to use the Prox1-CreER^{T2} line with timed tamoxifen injections to juvenile mice because labeling was restricted to GCs (Figures S1A and S1B). In contrast, in Prox1-Cre mice, because Cre is functional from birth, we observed developmentally dependent tdTomato labeling of unidentified interneurons (Figure S1C), likely vasoactive intestinal polypeptide-positive interneurons (Miyoshi et al., 2015). To express channelrhodopsin in a large number of GCs, we crossed the Prox1-CreER^{T2} line with an Ai32 (ChR2(H134R)-EYFP) line, injecting high doses of tamoxifen *in vivo* or applying high concentrations of 4-OH-tamoxifen *in vitro* (Figure 1B).

Reliable Optogenetic Activation of GCs and AP-Evoked Synaptic Transmission to CA3 Pyramidal Neurons

Next we determined the optimal settings for optogenetic stimulation (Figures 1C–1O). To achieve this, we performed electrophysiology experiments in acute slices and organotypic slice culture. The intensity of optical pulses was matched to the intensity reached in our HPF apparatus (5.5–8.0 mW mm^{-2}; STAR Methods; Figure 1A). In acute slices, although single 1-ms pulses reliably evoked action potentials (APs) in GCs with minimum latency (Figures 1C and 1D; 1-ms pulses 0.68 ± 0.13 ms

Figure 1. Targeted Labeling and Selective Optogenetic Activation of Hippocampal GCs

(A) Diagram of the "flash and freeze" experimental workflow.

(B) Confocal images of hippocampal acute slices (top) and slice cultures (bottom) of a mouse expressing ChR2-YFP under control of the Prox1 promoter (green), specifically targeting GCs in the dentate gyrus, superimposed with NeuN labeling (magenta). Scale bar size is indicated in the figure.

(C–H) Electrophysiology recordings from GCs in acute slices and slice cultures. Figure shows APs evoked by direct ChR2 activation (in C), measured latency from onset of light pulses of 1 or 5 ms to AP onset (in D), measured optimal frequency of stimulation (in E), and analysis of best frequency in combination with optimal pulse duration resulting in the most optimal AP success rate for both acute slices (in F and G) and slice cultures (in H).

(I–N) Electrophysiology recordings from CA3 pyramidal neurons. Figure shows example EPSCs evoked by synaptic transmission (in I and L), with measured latency from light pulse onset to EPSC onset, EPSC peak amplitude, rise time (in J); application of TTX to block APs evoked in GCs also blocked EPSCs in CA3 pyramidal neurons in acute slices and slice cultures (in K), effect of frequency of stimulation in a brief train of light pulses (in M), and PPR (in N).

(O) Graphic representation of optogenetic stimulus paradigms for HPF experiments, based on assessment of stimulus efficacy by electrophysiology. Light pulses of 5-ms duration applied at maximum 20-Hz frequency were the best parameters determined for EM experiments.

Green circles and whiskers denote mean ± SD. For graphical representation of statistics, *p < 0.05, **p < 0.01, ***p < 0.001, and ****p < 0.0001. See also Figure S1.

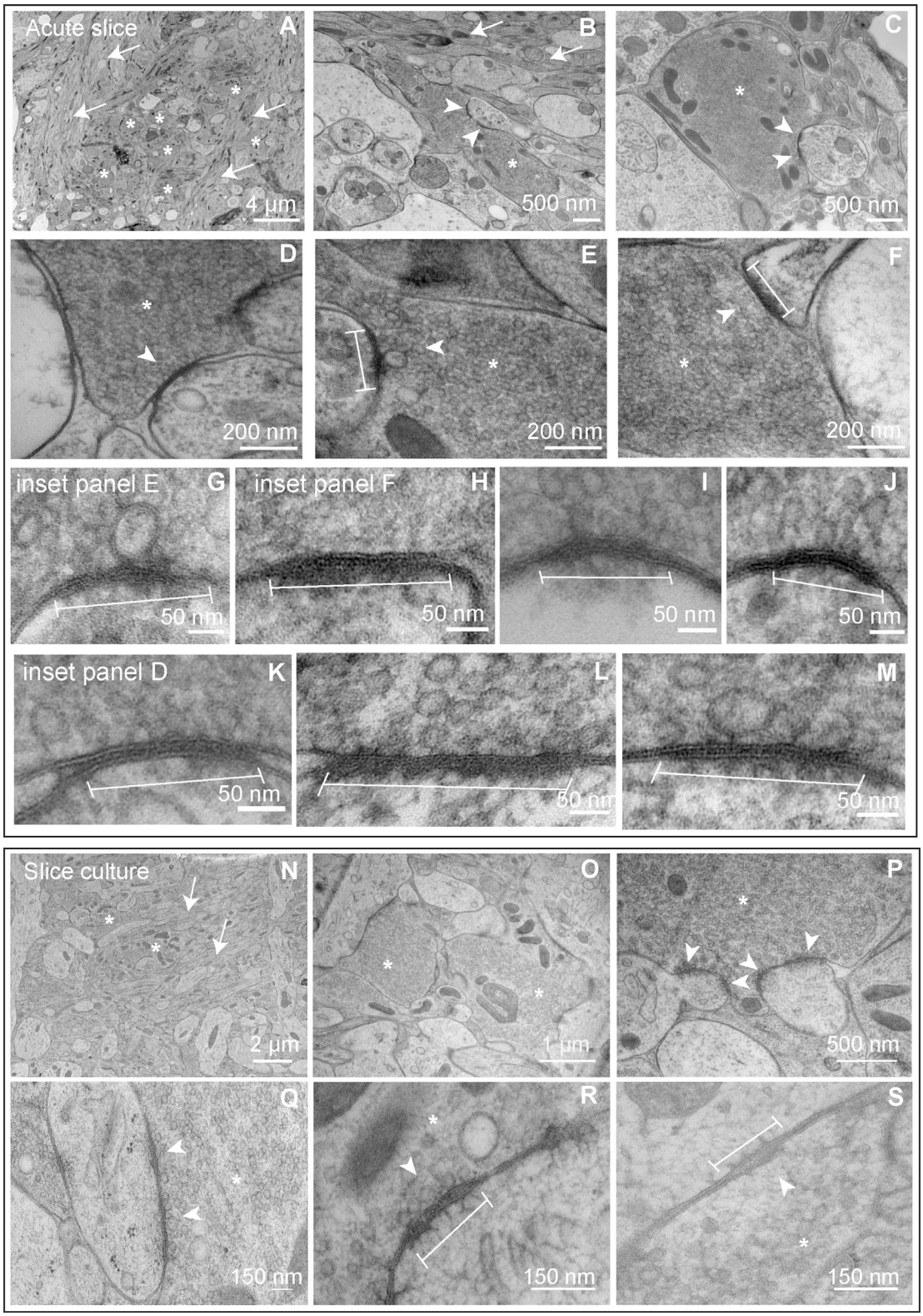

Figure 2. Ultrastructure of High-Pressure-Frozen Acute Slices and Organotypic Slice Cultures

(A–S) Example transmission electron microscopy (TEM) micrographs, showing the quality of the ultrastructure in acute slices (frozen in 15% PVP; A–M) and slice cultures (frozen in 15% BSA; N–S) from lower to higher magnification. Images were taken from the mossy fiber tract in the *stratum lucidum* of the CA3 region,

(legend continued on next page)

[mean ± SD] and 5-ms pulses 0.76 ± 0.18 ms, n = 8 GCs), prolonged trains of 1-ms pulses evoked APs with reduced reliability. This was noticeable in particular over the last 2 s of a 5-s stimulation protocol, with 100 light pulses at a 20-Hz repetition rate, whereas trains of 5-ms pulses reliably evoked APs throughout the stimulus train (Figures 1F and 1G; AP success rate for the entire 5 s stimulation train: 1-ms pulses 0.50 ± 0.32 [mean ± SD], 5-ms pulses 0.96 ± 0.10, p = 0.0034; AP success rate for last 2 s of train: 1-ms pulses 0.30 ± 0.27, 5-ms pulses 0.86 ± 0.22, p = 0.0014; n = 7 GCs). Trains of 10 pulses reliably evoked APs in GCs for stimulation frequencies of up to 20 Hz (Figure 1E). For organotypic slice culture, 1-ms pulses were not sufficient to elicit APs in GCs, whereas 5-ms pulses reliably evoked APs (Figures 1C and 1D; 5-ms pulse latency 0.82 ± 0.16 ms, n = 15 GCs). However, although we observed more failures in slice cultures than in acute slices, we noticed that, with 5-ms pulses, occasionally more than 1 AP was evoked (Figure 1H). Thus, Prox1-CreER^{T2}-driven expression of channelrhodopsin allows reliable optogenetic activation of GCs with single pulses of light and trains of pulses.

Single pulses of light and also 20-Hz trains of 5-ms pulse stimuli led to reliable synaptic transmission to CA3 pyramidal neurons (Figures 1I–1N). Consistent with our observations in GCs, we noted that, above 20-Hz frequency, temporal resolution and fidelity of transmission were lost. For a 5-pulse train, at frequencies greater than 20 Hz, peak amplitudes of excitatory postsynaptic currents (EPSCs) started to overlap, and the paired-pulse ratio (PPR) became variable (Figures 1M and 1N). Interestingly, we observed consistent differences between acute slices and slice cultures. Slice cultures had a longer and more variable latency and slower and more variable rise time, likely because of network rearrangement during the culture growth process (Figure 1J; latency acute slices 4.54 ± 0.62 ms [mean ± SD], n = 9 CA3 pyramidal neurons; slice culture 6.70 ± 2.02 ms, n = 14 CA3 neurons; p = 0.0036; 20%–80% rise time acute slices 1.72 ± 0.62 ms, n = 9 CA3 neurons; slice cultures 3.42 ± 2.14 ms, n = 14 CA3 neurons; p = 0.019). We observed very little recruitment of inhibition with 20-Hz trains of 5-ms pulses. This is presumably due to our experimental configuration, in which the holding potential was close to the chloride equilibrium potential.

Furthermore, bath application of 1 μM tetrodotoxin (TTX) blocked APs in GCs and EPSCs in CA3 pyramidal cells, excluding the possibility that Ca^{2+} inflow through channelrhodopsin channels directly triggered transmitter release (Figure 1K; percent change in EPSC amplitude, 93.2% ± 3.9%; p = 0.0005; n = 3 CA3 pyramidal cells). However, we cannot fully exclude the possibility that Ca^{2+} influx through channelrhodopsin, in combination with presynaptic APs, alters neurotransmitter release. Based on the electrophysiology experiments, single 5-ms pulses and trains of 5-ms pulses of light at 20 Hz were used in subsequent HPF experiments (Figure 1O). Notably, stimulus paradigms such as the long train, with 50 or 100 stimuli at 20 Hz, have been used previously to deplete the RRP (Rosenmund and Stevens, 1996; Murthy and Stevens, 1999).

HPF of Acute Slices for Functional EM Required Several Refinements for Ultrastructure Preservation

To examine central synapses in their native network environment and correlate structural and functional changes during synaptic transmission, we needed to develop a HPF technique for acute slices. Because standard HPF experiments have been demonstrated previously in non-fixed organotypic slice cultures (Studer et al., 2014; Imig et al., 2014), we developed HPF experiments in acute slices and organotypic slice cultures in parallel, using the latter as a reference point for our technical optimization (STAR Methods; Figures 2 and S2–S5).

Several improvements were made to successfully freeze acute slices (Figures 2A–2M, S2, and S3). First, to promote rapid freezing, we decreased the thickness of slices from the standard 250–400 μm used for electrophysiology to 150 and 200 μm (Figures 2A–2M, S2, and S3). Slices of 150-μm thickness had fewer ice crystals in the core of the tissue, whereas 200-μm slices were less fragile and easier to handle. Either could be used for experiments. Second, slices were subjected to a 30- to 45-min recovery period at ~35°C after slicing to improve tissue integrity and recovery of neuronal activity (Bischofberger et al., 2006a), which was important for optogenetic stimulation. Third, we used microcarriers large enough to accommodate the entire slice preparation (6-mm outer diameter) without further trimming (STAR Methods; Figures S2B and S2C). Thus, the entire hippocampal network and part of the surrounding tissue were kept intact. To allow optical stimulation, assembly of the HPF sample sandwich was performed with a pair of transparent sapphire disks (acute slices) or a hybrid sapphire-metal carrier assembly (slice cultures) (Figures S2A and S2B). For slice cultures, the hybrid system resulted in a more stable sandwich configuration because the metal carriers provided a tight fit to hold the membranes of each culture in place (Stoppini et al., 1991). Additionally, transfer of slices to the sapphire sandwich assembly was achieved using a number 4 paintbrush to keep the slice flat, constantly submerged in a drop of artificial cerebrospinal fluid (ACSF), and precisely centered. This is critical to maintain the slice intact as well as to avoid shift of placement, which could lead to sapphire breakage and/or poor freezing quality. Finally, cryoprotectant was added immediately before closing the sandwich assembly. We tested the use of bovine serum albumin (BSA), a commonly used cryoprotectant (Studer et al., 2014), and polyvinylpyrrolidone (PVP) (Möbius et al., 2016). Both are typically used at a 20% concentration. However, to identify the optimum cryoprotectant concentration that would lead to well-preserved ultrastructure without excess exposure, we tested freezing with different concentrations. In organotypic slice cultures, 15% BSA in ACSF resulted in the most well-preserved ultrastructure (STAR Methods). However, in acute slices, 15% PVP in ACSF gave the best result (STAR Methods). One advantage of the

primarily CA3b and CA3c, and show mossy fiber axons (arrows), putative mossy fiber boutons (asterisks), active-zones (arrowheads), and postsynaptic densities (bars). The micrographs in this figure and all supplemental figures associated with Figure 2, are representative of all samples from different mice, used for analysis of controls and light-stimulated tissue, to demonstrate the quality of the ultrastructure across experiments and conditions. Scale bar sizes are indicated in the figure. See also Figures S2–S6.

use of PVP for acute slices is that 15% PVP in ACSF can be equilibrated with carbogen gas (5% CO_2 and 95% O_2), keeping oxygenation and pH constant. To ensure that the addition of PVP did not affect responses to the optical stimulus, we recorded GC APs and optically evoked EPSCs in CA3 pyramidal cells in the presence of 15% PVP. The solution was bath applied by perfusion, and recording began after 1–2 min of equilibration and lasted up to 10 min. This time outlasts exposure to 15% PVP by frozen sections, which was only 1–2 min, at the final stages of sandwich assembly. No significant effects of PVP were observed on latency, EPSC peak amplitude, or PPR (Figure S2D; latency in PVP 5.03 ± 0.50 ms [mean ± SD], p = 0.930; EPSC amplitude in PVP 356.3 ± 18.4 pA; p = 0.6500; PPR in PVP 1.07 ± 0.09; p = 0.3345; n = 3 CA3 neurons). Nonetheless, although we kept the time of exposure to cryoprotectants to the minimum required and performed electrophysiology control experiments, we cannot rule out the possibility that BSA or PVP may have other adverse effects on cellular processes. HPF samples were maintained at physiological temperature (37°C) in the freezing chamber throughout optical stimulation.

Next we tested a variety of freeze substitution protocols based on previous studies that used HPF in fresh (non-fixed) tissue, both organotypic slice cultures and acute slices (Studer et al., 2014), and organotypic slice cultures alone (Imig et al., 2014). We implemented an agitation module that fits on top of the automated freeze substitution system (Goldammer et al., 2016) to shake the samples throughout the procedure. This provided two main benefits. First, by gently shaking the samples, the unopened sapphire sandwiches opened during freeze substitution without damaging the slices, allowing complete infiltration. Second, it notably shortened the duration of the freeze substitution protocol (STAR Methods). After the resulting accelerated procedure, samples underwent room-temperature Durcupan resin infiltration and embedding, followed by ultrathin sectioning and imaging (Figure 1A). Using this procedure, we obtained adequate preservation of the ultrastructure in acute slices, comparable with that of organotypic slice cultures frozen using more conventional procedures (15% BSA; Studer et al., 2014; Figures 2 and S4). Thus, our method is applicable to both acute slices and organotypic slice cultures. Using the same procedure, we also obtained well-preserved ultrastructure in acute 200-μm-thick slices obtained from cerebellum and brain stem (Figure S5). Therefore, our method is generally applicable to acute slices in a variety of brain circuits.

Ultrastructural analysis of HPF material from both acute slices and slice cultures confirmed several previously described properties of hippocampal mossy fiber terminals, including large size, high density of clear synaptic vesicles, presence of large dense-core vesicles, high density of mitochondria, multiple active-zones contacting large spines with dense accumulation of synaptic vesicles in close proximity to the presynaptic membrane, and nonsynaptic *puncta adherentia* contacts with dendritic shafts (Chicurel and Harris, 1992; Henze et al., 2002; Rollenhagen et al., 2007). We focused our ultrastructural analysis on active-zone profiles and peri-active-zone regions (STAR Methods; Figures 2, S2E, and S6). Active-zones were defined as the presynaptic membrane regions directly opposed to the postsynaptic density (asymmetric contacts), with accumulation of clear and round vesicles in close proximity to the membrane and characteristic widening of the synaptic cleft, often showing higher electron density and a disk in the center of the cleft (Chicurel and Harris, 1992; Rollenhagen et al., 2007; Zhao et al., 2012a, 2012b). For ultrastructure analysis, we focused on identifying vesicles docked at identified active-zone areas and also measured their diameters. We confirmed the previously characterized variability in vesicle diameter (Henze et al., 2002; Rollenhagen et al., 2007). We also observed active-zone profiles lacking docked vesicles (Figure S6C). The number of profiles lacking docked vesicles was marginal and not significant under control conditions and increased with stimulation in an activity-dependent manner. Finally, we also identified structures present in the peri-active-zone area within 150 nm of the edge of the active-zone that presumably represent endocytic structures.

The Numbers and Diameters of Docked Vesicles Are Higher in Acute Slices

We first sought to establish a baseline for the number and diameter of docked vesicles in the absence of optical stimulation. To identify any potential effects of the transgenic manipulations from the Prox1-CreER^{T2} x Ai32 mouse line, we compared unstimulated acute slices from wild-type (WT) animals (control) to slices from transgenic animals expressing channelrhodopsin, also without light stimulation (non-LS). Next we compared the non-LS samples from acute slices with non-LS samples from slice cultures to identify potential changes as a consequence of *in vitro* development of the circuit in culture (Figure 3). The number of docked vesicles was expressed as density per 100 nm of active-zone profile.

The numbers and diameters of docked vesicles were not significantly different between WT and non-LS control conditions (Figure 3; in WT: number of docked vesicles 1.25 ± 0.46 [mean ± SD], median 1.23; docked vesicle diameter 38.9 ± 13.4 nm, median 35.1 nm; n = 123 active-zone profiles, n = 366 vesicles, N = 2 mice; in non-LS: number of docked vesicles 1.16 ± 0.49, median 1.14; docked vesicle diameter 37.7 ± 13.4 nm; median 33.8 nm; n = 116 active-zone profiles, n = 280 vesicles, N = 3 mice; WT versus non-LS: number of docked vesicles p = 0.5428; vesicle diameter p = 0.1962). However, the numbers and diameters of docked vesicles were significantly higher in acute slices (Figure 3; in culture non-LS: number of docked vesicles [mean ± SD] 0.84 ± 0.52; median 0.77; docked vesicle diameter 36.7 nm ± 17.8 nm; median 31.5 nm; n = 170 active-zone profiles, n = 171 vesicles, N = 3 mice; non-LS acute slices versus non-LS slice cultures: number of docked vesicles p < 0.0001 and diameter p = 0.0145; Figure 3A, left and right panels, respectively). Furthermore, the docked vesicle diameter distribution was continuous and right-skewed in acute slices, whereas it was more bimodal in organotypic slice cultures (Figures 3D and 3E). Maximum likelihood analysis revealed no significant improvement of the fit with two components in acute slices (p = 0.59) but a better fit in organotypic slice cultures (p < 0.001; STAR Methods). For direct comparison across groups during analysis of the frequency distribution of vesicle diameters, raw histogram counts were divided by the total length of active-zone analyzed for each corresponding experimental condition. The resulting histograms display vesicle density (per 100 nm of active-zone) as a function of vesicle diameter, as shown in Figure 3D.

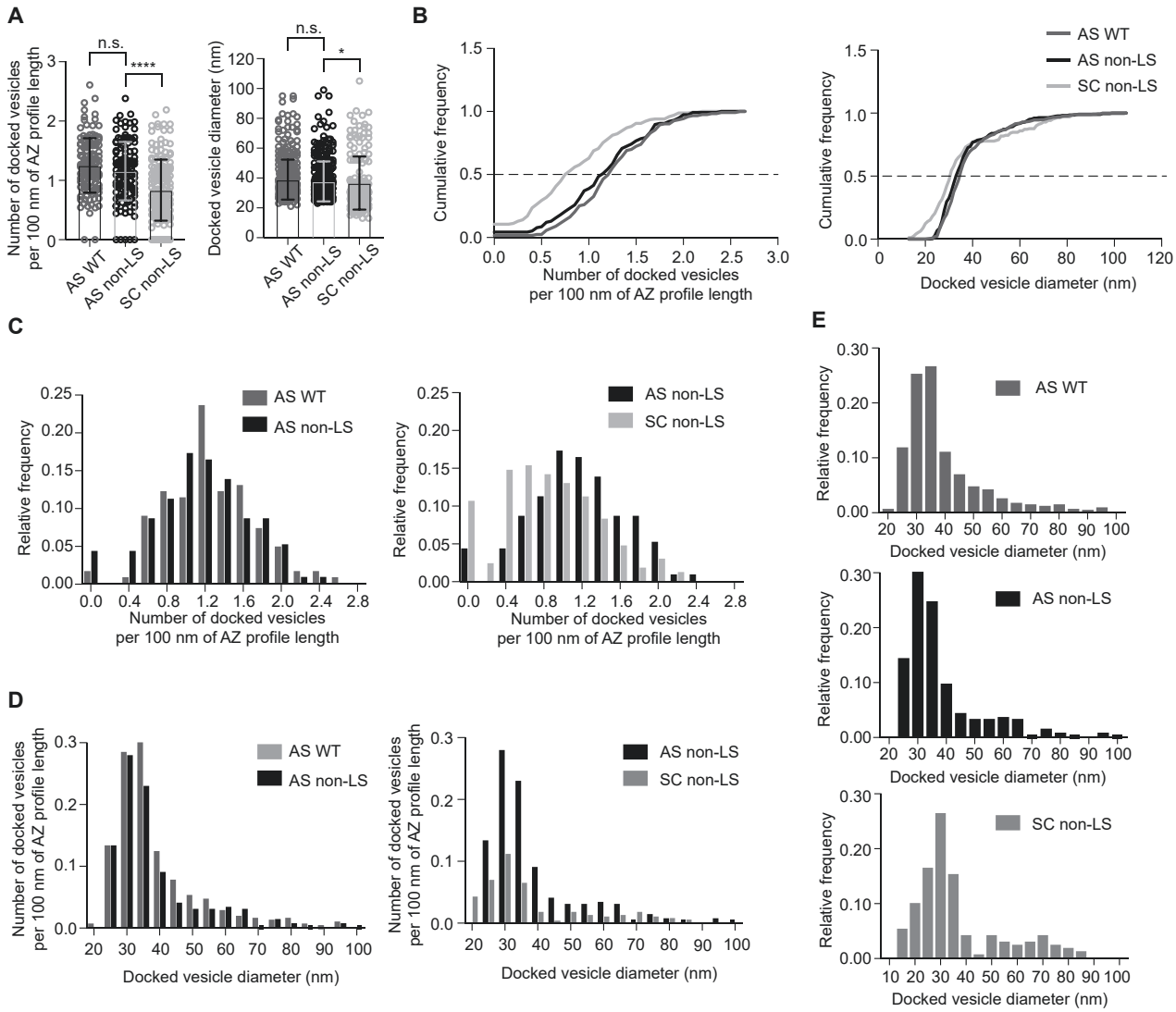

Figure 3. Mossy Fiber Boutons in Acute Slices Have More Docked Vesicles and Larger-Diameter Vesicles Than in Slice Cultures

(A) Left panel: scatterplot of the number of docked vesicles per 100 nm of active-zone length in acute slices (ASs) from wild-type (WT) animals and from non-light-stimulated transgenic animals (non-LS) and slice cultures (SCs) from non-light-stimulated transgenic animals (non-LS). Right panel: scatterplot of the diameter of docked vesicles in each group. Bars and whiskers show mean ± SD. For graphical representation of statistics, *$p < 0.05$, **$p < 0.01$, ***$p < 0.001$, and ****$p < 0.0001$.

(B) Cumulative plots of the data displayed in (A) for the number of docked vesicles (left) and docked vesicle diameter (right).

(C) Histograms with the relative frequency distribution of the number of docked vesicles per 100 nm of active-zone length compared between AS controls (WT versus non-LS) and between ASs and SCs (AS non-LS versus SC non-LS).

(D) Histograms of docked vesicle diameter compared between AS controls (WT versus non-LS) and between ASs and SCs (AS non-LS versus SC non-LS).

(E) Histograms showing the individual relative frequency distribution of docked vesicle diameter for ASs and SCs.

See also Figure S7.

Finally, to test whether any basal AP activity would affect the measurements of the size of the docked pool, we performed a TTX control of non-light-stimulated transgenic animals in the presence of 1 μM TTX (non-LS+TTX) (Figure S7). Neither numbers nor diameters of docked vesicles were significantly different across acute slice control conditions (in non-LS+TTX: number of docked vesicles 1.15 ± 0.57; median 1.07; docked vesicle diameter 39.7 ± 15.1 nm; median 34.4 nm; n = 102 active-zone profiles, n = 252 vesicles, N = 2 mice; WT versus non-LS+TTX: number of docked vesicles p = 0.6465 and vesicle diameter p = 0.8194; non-LS versus non-LS+TTX: number of docked vesicles p > 0.9999 and vesicle diameter p > 0.9999). There was also no significant difference for slice cultures (in non-LS+TTX: number of docked vesicles 0.77 ± 0.48; median 0.69; docked vesicle diameter 40.3 ± 20.1 nm; median 32.8 nm; n = 154 active-zone profiles, n = 124 vesicles, N = 2

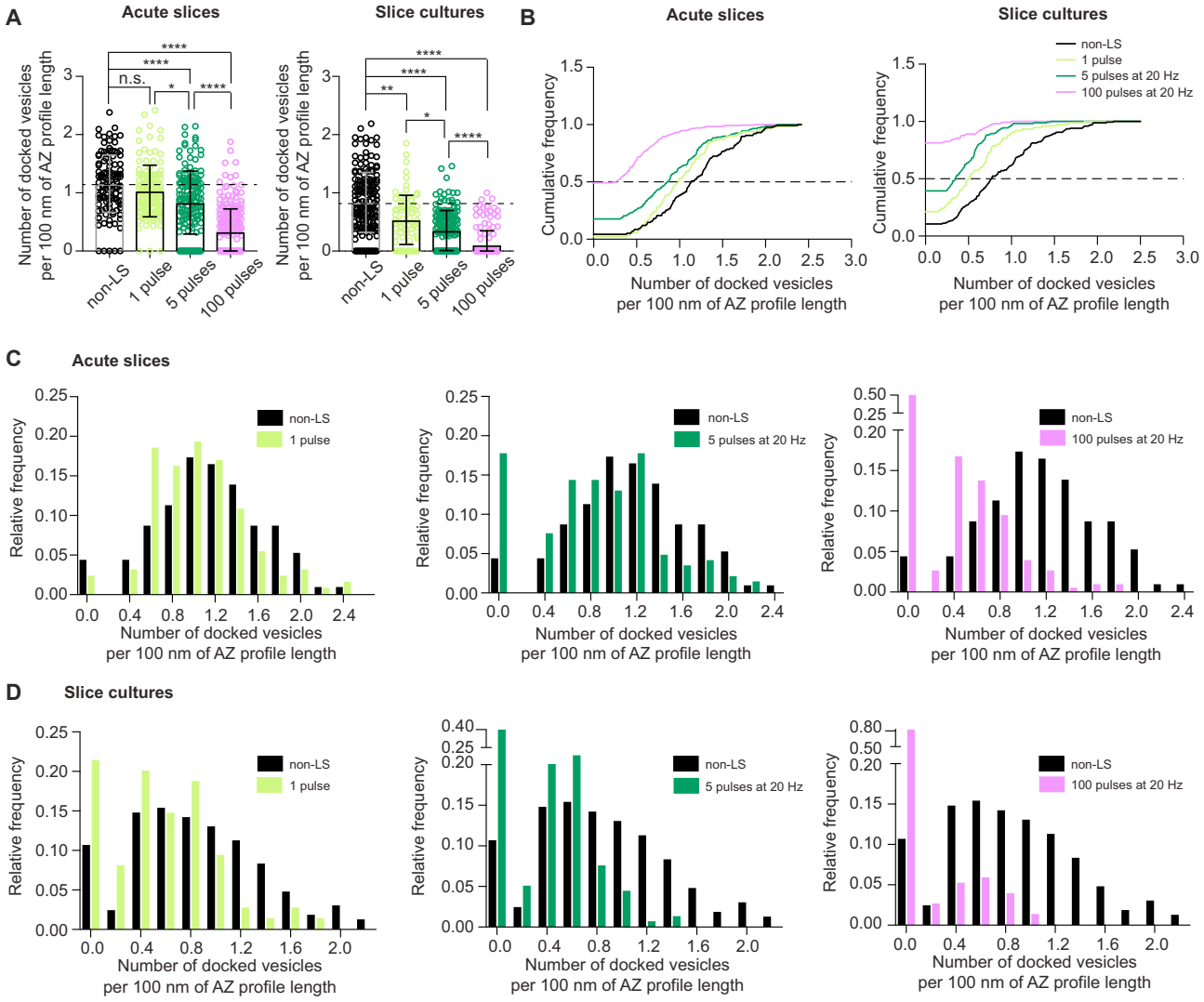

Figure 4. The Number of Docked Vesicles Decreases in an Activity-Dependent Manner in Both ASs and SCs

(A) Scatterplot of the number of docked vesicles per 100 nm of active-zone length in ASs (left) and SCs (right) for each stimulation paradigm. Bars and whiskers show mean ± SD. For graphical representation of statistics, *p < 0.05, **p < 0.01, ***p < 0.001, and ****p < 0.0001. Dashed line indicates the mean of non-LS control.

(B) Cumulative plots of the data displayed in (A). Dashed line indicates the median.

(C and D) Histograms showing the comparison of relative frequency distribution of docked vesicle numbers for ASs (C) and SCs (D). The histograms compare each stimulated sample with non-LS control.

mice; non-LS versus non-LS+TTX: number of docked vesicles p > 0.9999 and vesicle diameter p > 0.9999).

Taken together, these results indicate that the numbers and diameters of docked vesicles in slices from transgenic mice are similar to the WT and unaffected by basal AP activity. However, the numbers and diameters are slightly but significantly higher in acute slices than in organotypic slice cultures.

Stimulus-Dependent Depletion of the Docked Vesicle Pool

Finally, we analyzed the effect of mild and strong optical stimulation on the numbers and diameters of docked vesicles in active-zone profiles of mossy fiber boutons in acute slices and organotypic slice cultures (Figures 4 and 5). For this purpose, we applied three paradigms widely used in electrophysiology experiments (Figure 1O): 1 pulse of light that evoked 1 AP in acute slices or 1–2 APs in the case of slice cultures; a brief train of 5 pulses at 20 Hz; and a long train of 100 pulses at 20 Hz, a stimulus commonly used to deplete the RRP (Rosenmund and Stevens, 1996; Murthy and Stevens, 1999). Based on the time course of exocytosis measured previously with similar approaches (Watanabe et al., 2013a, 2013b), after a single optical pulse, samples were frozen 20 ms after pulse onset in an attempt to capture vesicle fusion evoked by a single AP. For the brief and long trains of pulses delivered at 20 Hz, samples were frozen 50 ms after last pulse onset (Figure 1O). We examined structural correlates of both exocytosis

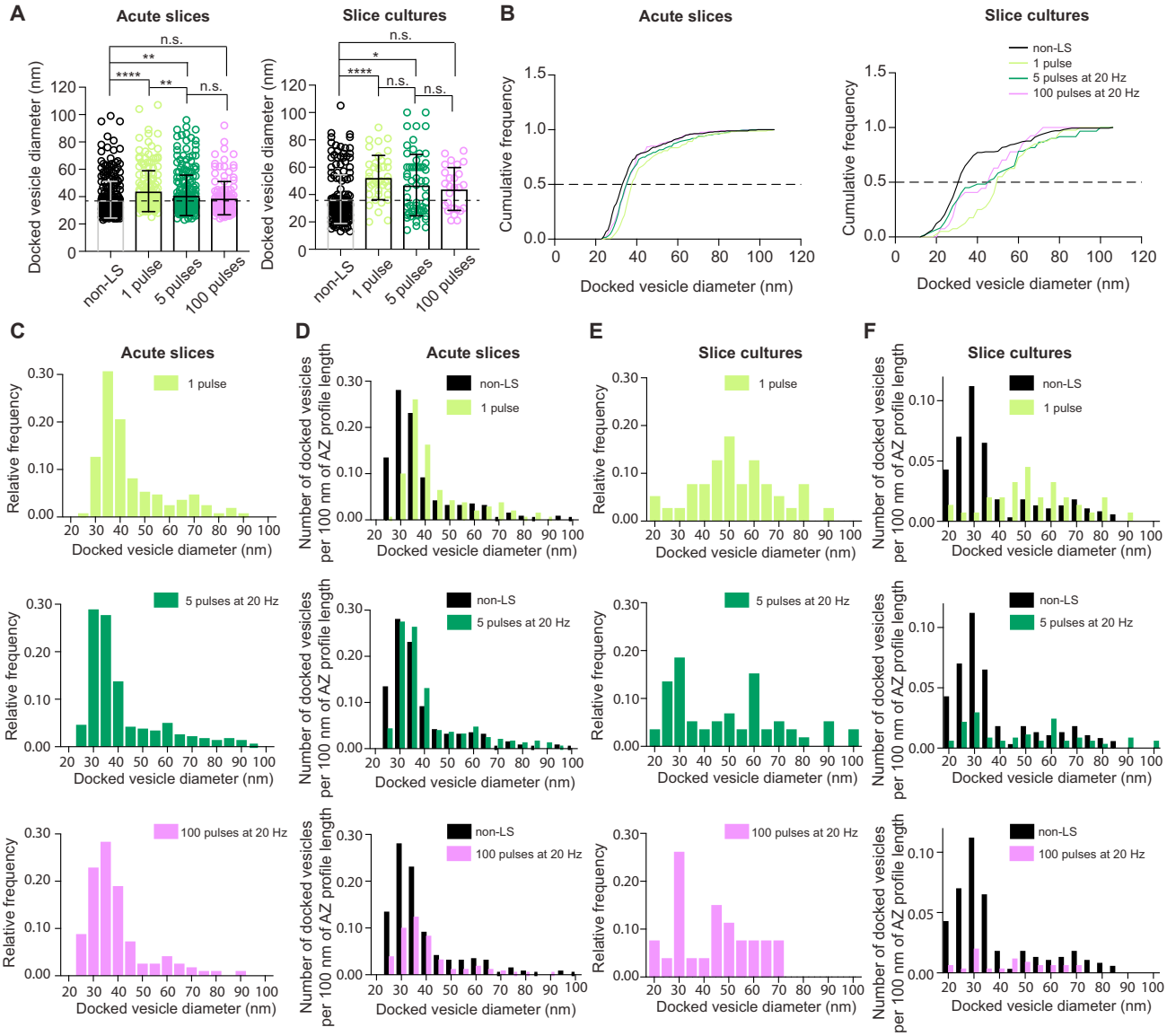

Figure 5. The Mean Diameter of Docked Vesicles Changes in an Activity-Dependent Manner in ASs and SCs

(A) Scatterplot of the diameter of docked vesicles measured in ASs (left) and SCs (right) for each stimulation paradigm. Bars and whiskers show mean ± SD. For graphical representation of statistics, *$p < 0.05$, **$p < 0.01$, ***$p < 0.001$, and ****$p < 0.0001$. Dashed line indicates the mean of non-LS control.

(B) Cumulative plots of the data displayed in (A). Dashed line indicates the median.

(C) Histograms showing the relative frequency distribution of docked vesicle diameter for stimulated groups in ASs.

(D) Comparison of docked vesicle diameter between non-LS control and stimulated groups in ASs.

(E) Histograms showing the relative frequency distributions of docked vesicle diameter for stimulated groups in SCs.

(F) Comparison of docked vesicle diameter between non-LS control and stimulated groups in SCs.

and endocytosis. As above, the number of docked vesicles was quantified as density per 100 nm of active-zone profile.

In samples exposed to a single pulse, we observed a decrease in the mean number of docked vesicles in comparison with non-LS control conditions, albeit only significant in slice cultures (acute slices, Figures 4A–4C; mean ± SD 1.03 ± 0.44; median 0.99; n = 130 active-zone profiles, N = 2 mice; p = 0.7015; Figure 4A, left panel; slice cultures: Figures 4A, 4B, and 4D; 0.54 ± 0.42; median 0.51; n = 75 active-zone profiles, N = 3 mice; p = 0.0017; Figure 4A, right panel). This could be due to our observation that, on occasion, a single pulse evoked more than 1 AP in slice cultures. Furthermore, we observed a significant increase in the mean diameter of docked vesicles (acute slices: Figures 5A–5D; mean ± SD 44.0 ± 15.0 nm; median 38.2 nm; n = 130 active-zone profiles, n = 177 vesicles, N = 2 mice; p < 0.0001; Figure 5A, left panel; slice cultures: Figures 5A, 5B, 5E, and 5F; mean ± SD 52.5 ± 16.2 nm; median 50.1 nm; n = 75 active-zone profiles, n = 40 vesicles, N = 3 mice; p < 0.0001; Figure 5A, right panel). These results suggest that, following a single

pulse of light, docked vesicles with smaller diameter were preferentially released.

In samples exposed to 5 pulses of light at 20 Hz, we observed a further significant decrease in the number of docked vesicles as compared with non-LS control in acute slices (Figures 4A–4C; mean ± SD 0.83 ± 0.54; median 0.86; n = 147 active-zone profiles, N = 3 mice; non-LS control versus 5 pulses $p < 0.0001$ and 1 pulse versus 5 pulses $p = 0.0169$; Figure 4A, left panel) and in slice cultures (Figures 4A, 4B, and 4D; mean ± SD 0.35 ± 0.34; median 0.35; n = 160 active-zone profiles, N = 3 mice; non-LS control versus 5 pulses $p < 0.0001$ and 1 pulse versus 5 pulses $p = 0.0203$; Figure 4A, right panel). Furthermore, the diameter of docked vesicles was significantly increased compared with non-LS control for both acute slices (Figures 5A–5D; mean ± SD 40.9 ± 14.8 nm; median 35.2 nm; n = 147 active-zone profiles, n = 251 vesicles, N = 3 mice; $p = 0.0029$; Figure 5A, left panel) and slice cultures (Figures 5A, 5B, 5E, and 5F; mean ± SD 46.9 ± 22.5 nm; median 45.3 nm; n = 160 active-zone profiles, n = 60 vesicles, N = 3 mice; $p = 0.0124$; Figure 5A, right panel). Although still larger than the non-LS control, the mean and the median diameter of docked vesicles, after a short train, were smaller than after a single pulse of light, albeit this was only significant in data from acute slices ($p = 0.0014$). These results suggest that, following a brief train of pulses, both smaller- and larger-diameter vesicles were released. Additionally, with this stimulus paradigm, we observed significantly more putative endocytic structures in the peri-active-zone area, within 150 nm from the active-zone edge, than under any other condition (Figure 6; acute slices non-LS control versus 1 pulse $p > 0.9999$, non-LS control versus 5 pulses $p < 0.0001$, non-LS control versus 100 pulses $p > 0.9999$ and slice cultures non-LS control versus 1 pulse $p > 0.9999$, non-LS control versus 5 pulses $p < 0.0001$, non-LS control versus 100 pulses $p > 0.9999$). Similar experimental approaches using "flash and freeze" in dissociated neuronal cultures (Watanabe et al., 2013b) revealed endocytic structures appearing between 100–300 ms after an optical pulse stimulus and cleaving off up to 1 s thereafter. Furthermore, capacitance measurements from hippocampal mossy fiber terminals suggested fast endocytosis with a time constant of 470 ms at near-physiological temperature (Hallermann et al., 2003; Delvendahl et al., 2016). The short stimulus train of 5 pulses at 20 Hz, used in the present experiments, lasted 250 ms from onset of the first pulse. Thus, putative endocytic structures may have originated as a consequence of the first 3–4 pulses on the train. The diameter of these putative endocytic structures was, on average, 63.6 ± 3.5 nm, approximately twice the size of a synaptic vesicle, and was not significantly different among any groups (Figure 6B). We also addressed whether the presence of endocytic pits was different between acute slices and slice cultures by further testing statistical significance. We only found a significant difference between the 5-pulse stimulation groups (acute slices versus slice culture non-LS control $p > 0.9999$, 1 pulse $p > 0.9999$, 5 pulse $p < 0.0001$, 100 pulse $p > 0.9999$) (Figure 6C).

In samples exposed to 100 optical pulses at 20 Hz, there was a substantial further decrease in the number of docked vesicles both in acute slices (Figures 4A–4C; mean ± SD 0.33 ± 0.39; median 0.25; n = 234 active-zone profiles, N = 3 mice; $p < 0.0001$; Figure 4A, left panel) and in slice cultures (Figures 4A, 4B, and 4D; mean ± SD 0.11 ± 0.24; median 0.00; n = 155 active-zone profiles, N = 3 mice; $p < 0.0001$; Figure 4A, right panel). This is consistent with the hypothesis that docked vesicles are part of the RRP (Schikorski and Stevens, 2001). However, although we observed a 71.5% decrease in the number of docked vesicles compared with the non-LS control, there were still docked vesicles present. This suggests that either not all docked vesicles are part of the RRP or that the docked vesicle pool undergoes rapid refilling during the 5-s stimulus train. The diameter of docked vesicles after the depleting stimulus was not different from the diameter under non-LS control conditions (acute slices, Figures 5A–5D; mean ± SD 38.9 ± 12.1 nm; median 35.4 nm; n = 234 active-zone profiles, n = 128 vesicles, N = 3 mice; $p > 0.9999$; Figure 5A, left panel; slice cultures: Figures 5A–5C; 44.1 ± 15.7 nm; median 45.1 nm; n = 155 active-zone profiles, n = 27 vesicles, N = 3 mice; $p > 0.9999$; Figure 5A, right panel) and neither from that observed with a short stimulus train. Thus, with an RRP-depleting stimulus, both smaller- and larger-diameter docked vesicles were released.

Is it possible that the large docked vesicles in the active-zones are confused with endocytic pits? Although we cannot completely exclude this, several observations argue against this possibility. First, the diameter of large putative docked vesicles (>40 nm in diameter) in the active-zone is significantly smaller than that of endocytic structures in the peri-active-zone area ($p < 0.0001$). Second, large putative docked vesicles are present under control conditions (Figure 3; Figure S7). Third, activity-dependent changes in large putative docked vesicles are opposite to those observed for endocytic pits. For instance, with the 5 pulses at 20-Hz stimulation, the absolute number of large putative docked vesicles in the active-zone remained unchanged (Figure 5D, center), whereas the number of endocytic pits in the peri-active-zone increased (Figure 6C). Conversely, with the 100 pulses at 20-Hz stimulation, the number of large putative docked vesicles in the active-zone declined (Figure 5D, bottom), whereas the number of endocytic pits in the peri-active-zone returned to control levels. Thus, it is more likely that the large structures within the active-zone region are "giant" synaptic vesicles, identified previously in mossy fiber terminals (Henze et al., 2002; Figures S2E and S6C).

DISCUSSION

In cellular neuroscience, a huge gap exists between structural analysis by EM and functional analysis by electrophysiology and optical imaging. Although EM has exquisitely high spatial resolution (Palay, 1956; Schikorski and Stevens, 1997; Harris and Weinberg, 2012), it only generates static pictures. In contrast, electrophysiology has microsecond temporal resolution but provides limited spatial information. Traditionally, completely different preparations are used for morphological and functional experiments. EM is typically applied in combination with perfusion fixation of whole brains for optimal tissue preservation, whereas electrophysiology is largely performed in acute slices (Bischofberger et al., 2006a; Blanton et al., 1989; Edwards et al., 1989). Thus, correlating structural and functional information is a major challenge. The present paper reports

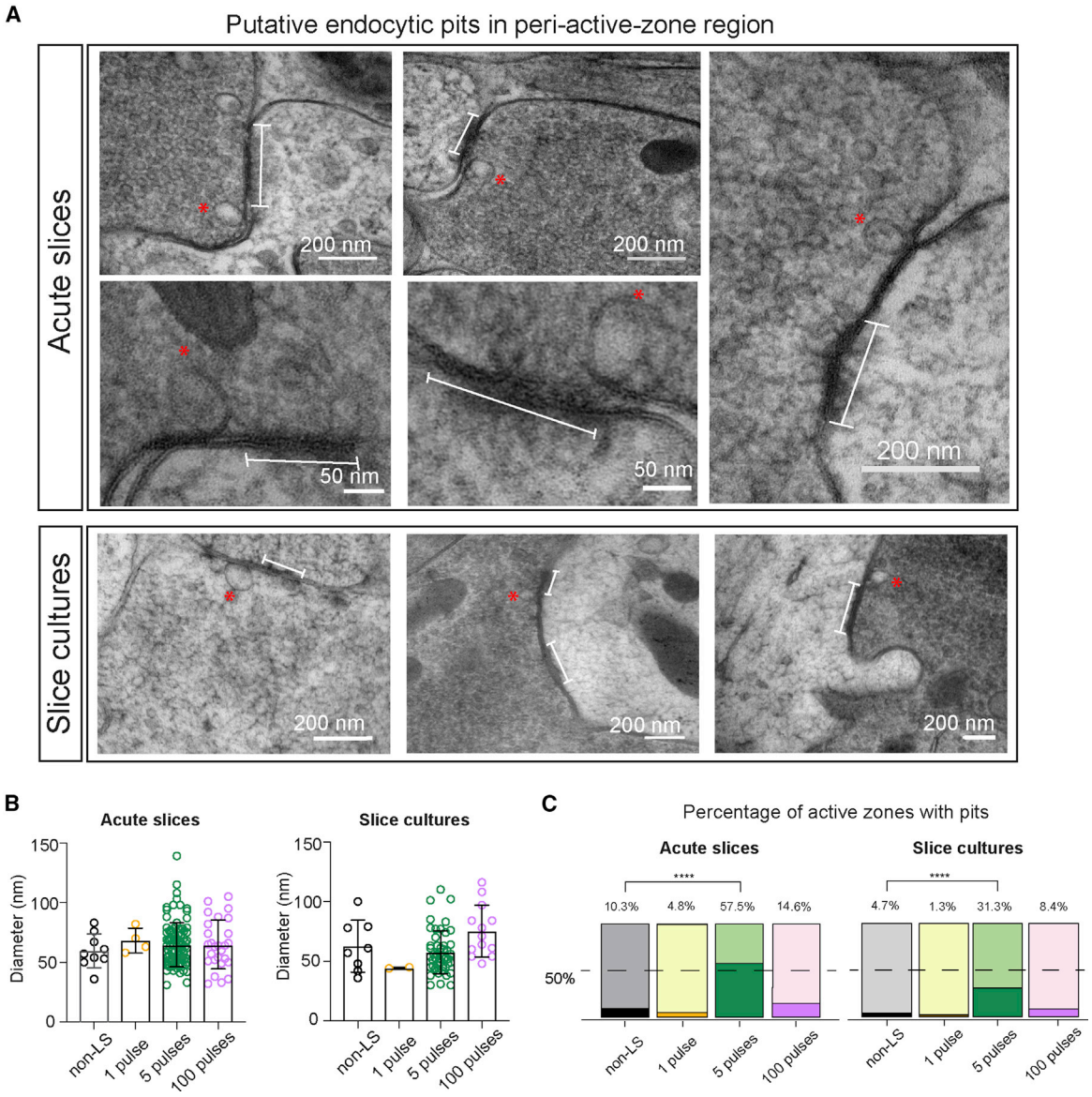

Figure 6. Presence of Putative Endocytic Pits in Peri-active-zone Regions

(A) Example EM micrographs depicting putative endocytic pits (red asterisks) in ASs (top) and SCs (bottom). Note that the AS bottom left corner panel is the same micrograph as shown in Figure S3A, center panel, as a reference to overall tissue morphology quality. Scale bar sizes are indicated in the figure.

(B) Scatterplot displaying the measured diameter of pits under each condition in both ASs and SCs. Bars show mean ± SD. Group statistic comparisons were not significant.

(C) Stacked bars displaying the percentage of active-zones with pits in peri-active-zone regions, per group, in ASs (total active-zones counted: non-LS n = 116 active-zones [AZs], 1 pulse n = 84 AZs, 5 pulses n = 146 AZs, 100 pulses n = 219 AZs) and SCs (total active-zones counted: non-LS, n = 170 AZs; 1 pulse, n = 78 AZs; 5 pulses, n = 160 AZs; 100 pulses, n = 155 AZs). Bars and whiskers denote mean ± SD. For graphical representation of statistics, *p < 0.05, **p < 0.01, ***p < 0.001, and ****p < 0.0001. Only statistically significant differences are shown in the graphs.

functional EM experiments at an identified synapse in an intact cortical network, bridging the gap between structural and functional levels.

Comparison with Previous Approaches

Functional EM ("flash and freeze") has been applied successfully to the *C. elegans* nervous system (Watanabe et al., 2013a) and to dissociated mammalian neurons in culture (Watanabe et al., 2013b). Although the technique is very powerful, it is difficult to apply to intact mammalian preparations, such as organotypic slice cultures or acute brain slices. However, such a development is critically important to use the technique for rigorously identified central synapses and to correlate structural and functional analysis of synaptic transmission (Bischofberger et al., 2006a; Blanton et al., 1989; Edwards et al., 1989; Neher, 2017). We have overcome the limitations of existing techniques

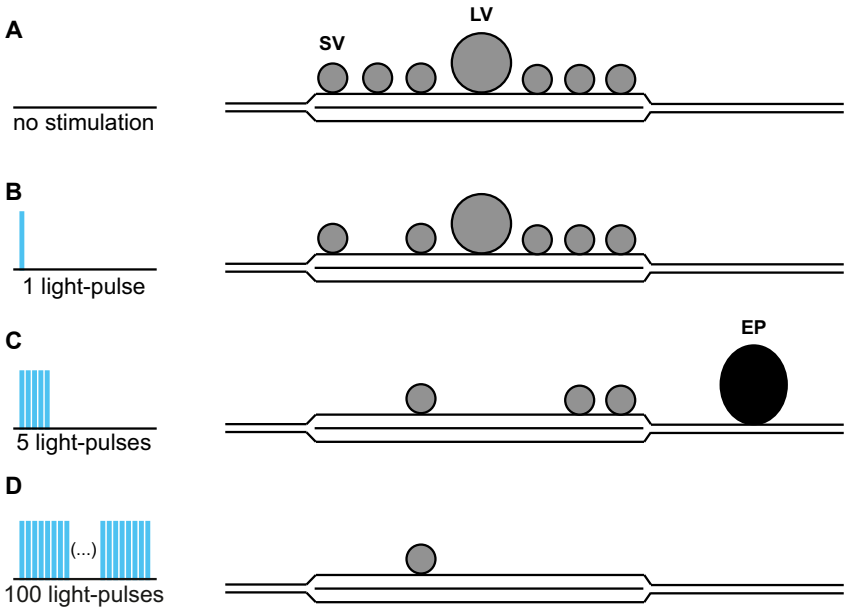

Figure 7. Docked Vesicle Pool Depletion, Activity-Dependent Vesicle Diameter Change, and Fast Endocytosis, as Revealed by Functional EM of Hippocampal Mossy Fiber Terminals

(A–D) From basal conditions (A), we observed a small decrease in docked vesicle numbers after mild stimulation (B and C) but a substantial decrease after a prolonged stimulus train (D). Thus, the docked vesicle pool and RRP overlap at hippocampal mossy fiber terminals. However, docked vesicles were still present at the AZs, indicating that either not all docked vesicles are part of the RRP or that the docked pool is rapidly refilled during the stimulus train. We additionally observed an activity-dependent change in the mean docked vesicle diameter. After a single stimulus (B), the vesicle diameter increased, suggesting that smaller vesicles (SVs) have a higher release probability. After a brief train of stimuli, the mean docked vesicle diameter decreased significantly from the previous group, suggesting that larger vesicles (LVs) were then released. Finally, after mild stimulation (C) with a short train, we observed putative endocytic pits (EPs), providing direct evidence of clathrin-independent endocytosis at the hippocampal mossy fiber synapse.

with a series of technical improvements. First, we reduced the thickness of the acute slices. Second, we introduced a recovery period at near-physiological temperature after slicing, a procedure well established to increase slice quality in electrophysiology experiments (Bischofberger et al., 2006a). Third, we redesigned the specimen sandwich to precisely match the slice thickness and lateral dimensions of the slice without further trimming to maintain the entire target network intact. Fourth, we optimized both concentration and timing of cryoprotection, adding PVP or BSA immediately before stimulation and freezing. We stimulated slices and cultures at physiological temperatures and kept both near physiological temperature for at least 10 min prior to freezing. Finally, we introduced an accelerated freeze substitution protocol. These improvements led to an optimally preserved ultrastructure in acute slices, comparable with the ultrastructure of high-pressure-frozen organotypic slice culture, the previous gold standard for HPF experiments without optogenetic stimulation (Imig et al., 2014; Studer et al., 2014; Zhao et al., 2012a, 2012b).

Potential Limitations

Although the new technique is very powerful, one needs to be aware of unavoidable limitations. First, optogenetics is used to stimulate presynaptic neurons. Although the optogenetically evoked release is clearly AP dependent (Figure 1K), we cannot fully discard the possibility that Ca^{2+} influx through channelrhodopsin may alter release probability, short-term dynamics, or the mode of release (Zhang et al., 2009). Furthermore, the kinetics of the channelrhodopsin set limits to the maximal stimulation frequency. This may be critical in synaptic plasticity experiments where high-frequency stimulation must be used for induction. Second, cryoprotection is an integral component of the technique. Although PVP does not affect transmitter release in electrophysiological experiments (Figure S2D), we cannot exclude that it affects unmeasured functional parameters or structural properties of the synapse. Third, slices are maintained in CO_2 and O_2-equilibrated solution prior to freezing for optimal slice preservation. Because the sandwich mounting is not absolutely gas tight, changes in CO_2 and O_2 partial pressure may negatively affect tissue quality as the time interval between stimulation and freezing is extended.

Insights into Mechanisms of Mossy Fiber Synaptic Transmission

Our results shed new light on the relationship between structure and function of the hippocampal mossy fiber synapse, a key synapse in the trisynaptic circuit of the hippocampus (Andersen et al., 1971; Bischofberger et al., 2006b; Rolls and Treves, 1994; Figure 7). First, our EM analysis shows that the docked vesicle pool at active-zones at hippocampal mossy fiber synapses is substantially reduced by 71.5% after strong stimulation. The most likely explanation is that vesicles are depleted because they undergo full fusion. Although we formally cannot rule out undocking of vesicles, we consider this unlikely because of the slow time course of this process (Murthy and Stevens, 1999). Thus, we conclude that the RRP and docked vesicle pool are highly overlapping (Schikorski and Stevens, 2001; Imig et al., 2014). However, the overlap is not complete. This may suggest that only a subset of docked vesicles is releasable (Ariel and Ryan, 2010) or may be explained by rapid refilling of the docked pool (Wang et al., 2016).

Second, our results confirm that the vesicle diameter at mossy fiber synapses is variable and skewed toward larger diameters, extending previous work on this synapse (Henze et al., 2002; Rollenhagen et al., 2007). Additionally, we found that stimulation reduces the mean diameter of docked vesicles. The most parsimonious explanation is that, during repetitive stimulation, the

smaller vesicles are released first, implying that they have a higher release probability. Consistent with this interpretation, the vesicle fusion rate increases with membrane curvature (Martens et al., 2007; Lin et al., 2012), presumably because curvature stress of the vesicular membrane provides additional energy for bilayer fusion.

Finally, our experiments reveal that moderate repetitive stimulation results in formation of endocytic pits, possibly by a clathrin-independent mechanism. Thus, we provide direct ultrastructural evidence of clathrin-independent endocytosis at the hippocampal mossy fiber synapse, as suggested previously on the basis of capacitance measurements (Hallermann et al., 2003; Delvendahl et al., 2016). However, we did not observe endocytic pits after prolonged stimulation, consistent with previous studies on ultrafast endocytosis (Watanabe et al., 2013a, 2013b). This suggests that endocytosis may be switched to an alternative mode while the initial endocytic pits are cleaved off (Renden and von Gersdorff, 2007; Chanaday and Kavalali, 2018). A potential caveat of our analysis is that we focused on the active-zone and peri-active-zone regions. Endocytic structures may also form at remote sites; for example, near *puncta adherentia* (Watanabe et al., 2013a). Moreover, we examined endocytosis only after 5 and 100 stimuli. Thus, formation of further endocytic structures at later stages cannot be excluded. Future studies with full terminal analysis and at multiple time points will be needed to distinguish between these possibilities. In conclusion, our findings represent a compelling demonstration of the power of this technique, enabling new insights into the basic mechanisms of transmission at identified central synapses.

Future Perspectives

The described method has huge potential for further development. For example, the technique may be combined with post-embedding immunogold or freeze-fracture replica labeling (Nakamura et al., 2015). Such a combination may not only reveal the static molecular organization of presynaptic proteins, such as Ca^{2+} channels, but could demonstrate dynamic changes in the topography of the active-zone. The technique can be also flexibly combined with chemogenetics. This might allow dissection of the mechanisms of presynaptic homeostatic plasticity (Davis and Müller, 2015) using experiments in which chronic chemogenetic manipulation of activity *in vivo* is followed by acute optogenetic stimulation of synapses *in vitro*. Finally, the method can be easily implemented together with pharmacological manipulation. Thus, functional EM may enable structural analysis of pharmacogenetically and pharmacologically manipulated synapses.

We further demonstrated that the technique can be applied to different brain regions and, thus, to a variety of different synapses in intact networks. By genetically targeting specific cell types across different brain areas and, therefore, their synapses, we can expand our understanding of similarities and differences in activity-dependent changes across central synapses. This, in turn, can provide answers to fundamental questions in neuroscience. For example, the new method may help to answer the controversial question of whether synaptic vesicles undergo exocytosis by full fusion or whether a transmitter is released by transient fusion pores (Aravanis et al., 2003; Lisman et al., 2007), as described for dense-core vesicles (Chiang et al., 2014). Furthermore, as a question raised from our data, this approach could address depletion and refilling characteristics of the RRP at mossy fiber boutons and other central synapses. Finally, it may shed light on the mechanisms of short-term plasticity, in which the phenomenon of strengthening of transmission can result from different underlying mechanisms, depending on the synapse; e.g., hippocampal mossy fiber boutons versus calyx of Held (Langdon et al., 1995; Alle et al., 2001; Habets and Borst, 2005).

Because the new method is applicable to both acute slices and organotypic slice cultures, it will enable characterization of the synaptic properties of mouse mutants with lethal phenotypes, which only can be studied in slice culture but not in acute slices (Kerr et al., 2008). The profound similarities as well as the subtle differences between acute slices and organotypic slice culture, quantified in the present paper, will provide a reference framework for interpretation of these results. In a complementary manner, the new technique may be useful to study structural changes induced by disease states, such as epilepsy, which only can be examined in slices but not in culture (Accardi et al., 2018; Wickham et al., 2018). Thus, functional EM techniques applied to intact preparations may help us reveal the structural and functional mechanisms of transmission in intact, genetically perturbed, and disease-affected synapses.

STAR★METHODS

Detailed methods are provided in the online version of this paper and include the following:

- KEY RESOURCES TABLE
- LEAD CONTACT AND MATERIALS AVAILABILITY
- EXPERIMENTAL MODEL AND SUBJECT DETAILS
  - Animals
  - Tamoxifen application
- METHOD DETAILS
  - Tissue preparation
  - Immunofluorescence for confocal microscopy
  - Electrophysiological recordings and light stimulation
  - Pharmacological experiments
  - Preembedding and immunolabeling for electron microscopy
  - High-pressure freezing with light stimulation
  - Freeze-substitution and ultramicrotomy
  - TEM imaging and active-zone profile analysis
- QUANTIFICATION AND STATISTICAL ANALYSIS
- DATA AND CODE AVAILABILITY

SUPPLEMENTAL INFORMATION

Supplemental Information can be found online at https://doi.org/10.1016/j.neuron.2019.12.022.

ACKNOWLEDGMENTS

This project has received funding from the European Research Council (ERC) and European Commission (EC), under the European Union's Horizon 2020 research and innovation programme (ERC grant agreement No.

692692 and Marie Sklodowska-Curie 708497) and from Fonds zur Förderung der Wissenschaftlichen Forschung (Z 312-B27 Wittgenstein award and DK W 1205-B09). We thank Johann Danzl and Ryuichi Shigemoto for critically reading the manuscript; Walter Kaufmann, Daniel Gütl, and Vanessa Zheden for extensive EM training, advice, and experimental assistance; Benjamin Suter for substantial help with light stimulation, ImageJ plugins for analysis, and manuscript editing; Florian Marr and Christina Altmutter for technical support; Eleftheria Kralli-Beller for manuscript editing; Julia König and Paul Wurzinger (Leica Microsystems) for helpful technical discussions; and Taija Makinen for providing the Prox1-CreER^{T2} mouse line.

AUTHOR CONTRIBUTIONS

C.B.-M. (acute slices) and O.K. (organotypic slice culture) performed all experiments and data analysis. C.B.-M., O.K., and P.J. conceived the study and designed experiments. C.B.-M. and P.J. wrote the manuscript. All authors jointly revised the paper.

DECLARATION OF INTERESTS

The authors declare no competing interests.

Received: August 12, 2019
Revised: November 20, 2019
Accepted: December 13, 2019
Published: January 9, 2020; corrected online: November 23, 2020

REFERENCES

Accardi, M.V., Huang, H., and Authier, S. (2018). Seizure liability assessments using the hippocampal tissue slice: Comparison of non-clinical species. J. Pharmacol. Toxicol. Methods *93*, 59–68.

Acsády, L., Kamondi, A., Sík, A., Freund, T., and Buzsáki, G. (1998). GABAergic cells are the major postsynaptic targets of mossy fibers in the rat hippocampus. J. Neurosci. *18*, 3386–3403.

Alabi, A.A., and Tsien, R.W. (2012). Synaptic vesicle pools and dynamics. Cold Spring Harb. Perspect. Biol. *4*, a013680.

Alle, H., Jonas, P., and Geiger, J.R.P. (2001). PTP and LTP at a hippocampal mossy fiber-interneuron synapse. Proc. Natl. Acad. Sci. USA *98*, 14708–14713.

Amaral, D.G., and Dent, J.A. (1981). Development of the mossy fibers of the dentate gyrus: I. A light and electron microscopic study of the mossy fibers and their expansions. J. Comp. Neurol. *195*, 51–86.

Andersen, P., Bliss, T.V.P., and Skrede, K.K. (1971). Lamellar organization of hippocampal pathways. Exp. Brain Res. *13*, 222–238.

Aravanis, A.M., Pyle, J.L., and Tsien, R.W. (2003). Single synaptic vesicles fusing transiently and successively without loss of identity. Nature *423*, 643–647.

Ariel, P., and Ryan, T.A. (2010). Optical mapping of release properties in synapses. Front. Neural Circuits *4*, 18.

Bazigou, E., Lyons, O.T., Smith, A., Venn, G.E., Cope, C., Brown, N.A., and Makinen, T. (2011). Genes regulating lymphangiogenesis control venous valve formation and maintenance in mice. J. Clin. Invest. *121*, 2984–2992.

Bischofberger, J., Engel, D., Frotscher, M., and Jonas, P. (2006b). Timing and efficacy of transmitter release at mossy fiber synapses in the hippocampal network. Pflügers Arch. *453*, 361–372.

Bischofberger, J., Engel, D., Li, L., Geiger, J.R.P., and Jonas, P. (2006a). Patch-clamp recording from mossy fiber terminals in hippocampal slices. Nat. Protoc. *1*, 2075–2081.

Blanton, M.G., Lo Turco, J.J., and Kriegstein, A.R. (1989). Whole cell recording from neurons in slices of reptilian and mammalian cerebral cortex. J. Neurosci. Methods *30*, 203–210.

Chanaday, N.L., and Kavalali, E.T. (2018). Optical detection of three modes of endocytosis at hippocampal synapses. eLife *7*, e36097.

Chiang, H.C., Shin, W., Zhao, W.D., Hamid, E., Sheng, J., Baydyuk, M., Wen, P.J., Jin, A., Momboisse, F., and Wu, L.G. (2014). Post-fusion structural changes and their roles in exocytosis and endocytosis of dense-core vesicles. Nat. Commun. *5*, 3356.

Chicurel, M.E., and Harris, K.M. (1992). Three-dimensional analysis of the structure and composition of CA3 branched dendritic spines and their synaptic relationships with mossy fiber boutons in the rat hippocampus. J. Comp. Neurol. *325*, 169–182.

Claiborne, B.J., Amaral, D.G., and Cowan, W.M. (1986). A light and electron microscopic analysis of the mossy fibers of the rat dentate gyrus. J. Comp. Neurol. *246*, 435–458.

Davis, G.W., and Müller, M. (2015). Homeostatic control of presynaptic neurotransmitter release. Annu. Rev. Physiol. *77*, 251–270.

Delvendahl, I., Vyleta, N.P., von Gersdorff, H., and Hallermann, S. (2016). Fast, temperature-sensitive and clathrin-independent endocytosis at central synapses. Neuron *90*, 492–498.

Edwards, F.A., Konnerth, A., Sakmann, B., and Takahashi, T. (1989). A thin slice preparation for patch clamp recordings from neurones of the mammalian central nervous system. Pflügers Arch. *414*, 600–612.

Efron, B., and Tibshirani, R.J. (1998). An introduction to the bootstrap (London: Chapman & Hall/CRC).

Goldammer, H., Hollergschwandtner, E., Elisabeth, N.H., Frade, P.R., and Reipert, S. (2016). Automatized freeze substitution of algae accelerated by a novel agitation module. Protist *167*, 369–376.

Guzman, S.J., Schlögl, A., and Schmidt-Hieber, C. (2014). Stimfit: quantifying electrophysiological data with Python. Front. Neuroinform. *8*, 16.

Habets, R.L., and Borst, J.G.G. (2005). Post-tetanic potentiation in the rat calyx of Held synapse. J. Physiol. *564*, 173–187.

Hallermann, S., Pawlu, C., Jonas, P., and Heckmann, M. (2003). A large pool of releasable vesicles in a cortical glutamatergic synapse. Proc. Natl. Acad. Sci. USA *100*, 8975–8980.

Harris, K.M., and Weinberg, R.J. (2012). Ultrastructure of synapses in the mammalian brain. Cold Spring Harb. Perspect. Biol. *4*, a005587.

Henze, D.A., McMahon, D.B., Harris, K.M., and Barrionuevo, G. (2002). Giant miniature EPSCs at the hippocampal mossy fiber to CA3 pyramidal cell synapse are monoquantal. J. Neurophysiol. *87*, 15–29.

Heuser, J.E., Reese, T.S., Dennis, M.J., Jan, Y., Jan, L., and Evans, L. (1979). Synaptic vesicle exocytosis captured by quick freezing and correlated with quantal transmitter release. J. Cell Biol. *81*, 275–300.

Imig, C., Min, S.W., Krinner, S., Arancillo, M., Rosenmund, C., Südhof, T.C., Rhee, J., Brose, N., and Cooper, B.H. (2014). The morphological and molecular nature of synaptic vesicle priming at presynaptic active zones. Neuron *84*, 416–431.

Kerr, A.M., Reisinger, E., and Jonas, P. (2008). Differential dependence of phasic transmitter release on synaptotagmin 1 at GABAergic and glutamatergic hippocampal synapses. Proc. Natl. Acad. Sci. USA *105*, 15581–15586.

Korogod, N., Petersen, C.C., and Knott, G.W. (2015). Ultrastructural analysis of adult mouse neocortex comparing aldehyde perfusion with cryo fixation. eLife *4*, e05793.

Langdon, R.B., Johnson, J.W., and Barrionuevo, G. (1995). Posttetanic potentiation and presynaptically induced long-term potentiation at the mossy fiber synapse in rat hippocampus. J. Neurobiol. *26*, 370–385.

Lavado, A., Lagutin, O.V., Chow, L.M., Baker, S.J., and Oliver, G. (2010). Prox1 is required for granule cell maturation and intermediate progenitor maintenance during brain neurogenesis. PLoS Biol. *8*, e1000460.

Lin, C.M., Li, C.S., Sheng, Y.J., Wu, D.T., and Tsao, H.K. (2012). Size-dependent properties of small unilamellar vesicles formed by model lipids. Langmuir *28*, 689–700.

Lisman, J.E., Raghavachari, S., and Tsien, R.W. (2007). The sequence of events that underlie quantal transmission at central glutamatergic synapses. Nat. Rev. Neurosci. *8*, 597–609.

Martens, S., Kozlov, M.M., and McMahon, H.T. (2007). How synaptotagmin promotes membrane fusion. Science *316*, 1205–1208.

Ming, G.L., and Song, H. (2011). Adult neurogenesis in the mammalian brain: significant answers and significant questions. Neuron *70*, 687–702.

Miyoshi, G., Young, A., Petros, T., Karayannis, T., McKenzie Chang, M., Lavado, A., Iwano, T., Nakajima, M., Taniguchi, H., Huang, Z.J., et al. (2015). Prox1 regulates the subtype-specific development of caudal ganglionic eminence-derived GABAergic cortical interneurons. J. Neurosci. *35*, 12869–12889.

Möbius, W., Nave, K.A., and Werner, H.B. (2016). Electron microscopy of myelin: Structure preservation by high-pressure freezing. Brain Res. *1641*, 92–100.

Murthy, V.N., and Stevens, C.F. (1999). Reversal of synaptic vesicle docking at central synapses. Nat. Neurosci. *2*, 503–507.

Nakamura, Y., Harada, H., Kamasawa, N., Matsui, K., Rothman, J.S., Shigemoto, R., Silver, R.A., DiGregorio, D.A., and Takahashi, T. (2015). Nanoscale distribution of presynaptic Ca^{2+} channels and its impact on vesicular release during development. Neuron *85*, 145–158.

Neher, E. (2017). Some subtle lessons from the calyx of Held synapse. Biophys. J. *112*, 215–223.

Palay, S.L. (1956). Synapses in the central nervous system. J. Biophys. Biochem. Cytol. *2*, 193–202.

Renden, R., and von Gersdorff, H. (2007). Synaptic vesicle endocytosis at a CNS nerve terminal: faster kinetics at physiological temperatures and increased endocytotic capacity during maturation. J. Neurophysiol. *98*, 3349–3359.

Rizzoli, S.O., and Betz, W.J. (2005). Synaptic vesicle pools. Nat. Rev. Neurosci. *6*, 57–69.

Rollenhagen, A., Sätzler, K., Rodríguez, E.P., Jonas, P., Frotscher, M., and Lübke, J.H.R. (2007). Structural determinants of transmission at large hippocampal mossy fiber synapses. J. Neurosci. *27*, 10434–10444.

Rolls, E.T., and Treves, A. (1994). Neural networks in the brain involved in memory and recall. Prog. Brain Res. *102*, 335–341.

Rosenmund, C., and Stevens, C.F. (1996). Definition of the readily releasable pool of vesicles at hippocampal synapses. Neuron *16*, 1197–1207.

Salin, P.A., Scanziani, M., Malenka, R.C., and Nicoll, R.A. (1996). Distinct short-term plasticity at two excitatory synapses in the hippocampus. Proc. Natl. Acad. Sci. USA *93*, 13304–13309.

Schikorski, T., and Stevens, C.F. (1997). Quantitative ultrastructural analysis of hippocampal excitatory synapses. J. Neurosci. *17*, 5858–5867.

Schikorski, T., and Stevens, C.F. (2001). Morphological correlates of functionally defined synaptic vesicle populations. Nat. Neurosci. *4*, 391–395.

Stoppini, L., Buchs, P.A., and Muller, D. (1991). A simple method for organotypic cultures of nervous tissue. J. Neurosci. Methods *37*, 173–182.

Studer, D., Zhao, S., Chai, X., Jonas, P., Graber, W., Nestel, S., and Frotscher, M. (2014). Capture of activity-induced ultrastructural changes at synapses by high-pressure freezing of brain tissue. Nat. Protoc. *9*, 1480–1495.

Vyleta, N.P., Borges-Merjane, C., and Jonas, P. (2016). Plasticity-dependent, full detonation at hippocampal mossy fiber-CA3 pyramidal neuron synapses. eLife *5*, e17977.

Wang, S.S.H., Held, R.G., Wong, M.Y., Liu, C., Karakhanyan, A., and Kaeser, P.S. (2016). Fusion competent synaptic vesicles persist upon active zone disruption and loss of vesicle docking. Neuron *91*, 777–791.

Watanabe, S., Liu, Q., Davis, M.W., Hollopeter, G., Thomas, N., Jorgensen, N.B., and Jorgensen, E.M. (2013a). Ultrafast endocytosis at Caenorhabditis elegans neuromuscular junctions. eLife *2*, e00723.

Watanabe, S., Rost, B.R., Camacho-Pérez, M., Davis, M.W., Söhl-Kielczynski, B., Rosenmund, C., and Jorgensen, E.M. (2013b). Ultrafast endocytosis at mouse hippocampal synapses. Nature *504*, 242–247.

Wickham, J., Brödjegård, N.G., Vighagen, R., Pinborg, L.H., Bengzon, J., Woldbye, D.P.D., Kokaia, M., and Andersson, M. (2018). Prolonged life of human acute hippocampal slices from temporal lobe epilepsy surgery. Sci. Rep. *8*, 4158.

Zhang, Q., Li, Y., and Tsien, R.W. (2009). The dynamic control of kiss-and-run and vesicular reuse probed with single nanoparticles. Science *323*, 1448–1453.

Zhao, S., Studer, D., Chai, X., Graber, W., Brose, N., Nestel, S., Young, C., Rodriguez, E.P., Saetzler, K., and Frotscher, M. (2012a). Structural plasticity of hippocampal mossy fiber synapses as revealed by high-pressure freezing. J. Comp. Neurol. *520*, 2340–2351.

Zhao, S., Studer, D., Graber, W., Nestel, S., and Frotscher, M. (2012b). Fine structure of hippocampal mossy fiber synapses following rapid high-pressure freezing. Epilepsia *53*, 4–8.

STAR★METHODS

KEY RESOURCES TABLE

REAGENT or RESOURCE	SOURCE	IDENTIFIER
Antibodies		
Rabbit Polyclonal anti-NeuN	Invitrogen (Thermo fisher)	RRID: AB_2554049
Goat anti-rabbit Alexa Fluor 647	Molecular Probes (Thermo fisher)	RRID: AB_141663
Rabbit Polyclonal anti-GFP	Abcam	RRID: AB_305564
Goat anti-rabbit Biotinylated IgG	Vector Laboratories	RRID: AB_2313606
Chemicals, Peptides, and Recombinant Proteins		
Tamoxifen	Sigma-Aldrich	Cat # T5648-1G
4-hydroxy-tamoxifen	Sigma-Aldrich	Cat # H7904-5mg
NaCl	VWR (Merck)	Cat # 1.06404.1000
Sucrose	Sigma-Aldrich	Cat # 16104
$NaHCO_3$	VWR (Merck)	Cat # 1.06329.1000
D-glucose	VWR (Merck)	Cat # 1.08342.1000
KCl	VWR (Merck)	Cat # 26764.232
NaH_2PO_4	VWR (Merck)	Cat # 1.06346.0500
$CaCl_2$	VWR (Merck)	Cat # 1.02382.0250
$MgCl_2$	Honeywell	Cat # M9272-1KG
HEPES	Sigma-Aldrich	Cat # M3375-100G
EGTA	Sigma-Aldrich	Cat # EO396-100G
Na_2ATP	Sigma-Aldrich	Cat # A3377-100G
Hank's Balanced Salt Solution (HBSS)	GIBCO	Cat # 24020091
20% D-Glucose	Braun	Cat # 2356746
Minimum Essential Medium	GIBCO	Cat # 11095-080
Basal medium eagle	Invitrogen	Cat # 41010026
Horse serum	GIBCO	Cat # 26050070
Glutamax	GIBCO	Cat # 35050-061
NaH_2PO_4 $2H_2O$ (for PBS)	VWR (Merck)	Cat # 1.06580.0500
Paraformaldehyde 20%	TAAB	Cat # FO 17/1
Normal goat serum	Dianova	Cat # 005-000-121
Trition X – 100	Sigma-Aldrich	Cat # X100-100ml
DAPI, dilactate	Sigma-Aldrich	Cat # D9564-10mg
Prolong Gold antifade	Invitrogen	Cat # P36934
Tetrodotoxin citrate	Alomone Labs	Cat # T-550
polyvinylpyrrolidone (PVP)	Sigma-Aldrich	Cat # PVP10-100G
Bovine serum albumin (BSA)	Sigma-Aldrich	Cat # A9647-100G
Glutaraldehyde 25%	Carl Roth	Cat # 4157.1
Sodium Azide	Sigma-Aldrich	Cat # S8032-25G
Tris (for TBS)	Sigma-Aldrich	Cat # 25,285-9
Streptavidin biotin complex (ABC Kit)	Vector laboratories	Cat # PK-6100
3,3′ DAB (Diaminobenzidin)	Sigma-Aldrich	Cat # D5637-5G
Osmium tetroxide	Science services (EMS)	Cat # 19130
Durcupan ACM Resin Single component A	Sigma-Aldrich	Cat # 44611-100ml
Durcupan ACM Resin Single component B	Sigma-Aldrich	Cat # 44612-100ml
Durcupan ACM Resin Single component C	Sigma-Aldrich	Cat # 44613-100ml
Durcupan ACM Resin Single component D	Sigma-Aldrich	Cat # 44614-100ml

(*Continued on next page*)

Continued		
REAGENT or RESOURCE	SOURCE	IDENTIFIER
Uranyl acetate $2H_2O$	Serva	Cat # 77870.02
Lead (II) Nitrate	Sigma-Aldrich	Cat # 228621-100G
Acetone, HPLC grade	ChemLab	Cat # CL00.0172.2500
Experimental Models: Organisms/Strains		
Prox1-CreER^{T2} mouse line	Bazigou et al., 2011	PMID: 21765212
C57BL6/J wild-type mice	Charles River Germany (from The Jackson Laboratory)	RRID: IMSR_JAX:000664
Tg(Prox1-Cre)SJ32Gsat/Mmucd mouse line	Mutant Mouse Resource & Research Centers	RRID: MMRRC_036644-UCD
B6;129S6-Gt(ROSA)26Sor$^{tm9(CAG-tdTomato)Hze}$/J mouse line	The Jackson Laboratory	RRID: IMSR_JAX:007905
B6;129S-Gt(ROSA)26Sor$^{tm32(CAG-COPA*H134R/EYFP)Hze}$/J mouse line	The Jackson Laboratory	RRID: IMSR_JAX:012569
Software and Algorithms		
Multiclamp (version 1.3.0.05)	Axon Instruments/Molecular Devices	https://www.moleculardevices.com/
Igor Pro (version 6.3.4.1)	WaveMetrics	https://www.wavemetrics.com/
Radius Software	EMSIS	https://www.emsis.eu/products/software/radius/
Stimfit (version 0.14.13)	Guzman et al., 2014	PMID: 24600389
AxoGraph (version 1.7.2)	AxoGraph	https://axograph.com/
Fiji (ImageJ version 2.0.0-rc-69/1.52n)	NIH, Open source	https://fiji.sc/
Graphpad Prism (version 8)	Graphpad	https://www.graphpad.com/
Adobe Illustrator (version 23.0.4)	Adobe	https://www.adobe.com/products/illustrator.html
Imaris	Oxford Instruments	https://imaris.oxinst.com/
Other		
Membrane insert (sterilized culture plate insert)	Millicell-CM, Millipore	PICMORG50

LEAD CONTACT AND MATERIALS AVAILABILITY

Further information and requests for resources and reagents should be directed to and will be fulfilled by the Lead Contact, Peter Jonas (peter.jonas@ist.ac.at). This study did not generate new unique reagents.

EXPERIMENTAL MODEL AND SUBJECT DETAILS

Animals

Experiments were performed in acute slices or organotypic slice cultures from male and female mice. For acute slice experiments, slices were prepared from 25–40-day-old mice (P25–40). This age range represents fully developed mossy fiber terminals, as maturation happens at P21 (Chicurel and Harris, 1992; Claiborne et al., 1986; Amaral and Dent, 1981). For organotypic slice culture experiments, tissue was extracted from 5–8-day-old mice (P5–8). Cre-driver lines used in this study were a Prox1-CreER^{T2} line (Bazigou et al., 2011; PMID: 21765212) and a Tg(Prox1-Cre)SJ32Gsat/Mmucd line (Mutant Mouse Resource & Research Centers; RRID:MMRRC_036644-UCD) (for Figure S1). Reporter lines were a B6;129S6-Gt(ROSA)26Sor$^{tm9(CAG-tdTomato)Hze}$/J line (The Jackson Laboratory; line #007905; RRID: IMSR_JAX:007905) and a B6;129S-Gt(ROSA)26Sor$^{tm32(CAG-COPA*H134R/EYFP)Hze}$/J line (The Jackson Laboratory; line #012569; RRID:IMSR_JAX:012569), as well as C57BL6/J wild-type animals (Charles River Germany, from The Jackson Laboratory; line #000664; RRID:IMSR_JAX:000664). Transgenic mice were genotyped by PCR, with DNA extracted from toe or ear clippings.

Tamoxifen application

For acute slice experiments, tamoxifen (Sigma-Aldrich) injections were made from a stock solution of 20 mg ml^{-1} in corn oil (Sigma-Aldrich). For maximum expression of channelrhodopsin in GCs, each mouse received two intraperitoneal (IP) injections of tamoxifen at 100 mg kg^{-1} of mouse body weight, given 2–3 days apart. Mice were used for experiments after a minimum of 7–10 days after

injections. For organotypic slice culture experiments, 5 μM of 4-hydroxy-tamoxifen (Sigma-Aldrich) was added to culture medium for 24 hours on the 7th day *in vitro* (DIV). Cultures were then used for experiments 2–3 weeks (21–28 DIV) after tamoxifen application. Animals were bred in a colony maintained in the preclinical animal facility at IST Austria. All procedures strictly complied with IST Austria, Austrian, and European ethical regulations for animal experiments, and were approved by the Bundesministerium für Wissenschaft, Forschung und Wirtschaft of Austria (BMWFW-66.018/0010-WF/V/3b/2015 and BMWFW-66.018/0008-V/3b/2018).

METHOD DETAILS

Tissue preparation

Acute slices were prepared as previously described for optimal preservation of the hippocampal mossy fiber tract (Bischofberger et al., 2006a). Mice were lightly anaesthetized with isoflurane and rapidly decapitated. The brain was dissected from the skull and blocked with a "magic-cut" under ice-cold high-sucrose solution containing: 87 mM NaCl, 75 mM sucrose, 25 mM $NaHCO_3$, 10 mM D-glucose, 2.5 mM KCl, 1.25 mM NaH_2PO_4, 0.5 mM $CaCl_2$, and 7 mM $MgCl_2$, equilibrated with 5% CO_2 and 95% O_2. Transverse hippocampal slices were sectioned at 200–300 μm thickness for electrophysiology experiments and at 150–200 μm for high-pressure freezing (HPF), using a vibratome (VT1200S, Leica Microsystems) in ice-cold high-sucrose solution. Slices were transferred to a maintenance chamber, and recovered at 35°C for 30–45 min. For HPF, slices from left and right hemisphere were stored in different chambers (see STAR Methods section for High-Pressure Freezing with Light Stimulation). After recovery, slices were kept at room temperature (~23°C) until recording, for up to 4–5 hours. For HPF, after recovery and until freezing, slices were transferred to a second set of maintenance chambers filled with ACSF solution, identical to solution used for electrophysiology recordings, containing: 125 mM NaCl, 25 mM $NaHCO_3$, 25 mM D-glucose, 2.5 mM KCl, 1.25 mM NaH_2PO_4, 2 mM $CaCl_2$, and 1 mM $MgCl_2$, equilibrated with 5% CO_2 and 95% O_2. Finally, 5–10 min prior to freezing, slices were transferred into a chamber filled ACSF at 37°C, as all freezing experiments were performed from physiological temperature (37°C). Sagittal cerebellum slices and coronal brainstem slices (200 μm thickness) were cut with identical procedures.

Hippocampal organotypic slice cultures were prepared from both hemispheres using the Stoppini-type method (Stoppini et al., 1991; Kerr et al., 2008). The entire hippocampus with entorhinal cortex was dissected and cut, perpendicularly to the longitudinal axes, using a McIllwain tissue chopper. Hippocampus extraction and cutting were performed in a medium containing Hanks' Balanced Salt Solution (HBSS, GIBCO) and 20% D-glucose (Braun). Slices were placed on microporous membrane inserts (Millicell, Millipore) floating on culture media containing 50% minimum essential medium, 25% basal medium Eagle, 25% heat-inactivated horse serum, 2 mM glutamax (all from GIBCO), and 0.62% D-glucose (Braun), pH 7.2. Slice cultures were kept at 37°C and 5% CO_2, until used for HPF or electrophysiology experiments. Note that there are limitations to the slice culture system, including the possibility of enhanced connectivity.

Immunofluorescence for confocal microscopy

For immunohistochemistry (Figure S1A and S1B), mice were anaesthetized with isoflurane and transcardially perfused with warm (~37°C) 0.1 M phosphate buffer (PB) solution, pH 7.35, followed by ice-cold 4% paraformaldehyde (PFA) in 0.1 M PB. Brains were dissected, incubated overnight in 4% PFA and rinsed with 0.1 M PB prior to sectioning. Hippocampal horizontal sections (50 μm thickness) were cut in 0.1 M PB using a vibratome (Leica VT1200S). Organotypic slice cultures were fixed using 4% PFA in 0.1 M PB at 4°C for 30 min, after 14 DIV. After sectioning or, for cultures, directly after fixing, the tissue was washed in 0.1 M PB and subsequently incubated for 1 hour in blocking solution (10% normal goat serum (NGS) in PB). Next, tissue was incubated for 72 hours with primary antibody (0.1 M PB with 0.4% Triton, 5% NGS and 1:500 rabbit anti-NeuN; Thermo Fisher Scientific Cat# PA5-37407, RRID: AB_2554049) at 4°C, followed by washes with 0.1 M PB. Subsequently, tissue was incubated for 24 hours with secondary antibody (0.1 M PB with 0.3% Triton, 5% NGS and 1:1000 goat anti rabbit Alexa 647; Molecular Probes Cat# A-21244, RRID: AB_141663). Samples were then washed and incubated in DAPI (0.00003 mg ml^{-1}) for 10 min. Finally, sections were mounted in Prolong Gold antifade embedding medium (Invitrogen). Fluorescence images were acquired using a confocal microscope (Leica SP5 upright) with sequential scanning of fluorescent signals using an air-objective (10x / numerical aperture 0.3 or 20x / numerical aperture 0.5). Confocal images were analyzed with Fiji open source software. Cell-counting for the tamoxifen dose-response curve was done in Imaris (Oxford Instruments).

Electrophysiological recordings and light stimulation

After tissue preparation, slices and cultures were transferred to a recording chamber and superfused with ACSF. Recordings were performed at near-physiological temperature. For acute slice recordings, slices were visualized with a Zeiss Axioskop 2 FS Plus microscope, equipped with DIC optics and a 60x water immersion Olympus objective. For slice culture experiments, a Zeiss Axio Examiner D1 microscope and a 63x water immersion Zeiss Plan-Apochromat objective was used. For excitation of tdTomato and channelrhodopsin, a high-power LED head (LED4D212; Thorlabs) and 4-channel LED driver (DC4104; Thorlabs) were used in combination with Semrock BrightLine single-band bandpass filters 536/40 nm and 607/70 nm with a 562 nm dichroic mirror for tdTomato excitation, and 458/64 nm and 531/40 nm with a 506 nm dichroic mirror for channelrhodopsin stimulation with 470 nm wavelength. The light path was optimized so that the light intensity at the tissue surface with wide-field stimulation with a 10x objective closely

resembled that of the Leica EM ICE high-pressure freezing machine LED range (intensity at specimen 5.5–8.0 mW mm^{-2}). Timing and intensity of light pulses were repeatedly checked by photodiode measurements.

Patch electrodes were pulled from borosilicate glass capillaries (2 mm outer diameter, 0.5 mm wall thickness; Hilgenberg) with a horizontal puller (P-1000, Sutter Instrument). For whole-cell recordings in acute slices and cultures, pipettes were filled with intracellular solution containing: 148 mM K-gluconate, 2 mM KCl, 2 mM $MgCl_2$, 2 mM Na_2ATP, 10 mM EGTA, and 10 mM HEPES (297–300 mOsm, pH 7.28), with a holding potential of −70 mV, and chloride reversal potential of −82 mV. Signals were recorded with a Multiclamp 700A (acute slices) or an Axopatch 200A amplifier (slice cultures) (Axon Instruments) and digitized with a CED 1401 plus interface (Cambridge Electronic Design). Pulse generation and data acquisition were performed using FPulse version 3.3.3 (U. Fröbe, Freiburg, Germany) and Igor Pro version 6.3.4.1 (WaveMetrics). Data were analyzed with Stimfit version 0.14.13 (Guzman et al., 2014) or Axograph Software version 1.7.2.

Pharmacological experiments

During electrophysiology recordings, tetrodotoxin (TTX) (voltage-gated Na^+ channels, BioTrend or Alomone Labs) and PVP were delivered by bath application at concentrations specified in the results section. For HPF control experiments, samples were incubated with TTX-containing ACSF for ~10 min prior to freezing.

Preembedding and immunolabeling for electron microscopy

For EM preembedding immunolabeling experiments (Figure S1D), animals were perfused as described for confocal light-microscopy, but with ice-cold 4% PFA and 0.05% glutaraldehyde in 0.1 M PB, pH 7.4. Brains were sectioned at 70 μm in 0.1 M PB and sections were stored in 0.025% NaN_3 in PB at 4°C. For cryo-protection, samples were transferred to sucrose solutions of increasing concentration (5%, 10%, and 20% in PB), for 1 hour each and left overnight in 20% sucrose solution at 4°C. Samples were transferred to a 12-well plate. Next, plates were placed directly onto liquid nitrogen (floating) for about 1 min. The plate was removed and samples were thawed rapidly with large volumes of 0.1 M PB. Samples were re-infiltrated with 20% sucrose and freeze-thaw was repeated 2 to 3 times. For immunolabeling, samples were first washed in 50 mM Tris-buffered saline (TBS; 0.9% NaCl, pH 7.4). Next, sections were incubated in 50 mM glycine in TBS for 1 hour, blocked in 10% normal serum and 2% BSA in TBS, and incubated in rabbit polyclonal anti-GFP primary antibody (1:5000, Abcam Cat# ab6556, RRID: AB_305564) for 36 hours at 4°C in TBS with 2% BSA. After wash in TBS, sections were incubated with biotinylated IgG anti-rabbit secondary antibody (1:400, Vector Laboratories Cat# BA-1000, RRID: AB_2313606) in TBS with 2% BSA overnight at 4°C. Next, samples underwent reaction with streptavidin biotin complex (ABC kit, Vector laboratories). Solution A (1/100) and B (1/100) were mixed in TBS with 0.2% BSA and samples were incubated for 3 hours. Samples were then washed in TBS, followed by only tris buffer (TB), at room temperature. Next, samples were incubated in 0.5 mg ml^{-1} DAB in TB for 5 min, with 0.003% hydrogen peroxide in TB, and washed in TB. Subsequently, samples were washed and post-fixed in 1% glutaraldehyde in 0.1 M phosphate buffer (PB) for 20 min. Samples were contrasted by incubation with 1% osmium tetroxide (Science Services) in 0.1 M PB for 45 min followed by incubation in 1% uranyl acetate and 50% ethanol for 30 min in darkness. Next they went through a series of dehydration steps in ethanol and infiltrated in propylene oxide, followed by infiltration with 1:2 and 2:1 Durcupan resin (10 g reagent A, 10 g B, 0.3 g C, and 0.3 g D) and propylene oxide mix, and embedded in pure Durcupan resin overnight.

High-pressure freezing with light stimulation

HPF was performed with a Leica EM ICE high-pressure freezing apparatus (Leica Microsystems) equipped with a blue LED light stimulation module 460 nm wavelength; LED intensity at specimen 5.5–8.0 mW mm^{-2}). The Leica EM ICE specimen assembly table was kept at 40°C at all times during specimen sandwich assembly to keep all materials and samples close to physiological temperature. The freezing chamber was kept at 37°C. After slicing and recovery procedures, hippocampal acute slices were frozen in filler medium containing 15% PVP (Sigma Aldrich) in ACSF, equilibrated with 5% CO_2 and 95% O_2 and kept at 37°C. We tested carrier filler medium with ACSF alone, ACSF with 20% BSA, and ACSF with varying concentrations of PVP from 5 to 20% (Möbius et al., 2016). We noticed that spontaneously opened sapphire sandwiches immediately after freezing had a higher likelihood of leading to damaged acute slice samples. The use of 15% PVP was ideal to both prevent sandwich opening after freezing, but also avoid irreversible tissue adherence to the sapphires. The specimen sandwich was assembled with a 6-mm diameter sapphire system, including transparent half-cylinder cartridges (Leica) for light stimulation, a middle-plate (Leica), two 120 μm sapphire disks, a 150 or 200-μm thick spacer ring, and a 450- or 400-μm thick top ring (Leica or Engineering Office M. Wohlwend, Sennwald, Switzerland) as required (Figure S2). The outer diameter of sapphire disks and rings was 6 mm. The inner diameter of the rings was 5 mm for larger slices and 4 mm for smaller slices. We found that sandwiches assembled with 4 mm inner diameter rings were more stable and the sapphire disks were less likely to break, however infiltration during freeze-substitution took longer. The order of assembly was as follows: the bottom sapphire disk was placed on the middle plate, followed by the spacer ring with a drop of filler medium over the ring to adhere it to the sapphire disk, the sample, and the top sapphire disk. Slices were transferred carefully but quickly to the sapphire disk, using a paintbrush number 4, always covered with solution, keeping the slice as flat as possible. The optical fiber for light stimulation was located on the top of the freezing chamber. Left and right hemispheres were frozen separately, for unequivocal tracking of the light-stimulated side based on hippocampal morphology, until embedding with the light-stimulated side facing down. Organotypic slice cultures were taken out of the incubator and the tissue attached to membrane was cut out with a 4-mm biopsy punch (Ted Pella). The time

from taking the slice cultures out of incubator until freezing was less than 10 min. Cryoprotectant use on cultures was tested at a range of 5%–20% BSA and the optimum concentration resulting in best ultrastructure was obtained with filler medium containing 15% BSA (Sigma-Aldrich) in ACSF at 37°C (Studer et al., 2014). For freezing cultures, "hybrid" sandwiches were used. They consisted of a 6 mm metal carrier (5 mm inner diameter, type A, Leica) at the bottom, and a 6 mm, 120-μm thick sapphire disk, and a 200-μm thick top ring (Wohlwend) on the top. Each culture, with the membrane facing down, was placed in the metal carrier well covered with filler solution and closed with the sapphire disk for subsequent light stimulation. This configuration increased the stability of the sandwich and the control of light-stimulated side orientation, as it was always facing the sapphire disk.

Freeze-substitution and ultramicrotomy

We tested different FS protocols based on other studies that used HPF in fresh (non-fixed) tissue, both organotypic slice cultures and acute slices (Studer et al., 2014), and organotypic slice cultures alone (Imig et al., 2014). As the previously used protocols were several days long, we implemented a shaking device that fits on top of the automated freeze-substitution (AFS) apparatus (Goldammer et al., 2016), to shake the samples throughout the procedure to improve infiltration and shorten the duration. Additionally, we tested protocols with and without tannic acid, with different concentrations of osmium tetroxide, with and without shaking (i.e., different duration), and different temperature steps and various post-staining parameters. The final protocol more closely resembled the one developed by Studer et al. (2014). For the first day of freeze-substitution, the HPF samples were transferred from liquid nitrogen to vials with 0.1% tannic acid in acetone, frozen in liquid nitrogen. Vials were then transferred to either a Leica EM AFS1 or AFS2 kept at −90°C and shaken for 22–24 hours. For acute slice samples frozen with spacer rings with 4 mm inner diameter, samples were shaken longer, for at least 26 hours to ensure that the sandwich opens for proper infiltration. On the second day, samples were washed 3–4 times, while kept inside the FS machines, with acetone chilled to −90°C for 10 min each. Next, the contrasting cocktail with 2% osmium and 0.2% uranyl acetate in acetone, also first chilled to −90°C, was added to each vial and shaken overnight. For acute slices, samples were kept at −90°C for 7–10 hours. For organotypic slice cultures, samples were kept at −90°C for 6 hours. Next, the temperature was raised to −60°C within 2 hours (15°C/hour) and kept at −60°C for 3 hours (3.5 hours for 4-mm diameter spacers); then raised to −30°C in 4 hours (7.5°C/hour), and kept at −30°C for 3 hours (3.5 hours for 4-mm inner diameter spacers); then raised to 0°C in 3 hours (10°C/hour). Samples were kept at 0°C only for ~10 min. Once the substitution protocol was concluded, the vials were transferred to ice for washes with ice-cold acetone, 3 times for 10 min each. They were then transferred to room-temperature glass dishes, always submerged in acetone, to visually check that the slices and cultures were intact, all sandwiches properly opened, and the tissue adequately infiltrated. They were then washed twice with propylene oxide for 10 min each and infiltrated with hard Durcupan resin (11.4 g reagent A, 10 g B, 0.3 g C, and 0.1 g D) at 2:1, 1:1, and 1:2 propylene oxide/Durcupan resin mix for 1 hour each, shaking. They were then left in pure resin overnight and embedded in BEEM capsules. Capsules were polymerized overnight at 100°C. Acute slices were embedded with care to ensure that the light-stimulated side of the slice was facing down. Each slice culture was separated from the carrier and embedded with stimulated tissue (not membrane side) facing down for ultramicrotomy. Cured resin blocks were trimmed with glass knives and 70 nm ultrathin sections were cut with a Leica EM UC7 ultramicrotome with Diatome Histo diamond knives. Sections were picked up on Formvar-coated copper slot grids for transmission electron microscopy (TEM) imaging. Post-staining was done in 2 or 4% uranyl acetate for 10 minutes followed by lead citrate for 2–3 minutes.

TEM imaging and active-zone profile analysis

Parameters used to recognize well-preserved frozen samples and identified synapses were: overall appearance with minimal evidence of extracellular space, smooth and continuous membrane surfaces, double membranes regularly spaced, easily recognizable compact mitochondria with regular and visible cristae, cell bodies and dendrites with abundant microtubules, and nuclei with uniform chromatin (Studer et al., 2014). Hippocampal mossy fiber boutons were identified in the hippocampal CA3b and CA3c subregions. They were found in high density along the mossy fiber tract in *stratum lucidum*, adjacent to *stratum pyramidale*. They were recognized based on previously well-characterized morphological features large size, high density of clear synaptic vesicles, presence of large dense core vesicles, high-density of mitochondria, multiple active-zones apposed to postsynaptic densities in large spines, and nonsynaptic *puncta adhaerentia* apposed to dendritic shafts. We found that near the surface of acute slices, ultrastructure was compromised, presumably by the cutting procedure. This observation was not unexpected, as it is also the case for electrophysiology experiments (Bischofberger et al., 2006a). Near the core of the slice, crystalline ice was occasionally formed during freezing. Thus, we focused our analysis on a region 20–50 μm below the surface of the slice. This range corresponds also to the acute slice depth used for electrophysiology recordings in Figure 1.

Images of ultrathin sections were taken with a transmission electron microscope (Thermo Fisher/FEI Tecnai 10, 80 kV acceleration voltage) with an OSIS Megaview III G3 camera and Radius acquisition software. All electron microscopy images were analyzed with Fiji open source software. Brightness and contrast were adjusted in Fiji, according to inherent contrast of the image, to optimize double membrane visualizations and accurate measurements. Vesicles that were less than 5 nm from the active-zone membrane were considered "docked" (Figure S6). Numbers of docked vesicles per profile were specified per 100 nm of active-zone length for reliable comparison. For direct comparison across groups, raw histogram counts were divided by the total length of active-zone analyzed for each corresponding experimental condition. The resulting histograms display vesicle density (per 100 nm of active-zone) as a function of vesicle diameter. All vesicle counting and imaging analyses were done with the experimenter blind to the condition tested on the sample.

QUANTIFICATION AND STATISTICAL ANALYSIS

Analyses were performed with Prism 8 (GraphPad Software). All data were first tested for normality with D'Agostino-Pearson test. Statistical comparison of all data groups were tested by Kruskal-Wallis non-parametric one-way ANOVA, followed by Dunn's post hoc multiple comparison test. Groups with only two datasets were compared using unpaired or paired t test (electrophysiology data) or two-tailed non-parametric Mann-Whitney U test (morphological data). For graphical representation of statistics, * indicates $p < 0.05$, ** $p < 0.01$, *** $p < 0.001$, and **** $p < 0.0001$. In figures and text, values report, as specifically stated, mean or median, and errors standard deviation.

To determine whether distributions of vesicle diameter were comprised of one or two components, unbinned vesicle diameter data were analyzed by maximum likelihood fitting. Data were fit with a single normal distribution, a sum of two normal distributions, a skewed normal distribution, and a function with a sigmoidal rise, exponential decline, and shift. The model with two normal distributions was compared against all other models, using the log-likelihood ratio. Statistical significance values were obtained by bootstrap analysis (Efron and Tibshirani, 1998). Original data were duplicated 1000 times, shuffled by random permutation, and re-segmented into blocks of original length, resulting in 1000 resampled datasets. These datasets were analyzed by maximum-likelihood fitting, similar to the original data. Finally, the distribution of the log–likelihood ratios was compared against the Akaike information criterion. To provide a rigorous testing of the two-component model, the log likelihood for the best one-component model was used for comparison.

DATA AND CODE AVAILABILITY

Original data and analysis programs will be provided by the corresponding authors (C.B.M. and P.J.) upon reasonable request. Computer code was not generated in this study.

Update

Neuron
Volume 108, Issue 5, 9 December 2020, Page 1011

DOI: https://doi.org/10.1016/j.neuron.2020.11.015

Neuron

CellPress
OPEN ACCESS

Correction

Functional Electron Microscopy, "Flash and Freeze," of Identified Cortical Synapses in Acute Brain Slices

Carolina Borges-Merjane,* Olena Kim, and Peter Jonas*
*Correspondence: carolina.borges-merjane@ist.ac.at (C.B.-M.), peter.jonas@ist.ac.at (P.J.)
https://doi.org/10.1016/j.neuron.2020.11.015

(Neuron *105*, 992–1006.e1–e6; March 18, 2020)

In the original version of the Supplemental Information of this paper, the electron micrographs in the fourth column of Figure S1D were a repetition of the bottom subpanel in the second column. This has now been corrected online, with the fourth column of Figure S1D now deleted. The authors apologize for this oversight.

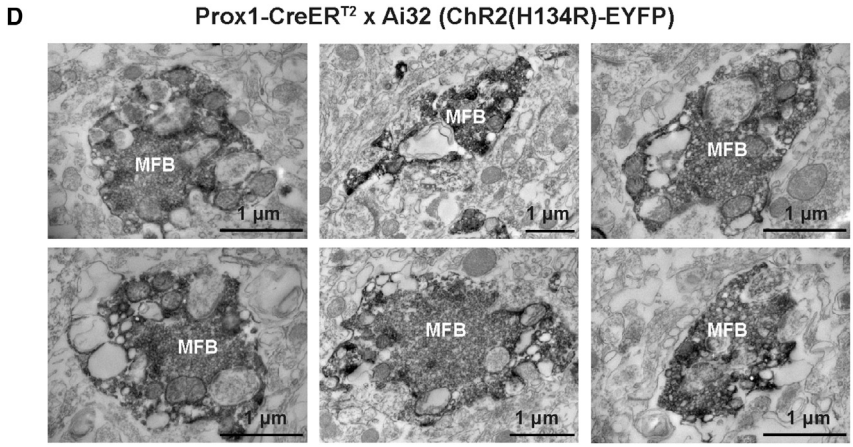

Figure S1. related to Figure 1. Specific labeling and channelrhodopsin expression in hippocampal granule cells (corrected)

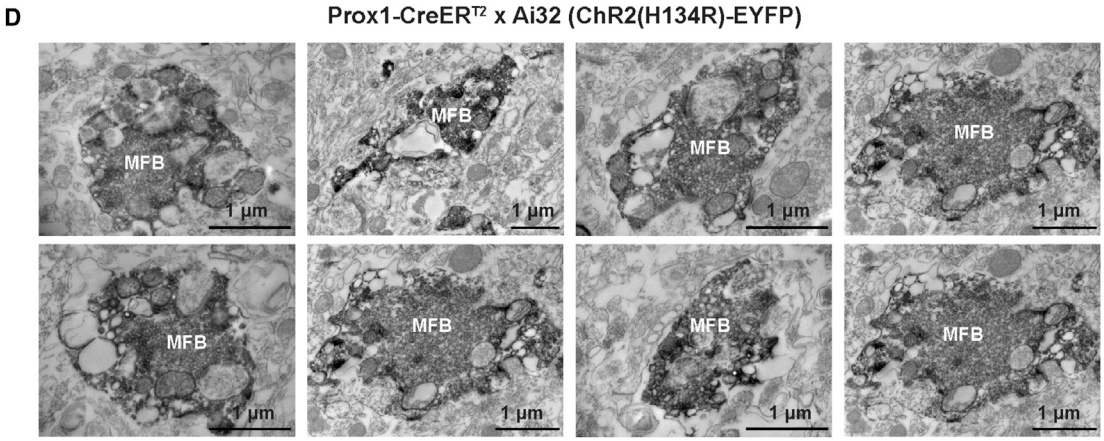

Figure S1. related to Figure 1. Specific labeling and channelrhodopsin expression in hippocampal granule cells (original)